THE UNIVERSITY *of* EDINBURGH

Modelling of monoliths for adsorption processes

Roberto Mennitto

THE UNIVERSITY *of* EDINBURGH

Thesis submitted for the degree of
Doctor of Philosophy

The University of Edinburgh

School of Engineering

Year of Submission 2021

Declaration of authorship

I hereby declare that this thesis has been composed solely by myself and that it has not been submitted, in whole or in part, in any previous application for a degree. Except where otherwise acknowledged, the work presented is entirely my own.

Roberto Mennitto

Abstract

Straight-channel monoliths are a promising means to achieve process intensification of adsorption processes compared to conventional packed beds. Their main benefits are handling of high throughputs and good thermal management. The efficiency of a straight-channel monolith can be assessed via the definition of its height equivalent to a theoretical plate (HETP) and pressure drop. This thesis aims at developing a systematic procedure for the derivation of HETP correlations for industrially relevant straight-channel monoliths and review the pressure drop correlations for monoliths available in the literature. The HETP correlations derived are validated against full 3D numerical simulations of the single representative channel of each straight-channel monolith under analysis. The HETP correlations predict with great accuracy the HETP from numerical simulations. Moreover, simplified reduced order models are developed. The models are able to capture the overall dynamics of the 3D simulations for both isothermal and linear conditions, and non-isothermal and non-linear ones. The reduced order models are fully predictive, and strongly rely on accurate equilibrium and kinetic parameters. Given the relevance of reliable equilibrium and kinetic parameters for the simulation of monoliths, this thesis further investigates how to model multicomponent adsorption on heterogeneous solids, and how to extract kinetic parameters from experiments.

The second part of this work presents the multisite rigid adsorbent lattice fluid (multi-RALF) model, a novel thermodynamic theory to model multicomponent adsorption on heterogeneous adsorbents. The parameterisation of multi-RALF is analysed in regard to the azeotropic adsorption of benzene and propene on silicalite and to the adsorption of CO_2 on the flexible synthetic zeolite (Na,TEA)-ZSM-25. The former study is carried out using molecular simulations, while the latter uses experimental data. The results of the molecular simulations show that the azeotrope is caused by steric hindrance of benzene in the adsorbent framework. Once correctly parametrised using single component isotherms, multi-RALF can predict the azeotrope of the system. Multi-RALF has been

proven to be an effective model for the flexibility of (Na,TEA)-ZSM-25 upon CO_2 adsorption, as well. Experimental isotherms of CO_2 adsorption on (Na,TEA)-ZSM-25 always present an inflection at a constant adsorbed amount. This has been explained as a gate opening effect. The adsorbent is made of two sites, α and β. The site β becomes accessible only after a critical uptake of 0.6 mol/kg. At this uptake, the cations blocking the site β interact with the adsorbate and move away from the windows of the β site. This effect leads to the inflection in the isotherm and a relaxation of the solid framework with a small breathing effect. The breathing behaviour effect on the system kinetics is then investigated using the zero length column (ZLC) technique. The ZLC curves at different flowrates and temperatures always present a transition between an equilibrium controlled regime at high partial pressures of CO_2, while becoming kinetically controlled in the limit of zero-loading. The transition between the two regimes is related to the cation movement, and it is carefully accounted for in a ZLC numerical model which successfully fits the experimental data.

Finally, thermal frequency response (TFR) measurements for air separation on the zeolite LiLSX are presented. This is a fast diffusing system, difficult to study with commercial equipment. Hence, the purpose-built dual piston pressure swing adsorption apparatus is used for the experiments. Two models are developed to analyse both single- and multi-component measurements. From the single component model, a tortuosity of 3.3 is regressed, while the multicomponent data show a N_2/O_2 selectivity of 6. Both values are in accordance with the available literature. TFR has proven to be a powerful technique to handle challenging diffusing systems, able to effectively discriminate the relevant mass and heat transfer time constants as shown from experiments at conditions relevant to process application. The work here presented aimed at providing a reliable methodology for modelling of monoliths and derivation of the relevant equilibrium and kinetic parameters. In future, the combination of the monoliths' models and multi-RALF could become a robust and reliable tool for the deployment of monoliths for process intensification.

Lay summary

Gas separation processes account for up to 70% of total plant costs. To reduce the environmental impact as well as the costs of energy and chemical productions, greener and more efficient separation technologies are needed. In the past decades, the selective removal of gas compounds from streams using porous material, a process known as adsorption, has found widespread use in both trace impurity removal, as well as bulk gas separation processes.

Conventionally, adsorption units consist of beads or pellets of porous adsorbent randomly packed in a column. This configuration has been proven to be efficient for moderate flowrates and discrete thermal management. Straight-channel monoliths provide significant improvement in terms of high throughput handling and thermal management. Straight-channel monoliths are made of parallel channels with a fixed cross-section, coated with adsorbent porous solid, i.e. the adsorbent. This thesis derives correlations to assess the performance of straight-channel monoliths for gas adsorption processes. Furthermore, a numerical model is proposed to model straight-channel monoliths in several operating conditions.

Since the numerical model requires the knowledge of several parameters related to the affinity between the gas molecules and the porous adsorbent, a novel thermodynamic model is presented. The model describes the equilibrium between a multicomponent fluid phase and an adsorbent comprising different adsorbing sites. Moreover, two experimental studies are presented aimed at deriving kinetics information for adsorbents which present flexibility, and in systems in which the diffusion of the molecules in the solid is extremely fast. The equilibrium model and the kinetic experimental techniques provide a background for a reliable estimation for the parameters needed to model straight-channel monoliths.

Future work could combine the model for straight-channel monoliths with the thermodynamic model, and implemented in a process simulator to present a powerful tool for the design and optimisation of adsorption processes.

When I was nineteen, I took a bus to go to my first day at university. I did not know which course I wanted to attend. While on the bus, I seated next to a wonderful girl who told me she was going to attend the first lecture of mathematics. I lied saying that I was going to attend mathematics, too. It was during that first lecture that I fell in love. But not with the girl. I fell in love with the professor that was giving the lecture.
He was Renato Caccioppoli.

(L. De Crescenzo)

Acknowledgments

First of all, I want to thank the University of Edinburgh for the financial support and my supervisor Prof. Brandani for his support and help in growing as a better person and engineer. The hours spent in your office have taught me a lot on my profession, and on the giants to which I stand on the shoulders. There are also other talented academics which I would like to acknowledge: Dr. Friedrich, Dr. Mangano, Dr. Luberti, Prof. Ferrari and Prof. Sarkisov. Thank you for the enjoyable moments spent together.

I would also like to thank the adsorption group past and current members, to whom I wish all the best. The daily coffee breaks and discussions have been among the dearest memories of the past years.

Among the colleagues of the coffee break, Simona is the one with whom I had the privilege to share my life. It is still astonishing for me how her universe can be so vast and beautiful to explore. Thank you, Simona, for allowing me to be in your universe. It has been, and it will be, a privilege to share life with you.

Family is never acknowledged enough. I hope to remedy with these few lines. Thank you, Giacomo and Maddalena for the support and for the hard work you put in growing me and my twin. You are always in my thoughts.

To conclude, I would like to acknowledge my brother Gianluca. I would have not been what I am without your presence in my life. I hope to be good enough to support you in your future. Life has taught us that no distance can weaken the fondness of two brothers which share a common soul.

Publications

Published

Sharma, I.; Mennitto, R.; Friedrich, D.; Brandani, S. Combining the Nonuniform Structure and Flow Maldistribution for the Accurate Prediction of the Process Performance of Monolithic Adsorbent Systems. *Ind. Eng. Chem. Res.* **2020,** 59 *(7)*, 3162–3172 (2020).

Verbraeken, M. C.; Mennitto, R.; Georgieva, V. M.; Bruce, E. L.; Greenaway, A. G.; Cox, P. A.; Min, J. G.; Hong, S. B.; Wright, P. A.; Brandani, S. Understanding CO_2 Adsorption in a Flexible Zeolite through a Combination of Structural, Kinetic and Modelling Techniques. *Sep. Purif. Technol.* **2021**, *256*, 117846

Luberti, M.; Mennitto, R.; Brandani, S.; Santori, G.; Sarkisov, L. Activity Coefficient Models for Accurate Prediction of Adsorption Azeotropes. *Adsorption* **2021**

Mennitto, R.; Sharma, I.; Brandani, S. Extruded Monoliths for Gas Separation Processes: the Height Equivalent to a Theoretical Plate and Pressure Drop Correlations. *AIChE J.* **2022** *(accepted for publication)*

Mennitto, R.; Sarkisov, L.; Brandani, S. Predictive Models of Azeotropic Adsorption from Molecular Simulations and Macroscopic Theories. In *AIChE Annual Meeting, November 10-15*; Orlando, FL, 2019

Mennitto, R.; Sarkisov, L.; Brandani, S. The Rigid Adsorbent Lattice Fluid Model Applied to the Correlation of Liquid Phase Partition Coefficients of Different Solvents in MFI Zeolites. In *AIChE Annual Meeting, November 10-15*; Orlando, FL, 2019

Sharma, I.; Mennitto, R.; Friedrich, D.; Brandani, S. Significance of Flow Mal-Distribution and Channel Imperfections in Structured Monolith-Based

Adsorption Processes. In *AIChE Annual Meeting, November 10-15*; Orlando, FL, 2019

Mennitto,R.; Holtermann, M.; Mangano, E.; Brandani, S.; Brandani, F.; Pullumbi, P.; Transport Coefficients in Commercial Beads Measured using a Thermal Frequency Response Method. In *AIChE Annual Meeting, November 10-15*; Orlando, FL, 2019

In preparation

Mennitto, R.; Luberti, M.; Brandani, S. Numerical modelling of a corrugated monolith for adsorption separations.

Mennitto R.; Olkis C.; Wang J.; Dang W.; Mangano E.; Brandani S.; Brandani F.; Pullumbi P. Transport coefficients in commercial beads measured using thermal frequency response method.

Verbraeken M.C.; Mennitto R.; Brandani S. Binary predictions for CH_4/CO_2 separation in MIL-53(Al) using the Rigid Adsorbent Lattice Fluid model

Table of Contents

List of figures

List of tables

Nomenclature

a_s	Specific surface area of the solid [1/m]
a_w	Specific surface area of the column walls [1/m]
A	Area of the free cross-section [m^2]
A_S	Surface area of the solid [m^2]
A_w	Surface area of the wall [m^2]
A^*	Dimensionless area [−]
b	Langmuir isotherm affinity parameter [1/Pa]
$b_{0,i}$	Pre-exponential factor of the Langmuir isotherm for the i-th component (1/Pa)
$c_{ave,i}\big\vert_{z=L}$	Average outlet concentration of the i-th component [mol/m^3]
c_g	Gas concentration in the TFR column [mol/m^3]
$\boldsymbol{c_g}$	Vector of the concentrations in the gas phase in the multicomponent TFR model [mol/m^3]
c_i	Concentration of the i-th component in the free channel [mol/m^3]
$c_{in,i}$	Inlet concentration of the i-th component [mol/m^3]
$\boldsymbol{c_p}$	Vector of the concentrations in the macropores in the multicomponent TFR model [mol/m^3]
$c_{p,g}$	Heat capacity at constant pressure of the gas [J/kg/K]

$c'_{p,g}$	Heat capacity at constant pressure of the gas in mole units [J/mol/K]
$c_{p,i}$	Gas concentration of the i-th component in the macropores [mol/m^3]
$\overline{c_{p,i}}$	Average gas phase concentration of the i-th component in the macropores [mol/m^3]
$c_{p,s}$	Heat capacity of the solid [J/kg/K]
c_{tot}	Total concentration of fluid [mol/m^3]
c_{Vg}	Heat capacity at constant volume of the gas [J/mol/K]
c_0	Initial/average concentration [mol/m^3]
$c_{0,tot}$	Initial/average total concentration in the TFR column [mol/m^3]
C_M	Taylor-Aris dispersivity coefficient [−]
d	Diameter of a circular cross-section [m]
D	Diffusivity [m^2/s]
D_{ax}	Axial dispersion [m^2/s]
D_{eff}	Effective macropore diffusivity [m^2/s]
$D_{K,i}$	Knudsen diffusion of the i-th component [m^2/s]
D_m	Molecular diffusion [m^2/s]
D_p	Pore diffusion [m^2/s]

$\boldsymbol{D_p}$	Matrix of the pore diffusivities in the multicomponent TFR model [m^2/s]
D_s	Diffusion in the solid [m^2/s]
D_{vis}	Viscous contribution to diffusion [m^2/s]
D_0	Corrected diffusivity at zero loading [m^2/s]
E_a	Activation energy [J/mol]
f	Factor accounting for curvature of the cross-section in the HETP for a hollow fiber [–]
$f_{i,F}$	Fugacity of the i-th component in the fluid phase [Pa]
f_{uw}	Function to draw the upper wall [m]
f_1	Contribution to dispersion given by the retention of the solute in the solid [–]
f_2	Contribution to dispersion given by the dispersion of the non-uniform velocity profile [–]
fRe_Σ	Fanning-Reynolds product with respect to the characteristic length Σ [–]
F	Outlet flowrate of the ZLC [m^3/s]
F_{in}	Inlet flowrate at the ZLC [m^3/s]
$g_1(\alpha)$	Effect of wall retention with a uniform flow in the free cross-section [–]
$g_2(\alpha)$	Resistance given by the flow in a channel with no adsorbing walls [–]

$g_3(\alpha)$	Interaction term between $g_1(\alpha)$ and $g_2(\alpha)$ [–]
G_A^R	Residual Gibbs energy of the adsorbed phase [J]
G_X	Arbitrary transfer function of variable X with respect to volume perturbation in the TFR model [–]
h	Characteristic dimension of the free cross-section [m]
h_g	Specific molar enthalpy of the gas in the TFR column [J/mol]
h_{gs}	Heat transfer coefficient between gas and solid [W/m^2/K]
h_o	Height of the upper wall for corrugated channel [m]
h_{Sg}	Specific molar enthalpy of the gas in the macropores [J/mol]
h_w	Heat transfer coefficient of the wall [W/m^2/K]
I	Identity matrix [–]
i	Characteristic dimension of the free cross-section [m]
i_o	Outer base of a corrugated channel [m]
j	Fitting parameter [–]
J	Molar flux per density of solid [mol·m/kg/s]
k	Retention factor [–]

k_B	Boltzmann constant [J/K]
K	Henry's law constant [−]
K_c	Derivative of the isotherm with respect to concentration [m^3/kg]
$\boldsymbol{K_c}$	Matrix of the derivatives of the isotherms with respect to concentrations in the multicomponent TFR model [m^3/kg]
K_p	Derivative of the isotherm with respect to pressure [mol/kg/Pa]
K_T	Derivative of the isotherm with respect to temperature [mol/kg/K]
$\boldsymbol{K_T}$	Matrix of the derivatives of the isotherms with respect to temperature in the multicomponent TFR model [mol/kg/K]
L	Length of the monolith [m] (Chapter 2); Ratio between diffusion time constant and wash-out of the solid in the ZLC analytical model [−] (Chapter 4)
m_i	Mass of i-th component [kg]
m_s	Mass of the solid [kg]
m_T	Total mass adsorbed including the solid [kg]
Mw	Molecular weight [kg/mol]
n	Number of sites occupied by a molecule for Nitta isotherm [−]

$\overline{n_A}$	Average number of moles adsorbed [mol]
n_g	Moles of gas in the TFR column [mol]
$\overline{n_p}$	Average moles of gas in the macropores [mol]
N	Number of moles [mol]
N_a	Avogadro's number [1/mol]
N_c	Number of components [–]
Nu	Nusselt number [–]
p_1, p_2, p_3	Fitting parameters for the dimensionless corrected thickness [–]
P	Total pressure [Pa]
P_i	Partial pressure of i-th component [Pa]
P_0	Initial/average pressure [Pa]
$P_{0,tot}$	Initial/average total pressure in the multicomponent TFR model [Pa]
P^*	Dimensionless perimeter [–] (Chapter 2); Characteristic energy density [Pa] (Chapter 3)
P_s^*	Characteristic energy density of the solid [Pa]
$\tilde{P}$	Reduced energy density in RALF [–]
Pe	Mass Peclet number [–]
Pe_T	Thermal Peclet number [–]
$Perim$	Perimeter of the free cross-section [m]

$\boldsymbol{q}$	Vector of the amounts adsorbed in the multicomponent TFR model [mol/kg]
q_i	Adsorbed concentration of the i-th component. Units are [mol/m^3] in Section 2.2, and [mol/kg] elsewhere
$\bar{q}_i$	Average adsorbed concentration of the i-th component in the solid [mol/kg]
q_s	Saturation capacity [mol/kg]
q_{trans}	Fitting parameter for ZLC model [mol/kg]
q'_{trans}	Fitting parameter for volume flexibility in multi-RALF [mol/kg]
q_0	Initial/average amount adsorbed [mol/kg]
$\bar{Q}_i$	Total average amount adsorbed of the i-th component [mol/m^3]
r	Number of mers in a molecule [–] (Chapter 3); Radial coordinate [–] (Chapter 4)
r_i	Number of mers in the i-th molecule [–]
r_i^0	Number of mers in the i-th molecule as pure fluid [–]
r_{pore}	Radius of the pore [m]
R_{ax}	Axial dispersion resistance [–]
R_g	Ideal gas constant [J/mol/K]
R_p	Particle/bead radius [m]

R_S	Resistance given by the diffusion in the solid [−]
R_v	Resistance given by the velocity profile [−]
s	Fitting parameter [−] (Chapter 2), Laplace variable [−] (Chapter 4)
S_{N_2/O_2}	Nitrogen-oxygen selectivity [−]
t	Time [s]
t_0	Initial time of the exponential decay [s]
T_g	Gas temperature [K]
T_{ref}	Reference temperature of the isotherm [K]
T_s	Solid temperature [K]
T_s^*	Characteristic temperature of the solid [K]
T^*	Characteristic temperature [K]
T_0	Inlet/initial temperature [K]
$\tilde{T}$	Reduced temperature in RALF [−]
u	Energy of interaction for Nitta isotherm [J]
u_A	Specific molar internal energy of the adsorbed phase [J/mol]
u_g	Specific molar internal energy of the gas in the TFR column [J/mol]
u_{Sg}	Specific molar internal energy of the gas in the macropores [J/mol]

U_g	Internal energy of the gas in the TFR column [J]
U_s	Internal energy of the solid [J]
v	Velocity field [m/s]
v_{ave}	Average velocity [m/s]
v_{in}	Inlet velocity [m/s]
v^*	Average close-packed volume of mers in a mixture [m^3/mer-mol]
v_i^*	Close-packed volume of the mers of the i-th molecule [m^3/mer-mol]
v_{iA}^*	Close-packed volume of the mers of the i-th molecule in the adsorbed phase [m^3/mer-mol]
V_f	Volume of fluid in the ZLC [m^3]
V_g	Gas volume in the TFR column [m^3]
V_{mic}	Volume of the micropores per mass of solid [m^3/kg]
V_0	Initial/average volume [m^3]
V_s	Volume of the solid including the micropores per mass of solid [m^3/kg] (Chapter 3); Volume of the solid in [m^3] elsewhere
$V_{s,\alpha}$	Volume of site α of (Na,TEA)-ZSM-25 per mass of solid [m^3/kg]
$V_{s,\beta}$	Volume of site β of (Na,TEA)-ZSM-25 per mass of solid [m^3/kg]

w	Thickness of the solid [m] (Chapter 2); Fitting parameter [−] (Chapter 3)
w_c	Corrected thickness of the solid [m]
w_i/w_j	Mass fraction of the i-th/j-th component in the adsorbed phase [−]
x, y	Coordinates on the cross-section
x_i	Mole fraction of the i-th component in the adsorbed phase [−]
x_c	x-coordinate for the drawing of the interface
x_2^*	Intercept of the wavy interface with the solid base [m]
y_i	Mole fraction of the i-th component in the fluid phase [−]
z	Axial coordinate (Chapter 2); Compressibility factor [−] (Chapter 3)

Greek symbols

α	Aspect ratio of the free cross-section [−] (Chapter 2); Dimensionless parameter of the TFR model [−] (Chapter 4)
α_w	Dimensionless parameter of the TFR model [−]
α_o	Aspect ratio of the outer cross-section for a corrugated monolith [−]
$\beta_s, \beta_{\Delta H}$	Dimensionless parameters of the TFR model [−]

γ	Effective aspect ratio [−] (Chapter 2); Ratio between accumulation in the fluid and solid phase of the ZLC [−] (Chapter 4)
γ_c, γ_T	Dimensionless parameters of the TFR model [−]
Γ	Darken correction factor [−]
$\boldsymbol{\Gamma}$	Diagonal matrix of the eigenvalues of $[\boldsymbol{D}'']$ (see equation 4.71) [−]
δ	Dimensionless thickness of the solid [−]
δ_c	Dimensionless corrected thickness of the solid [−]
δ_1, δ_2	Dimensionless parameters of the TFR model [−]
$\delta_{in}, \delta_{out}$	In- and out-of-phase function [−]
ΔH	Enthalpy of adsorption [J/mol]
ΔH_0	Enthalpy of adsorption at zero loading [J/mol]
ΔP	Pressure drop [Pa]
ΔU_0	Internal energy of adsorption at zero loading [J/mol]
ΔX	Dimensionless arbitrary deviation variable $\Delta X = \frac{X - X_0}{X_0}$ [−]
$\Delta' X$	Arbitrary deviation variable $\Delta X = X - X_0$
ϵ	Channel void fraction [−]
ϵ_p	Pellet void fraction [−]

ϵ_{pb}	Packed bed void fraction [–]
ϵ^*	Mer-mer interaction parameter [J]
ϵ_β	Porosity of site β of (Na,TEA)-ZSM-25 [–]
η	Viscosity [Pa×s]
ϑ	Square root of the second moment [s]
θ	Shape factor [–], 0 for flat geometries and 1 for rounded ones (Chapter 2); surface coverage [–] (Chapter 3);
κ_{ax}	Axial thermal conductivity [W/m/K]
κ_g	Thermal conductivity of the gas [W/m/K]
κ_{jk}	Interaction parameter in RALF between j-th and k-th component [–]
κ_s	Thermal conductivity of the solid [W/m/K]
$\lambda_{1,2}$	Eigenvalues of the matrix $[\boldsymbol{D}'']$ (see equation 4.72)
$\boldsymbol{\Lambda}$	Modal matrix of $[\boldsymbol{D}'']$ (see equation 4.71)
μ	Mean residence time [s]
μ_i^R	Residual chemical potential of the i-th component in the adsorbed phase [J/mol]
μ_{iF}^R	Residual chemical potential of the i-th component in the fluid phase [J/mol]

ξ_i	Confinement parameter of the i-th molecule in the adsorbed phase [–] (Chapter 3); Dimensionless radial coordinate (Chapter 4)
π_s	Spreading pressure [N/m]
ρ	Fluid density [kg/m^3]
ρ_p	Pellet density [kg/m^3]
ρ_s	Density of the solid including micropores [kg/m^3]
ρ_s^*	Skeletal density of the solid [kg/m^3]
ρ^*	Characteristic density in RALF [kg/m^3]
ρ_{jA}^*	Close packed characteristic density of the j-th molecule in the adsorbed phase [kg/m^3]
$\tilde{\rho}$	Reduced density in RALF [–]
$\tilde{\rho}_s$	Reduced solid density [–]
σ_{12}	Average kinetic diameter of the pair molecule 1 – molecule 2 [m]
Σ	Characteristic length of a monolith's channel [m]
τ	Tortuosity [–]
τ_D	Diffusion time constant [s]
$\tau_{D,eff}$	Effective diffusion time constant [s]
τ_{TC}	Time constant of the thermocouple [s]
τ_{vis}	Stress tensor of the Navier-Stokes equations [N/m^2]

φ	Phase lag $[-]$
ϕ_i	Volume fraction of the i-th component in the lattice $[-]$
ϕ_s	Volume fraction of the solid $[-]$
χ	Dimensionless parameter of the TFR model $[-]$
ω	Mass fraction of the site $[-]$ (Chapter 3); Frequency [Hz] (Chapter 4)
Ω_{12}	Collision integral diameter of the pair molecule 1 – molecule 2 $[-]$

Abbreviations

AR	Amplitude ratio
AST	Adsorbed solution theory
CM	Corrugated monolith
CSS	Cyclic steady state
DP-PSA	Dual piston pressure swing adsorption apparatus
EoS	Equation of state
ERM	Equivalent rectangular model
FH-VSM	Flory Huggins vacancy solution model
FR	Frequency response
HIAST	Heterogeneous ideal adsorption solution theory
IAST	Ideal adsorbed solution theory

LHS	Left hand site
LiLSX	Lithium exchange low silica X-type zeolite
LSE	Linear set of equations
Multi-RALF	Multisite rigid adsorbent lattice fluid
NELF	Non-equilibrium lattice fluid
PSA	Pressure swing adsorption
RALF	Rigid adsorbent lattice fluid
RAST	Real adsorbed solution theory
RHS	Right hand side
SL-EoS	Sanchez and Lacombe equation of state
TFR	Thermal frequency response
TSA	Temperature swing adsorption
VSM	Vacancy solution model
ZLC	Zero length column

Chapter 1 Introduction

Gas separation by means of adsorption has gained increasing interest in the past decades as an alternative to conventional separation techniques[1–3]. Major applications of adsorption include carbon capture, air separation, hydrogen purification and VOC removal. In the last years, adsorption has found place in applications such as gas storage[4] and biogas upgrading[5], as well.

An increasing number of studies have focused on the development of tailored porous adsorbents for targeted applications. Adsorbents such as metal-organic frameworks (MOFs)[6,7], synthetic zeolites[8], zeolitic-imidazolate frameworks (ZIFs)[9] and many others have shown considerable improvement over traditional zeolitic or carbonaceous materials in terms of uptake, selectivity for targeted applications, and faster kinetics. Furthermore, the advent of *in-silico* synthesis and screening of porous materials has unlocked a powerful tool in material design[10–12]. The use of computational synthesis and screening of porous materials has helped in the ranking and optimisation of several classes of porous materials[13–15].

If the tuning of the adsorbent's property to a specific separation is crucial for an efficient process, it should be noted that structural and equilibrium properties of the adsorbent are not enough to discriminate between an efficient adsorption process and an inefficient one. Swing adsorption processes, mainly pressure swing (PSA) and temperature swing adsorption (TSA), often require the knowledge of the system kinetics[16,17], information on the fluid dynamics of the bed to determine pressure drop and thermal management[18,19], and power consumption of the auxiliary parts to determine the efficiency of the process[20,21].

Conventionally, adsorption processes are run using packed beds of porous beads or pellets. Several studies have dealt with the optimisation of packed beds for adsorption purposes, and their relative process schedule[22–24]. Among the vast literature on the topic, it is worth to mention the work of Jain et al.[25] which provides a series of heuristic rules in the design of both the packed bed

and the process operating schedule, which can drive a preliminary design of an adsorption unit. Considerable effort has been put into the development of fast cycle processes, aimed to increase the overall productivity of the process for a given amount of adsorbent[26–28]. Both Ruthven[2] and Sircar[3] describe as paramount the deployment of fast cycle processes for process miniaturization and intensification. Nevertheless, fast cycle processes come at a cost of high pressure drop if run in packed beds. The increase in pressure drop has a significant impact on the energy consumption of the process, making adsorption unfeasible for processes dealing with high throughput.

Structured adsorbents have been recently promoted as an alternative to packed beds[29–32]. Structured adsorbents can achieve better performance in terms of handling high throughputs, thermal management and faster cycle times than packed bed adsorption columns[2,29,30,32,33]. Several types of structured adsorbents have been reported in the literature, such as foams[34–36], fibres[37,38] laminates[33,39–42], and straight-channel monoliths[43,44] as potential candidates to overcome the limitations of packed beds. Ruthven and Thaeron[33] were among the first to promote the use of structured adsorbents over packed beds. They analysed the use of a parallel passage contactor to improve the trade-off between mass transfer and pressure drop. A comprehensive overview of structured adsorbents is provided in the works of Rezaei and Webley[29,30] which compared different structures in terms of volumetric working capacity, mass transfer and thermal management, and pressure drop. The work of Rezaei and Webley[29,30] made use of empirical correlations to derive mass transfer parameters of the monolith and used the correlation derived by Taylor[45] to calculate the axial dispersion in straight-channel monoliths of arbitrary geometry. The work of Rezaei and Webley[29,30] concluded that structured adsorbents, in particular, straight-channel monoliths and laminates can offer better performance compared to packed beds if their properties such as cell density for monoliths, and sheet width and spacing for laminates are properly tuned. A small and uniform spacing between sheets was already postulated by Ruthven and Thaeron[33] as a necessary condition to make the laminate structure more attractive than packed beds. Rezaei et

al.[46] also investigated the effect of thickness and porosity of the coated adsorbent on straight-channel monoliths on the overall dynamics of an extruded monolith. They concluded that a trade-off between high uptake and mass transfer has to be optimised for a given monolith tuning its film thickness. Several progresses have also been made in the use of 3D printing to overcome the limitations of conventional manufacturing techniques. The use of 3D printing enabled unusual geometries (gyroids) to be investigated, as in the work of Dimartino and co-workers[47–49], which showed superior fluid dynamics with very low pressure drop and high available surface area for adsorption. Denayer and co-workers[50–52] also investigated the use of 3D printing for two main applications: self-standing ZSM-5 monoliths with high CO_2/N_2 and CO_2/CH_4 selectivity[51], and ZIF-8 monolith for bio-butanol recovery[50,53].

Ritter et al.[54] investigated the use of a Catacel monolith for carbon capture applications. The Catacel monolith consisted of corrugated metal foil wrapped around a central rod, with the adsorbent deposited on the metal foil. Amalraj et al.[55] studied the thermal properties of the Catacel monolith proposed by Ritter et al.[54] using computational fluid dynamics simulations, concluding that the main factor for a substantial improvement in thermal management of heat effects is an accurate choice of the metal support. Mohammadi[56] reported both breakthrough and full-cycle experiments on the Catacel monolith, showing promising results for carbon capture applications. It is interesting to note that Mohammadi[56] made use of two different mass transfer coefficients to match the breakthrough and the full-cycle experiments. Sharma et al.[26] proved that the discrepancy between the two mass transfer coefficients was indeed flow maldistribution inside the channels of the monolith. Sharma et al.[26] proposed a model which used a unique mass transfer constant, independent of the experiment run, and a flow maldistribution that was fitted to breakthrough data. The model of Sharma et al.[26] was able to predict the full-cycle data of Mohammadi[56], showing that the intrinsic equilibrium and kinetic properties of the adsorbent are not affected by the type of monolith used or experiment run.

It should be noted that the work of Ahn and Brandani[57] already highlighted the importance of reliable estimates of the intrinsic properties of the adsorbent which constitutes the monolith. They made use of a carbon monolith for CO_2 adsorption. The equilibrium and kinetic properties of the monolith were studied with zero length column (ZLC) measurements using fragments of the monolith by Brandani et al.[58]. Once the properties of the adsorbent were established, breakthrough experiments on the whole monolith were performed. The breakthrough experiments performed by Ahn and Brandani[57] showed the great impact of nonuniform channel shape in the spreading of the breakthrough profiles since the mass transfer constant from ZLC experiments was not able to capture the spreading of the breakthrough experiments. Hence, they modelled the monolith dynamics including distributions of both channel sizes and wall thicknesses which were known from an accurate analysis of the monolith's cross-section. This approach allowed the match of adsorption and desorption breakthrough curves of the monolith without any fitting parameter. A similar approach was adopted by Crittenden[59] to model a carbon monolith using only the channel's size distribution. The model of Crittenden[59] can be considered as a sub-class of the more general approach of Ahn and Brandani[57].

The brief literature reviewed highlights two main needs in the design of monoliths for adsorption processes: reliable correlations and numerical models to estimate the performance of extruded adsorbents in terms of efficiency and energy penalty, and the need for an accurate study of the equilibrium and kinetic properties of the adsorbent-adsorbate system.

The aim of this thesis is to provide a comprehensive analysis of the performance of extruded adsorbents in terms of separation efficiency and energy penalty. More specifically, the behaviour of extruded adsorbents is studied to derive simple and reliable height equivalent to a theoretical plate (HETP) and pressure drop correlations. These two properties provide enough information for a given separation at a design stage to choose the most promising structure to be then optimised with the use of numerical simulations.

Since the HETP correlations for a given structure strongly depend on the equilibrium and kinetic properties of the adsorbent used, this thesis also presents how these properties can be separately estimated with the use of a novel thermodynamic framework, the multisite rigid adsorbent lattice fluid (multi-RALF) model, and with the use of ZLC and thermal frequency response (TFR) measurements. It should be noted that the study of equilibrium and kinetic properties of the system adsorbents-adsorbate are not dependent on the type of bed used for the separation. Therefore, what presented can be used to assess the properties of a structured adsorbent and a packed bed, as well.

The present thesis is organised as follows:

- Chapter 2 presents an analysis of the main extruded adsorbents of industrial relevance. The analysis aims at deriving HETP correlations and review pressure drop ones from literature which can be used at a design stage. Furthermore, numerical models are developed to validate the aforementioned correlations and reduced order models are discussed as viable means to optimise extruded adsorbents for industrial processes;
- Chapter 3 presents the multi-RALF model for the analysis of multicomponent adsorption on heterogeneous adsorbents. The focus of the chapter is the parametrisation of multi-RALF from both molecular simulations and experimental data;
- Chapter 4 presents the use of ZLC measurements to investigate the kinetics of CO_2 in a flexible synthetic Rho-type zeolite. Furthermore, the development of TFR technique to measure the kinetics of a fast diffusing system, such as air separation using LiLSX zeolite, is discussed;
- Chapter 5 will briefly summarise the main results of the previous chapters, and it will aim to draw some guidelines for future works on extruded adsorbents.

Chapter 2 Modelling of straight-channel monoliths

2.1 Introduction

Straight-channel monoliths are structured adsorbents consisting of straight parallel channels, whose cross-section is identical for all the channels and fixed to a given shape. Straight-channel monoliths have been used in several areas, ranging from adsorption[29,60] to catalysis[61], to microfluidic applications[62]. The main interest of this work is their application to gas adsorption processes. Straight-channel monoliths can either be made of a metallic frame then coated with a sorbent[54], or they can be manufactured as extrudates of active material, usually a binder with adsorbent crystals dispersed in it[63].

The most used straight-channel monoliths are the ones whose free cross-section is either a square/rectangle, a hexagon, or a corrugated channel. However, triangular, rhombic, and circular cross-section can also be of interest. A schematic diagram of the geometries can be found in Figure 2.1.

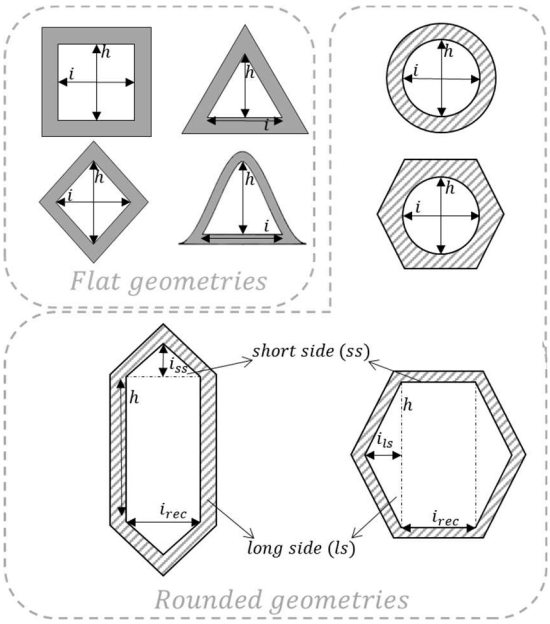

Figure 2.1: Cross-section of common straight-channel monoliths. From left to right, from top to bottom: rectangular channel, triangular channel, hollow fibre, rhombic channel, corrugated channel, hex-cir channel, hex-hex channel with $\alpha_{ss} > 0$ and hex-hex channel with $\alpha_{ls} > 0$.

As it can be noted from Figure 2.1, the representative channel of a straight-channel monolith is constrained to geometries that can be the repeating unit cell of an infinite matrix. For instance, triangular channels will be limited to isosceles triangles, since the repeating of an irregular triangular channel would be inefficient and of not easy manufacture. This is the reason why the manufacturing of straight-channel monoliths is limited to a finite number of geometries. This limitation could potentially be overcome with additive manufacturing[50,53], which however comes at a higher manufacturing cost.

We can split into two main categories the cross-sections in Figure 2.1: flat and rounded geometries. The flat cross-sections are the ones where the diffusion of the solute in the solid can be approximated as the diffusion in a slab. By contrast, the rounded geometries are the ones where the diffusion in the solid can be approximated to the diffusion in a hollow cylinder.

It can be noted from Figure 2.1 that two types of hexagonal channels are considered: the hexagonal channel with a hexagonal cross-section, and the one with a circular cross-section. The hexagonal channel with circular cross-section, hereafter called the hex-cir channel, can be seen as representative of a honeycomb monolith on which the adsorbent is deposited. Only the hex-cir channel with a regular hexagon and circular cross-section can be analysed for any practical purpose since non-regular hexagons with a non-uniform coating would result in unusual shapes, that would find little application. Furthermore, irregular hex-cir channel would be difficult to analyse to derive general correlations for their use, as we aim in this work. Hence, their behaviour should be studied on a case-by-case analysis. On the other hand, the hexagonal channel with a hexagonal free cross-section (hex-hex channel) represents a monolith extruded using the adsorbent.

The parameter needed to fully characterise the free cross-section of the geometries in Figure 2.1 is the aspect ratio, here defined as $\alpha = i/h$, where i and h are the characteristic dimensions of the geometry highlighted in Figure 2.1. For the hex-hex channel, the aspect ratios needed are two: the aspect

ratio of the internal rectangle, $\alpha_{rec} = \frac{i_{rec}}{h}$, and the aspect ratio of the two triangles which can be attached on the short or long side of the rectangle. If the triangles are attached on the short sides, the second aspect ratio is defined as $\alpha_{ss} = \frac{i_{ss}}{i_{rec}}$. If the triangles are attached on the long sides, the aspect ratio is defined as $\alpha_{ls} = \frac{i_{ls}}{h}$. It will be assumed in the following that whenever $\alpha_{ss} > 0$ then $\alpha_{ls} = 0$, and vice-versa. The values of the aspect ratios for a regular hex-hex channel are: $\alpha_{rec} = \frac{1}{\sqrt{3}}$, $\alpha_{ls} = \frac{1}{2\sqrt{3}}$.

The corrugated channel in Figure 2.1 is the representative channel of a spiral wound monolith, that consists of alternated flat and corrugated foils of adsorbent material, or metal foils which are then coated with an adsorbent.

Once the geometries of interest are identified, a procedure to model straight-channel monoliths needs to be outlined. The modelling of straight-channel monoliths can start from simple and effective design correlations of their height equivalent to a theoretical plate (HETP) and their pressure drop. The HETP and pressure drop correlation for each monolith can describe how efficient the monolith is and what can be its energy penalty.

Generally, the HETP can be written as the sum of three main resistances as in eq.(2.1)[64,65]: the molecular diffusion in the axial direction (R_{ax}), the resistance given by the diffusion in the solid (R_S), and the contribution from the velocity profile (R_v).

$$\frac{HETP}{L} = R_{ax} + R_S + R_v \qquad 2.1$$

The first approach to the study of solute dispersion in a channel was carried out by Taylor[45], who studied the dispersion of an arbitrary solute in a circular channel with no-adsorbing walls. Aris[66,67] reviewed and broadened the work of Taylor to include an elliptical cross-section and also adsorbing walls around the free channels. Aris[66] derived as limiting cases of an elliptical geometry both the circular cross-section and the parallel plate cross-section.

Golay[65] made use of the analysis of moments to derive the HETP for a solute flowing in a rectangular channel. The rectangular channel gained particular attention after the work of Golay, given its widespread use in both gas and liquid adsorption[57,64,68].

The analysis of moments was also used by Dutta and Leighton[69–71] to study the dispersion of a solute in an arbitrary cross-section for chromatographic purposes. Dutta and Leighton presented also a detailed analysis of the resistance given by the velocity profile, R_v, and how to break it down to three main constituents. The description of this analysis is given in section 2.2.1.

Patton et al.[72] provide the linear-driving-force (LDF) approximation for triangular and hex-hex geometry. In their work, each arbitrary channel is reduced to an equivalent hollow cylinder which keeps constant the surface of the free cross-section and the volume of solid.

A further improvement to the HETP analysis of a rectangular channel was given by Ahn and Brandani[73] who pointed out that the resistance given by the diffusion in the solid should consider not only the solid which surrounds the perimeter of the free cross-section, but also the corners of the rectangular channel. They redistributed the solid at the corners on the sides of the geometry, thus increasing the solid diffusion length. They defined a new "corrected thickness"[57,73] which preserves the volume of solid around the free cross-section and considers the dispersion given by the corners, as well.

The literature has also thoroughly investigated possible correlations for the pressure drop in an extruded monolith[30,74,75]. The main assumption of the available models is of laminar flow in the free channel. Given the laminar flow assumption, the velocity profile can be derived, either analytically[73] or numerically[76], and the pressure drop calculated from it[77]. Generally, for an arbitrary cross-section, the pressure drop can be expressed as in eq.(2.2):

$$\frac{\Delta P}{L} = \eta v_{ave} \frac{Perim}{A\Sigma} \frac{fRe_{\Sigma}}{2} \qquad 2.2$$

where ΔP is the pressure drop, L the length of the channel, η the viscosity, v_{ave} the average velocity in the channel, $Perim$ the perimeter of the free cross-section, A the free area of the channel, fRe_{Σ} the Fanning-Reynolds product written with respect to Σ, the characteristic length of the channel. It is usually assumed that Σ is equal to the hydraulic diameter of the channel[76]. This approach leads to specific values of the fRe for each geometry under analysis at specific aspect ratios of the geometry. Shah[76] reported tabulated values of the fRe for several cross-sections and different aspect ratios.

Attempts to derive a more general correlation for the pressure drop can be found in the work of Yilmaz[78]. Although the work of Yilmaz leads to a more general description of the pressure drop in an arbitrary channel, his model requires several coefficients which can be somehow difficult to calculate.

A more practical approach to the generalisation of the pressure drop correlation for an arbitrary cross-section has been proposed by Bahrami et al.[77]. They considered as characteristic length the square root of the free cross-sectional area, $\sqrt{A}$, to analyse the pressure drop in an elliptical channel. They also showed that this approach leads to a simple correlation that can be in principle applied to any arbitrary geometry. Muzychka and Yovanovich[79,80] chose $\sqrt{A}$ to derive the equivalent rectangle model (ERM) for the calculation of the $fRe_{\sqrt{A}}$ in an arbitrary geometry. The ERM derives analytically the pressure drop correlation for a rectangular channel. The ERM can then be extended to any channel by the appropriate calculation of an “effective” aspect ratio, as it will be shown in section 2.3. The main advantage of the ERM is to be easy to implement, compared to the works of Bahrami et al.[77] and Yilmaz[78], and it can be easily extended to several cross-sections without the need of tabulated values as for the work of Shah[76].

In the following, both HETP and pressure drop correlations will be discussed for the geometries of interest. The analysis will make use of the analysis of moments presented by Dutta and Leighton[70] to derive the resistance given by the velocity profile R_v. Then, the corrected thickness approach of Ahn and

Brandani[73] for a rectangular channel will be extended to the geometries in Figure 2.1. The proposed correlations will be validated against 3D numerical simulations. The focus of this work is gas systems, for which the developed correlations are going to be tested. It is of course necessary validation of the following HETP correlations for liquid systems to prove their general applicability, as shown in the work of Ahn and Brandani[73] for a rectangular channel. In addition, a simplified reduced order model will be presented. The reduced order model aims at providing quantitatively similar results to the 3D model with the main benefit of greatly reduced computational time.

Since the corrugated channel finds widespread use in drying processes and involves a more convoluted analysis given its wavy shape, its analysis is presented separately in section 2.5.

2.2 The Height Equivalent to a Theoretical Plate

For a linear and isothermal system, and flat geometry the expression of the HETP can be written as[64]:

$$HETP = 2\frac{D_m}{v_{ave}} + \frac{2k}{3(1+k)^2}\frac{w^2}{D_s}v_{ave} + C_M\frac{h^2}{D_m}v_{ave} \qquad 2.3$$

where D_m is the molecular diffusivity, $k = \frac{1-\epsilon}{\epsilon}K$ the retention factor with ϵ as channel void fraction and K as Henry's law constant, w the thickness of the solid, D_s the diffusivity in the solid and C_M the Taylor-Aris coefficient. The Taylor-Aris coefficient can be written as in eq.(2.4)[73].

$$C_M = \frac{1}{6}\left(\frac{k}{1+k}\right)^2 g_1(\alpha) + \frac{1}{105}g_2(\alpha) + \frac{1}{15}\left(\frac{k}{1+k}\right)g_3(\alpha) \qquad 2.4$$

where the function $g_1(\alpha)$ quantifies the effect of wall retention with a uniform flow in the free cross-section, $g_2(\alpha)$ accounts for the resistance given by the flow in the same channel with non-adsorbing walls, and $g_3(\alpha)$ quantifies the interaction between the previous two functions. The equations to derive the $g_i(\alpha)$ functions are presented in the next section.

For a rounded geometry, Aris[67] showed that the R_S term in eq.(2.1) has to take into account the curvature of the solid cross-section. Hence, for rounded geometry, eq.(2.5) has to be used to calculate the HETP[81,82].

$$HETP = 2\frac{D_m}{v_{ave}} + \frac{2fk}{(1+k)^2}\frac{(dw+w^2)}{D_s}v_{ave} + C_M\frac{d^2}{D_m}v_{ave} \qquad 2.5$$

where d is the diameter of the circular cross-section. The term f arises from the curvature of the solid, and its expression is:

$$f = \frac{\frac{2p^4\,ln(p^2)}{p^2-1} - (3p^2-1)}{8(p^2-1)} \qquad 2.6$$

where $p = \frac{d+2w}{d}$. The Taylor-Aris coefficient for a rounded geometry can be written as in eq.(2.7).

$$C_M = \frac{1+6k+11k^2}{96(1+k^2)} \qquad 2.7$$

2.2.1 The velocity profile contribution

To derive the contribution to the HETP from the velocity profile, we follow the analysis of the moments of a solute dispersing in a channel of arbitrary cross-section presented by Dutta and Leighton[70].

For a channel of arbitrary cross-section as in Figure 2.2:

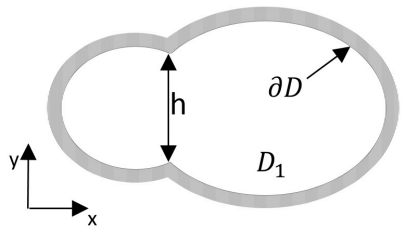

Figure 2.2: Arbitrary cross-section

we define ∂D as the boundary of the arbitrary free cross-section D_1, and h as the characteristic dimension of the free cross-section. The dimensionless variables in eq.(2.8) can be defined.

$$P^* = \frac{Perim}{h}; A^* = \frac{A}{h^2}; \xi = \frac{x}{h}; \phi = \frac{y}{h}; \nabla^* = \frac{\nabla}{h} \qquad 2.8$$

The following set of equations, eq.(2.9-2.11), has to be solved to derive the $g_i(\alpha)$ functions.

$$\frac{\partial^2 v(\xi,\phi)}{\partial \xi^2} + \frac{\partial^2 v(\xi,\phi)}{\partial \phi^2} = -1; \qquad v(\xi,\phi)|_{\partial D} = 0 \qquad 2.9$$

$$\frac{\partial^2 f_1}{\partial \xi^2} + \frac{\partial^2 f_1}{\partial \phi^2} = -\frac{P^*}{A^*}; \qquad \overrightarrow{\nabla^*} f_1 \cdot \vec{n}_{\partial D} = -1 \qquad 2.10$$

$$\frac{\partial^2 f_2}{\partial \xi^2} + \frac{\partial^2 f_2}{\partial \phi^2} = 1 - \frac{v(\xi,\phi)}{v^*_{ave}}; \qquad \overrightarrow{\nabla^*} f_2 \cdot \vec{n}_{\partial D} = 0 \qquad 2.11$$

where $\vec{n}_{\partial D}$ is the normal vector to the surface ∂D, and $v^*_{ave} = \frac{1}{A^*}\int_{D_1} v(\xi,\phi) d\xi d\phi$. The variable f_1 and f_2 represent the contribution to dispersion given by the retention of the solute in the solid and the contribution to dispersion from the non-uniform velocity profile, respectively. The set of equations presented is underdetermined since eq.(2.10) and (2.11) need an additional boundary condition or constraint. Dutta and Leighton[69] proposed eq.(2.12) as integral condition for eq.(2.10), and eq.(2.13) as condition for eq.(2.11):

$$\int_{D_1} f_1 dA^*_m + \frac{Kw}{h}\oint_{\partial D} f_{1\partial D}\, dl^* = 0 \qquad 2.12$$

$$\int_{D_1} f_2 dA^*_m + \frac{Kw}{h}\oint_{\partial D} f_{2\partial D}\, dl^* = 0 \qquad 2.13$$

where l^* is a coordinate that travels along the boundary of the free cross-section. Once the set of equations eq.(2.9-2.13) is solved numerically, the $g_i(\alpha)$ functions can be calculated as:

$$g_1 = \frac{12}{P^*}\int_{D_1} f_1 dA^*_m - \frac{12A^*_m}{P^{*2}}\oint_{\partial D} f_{1\partial D}\, dl^* \qquad 2.14$$

$$g_2 = \frac{210}{A_m^*}\int_{D_1} v(\xi,\phi) f_2 dA_m^* - \frac{210}{A_m^*}\int_{D_1} f_2 dA_m^* \qquad 2.15$$

$$g_3 = \frac{30}{P^*}\int_{D_1} (v(\xi,\phi)-1) f_1 dA_m^* + \frac{30}{A_m^*}\int_{D_1} f_2 dA_m^* - \frac{30}{P^*}\oint_{\partial D} f_{2\,\partial D}\, dl^* \qquad 2.16$$

The equations presented above have been implemented in COMSOL[83] to generate numerical values of the $g_i(\alpha)$ functions at different values of α for the geometries of interest. The procedure has been validated with the analytical solution presented by Ahn and Brandani[73] for a rectangular channel. The results are shown in Figure 2.3. The numerical results from COMSOL are in agreement with the analytical solution of Ahn and Brandani[73]. The limits of squared channel for $\alpha = 1$ and parallel passage for $\alpha \to \infty$ are correctly predicted, as well.

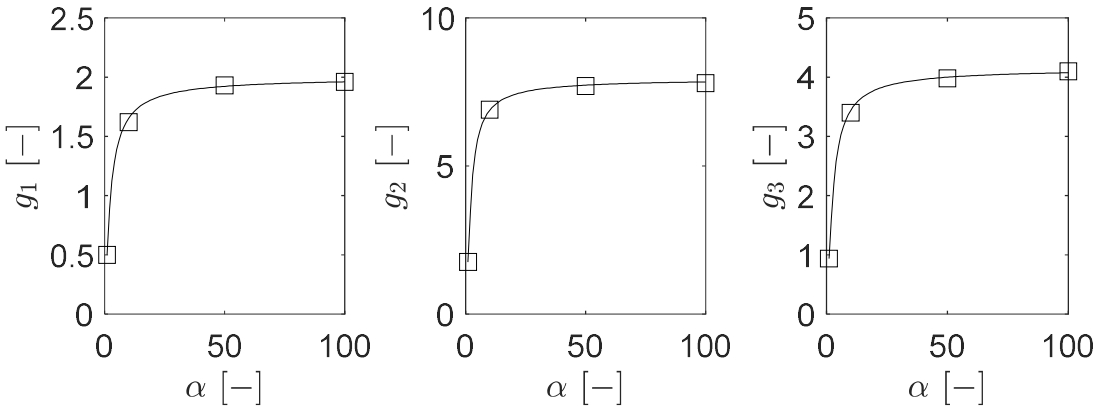

Figure 2.3: $g_i(\alpha)$ functions for a rectangular channel. Squares are numerical solutions from analysis of moments as in Dutta and Leighton[69]; the solid black line refers to the analytical solutions of the $g_i(\alpha)$ functions from Ahn and Brandani[73].

The results for triangular and rhombic channel are presented in Figure 2.4.

The results for the triangular channel are in agreement with what previously presented by Dutta and Leighton[70]. It is interesting to point out that the point of minimum dispersion for a triangular channel does not occur when the triangle is regular, but when its top angle is 44°.

The trend of the rhombic channel starts from the dispersion of the squared channel for $\alpha = 1$, to then increase for lower aspect ratios. The increase can be attributed to the increased dispersion at the edges of the free cross-section.

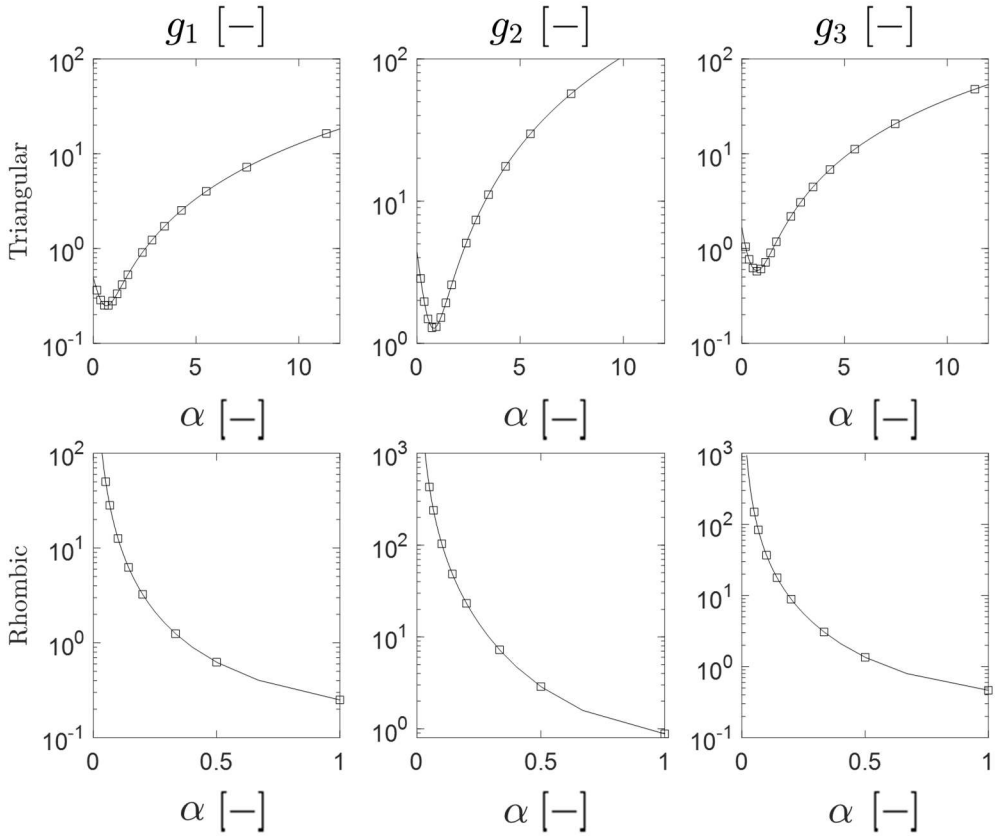

Figure 2.4: $g_i(\alpha)$ functions for the triangular (top) and rhombic channel (bottom). Squares are numerical results, and the solid line is the fitting correlation, eq.(2.17) for triangular and eq.(2.18) for rhombic channel.

The numerical results are regressed with empirical functions to provide simple correlations for design purposes. For the triangular channel the correlation is:

$$g_i(\alpha) = \frac{j_{1i}\alpha^5 + j_{2i}\alpha^4 + j_{3i}\alpha^3 + j_{4i}\alpha^2 + j_{5i}\alpha + j_{6i}}{\alpha^3 + s_{1i}\alpha^2 + s_{2i}\alpha + s_{3i}} \qquad 2.17$$

while, for the rhombic channel the correlation is reported in eq.(2.18).

$$g_i(\alpha) = j_{1i}\alpha^{j_{2i}} + j_{3i}\alpha^{j_{4i}} + j_{5i} \qquad 2.18$$

The regressed parameters j and s are reported in Table 2.1.

Table 2.1: Parameters used to correlate the $g_i(\alpha)$ functions with eq.(2.17) for the triangular channel, and eq.(2.18) for the rhombic one.

	Triangular			***Rhombic***		
	$\boldsymbol{g_1(\alpha)}$	$\boldsymbol{g_2(\alpha)}$	$\boldsymbol{g_3(\alpha)}$	$\boldsymbol{g_1(\alpha)}$	$\boldsymbol{g_2(\alpha)}$	$\boldsymbol{g_3(\alpha)}$
$\boldsymbol{j_{1i}}$	0.1247	1.072	–0.042	0.125	–2.272	0.1142
$\boldsymbol{j_{2i}}$	0.4665	9.463	33.54	–2	–0.8083	38.67
$\boldsymbol{j_{3i}}$	0.6002	–5.848	784.8	0.125	1.249	0.3498
$\boldsymbol{j_{4i}}$	1.79	33.32	756.2	0	–1.968	–2.022
$\boldsymbol{j_{5i}}$	–1.271	–33.58	–969.1	0	1.922	0
$\boldsymbol{j_{6i}}$	1.631	29.79	1589	-	-	-
$\boldsymbol{s_{1i}}$	3.675	7.998	57.73	-	-	-
$\boldsymbol{s_{2i}}$	3.378	9.502	2408	-	-	-
$\boldsymbol{s_{3i}}$	3.334	6.81	958.8	-	-	-

The results for the hex-hex channel are shown in Figure 2.5. The regular hexagon provides the lowest dispersion compared to other hex-hex cross-sections. The correlated functions for the hex-hex channel are reported in Appendix A. The functions used have been constructed such that they will be function of α_t and a vector of fitted parameters at fixed α_{rec},i.e. $\boldsymbol{p}(\alpha_{rec})$. Hence, to derive $g(\alpha_t, \boldsymbol{p}(\alpha_{rec}))$, the values of $\boldsymbol{p}(\alpha_{rec})$ have to be calculated first. Then, once fixed the $\boldsymbol{p}(\alpha_{rec})$, the functions $g(\alpha_t, \boldsymbol{p}(\alpha_{rec}))$ can be calculated at a fixed α_t.

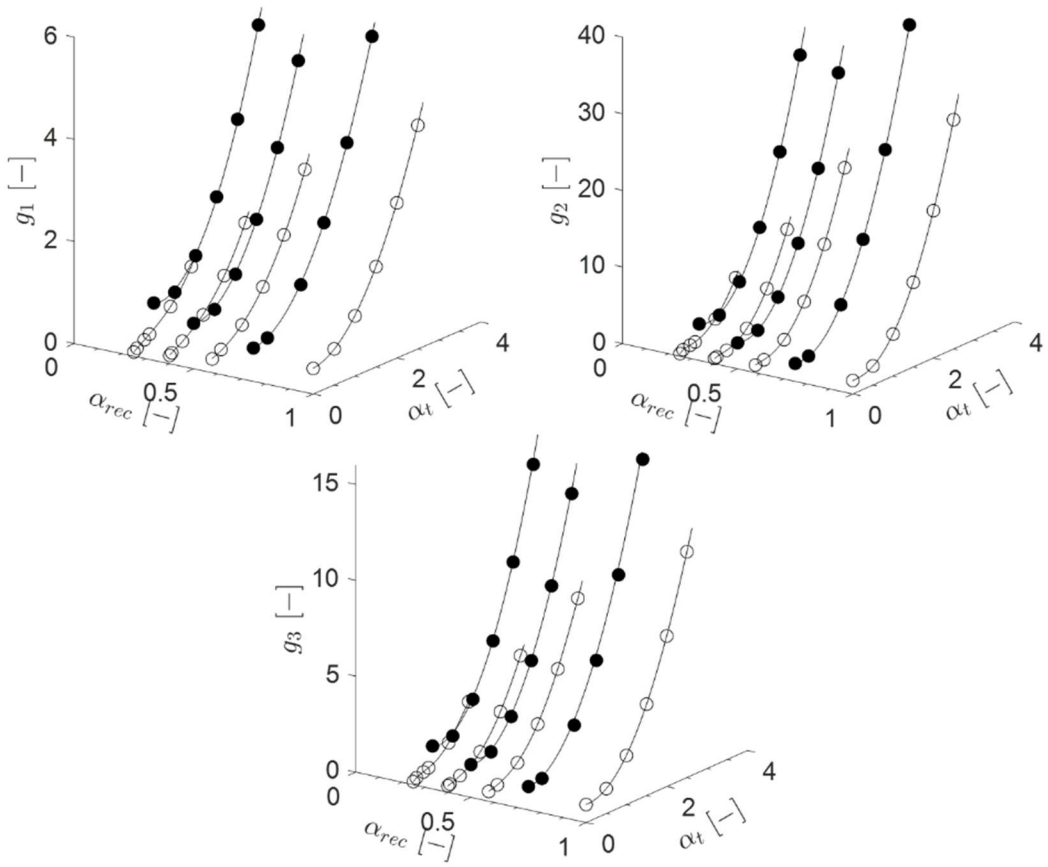

Figure 2.5: $g_i(\alpha)$ functions for the hex-hex channel. Solid lines are the fitted correlations while circles are the results from the numerical simulations: filled symbols for $\alpha_{ss} > 0$ and empty symbols for $\alpha_{ls} > 0$. On the y-axis $\alpha_t = \alpha_{ss}$ for $\alpha_{ss} > 0$ (filled circles), while $\alpha_t = \alpha_{ls}$ for $\alpha_{ls} > 0$ (empty circles).

2.2.2 The "corrected" thickness

Ahn and Brandani[73] have shown that, if the actual thickness of the solid is used to estimate the resistance given by the diffusion in the solid (R_S in eq.(2.1)), the HETP for a rectangular channel is systematically underestimated. To correctly estimate the solid resistance, they introduced the concept of "corrected" thickness, which consists of a thicker solid dimension to be used to calculate the HETP compared to the physical thickness of the solid. To calculate w_c, the corrected thickness, Ahn and Brandani[73] redistributed the solid around the rectangular free cross-section from the corners of the geometry to the free cross-section's perimeter, as graphically shown in Figure 2.6(top).

The corrected thickness introduced by Ahn and Brandani[73] is here generalised for an arbitrary cross-section. An example of the redistribution for the hex-cir channel is shown in Figure 2.6(bottom). For both squared and hex-cir channel, the solute will firstly travel in the solid around the free cross-section (grey in Figure 2.6), and then in the corners of the geometry (black in Figure 2.6) in both horizontal and vertical direction. By redistributing the solid, the 2D diffusion in the solid is reduced to a 1D diffusion problem, while preserving the total amount of solid of the channel.

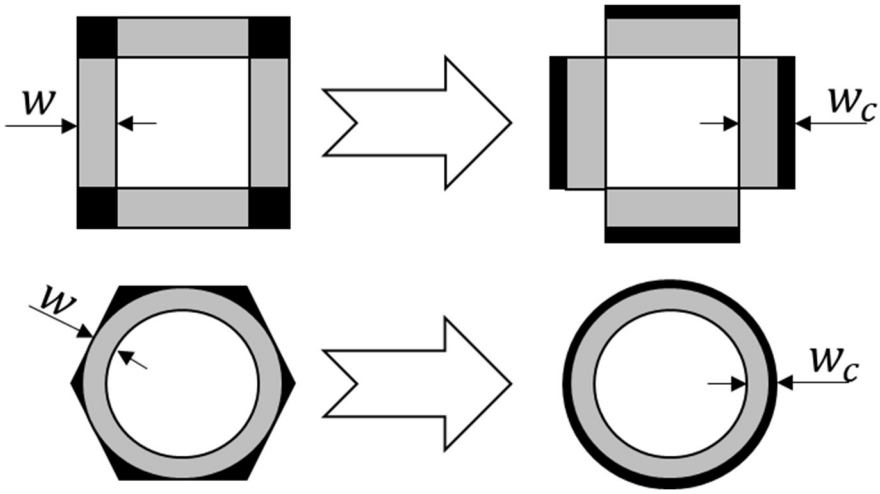

Figure 2.6: Redistribution of the solid for a squared channel (top), and a hex-cir channel (bottom). In grey the solid around the perimeter of the free cross-section, in black the corners.

The graphical redistribution presented for a squared and hex-cir channel can be held valid for all the geometries under analysis, since they always present corners which are not directly in contact with the free perimeter of the channel.

For flat geometries, the mathematical representation of the redistribution can be written as:

$$w_c = \frac{A_S}{Perim} \tag{2.19}$$

where A_S is the solid area. For a rounded geometry, we can write the corrected thickness as in eq.(2.20).

$$w_c = \frac{\sqrt{\frac{4A_S}{\pi} + d^2} - d}{2} \qquad 2.20$$

Analytical equations can be derived for several cross-sections. Table 2.2 provides the equations to estimate accurately w_c for the geometries under analysis.

Table 2.2: Analytical expression of the corrected thickness for different channels

Channel	***Analytical Expression***
Triangle	$w_c = w + \frac{w^2}{2h}\left(1 + \frac{1}{sin(arctan(\alpha/2))}\right)$
Rhombus	$w_c = \frac{\left(1 + 2\frac{w/h}{sin(atan(\alpha))}\right)\left(\alpha + 2\frac{w/h}{sin(atan(\alpha^{-1}))}\right) - \alpha}{4\sqrt{1+\alpha^2}}h$
Hex-Cir	$w_c = \frac{\sqrt{\frac{4}{\pi}\left[\left(2\sqrt{3} - \pi\right)\frac{d^2}{4} + 2\sqrt{3}\,w(d+w)\right] + d^2} - d}{2}$
Rectangle*	$w_c = \frac{1 + \alpha + 2w/h}{2(\alpha+1)}w$

*From Ahn and Brandani[73]

For the hex-hex channel, a simple procedure is presented in Table 2.3 to estimate the corrected thickness.

Having defined the corrected thickness, and derived the velocity resistance, the HETP can be now calculated for different geometries. To validate the correlations provided, full 3D numerical simulations can be used. The mathematical equations are presented in the next section.

Table 2.3: Procedure to calculate the corrected thickness of a hex-hex channel.

Step	Hex-Hex with $\alpha_{ls} > 0$	Hex-Hex with $\alpha_{ss} > 0$
1	Calculate $A_{in} = (\alpha_{ls} + \alpha_{rec})h^2$ and $d = \sqrt{\frac{4A_{in}}{\pi}}$	Calculate $A_{in} = (1 + \alpha_{rec}\alpha_{ss})\alpha_{rec}h^2$ and $d = \sqrt{\frac{4A_{in}}{\pi}}$
2	Define $b = \frac{\alpha_{rec}h}{2} - 2\alpha_{ls}w\left[1 - \sqrt{1 + \left(\frac{1}{2\alpha_{ls}}\right)^2}\right]$ and $B = \frac{\alpha_{rec}h}{2} + 2\alpha_{ls}\left[w\sqrt{1 + \left(\frac{1}{2\alpha_{ls}}\right)^2} + \frac{h}{2}\right]$	Define $b = h + 2w\left[\sqrt{1 + (2\alpha_{ss})^2} - 2\alpha_{ss}\right]$ and $B = h + 2h\left[\alpha_{rec}\alpha_{ss} + \frac{w}{h}\sqrt{1 + (2\alpha_{ss})^2}\right]$
3	Calculate $A_{out} = 2(b + B)\left(\frac{h}{2} + w\right)$	Calculate $A_{out} = (b + B)\left(\frac{\alpha_{rec}h}{2} + w\right)$
4	Calculate the corrected thickness as $w_c = \frac{\sqrt{\frac{4(A_{out} - A_{in})}{\pi} + d^2} - d}{2}$	

2.2.3 3D numerical simulations

2.2.3.1 Mathematical model

The main assumptions of the 3D model are as follows:

- Isothermal conditions
- Linear isotherm
- Trace binary system with one adsorbing molecule in an inert carrier
- Fully-developed laminar flow in the channel
- Negligible axial (z-axis) diffusion in the solid
- Equilibrium at the fluid-solid interface

The differential mass balance of the adsorbing i-th component in the fluid phase is:

$$\frac{\partial c_i}{\partial t} - D_m \nabla^2 c_i + \nabla(v c_i) = 0 \qquad 2.21$$

where the axial dispersion term has been written in terms of fluid concentration c and not mole fraction y, since the pressure drop in straight channels is

negligible. The boundary conditions are of the Danckwert's type, as in eq.(2.22) and (2.23).

$$-D_m \nabla c_i + v c_i = v_{in} c_{in,i} \quad @\ z = 0 \tag{2.22}$$

$$D_m \nabla c_i = 0 \quad @\ z = L \tag{2.23}$$

where v_{in} and c_{in} are the inlet velocity and concentration, respectively. The mass balance in the solid can be written as:

$$\frac{\partial q_i}{\partial t} = D_s \left(\frac{\partial^2 q_i}{\partial x^2} + \frac{\partial^2 q_i}{\partial y^2} \right) \tag{2.24}$$

where q_i is the amount adsorbed of the i-th component per unit volume. At the interface between the fluid and the solid:

$$q_i = K c_i \ \ \& \ \ D_m \nabla c_i = D_s \nabla q_i \tag{2.25}$$

Finally, the initial conditions assume that the bed is filled with the non-adsorbing carrier.

The average outlet concentration in the fluid phase is calculated using eq. (2.26).

$$c_{ave}|_{z=L} = \frac{\oiint v c_i|_{z=L} dxdy}{\oiint v \, dxdy} \tag{2.26}$$

The set of equations is converted in dimensionless form with the use of the following dimensionless variables:

$$C_i = \frac{c_i}{c_{in,i}} \ ; \ Q_i = \frac{q_i}{K c_{in,i}} \ ; \ \tau = \frac{t}{\mu} \quad \xi = \frac{x}{h} \ ; \ \phi = \frac{y}{h} \ ; \ \zeta = \frac{z}{L} \ ; \ V = \frac{v_{(x,y)}}{v_{ave}} \tag{2.27}$$

where μ is the first moment, i.e. the mean residence time, of the breakthrough curve. The first moment of the breakthrough curve, μ, can be directly estimated with the use of an integral mass balance on the channel, as in eq.(2.28).

$$\mu = \frac{L}{v_{ave}}\left[1 + \frac{1-\epsilon}{\epsilon}K\right] \qquad 2.28$$

The velocity profile is modelled using Navier-Stokes equations in viscous regime at steady-state. The boundary conditions are of fixed pressure of 100 kPa at the outlet, and fully-developed laminar flow at the inlet with an average velocity v_{ave}. The no-slip boundary condition is used at the interface between fluid and solid domains.

The parameters of equilibrium and kinetics for the 3D simulations are reported in Table 2.4. They refer to the system CO_2/N_2 separation with an activated carbon monolith, already reported by Ahn and Brandani[73]. The data are fitted to zero-length-column experiments presented in Brandani et al[58] on a commercial sample of activated carbon monolith. The diffusion in the solid has to be intended as effective diffusion of the system.

Table 2.4: Parameters for the 3D simulations.

Parameter	***Unit***	***Value***
$\boldsymbol{K}$	$[-]$	40
$\boldsymbol{D_m}$	$[m^2/s]$	$1.7\text{x}10^{-5}$
$\boldsymbol{D_s}$	$[m^2/s]$	$7.4\text{x}10^{-10}$

The dimensionless equations have been implemented in COMSOL. The integration limit of the simulation was set to twice the first moment of the system. A mesh-refinement study has been carried out to make sure that the results were independent of the mesh size and number of elements used.

The first and second moment of the adsorbing component can be calculated as in eq.(2.29) and (2.30).

$$1^{st}\ Moment\ \ \mu = \int_0^{\infty} \frac{c_i}{c_{in,i}}\,dt \qquad 2.29$$

$$2^{nd}\ Moment\ \vartheta^2 = 2\int_0^{\infty} \frac{c_i}{c_{in,i}} t\, dt - \mu^2 \qquad 2.30$$

Since the second moment can be strongly affected by numerical oscillations[84], an exponential function of the form ae^{-bt}, has been used to approximate the tail of the breakthrough curve. Hence, the second moment can be written as:

$$\vartheta^2 = 2\int_0^{t_0} \frac{c_i}{c_{in,i}} t\, dt + 2\frac{a}{b} e^{-bt_0}\left(t_0 + \frac{1}{b}\right) - \mu^2 \qquad 2.31$$

where, t_0 is the starting time of the exponential decay. Finally, the HETP can be calculated as in eq.(2.32).

$$\frac{HETP}{L} = \frac{\vartheta^2}{\mu^2} \qquad 2.32$$

To check the 3D simulations, as well as the procedure to calculate the HETP, a case study of a hollow fibre has been used. Indeed, eq.(2.5) is the analytical expression of the HETP for an hollow fibre. The results are presented in Figure 2.7. The 3D model implemented in COMSOL provides reliable results for the hollow fibre case, hence it can be safely used to test the HETP correlations for the other geometries.

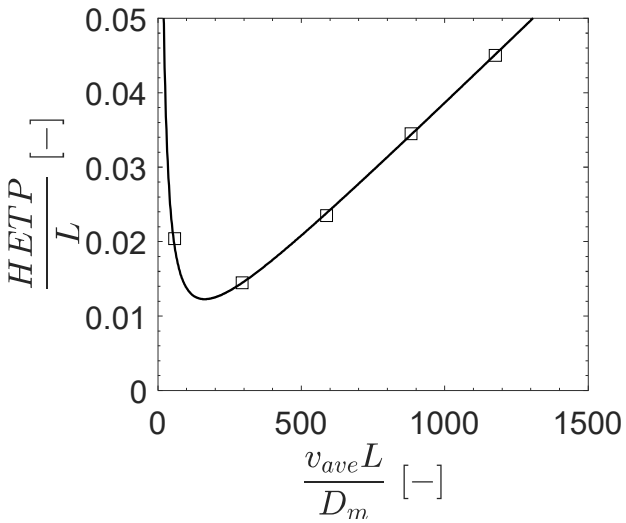

Figure 2.7: Comparison between 3D simulations and HETP correlation for a hollow fibre. Squares are the 3D simulations and the solid line is eq.(2.5). The physical parameters are reported in Table 2.4, and the geometrical parameters are: w/h=0.105, and L/h=700.

2.2.3.2 Comparison between 3D simulations and HETP correlations

The comparison between the 3D simulations for different straight-channel monoliths and their respective HETP correlation is presented in Figure 2.8.

The proposed HETP correlation accurately match the dispersion given by the 3D simulations. Furthermore, the simulations confirm what already stated by Ahn and Brandani[73] for a rectangular channel: the diffusion in the solid is the main resistance responsible for the dispersion of the solute in the channel. As it can be seen from Figure 2.8, the sum of axial dispersion and velocity profile only provide a minor contribution to the overall HETP.

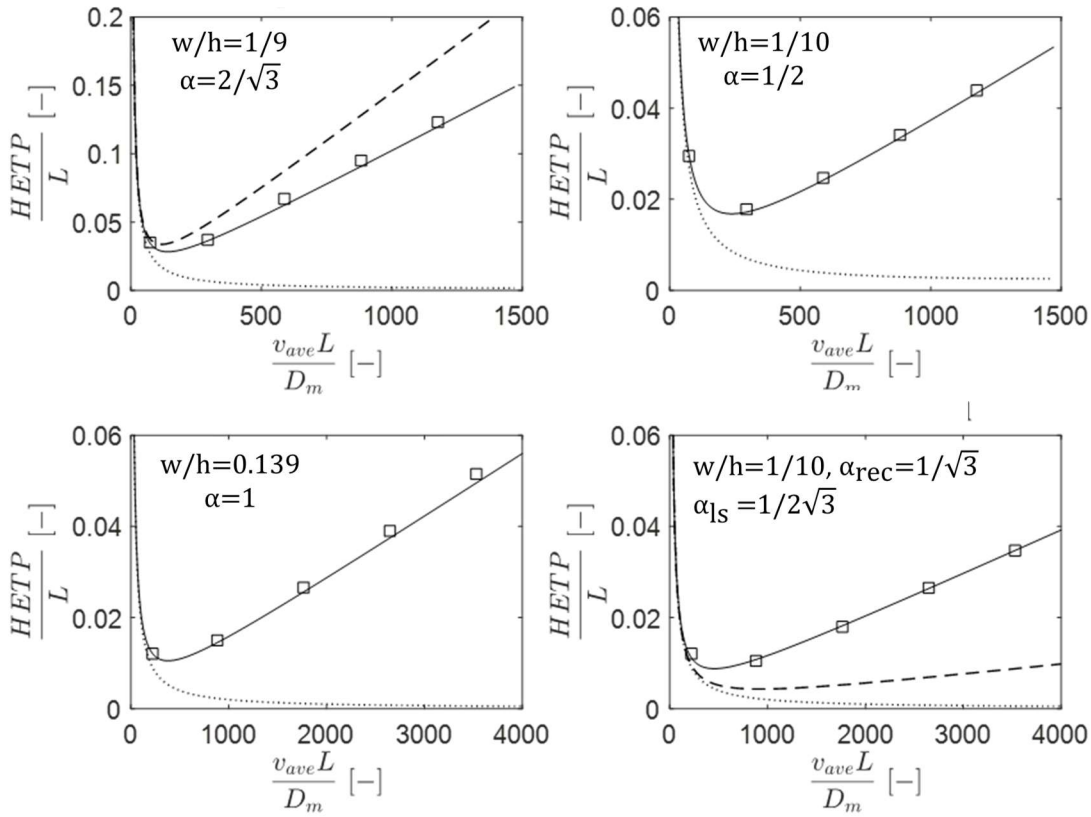

Figure 2.8: HETP plot for different geometries. From top to bottom, from left to right: triangular channel, hex-cir channel, rhombic channel, and hex-hex channel. Squares are 3D simulation results, the dotted line is the fluid resistance only, the dashed line is the HETP calculated using the model of Patton et al.[72] (triangular and hex-hex geometries) and the solid line the HETP with corrected thickness.

The transversal diffusion of the solute on the free cross-section balances the dispersion of the solute along the channel given by the velocity profile. This effect leads to a near plug flow in the free channel. For all the simulations, and

in general for gas separation processes, the dimensionless parameter $\frac{LD_m}{vh^2}$ is higher than 1, which explains why the concentration of the solute at a given cross-section assumes a homogeneous profile. It is therefore important to focus on the resistance given by the solid when optimising and straight-channel monoliths for gas adsorption applications.

The model of Patton et al.[72] is also compared to the 3D simulations. Indeed, Patton et al.[72] provide a LDF approximation for triangular and hex-hex geometry. In their work, each cross-section is reduced to an hollow cylinder. As it can be seen in Figure 2.8, the LDF approximation of Patton et al.[72] does not follow the trend of the 3D simulations. The reasons for the mismatch can be attributed firstly to the approximation of every channel to hollow cylinder, and then to the changed void fraction of the system. The former does not take into account that the diffusion process in a triangular channel can be quite different from the one of a hollow cylinder. As matter of fact, the diffusion process in a triangular channel can be represented as an equivalent 1D diffusion in a slab. The latter reason comes from the fact that the void fraction of the channel will not be kept constant if the volume of the free cross-section is not fixed also in the LDF approximation. This leads to a decrease in the triangular channel's void fraction in Figure 2.8 by roughly 40%, which explains the sharp increase of the HETP compared to the 3D simulations. In the hex-hex channel the LDF approximation from Patton et al. leads to a very thin layer of solid around the free cross-section, which explains the very low HETP compared to 3D simulations.

It could be argued that the hex-hex channel should be modelled with the HETP of a flat geometry, eq.(2.3). Indeed, the expression of Aris for the HETP of a hollow fibre, eq.(2.5), reduces to the diffusion in a slab geometry for thin films of solid surrounding the free cross-section, as shown by Schisla and Carr[82]. Moreover, the hex-hex channel already approximates the limit of a polygon with a number of sites which tend to infinity, hence a circle. For any practical purpose, honeycomb monoliths will have either regular hexagons or slightly different from regular hexagons as free cross-section. Hence, the

approximation of hex-hex to rounded geometry holds for any practical design use.

It can be noted a slight discrepancy between the HETP from 3D simulations of triangular and rhombic channel and the predicted HETP from correlations. This difference might be attributed to the local meshing of the corners of the geometries from both fluid and solid side. As default, an unstructured prismatic meshing is generated by COMSOL. However, local refinement of the mesh at the corners of the geometry might reduce the extra-dispersion present in the current simulations. Indeed, geometries which do not have sharp corners (i.e. hex-hex, hex-cir channel and circular channel) and geometries for which a structured mesh of hexahedral elements can be used (i.e. rectangular channel) provide excellent match between 3D simulations and the HETP correlation. Future works could study the effect of local mesh-refinement on the HETP that different meshing might show, especially for geometries which possess sharp corners.

It is worth pointing out that the HETP correlation is valid in the limit of very long columns. As pointed out by Ahn and Brandani[73], a quick way to establish if the system achieved the HETP in the limit of very long column is to check that the ratio between the first moment and, for a gas system, the time constant for diffusion in the solid is higher than 0.22. For all the simulations performed, the value of $\frac{\mu D_s}{w_c^2}$ ranged between 4 and 12. It has to be noted that, for liquid systems, the time constant to be used will be h^2/D_m, since the limiting kinetic process will be the diffusion in the liquid phase.

2.2.4 Reduced order model

2.2.4.1 Mathematical model

The use of 3D simulations can be limited to HETP validation, since its computational time and resources are not feasible for any design or optimisation purpose. Since multiple simulations are needed to firstly design and then optimise the operating parameters of common adsorption processes, a simpler, faster and nevertheless accurate model is needed. In this section, a

reduced order model is proposed, which is able to capture the overall dynamics of the 3D simulations. The model will have one dimension along the channel's axis for the fluid phase (z-axis), and one dimension for the diffusion of the solute in the solid (x-axis). The model makes use of the average velocity in the channel, which comes from the 3D simulations. Given the assumption of trace system, the average velocity will remain constant along the axis.

The modelling assumptions are the same as in the 3D model. The mass balance for the fluid phase is:

$$\frac{\partial c_i}{\partial t} - D_{ax}\frac{\partial^2 c_i}{\partial z^2} + v_{ave}\frac{\partial c_i}{\partial z} + \frac{1-\epsilon}{\epsilon}\frac{d\overline{q_i}}{dt} = 0 \qquad 2.33$$

where D_{ax} , the axial dispersion, can be derived by the sum of molecular diffusion and velocity profile resistances in eq.(2.3) and (2.5), and $\overline{q_i}$ is the average adsorbed amount of the i-th component. The boundary conditions are of the Danckwert's type:

$$-D_{ax}\frac{\partial c_i}{\partial z} + v_{ave}c_i = v_{ave}c_{in,i}; \quad @ \quad z = 0 \qquad 2.34$$

$$D_{ax}\frac{\partial c_i}{\partial z} = 0; \quad @ \quad z = L \qquad 2.35$$

The mass balance in the solid can be written as:

$$\frac{dq_i}{dt} = D_s\left(\frac{\partial^2 q_i}{\partial x^2} + \frac{\theta}{x}\frac{\partial q_i}{\partial x}\right) \qquad 2.36$$

where for flat geometries $\theta = 0$ and $\theta = 1$ for rounded ones. The boundary conditions for eq.(2.36) are given below.

$$q_i = Kc_i; \quad @\, x = h \qquad 2.37$$

$$D_s\frac{\partial q_i}{\partial r} = 0; \quad @ \quad x = h + w_c \qquad 2.38$$

The average adsorbed amount has been calculated from eq.(2.39).

$$\overline{q_i} = \frac{\int_h^{h+w_c} q_i x^\theta dx}{\int_h^{h+w_c} x^\theta dx} \qquad 2.39$$

The reduced model has been solved in gPROMS using orthogonal collocation on finite elements to discretise both the fluid and solid domains. A mesh-refinement has been carried out to assure results independent on the number of elements used.

The parameters of the reduced model can be derived from the knowledge of physical and geometrical parameters of the system. The two main parameters that are different with respect to the 3D simulations are the effective axial dispersion, D_{ax}, and the thickness of the solid. The axial dispersion of the reduced model is not going to be the molecular diffusion, as in the 3D simulations. Instead, the axial dispersion of the reduced model can be calculated as sum of the axial and velocity profile resistance of the HETP correlation[85], as shown in eq.(2.40):

$$D_{ax} = D_m\left(1 + \frac{C_M}{2}Pe^2\right) = D_m\left(1 + \frac{C_M}{2}\left(\frac{v_{ave}h}{D_m}\right)^2\right) \qquad 2.40$$

where Pe is the Peclet number of the system. The second relevant parameter is the thickness of the solid for the reduced simulation, which will be set to the corrected thickness of the channel.

It should be noted that the reduced model does not make use of any adjustable parameters, and its derivation is solely based on the knowledge of the properties of the system under consideration. Moreover, the reduced model has the main benefit to be faster than the 3D model, since the different in computational time is of almost 3 orders of magnitude, which makes it particularly suitable for design and optimisation purposes.

2.2.4.2 Comparison between 3D simulations and reduced model

The comparison between 3D simulations and the reduced model is shown in Figure 2.9. The values of $\frac{v_{ave}L}{D_m}$ for each simulation are reported in Table 2.5.

Table 2.5: Values of $\frac{v_{ave}L}{D_m}$ $[-]$ for the breakthrough simulations in Figure 2.9. The symbols in the first column refer to the symbols in Figure 2.9.

	Triangular	***Rhombic***	***Hex-Cir***	***Hex-Hex***
Circles	294	294	882	1764
Squares	882	2059	4412	8824
Diamonds	2059	5882	8824	30884

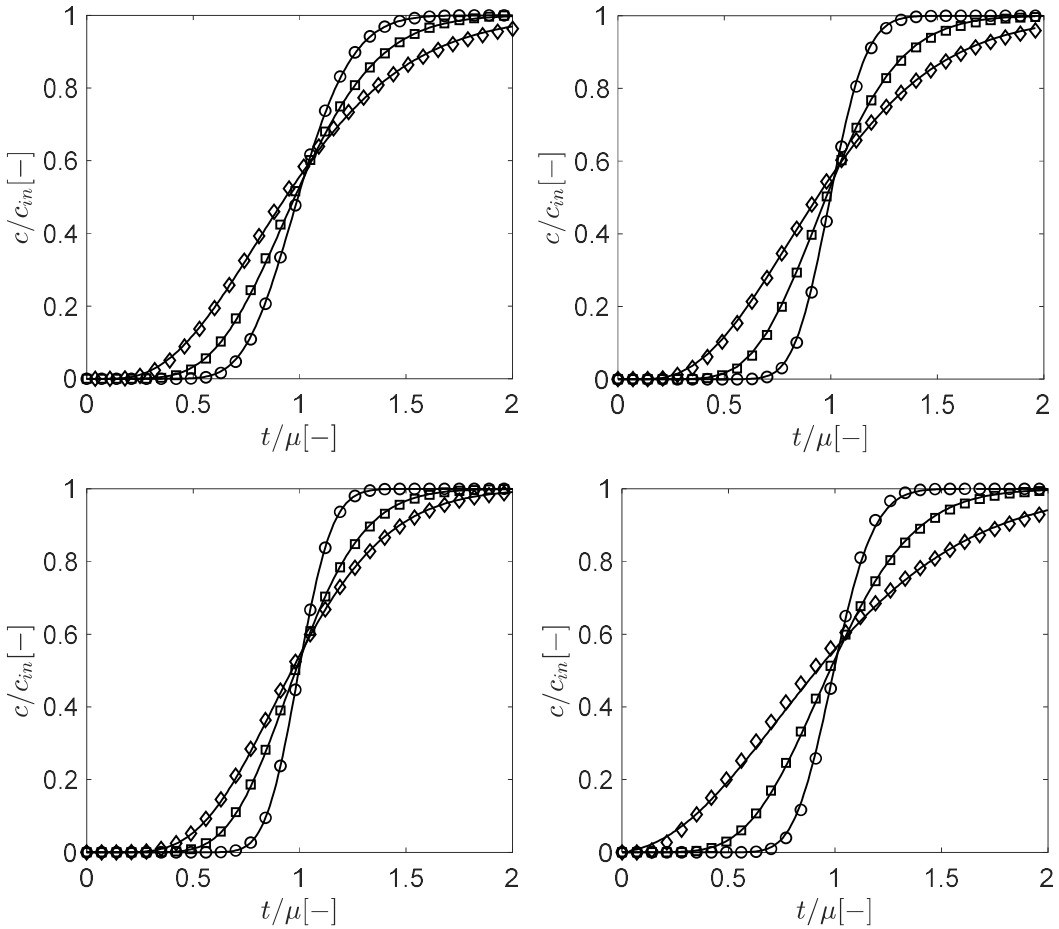

Figure 2.9: Comparison between 3D simulations and reduced order model. From top to bottom, from left to right: triangular channel, hex-cir channel, rhombic channel, and hex-hex channel. The geometrical parameters are the same as in Figure 2.8. The values of $\frac{v_{ave}L}{D_m}$ for each simulation are reported in Table 2.5. Symbols are 3D simulations and solid line is the reduced order model.

The agreement between 3D and reduced model is excellent. The reduced model correctly captures both first and second moment of the 3D simulations. The match of the second moment can be mainly attributed to the inclusion of

the dispersion given by the corrected thickness. The numerical problem's size, and hence the computational time, is more than two order of magnitude smaller for the reduced order model. Therefore, the reduced order model can potentially act as an effective tool for fast screening of different straight-channel monoliths for targeted applications, at a design stage.

2.3 The pressure drop correlation

Among the factors influencing the energy penalty of an adsorption process, pressure drop plays a crucial role. Indeed, the extremely low pressure drop of straight-channel monoliths make them a suitable alternative to conventional packed beds. Nevertheless, it is important to accurately estimate the pressure drop in straight-channel monoliths, especially at a design stage. In this work, the ERM of Muzychka and Yovanovich[79] is employed, given its broad application to all the straight-channel monoliths under analysis.

The general expression of the pressure drop in eq.(2.2) can be specialised for a given straight-channel monolith by means of the fRe_{Σ} and the ratio $\frac{Pr}{A\Sigma}$ which will depend on the geometry of the free cross-section of the channel. Muzychka and Yovanovich[79] showed that the analytical solution fRe_{Σ} for a rectangular channel, when $\Sigma = \sqrt{A}$, can be written as:

$$fRe_{\sqrt{A}} = \frac{12}{\sqrt{\gamma}(1+\gamma)\left[1 - \frac{192\gamma}{\pi^5} tanh\left(\frac{\pi}{2\gamma}\right)\right]} \qquad 2.41$$

where γ is the effective aspect ratio of the rectangular channel. For the rectangular channel, the effective aspect ratio has the same value of the nominal aspect ratio of the geometry defined earlier in the chapter. The equations of the effective aspect ratios of the different channels, as presented by Duan and Yovanovich[86] and developed in this work, are reported in Table 2.6.

Table 2.6: Correlations for the effective aspect ratio of different channels

Geometry	***Effective Aspect Ratio, γ***
Regular Polygons with $n_{sides} \in [4;\infty]$*	1
*Triangle**	$[(2\alpha)^{0.53} + (2/\alpha)^{0.53}]^{-1/0.53}$
*Rhombus**	$[(2\alpha)^{0.68} + (2/\alpha)^{0.68}]^{-1/0.68}$
Hex-Hex with $\alpha_{ss} = 0$**	$\left[\left(\frac{\sqrt{3}}{2(\alpha_{rec}+\alpha_{ls})}\right)^{90} + \left(\frac{2(\alpha_{rec}+\alpha_{ls})}{\sqrt{3}}\right)^{90}\right]^{-1/95}$
Hex-Hex with $\alpha_{ls} = 0$**	$\frac{1}{1/\alpha_{rec} + \alpha_{ss}}$

*From Duan and Yovanovich[86]; **Developed in this work

With the use of the correlations in Table 2.6, eq.(2.2) and (2.41) the pressure drop for a straight-channel monolith can be evaluated.

The correlations for the hex-hex channel have been regressed on numerical simulations of fluid flow in hex-hex channels. The Navier-Stokes equations are solved in the free cross-section and the $fRe_{\sqrt{A}}$ is regressed from that. The results are presented in Figure 2.10.

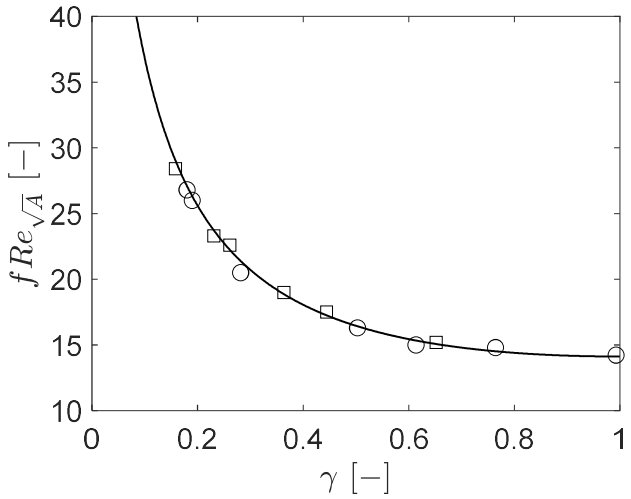

Figure 2.10: $fRe_{\sqrt{A}}$ correlation for hex-hex channel. Squares are hex-hex channel with $\alpha_{ss} > 0$, circles are hex-hex channel with $\alpha_{ls} > 0$ and solid line eq.(2.41) with γ calculated from the correlations in Table 2.6.

The main advantage of the ERM is that the $fRe_{\sqrt{A}}$ is constant at 14.13 for the vast majority of industrially relevant straight-channel monoliths, i.e. regular

polygons and circular cross-section. Furthermore, only one equation is needed to calculate the $fRe_{\sqrt{A}}$ of different geometries when $\alpha \neq 1$. The approach of using the hydraulic diameter as characteristic length would have led to different equations of fRe_{D_h} for each geometry, even for $\alpha = 1$.

2.4 Comparison between straight-channel monoliths and packed bed for gas systems

Once the HETP and pressure drop correlation for a straight-channel monolith are known, a comparison between them can be made based on the pressure drop per theoretical stage, i.e. $HETP\Delta P/L$. Ruthven and Thaeron[33] were the first to use the pressure drop per theoretical stage to compare a conventional packed bed with a parallel passage contactor. Their analysis showed that under all practical conditions, a parallel passage would perform better than a packed bed. This section aims to broaden their analysis to an arbitrary extruded monolith. The following analysis excludes the resistance given by the velocity profile in the HETP correlation, since this analysis is limited to gas systems, for which the HETP correlations have been validated.

For a packed bed of porosity ϵ_{pb} and bead radius R_p, the pressure drop can be described as the Ergun equation:

$$\frac{\Delta P_{Packed}}{L} = 37.5\eta \frac{\epsilon_{pb} v}{R_p^2} \frac{\left(1-\epsilon_{pb}\right)^2}{\epsilon_{pb}^3} \qquad 2.42$$

where the turbulent term has been neglected in the assumption that the particles are big enough to avoid turbulent effects.

In the assumption that $K \gg \epsilon$, the HETP for a packed bed can be written as[33]:

$$\frac{HETP_{Packed}}{L} = \frac{2\epsilon_{pb} D_{ax}}{\epsilon_{pb} v} + \frac{2}{15} \frac{\epsilon_{pb} v}{\left(1-\epsilon_{pb}\right) K} \frac{R_p^2}{D_s} \qquad 2.43$$

where, under these conditions, the axial dispersion can be written as $D_{ax} = 0.7 D_m$[87]. Now that HETP and ΔP correlation for a packed bed are given, we can define the ratio of pressure drop per theoretical stage of an arbitrary

straight-channel monolith with a packed bed, using eq.(2.2,2.3,2.42,2.43). It should be noted that, in the assumption of $K \gg \epsilon$, the solid resistance in eq.(2.3) can be simplified to $\frac{2k}{3(1+k)^2}\frac{w^2}{D_s}v_{ave} = \frac{2}{3(1-\epsilon)K}\frac{w^2}{D_s}v_{ave}$. In addition, only the contribution from axial dispersion and solid diffusion will be considered for the HETP of the monolith. Under these conditions, we can write the ratio of the pressure drop per theoretical stage as in eq.(2.44)

$$R = \frac{(\Delta PHETP/L)_{Packed}}{(\Delta PHETP/L)_{monolith}} = 75\frac{\left(1-\epsilon_{pb}\right)^2\epsilon}{\epsilon_{pb}^3}\frac{A\sqrt{A}}{R_p^2 Perim}\frac{\frac{1.4\epsilon_p D_m}{\epsilon_p v} + \frac{2}{15}\frac{\epsilon_{pb}v}{\left(1-\epsilon_{pb}\right)K}\frac{R_p^2}{D_s}}{2\frac{D_m}{v_{ave}} + \frac{2}{3(1-\epsilon)K}\frac{w^2}{D_s}v_{ave}} \quad 2.44$$

to compare both packed bed and monolith at the same throughput, we need to set $v_{ave} = \frac{\epsilon_{pb}}{\epsilon}\ v$. To obtain a quantitative estimate of the ratio in eq.(2.44), we can fix $\epsilon_{pb} = 0.35, \epsilon = 0.5$, and $R_p = w$. The ratio can then be written as:

$$R = \frac{(\Delta PHETP/L)_{Packed}}{(\Delta PHETP/L)_{monolith}} = 369.5\frac{A\sqrt{A}}{R_p^2 Perim}\left[\frac{\frac{1.4\epsilon_{pb} D_m}{\epsilon_{pb} v} + \frac{2}{15}\frac{\epsilon_{pb}v}{\left(1-\epsilon_{pb}\right)K}\frac{R_p^2}{D_s}}{2\frac{\epsilon D_m}{\epsilon_{pb}v} + \frac{2}{3(1-\epsilon)\epsilon K}\frac{R_p^2}{D_s}\epsilon_p v}\right] \quad 2.45$$

Finally, we can rearrange the ratio in brackets on the RHS of eq.(2.45) such that R will be function of the dimensionless groups $\frac{D_m}{\epsilon_p v R_p}$ and $\frac{D_m}{K D_s}$:

$$R\left(\frac{D_m}{\epsilon_p v R_p},\frac{D_m}{KD_s}\right)$$
$$= 369.5\frac{A\sqrt{A}}{R_p^2 Perim}\left[\frac{1.4\epsilon_{pb}\left(\frac{D_m}{\epsilon_{pb}vR_p}\right)+\frac{2}{15(1-\epsilon_{pb})}\left(\frac{\epsilon_{pb}vR_p}{D_m}\right)\frac{D_m}{KD_s}}{2\epsilon\left(\frac{D_m}{\epsilon_{pb}vR_p}\right)+\frac{2}{3(1-\epsilon)\epsilon}\left(\frac{\epsilon_{pb}vR_p}{D_m}\right)\frac{D_m}{KD_s}}\right] \quad 2.46$$
$$= 369.5\frac{A\sqrt{A}}{R_p^2 Perim}R_{HETP}$$

the expression of $R\left(\frac{D_m}{\epsilon_{pb}vR_p},\frac{D_m}{KD_s}\right)$ in eq.(2.46) represents the ratio of the pressure drop per theoretical stage between packed bed and an arbitrary monolith with flat geometry as free cross-section. The higher the ratio, the better will be the monolith's performance with respect to the packed bed. The plot of the ratio $R\left(\frac{D_m}{\epsilon_{pb}vR_p},\frac{D_m}{KD_s}\right)$ for flat geometries is shown in Figure 2.11.

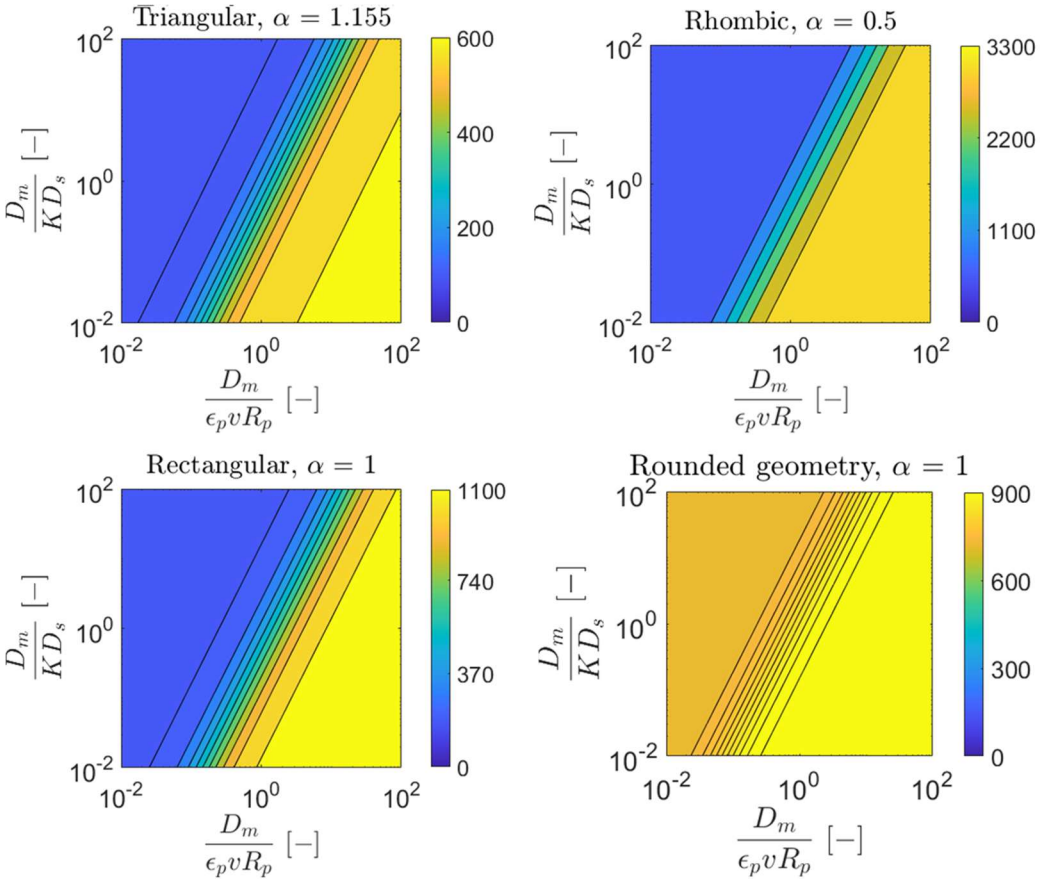

Figure 2.11: Plot of the function $R\left(\frac{D_m}{\epsilon_p vR_p},\frac{D_m}{KD_s}\right)$, eq.(2.46), for triangular, rhombic, rectangular and eq.(2.47) for rounded channels. The values of porosities are: $\epsilon_p = 0.35$; $\epsilon = 0.5$, and $R_p = w$.

The monoliths with flat cross-sections show better performance in terms of pressure drop per theoretical stage under all practical conditions. To further prove it, the limits of the function $R\left(\frac{D_m}{\epsilon_{pb}\upsilon R_p}, \frac{D_m}{KD_s}\right)$ with respect to its variables are presented in Table 2.7.

Table 2.7: Limits of the function $\boldsymbol{R\left(\frac{D_m}{\epsilon_p \upsilon R_p}, \frac{D_m}{KD_s}\right)}$.

	$\boldsymbol{\lim_{\frac{D_m}{KD_s}\to 0^+} R\left(\frac{D_m}{\epsilon_p \upsilon R_p}, \frac{D_m}{KD_s}\right)*}$	$\boldsymbol{\lim_{\frac{D_m}{KD_s}\to \infty} R\left(\frac{D_m}{\epsilon_p \upsilon R_p}, \frac{D_m}{KD_s}\right)*}$
Triangular	601.28	94.39
Rectangular	1055	165.55
Rhombic	3341	524.6
Rounded	936	720

$^*\lim_{\frac{D_m}{KD_s}\to 0^+} R\left(\frac{D_m}{\epsilon_p \upsilon R_p}, \frac{D_m}{KD_s}\right) = \lim_{\frac{D_m}{\epsilon_p \upsilon R_p}\to \infty} R\left(\frac{D_m}{\epsilon_p \upsilon R_p}, \frac{D_m}{KD_s}\right)$ and $\lim_{\frac{D_m}{KD_s}\to \infty} R\left(\frac{D_m}{\epsilon_p \upsilon R_p}, \frac{D_m}{KD_s}\right) = \lim_{\frac{D_m}{\epsilon_p \upsilon R_p}\to 0+} R\left(\frac{D_m}{\epsilon_p \upsilon R_p}, \frac{D_m}{KD_s}\right)$.

The discussion on flat geometries can be easily extended to rounded ones. The HETP for a rounded geometry can be written as in eq.(2.5). The ratio of pressure drop per theoretical stage can then be written as:

$$R^{rounded}_{\left(\frac{D_m}{\epsilon_{pb}\upsilon R_p}, \frac{D_m}{KD_s}\right)} = 369.5 \frac{A\sqrt{A}}{R_p^2 Perim}\left[\frac{1.4\epsilon_{pb}\left(\frac{D_m}{\epsilon_{pb}\upsilon R_p}\right) + \frac{2}{15(1-\epsilon_{pb})}\left(\frac{\epsilon_{pb}\upsilon R_p}{D_m}\right)\frac{D_m}{KD_s}}{2\epsilon\left(\frac{D_m}{\epsilon_{pb}\upsilon R_p}\right) + \frac{2f_1}{(1-\epsilon)\epsilon}\left(\frac{\epsilon_{pb}\upsilon R_p}{D_m}\right)\frac{D_m}{KD_s}}\right] \quad 2.47$$

where R_p has been assumed equal to the corrected thickness of the solid. The results for a rounded geometry are shown together with flat geometries in Figure 2.11 and Table 2.7.

It can be concluded from this brief discussion, that straight-channel monoliths offer better performance in terms pressure drop per theoretical stage compared to conventional packed beds. This comparison did not take into account several other factors such as manufacturing costs, installation costs and sizing of monoliths and packed beds. These factors will of course orient the choice at design stage for a given separation. However, the analysis

presented can help to assess the energy penalty that an adsorption process might have in comparison to conventional packed beds, especially when handling high throughputs.

2.5 The corrugated monolith

A particular type of straight-channel monolith is the corrugated monolith (CM). It finds wide application in air drying[88,89], and recently its performance for carbon capture application have been investigated[54–56]. As with other straight-channel monoliths, CMs can either be fully formed of adsorbent material[89,90] or consist of alternated flat and corrugated metal foils then coated with active adsorbent[54].

An example of CM is shown in Figure 2.12, together with the schematic drawing of its representative channel. The image of the CM is taken from the work or Amalraj et al[55]. The characteristic dimensions highlighted in Figure 2.12 are: the height of the outer boundary h_o, the base of the outer boundary i_o, the height of the free cross-section h, the base of the free cross-section i, and the thickness of the solid w. The aspect ratio of the outer boundary can be defined as $\alpha_o = i_o/h_o$, the aspect ratio of the free cross-section as $\alpha = i/h$ and the dimensionless thickness as $\delta = w/h_o$. To fully describe the channel's geometry, only two of the dimensionless parameters are needed.

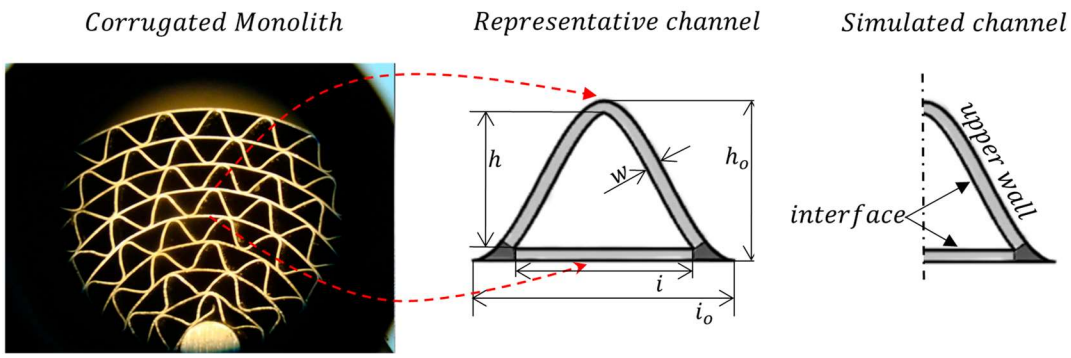

Figure 2.12: Example of the corrugated monolith (left), the schematic drawing of its single representative channel (centre), and the domain for modelling purposes (right). In light grey the area of solid surrounding the perimeter of the free cross-section and in dark grey the corners of the solid. The image of the CM is taken from Amalraj et al[55].

Several studies in literature can be found whose aim is the numerical modelling of CMs for the design and optimisation of adsorption applications[63,91–99]. Two

main categories can be distinguished: 1D[63,89,92,93,95] and 2D[88,99,100] models. Both types of models assume that the monolith is ideal, hence only a single representative channel of the CM can be studied. Besides, it is often assumed that axial mass and thermal dispersion are negligible and that the ideal channel is adiabatic. While the adiabatic assumption can represent the actual behaviour of a CM's channel entirely made of adsorbent material, the assumption of negligible dispersion in the channel can have a strong impact on the numerical predictions of CM's performance, as will be discussed later.

The 1D models consider relevant only the variations of mass and energy variables in the axial direction of the ideal CM. The mass and energy transfer in the adsorbent is modelled with lumped 0D equations whose physical parameters are calculated from Sherwood, Sh, and Nusselt, Nu, number correlations. The correlations available in the literature rely mostly on the work of Shah[76] who estimated Nu number from numerical simulations of momentum and energy balances in several ducts of arbitrary cross-sections. The Sh is either assumed equal to the Nu number, as in the work of De Antonellis et al.[92], or calculated from the Chilton-Colburn analogy[63], $Sh = NuLe^{1/3}$, where the Lewis number, Le, is the ratio between thermal and molecular diffusivity of the gas flowing in the channel.

The 2D model considers both the axial direction along the ideal CM and 1D for the diffusion and conduction in the solid. The 2D models generally study the water adsorption on desiccant wheels. They assume molecular, Knudsen and surface diffusion in the solid. The use of physical models to derive the parameters which do not rely on empirical correlations provides a higher degree of accuracy while keeping the computational time in the range of tens of seconds, which is still acceptable for optimisation purposes.

To the best of the author's knowledge, only the work of Cheng et al.[101] reported the 3D modelling of an ideal CM for air drying application. They considered the complete set of mass and energy balance equations in the 3D CM's channel. They firstly solved the Navier-Stokes equations to derive the flow profile in the

channel and, once the velocity profile was fixed, they solved the mass and energy balances. However, this can lead to inconsistencies if the temperature variation is substantial, given that the velocity profile will be affected by the temperature change[101]. They also report a simplified 1D model that is compared to the 3D model and experimental data. They conclude that 3D simulations better match the experimental data. Instead, the 1D model strongly relies on Nu and Sh numbers, as can be expected. As matter of fact, available Nu correlations are derived from numerical simulations assuming either constant and uniform temperature on the wall of the free channel, or constant and uniform heat flux at the walls of the free channel. However, neither one or the other condition are completely true. Cheng et al.[101] arrive at the conclusion that a 3D model should generally be used to predict mass and thermal profiles for ideal CMs, since an accurate reduced model cannot be produced.

From the brief literature review outlined above, it is evident that the modelling of CM still remains an open problem. The use of empirical correlations to estimate mass and energy parameters can be of limited use. By contrast, full 3D simulations appear prohibitive for design and optimisation purposes since they require a long time to run. Ideally, a trade-off between accuracy and fast computation has to be found.

The aim of this section is to apply the methodology presented for the straight-channel monoliths in Figure 2.1 to CM, as well. Furthermore, the CM can also offer the chance to include energy balances in the reduced model to broaden it to non-isothermal conditions, and to include non-linear isotherms. Moreover, the newly developed 3D model will assume macropore diffusion control and directly calculate the diffusivity of the molecules from available correlations, without the need of a diffusion time constant from experimental data. The following work will show the results from the analysis of a CM as done for the straight-channel monoliths, and the description of the non-isothermal and non-linear reduced model. The results from non-isothermal conditions can provide a further point of discussion on the need of accurate correlations for the prediction of a monolith performance.

2.5.1 Drawing of a corrugated monolith channel

In Figure 2.12(right) the channel representation used for modelling purposes is shown. To draw it, firstly the upper wall is drawn with a function of the form:

$$f_{uw}(x) = \frac{h_o}{2}\left[1 - cos\left(\frac{2\pi}{i_o}\left(x + \frac{i_o}{2}\right)\right)\right] \text{ with } x \in \left[0, \frac{i_o}{2}\right] \quad 2.48$$

then, a constant thickness of solid has to be drawn from the upper wall. To do so, we can calculate the displacement in both x and y direction needed to achieve the constant thickness from the wall. The displacements are in eq.(2.49) and (2.50).

$$\Delta y = \frac{w^2}{1 + \left(\frac{df_{uw}(x)}{dx}\right)^2} \quad 2.49$$

$$\Delta x = \left(\frac{df_{uw}(x)}{dx}\right)^2 \Delta y \quad 2.50$$

Next, we define a new reference system in the x direction:

$$x_c = \ x - \sqrt{\Delta x} \quad 2.51$$

to then formulate the mathematical expression to draw the interface between free and solid domains:

$$y_c(x_c(x)) = y(x_c(x)) - \sqrt{\Delta y(x_c(x))} \quad 2.52$$

such that the points $P_{(x_c,y_c)}$ represent the interface. The solid base can be simply drawn with straight lines intercepting the wavy interface and upper wall.

2.5.2 HETP correlation

Following the procedure outlined in Section 2.2 of this chapter, we can derive the HETP correlation for a corrugated channel based on the analysis of moments of Dutta and Leighton[70], and the derivation of a corrected thickness.

To calculate the values of $g_i(\alpha)$ for a corrugated channel, we can simplify the free cross-section as a wavy boundary and a straight line between the edges at the base. As done before (see section 2.2.1), the numerical values are correlated with an empirical function of the form:

$$g_i(\alpha) = \frac{j_{1i}\alpha^5 + j_{2i}\alpha^4 + j_{3i}\alpha^3 + j_{4i}\alpha^2 + j_{5i}\alpha + j_{6i}}{\alpha^5 + s_{1i}\alpha^4 + s_{2i}\alpha^3 + s_{3i}\alpha^2 + s_{4i}\alpha + s_{5i}} \qquad 2.53$$

where j and s are fitting parameters. The results are shown in Figure 2.13.

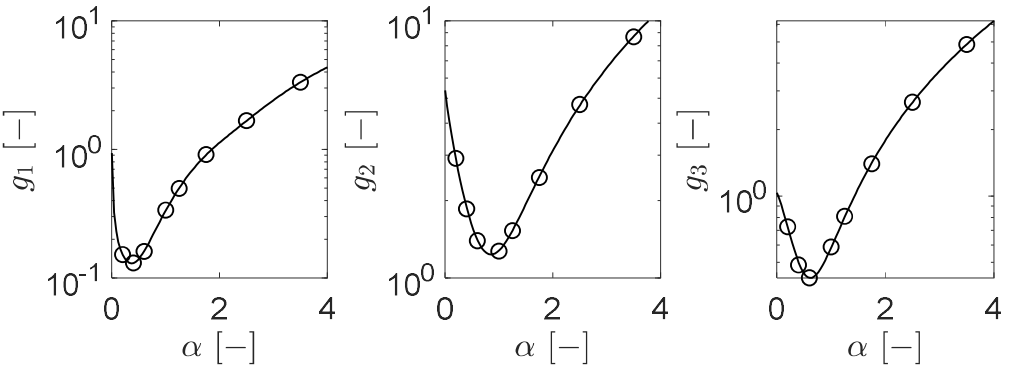

Figure 2.13: $g_i(\alpha)$ functions for the corrugated channel. Circles are numerical data, the solid line is eq.(2.53) with the parameters from Table 2.8.

The regressed j and s are reported in Table 2.8.

Table 2.8: Regressed parameters for the $g_i(\alpha)$ functions, in eq.(2.53).

	g_1	g_2	g_3
j_{1i}	4.438	1808	5.937
j_{2i}	−21.06	7206	330.4
j_{3i}	35.18	−8456	635
j_{4i}	−18.14	8812	17.88
j_{5i}	6.157	1434	−311.4
j_{6i}	0.5466	3430	436.4
s_{1i}	0	0	0
s_{2i}	4.984	3919	0
s_{3i}	−31.11	2245	1216
s_{4i}	45.86	2093	275.7
s_{5i}	0.5837	639.7	421.8

Once the $g_i(\alpha)$ functions have been obtained, only the corrected thickness for a corrugated channel must be derived to characterise the HETP of a CM.

The corrugated channel is a flat geometry, hence eq.(2.19) can be used to derive an expression of the corrected thickness. With reference to Figure 2.12(right), the area of solid can be calculated as:

$$A_S = \int_0^{i_o/2} f_{uw}(x)dx - \int_0^{x_2^*} y_c\big(x_c(x)\big)dx_c \qquad 2.54$$

while the perimeter:

$$Perim = \oint_0^{x_2^*} y_c\big(x_c(x)\big)dx + [x_c(x_2^*)] \qquad 2.55$$

where x_2^* is the intercept between the wavy interface and the solid base of the channel. With the use of eq.(2.54) and (2.55) we can calculate the corrected thickness using eq.(2.19). However, a simple analytical solution cannot be derived. Therefore, a numerical solution has to be calculated using numerical integration.

To provide a simple, yet reliable, correlation for the corrected thickness of a CM channel, several values of the dimensionless corrected thickness, $\delta_c = w_c/h_o$, have been generated using different values of δ and α_o. The correlation is reported in eq.(2.56).

$$\delta_c = p_1(\alpha_o)\delta^2 + p_2(\alpha_o)\delta + p_3(\alpha_o) \qquad 2.56$$

The correlations for the parameters $p_i(\alpha_o)$ are reported in eq.(2.57)-(2.59).

$$p_1(\alpha_o) = 0.9742\alpha_o^2 + 0.1956\alpha_o - 0.3833 \qquad 2.57$$

$$p_2(\alpha_o) = -0.4641\alpha_o^2 + 0.8098\alpha_o + 0.7588 \qquad 2.58$$

$$p_3(\alpha_o) = 0.0326\alpha_o^4 - 0.137\alpha_o^3 + 0.2145\alpha_o^2 - 0.1446\alpha_o + 0.0331 \qquad 2.59$$

The ranges with which this equation has been generated are: $\alpha_o \in [0.5,2]$, and $\delta \in [0.01,0.22]$. The correlation in eq.(2.56) is shown in Figure 2.14.

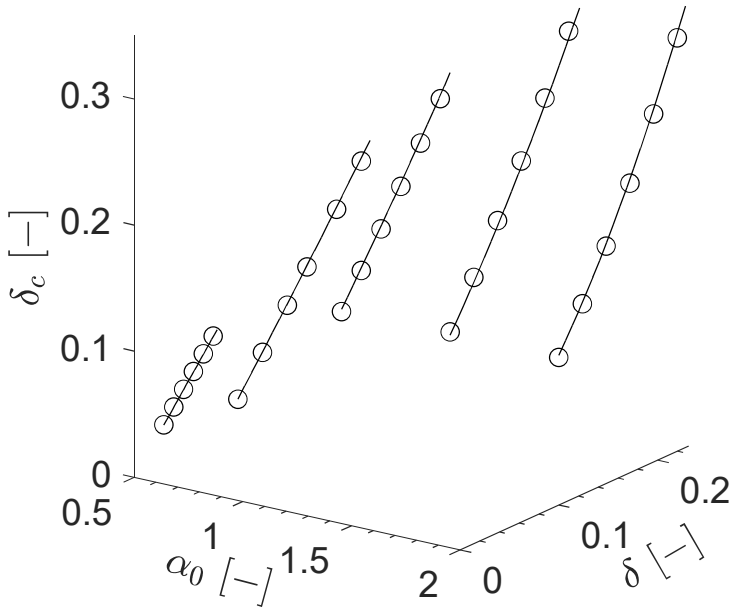

Figure 2.14: Plot of the dimensionless corrected thickness against α_o and δ. Circles are numerical values from eq.(2.19) and solid line is the fitted correlation, eq.(2.56).

Once the correlations to derive the HETP are known, the HETP expression, eq.(2.3), can be compared with the 3D simulations. In the following, the non-isothermal 3D model is presented.

2.5.3 Non-isothermal 3D model

The following set of equations are used to validate the HETP correlation for the CM and to extend the reduced order model to non-isothermal and non-linear conditions.

The assumptions of the non-isothermal 3D model are:

- Trace-component system
- The feed consists of a target molecule and an inert carrier
- Fully-developed laminar flow in the channel
- Macropore diffusion control
- Negligible energy accumulation of the gas phase in the pores and of the adsorbed phase
- The gas phase follows the ideal behaviour

The assumption of trace-component for a non-isothermal system is due to the inability to correctly implement the total mass balance in COMSOL, which

writes the total mass balance as a compressible Euler equation (see eq.2.67) without considering the adsorption term. Hence, the non-isothermal case study considered will simulate up to 5% mole fraction of adsorbate in the feed stream. For the purpose of 3D model comparison with a reduced order model, the trace-component assumption can be made valid for the case studies investigated in this work. However, it would be beneficial to develop a more sophisticated 3D model that accounts for non-trace systems, as well. A possible solution might be the use of self-defined equations in COMSOL, without the use of the available ones from the software.

This model assumes macropore diffusion control and calculated Knudsen and molecular diffusion contributions from available correlations. Therefore, it can be seen an extension of the previous EM 3D model for which a fixed value of the diffusivity had to be provided manually. It is of course limited to the contributions aforementioned. If viscous flow, surface diffusion or micropore diffusion have to be included, the diffusion correlations and the mass balance on the solid have to be changed accordingly.

The mass balance on the i-th component in the free channel is already reported in eq.(2.21) with boundary conditions in eq.(2.22) and (2.23).

Then, given the assumption of macropore diffusion control, the mass balance in the solid can be written as:

$$\epsilon_p \frac{\partial c_{p,i}}{\partial t} + \rho_p \frac{\partial q_i}{\partial t} = \frac{\epsilon_p}{\tau} \nabla \cdot (D_{p,i} \nabla c_{p,i}) \qquad 2.60$$

where the amount adsorbed q is expressed per mass of solid and ρ_p is the pellet density, ϵ_p the porosity of the adsorbent, τ the tortuosity, and $D_{p,i}$ the pore diffusivity of the i-th component. The boundary conditions are:

$$c_{p,i} = c_i; \quad @ \quad interface \qquad 2.61$$

$$D_m \nabla c_i = \frac{\epsilon_p}{\tau} D_{p,i} \nabla c_{p,i} \quad @ \quad interface; \qquad 2.62$$

the pore diffusivity, $D_{p,i}$, can be calculated as sum of molecular diffusivity, D_m, and Knudsen diffusivity, $D_{K,i}$:

$$\frac{1}{D_{p,i}} = \frac{1}{D_m} + \frac{1}{D_{K,i}} \qquad 2.63$$

where D_m and $D_{K,i}$ are calculated as in eq.(2.64) and (2.65)[102].

$$D_m = \frac{3}{16}\frac{\sqrt{2\pi\left(R_g T_s\right)^3\left(\frac{1}{Mw_1}+\frac{1}{Mw_2}\right)}}{N_a P \sigma_{12}^2 \Omega_{12}} \qquad 2.64$$

$$D_{K,i} = \frac{9}{13}\left[\frac{2}{3} r_{pore}\sqrt{\frac{8R_g T_s}{\pi Mw_i}}\right] \qquad 2.65$$

where N_a is the Avogadro's number, R_g is the ideal gas constant, Mw is the molecular weight, Ω_{12} the collision integral of the pair "molecule 1−molecule 2", σ_{12} the average kinetic diameter of the pair, r_{pore} the pore radius of the adsorbent and T_s is the solid temperature. The expression of $D_{K,i}$ already considers the correction factor introduced by Levitz[103], equal to $9/13$. The isotherm is of Langmuir type:

$$q_i = q_s \frac{b_{0,i} e^{-\frac{\Delta H_i}{R_g T_s}} P_i}{1 + b_{0,i} e^{-\frac{\Delta H_i}{R_g T_s}} P_i} \qquad 2.66$$

where q_s is the saturation capacity, $b_{0,i}$ the pre-exponential factor, ΔH_i the heat of adsorption, T_s the solid temperature, and $P_i = c_{p,i} R_g T_s$ according to the ideal gas law. The average outlet concentration in the fluid phase is calculated as in eq.(2.26).

The compressible Euler equation, eq.(2.67), is used to model the total mass balance in the free cross-section.

$$\frac{\partial \rho}{\partial t} + \nabla \cdot (v\rho) = 0 \qquad 2.67$$

where ρ is the mass density of the fluid. The total mass balance should contain also a term taking into account the adsorption of the adsorbing component. However, given the assumption of a trace system, that term can be neglected.

The velocity profile is found solving the compressible Navier-Stokes equations:

$$\frac{\partial \rho}{\partial t} + \rho(v \cdot \nabla)v = \nabla \cdot (-P \cdot I + \tau_{vis}) \qquad 2.68$$

where $\tau_{vis} = \eta(\nabla v + \nabla v^T) - \frac{2}{3}\eta(\nabla \cdot v)I$, with I as the identity matrix and η as viscosity. The boundary conditions for the Navier-Stokes equations is of fully-developed flow at the inlet of the free cross-section and atmospheric pressure at the outlet of the channel, $P_0 = 101.325\ kPa$. The viscosity of the gas phase is automatically calculated from COMSOL once the components of the mixture are specified.

The differential energy balance in the free channel is:

$$\rho c_{p,g} \frac{\partial T_g}{\partial t} - \nabla \cdot \left(\kappa_g \nabla T_g\right) + \rho c_{p,g} v \cdot \nabla T_g = 0 \qquad 2.69$$

where T_g is the gas temperature, $c_{p,g}$ is the heat capacity of the gas, and κ_g its thermal conductivity. The boundary conditions are:

$$-\kappa_g \nabla T_g + v\rho c_{p,g} T_g = v_{in} \rho c_{p,g} T_0; \quad @ \quad z = 0 \qquad 2.70$$

$$\kappa_g \nabla T_g = 0; \quad @ \quad z = L \qquad 2.71$$

instead, the differential energy balance on the sorbent can be written as:

$$\rho_p c_{p,s} \frac{\partial T_s}{\partial t} - (1 - \epsilon_p)\kappa_s \nabla^2 T_s + \rho_p \sum_{i=1}^{N_C} \Delta H_i \frac{\partial q_i}{\partial t} = 0 \qquad 2.72$$

where $c_{p,s}$ is the heat capacity of the adsorbent, and κ_s its thermal conductivity. The boundary conditions are reported below.

$$T_g = T_s; \quad @ \quad interface \tag{2.73}$$

$$\kappa_g \nabla T_g = \left(1 - \epsilon_p\right)\kappa_s \nabla T_s \quad @ \quad interface \tag{2.74}$$

The thermal conduction of the gas is calculated as in eq.(2.75)[83].

$$\begin{aligned}\kappa_g \ = 3.6969x10^{-4} + 9.7435x10^{-5}T_g - 4.0758x10^{-8}T_g^2 \\ + 7.6845x10^{-5}T_g^3\end{aligned} \tag{2.75}$$

The non-isothermal 3D model is solved in COMSOL. The initial condition of the channel is of fully developed flow of a pure inert stream at T_0.

The set of equations is solved simultaneously, without decoupling momentum balances from mass and heat balances, as done in Cheng et al.[101]. The simulations are firstly initialised using a steady flow of inert in the channel, and then the feed is switched to the binary mixture. As done for the linear and isothermal model, a mesh-refinement study is carried out to assure mesh-independent results. The HETP is calculated as in eq.(2.32).

2.5.4 Non-isothermal reduced order 2D model

From the HETP correlation, a reduced order model can be derived. The reduced model considers 1D along the axis of the channel, the z-direction, and 1D for the diffusion in the solid. The thickness of the solid is set to the corrected thickness of the system, calculated with eq.(2.56). The modelling assumptions are the same as in the 3D model. The additional assumptions are that the pressure drop along the channel is negligible and that the solid temperature is uniform at a given cross-section.

The mass balance for the fluid phase on the adsorbing component is:

$$\frac{\partial c_i}{\partial t} - \frac{\partial}{\partial z}\left(D_{ax}\frac{\partial c_i}{\partial z} - v c_i\right) + \frac{1-\epsilon}{\epsilon}\frac{\partial \bar{Q}_i}{\partial t} = 0 \tag{2.76}$$

where $\overline{Q_i} = \epsilon_p \overline{c_{p,i}} + \rho_p \overline{q_i}$. The boundary conditions are:

$$-D_{ax} \nabla c_i + v c_i = v_{ave} c_{in,i} \quad @\ z = 0; \tag{2.77}$$

$$D_{ax} \nabla c_i = 0 \quad @\ z = L; \tag{2.78}$$

The differential mass balance in the adsorbent solid is:

$$\epsilon_p \frac{\partial c_{p,i}}{\partial t} + \rho_p \frac{\partial q_i}{\partial t} = \frac{\epsilon_p}{\tau} \frac{\partial}{\partial x} \left(D_{p,i} \frac{\partial c_{p,i}}{\partial x} \right) \tag{2.79}$$

where the boundary conditions are:

$$c_{p,i} = c_i \qquad @\ x = w_c; \tag{2.80}$$

$$D_p \frac{\partial c_{p,i}}{\partial x} = 0 \qquad @\ x = 0; \tag{2.81}$$

The isotherm is in eq.(2.66). The average total adsorbed amount can be calculated from:

$$\frac{\partial \overline{Q_i}}{\partial t} = -\frac{1}{w_c} \frac{\epsilon_p}{\tau} D_{p,i} \frac{\partial c_{p,i}}{\partial x} \Big|_{x=w_c} \tag{2.82}$$

The total mass balance can be written as:

$$\frac{\partial c_{tot}}{\partial t} + \nabla (v c_{tot}) = 0 \tag{2.83}$$

where $v = v_{ave}$ at $z = 0$. The molar density $c_{tot} = \frac{P_0}{R_g T_g}$ is used as variable for the total mass balance in the reduced order model instead of the mass density. The energy balance for the gas phase is:

$$c_{tot} c'_{p,g} \frac{\partial T_g}{\partial t} - \frac{\partial}{\partial z} \left(\kappa_{ax} \frac{\partial T_g}{\partial z} \right) + c_{tot} c'_{p,g} v \frac{\partial T_g}{\partial z} = -\frac{1 - \epsilon}{\epsilon} h_{gs} a_s (T_g - T_s) \tag{2.84}$$

where $c'_{p,g}$ is the heat capacity of the gas in mole units, κ_{ax} the axial thermal conductivity, h_{gs} is the heat transfer coefficient between the gas and solid

phase and a_s the surface to volume ratio of the solid. The boundary conditions for eq.(2.84) are of the Danckwert's type as eq.(2.70) and eq.(2.71). For the solid, the energy balance is:

$$\rho_p c_{p,s} \frac{\partial T_s}{\partial t} = h_{gs} a_s \left(T_g - T_s\right) - \rho_p \sum_{i=1}^{N_C} \Delta H_i \frac{\partial \overline{q_i}}{\partial t} \qquad 2.85$$

where $\overline{q_i}$ is calculated as in eq.(2.86).

$$\overline{q_i} = \frac{1}{w_c} \int_0^{w_c} q_i dx \qquad 2.86$$

The initial condition of the model assumes the channel filled with the inert carrier at a temperature of T_0.

As for the isothermal reduced model presented in Section 2.2.4.1 of this chapter, the non-isothermal model is solved in gPROMS using the method of lines and orthogonal collocation to discretise both the axial dimension and the solid diffusion one. The mass and heat transfer parameters are calculated as in the 3D model.

Two case studies are considered to test the reduced order model and the HETP correlation for a corrugated channel against 3D simulations: linear & isothermal, and non-linear & non-isothermal. The list of parameters used for both case studies is reported in Table 2.9

Table 2.9: List of parameters for the simulation of a corrugated channel.

Parameter	*Units*	*Linear & isothermal*	*Non-linear & non-isothermal*
L	$[m]$	0.1	0.15
v_{ave}	$[m/s]$	0.005-0.5	0.5,1
h_o	$[m]$	2.03e-3	
δ	$[-]$	0.074	0.098
α_o	$[-]$	1.3	1.155
ϵ	$[-]$	0.636	0.506
${\epsilon_p}^*$	$[-]$	0.269	
τ^*	$[-]$	2.62	
T_0	$[K]$	303	293
P_0	$[kPa]$	101.325	
${q_s}^{**}$	$[mol/kg]$	5.22	
${b_{0,CO2}}^{**}$	$[1/Pa]$	3.95e-10	
ΔH^{**}	$[J/mol]$	-32600	
${\rho_p}^{**}$	$[kg/m^3]$	1200	
$c_{p,g}$	$[J/kg/K]$	29.2	
${c_{p,s}}^{**}$	$[J/kg/K]$	920	
${\kappa_s}^{***}$	$[W/m/K]$	0.15	
$y_{CO2,in}$	$[-]$	0.0004	0.05

* From Hu et al.[102]; ** From Oreggioni et al.[104]; *** From Amalraj et al.[55]

2.5.4.1 Parameters of the reduced model

The information from the 3D model can be effectively transposed in the reduced model with the use of three parameters: D_{ax}, κ_{ax} and h_{gs}. The axial dispersion has to be calculated as shown in eq.(2.40), so that it will take into account both the molecular diffusion in the free cross-section and the dispersion given by the velocity profile. It should be noted that in eq.(2.40) the Pe number has to take into account the local velocity v and not the average velocity, since in a non-isothermal system the velocity will change along the main channel's axis.

Similarly, the axial conduction can be calculated as:

$$\kappa_{ax} = \kappa_g \left[1 + \frac{C_M}{2} Pe_T^2\right] = \kappa_g \left[1 + \frac{C_M}{2}\left(vh\frac{c_{tot}c'_{p,g}}{\kappa_g}\right)^2\right] \quad 2.87$$

such that the velocity profile contribution is taken into account thanks to the Taylor-Aris dispersion coefficient and the thermal Peclet number, Pe_T.

The last parameter to calculate is the heat transfer coefficient between gas and solid, h_{gs}, which can be written as a linear driving force coefficient for a slab geometry, as shown in eq.(2.88).

$$h_{gs} = \frac{3\kappa_s(1-\epsilon_p)}{w_c} \quad 2.88$$

the remaining parameters of the 2D model are all fixed by the physics of the system investigated. The reduced model relies on the knowledge of the physics and geometry of the channel, without any use of empirical correlations, as done before for the other straight-channel monoliths.

2.5.5 Case study 1: Linear and isothermal conditions

Direct air capture with a corrugated monolith can be seen as an example of linear and isothermal separation[105]. The corrugated monolith is assumed to be a corrugated metal foil coated with 13X. The separation considers trace quantity of CO_2 to be removed from a non-adsorbing carrier, i.e. dry air. The parameters of the simulations are reported in Table 2.9.

The results from the comparison of the HETP correlation of a corrugated monolith, eq.(2.3), and the 3D simulations are shown in Figure 2.15.

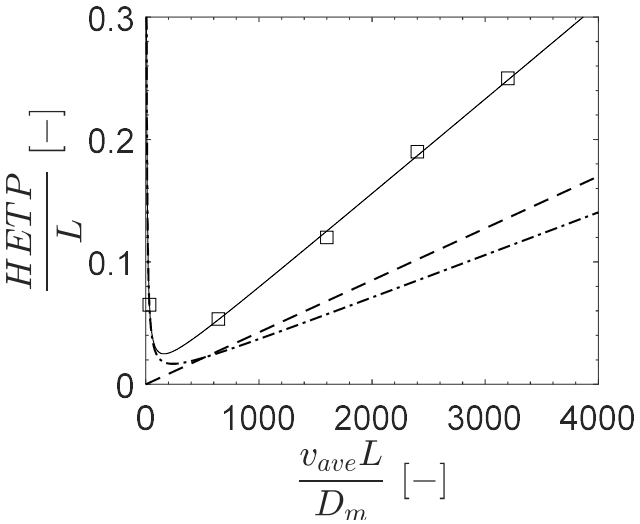

Figure 2.15: Comparison between the 3D simulations and HETP for isothermal and linear case study. Squares are 3D simulations, solid line the HETP in eq.(2.3), dashed line is the solid resistance and dash-dotted line is the fluid resistance.

It should be noted that the diffusivity used in eq.(2.3) is the effective diffusivity which takes into account the effect of equilibrium on the diffusion of CO_2 in 13X. The expression of the effective diffusivity, D_{eff}, is reported in eq.(2.89). where K_c is the Henry's law constant derived from the isotherm.

$$D_{eff} = \frac{\frac{\epsilon_p}{\tau} D_p}{\epsilon_p + \rho_p K_c} \qquad 2.89$$

As for the straight-channel monoliths, the HETP correlation together with an accurate analysis of the velocity profile resistance and the use of the corrected thickness accurately captures the dispersion of the solute in a corrugated channel. It is interesting to point out that for this case study the resistance given by the velocity profile plays a considerable role in the overall HETP. However, still the diffusion in the solid remains the main cause of dispersion.

The prediction of the reduced model are presented in Figure 2.16 together with the 3D simulations. The agreement is remarkable, and the computational cost is greatly reduced. The reduced order model heavily relies on the accurate experimental estimation of the transport parameters of the system. It highlights the relevance of reliable mass transport parameters in the solid, given its major contribution to dispersion.

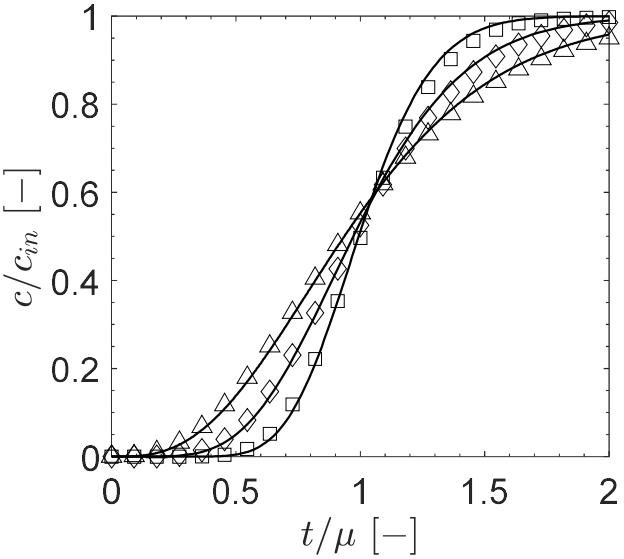

Figure 2.16: Prediction of the reduced order model against 3D simulations at $v_{ave} = 0.1\ m/s$ (squares), $v_{ave} = 0.25\ m/s$ (diamonds), and $v_{ave} = 0.5\ m/s$ (triangles). The solid line is the reduced order model.

To clarify why this case-study presents a major impact of the fluid resistance on the HETP, a comparison between the resistances of the sinusoidal HETP here considered and the triangular channel HETP considered in section 2.2 are compared. The list of parameters used for the simulations of both channels are reported in Table 2.10. Moreover, the table reports both the solid and fluid diffusion time constants for both systems.

Table 2.10: List of parameters used for the simulations of triangular and sinusoidal channels. The parameters are used to calculate the resistances shown in Fig. 2.17.

	Triangular	**Sinusoidal**
$D_m\ [m^2/s]$	1.7×10^{-5}	1.56×10^{-5}
$D_{eff}[m^2/s]$	7.4×10^{-10}	4.74×10^{-10}
$\epsilon\ [-]$	0.561	0.636
$K\ [-]$	40	2599
$w_c\ [m]$	2.33×10^{-4}	1.70×10^{-4}
$h\ [m]$	1.8×10^{-3}	1.75×10^{-3}
$v_{ave}\ [m/s]$	1	1
$C_M\ [-]$	0.113	0.112
$w_c^2 D_{eff}\ [s]$	73.55	60.75
$h^2/D_m\ [s]$	0.20	0.20

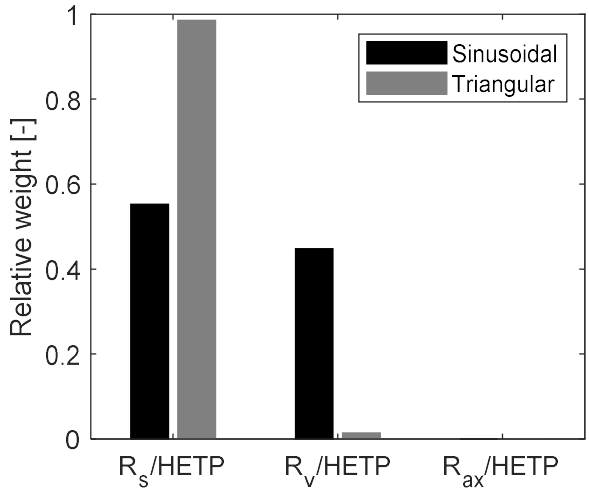

Figure 2.17: Relative weight of the HETP resistances for both sinusoidal and triangular channel. The parameters used for the calculation are the same as for the 3D simulations, and are reported in Table 2.10.

The relative weight of each resistance of the HETP for both channels is shown in the Figure 2.17.

The solid resistance for a triangular channel is higher than what shown from the sinusoidal one. This can be attributed to the higher solid diffusion time constant of the triangular channel, roughly 20% higher than the solid diffusion time constant of the sinusoidal channel. Furthermore, the solid resistance depends also on the retention factor, which is accounted for in the term $\frac{2k}{3(1+k)^2}$. This value of $\frac{2k}{3(1+k)^2}$ is 0.02 for the triangular channel, while for the sinusoidal channel is 4.47×10^{-4}. Therefore, the lower weight of the solid resistance shown by the sinusoidal channel is caused by a combined effect of faster solid diffusion time constant and higher retention factor compared to the triangular channel. By contrast, the resistance given by the velocity profile is almost identical for both channels, given the very similar value of the Taylor-Aris coefficient, and the fluid diffusion time constant.

2.5.6 Case Study 2: Non-linear and non-isothermal conditions

The removal of CO_2 from a nitrogen stream from a natural gas combined-cycle power station has been chosen as representative of non-linear and non-

isothermal separation. The carbon dioxide content from this process is usually around 3-5%[106]. The parameters of the simulations are reported in Table 2.9.

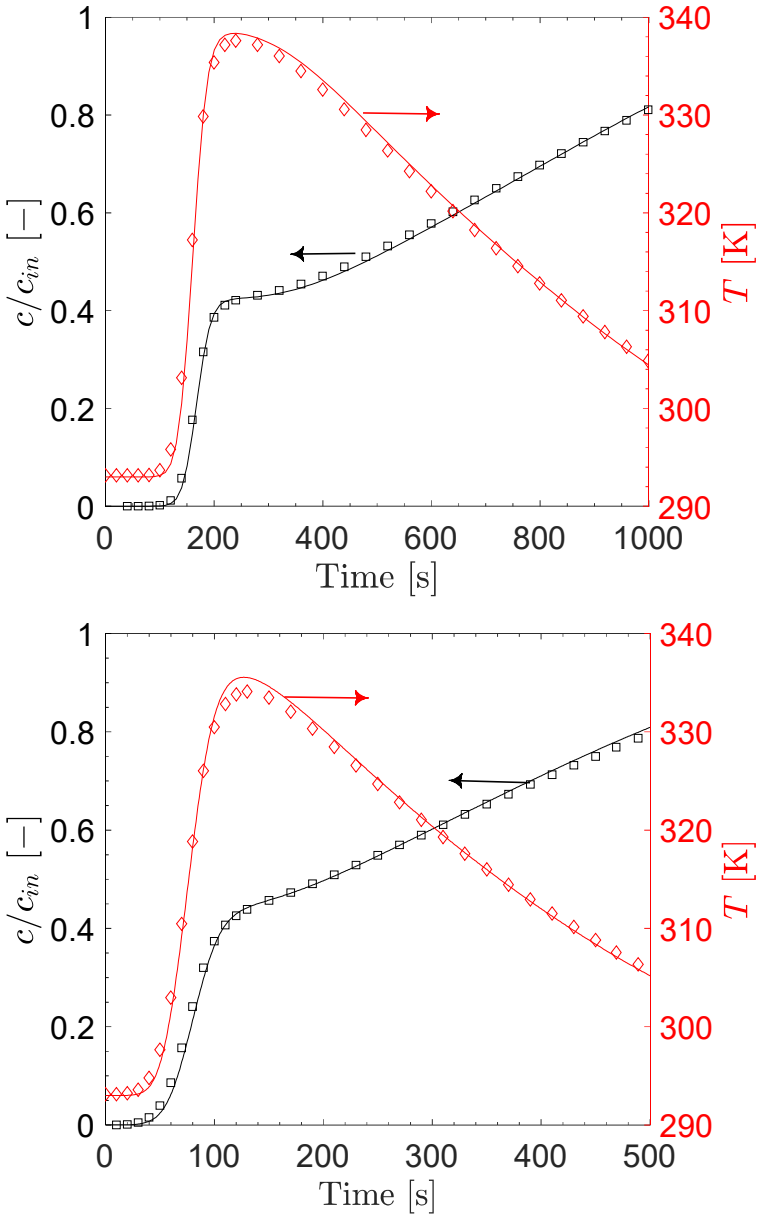

Figure 2.18: Comparison between reduced order model and 3D simulations for non-linear and non-isothermal conditions at $v_{ave} = 0.5\ m/s$ (top) and $v_{ave} = 1\ m/s$ (bottom). Black squares are the concentration profile from 3D simulations, red diamonds the temperature from 3D simulations, and the lines are the reduced order model.

The comparison between 3D simulations and the reduced model is presented in Figure 2.18. The reduced model captures the overall dynamics of the system, for both the concentration and temperature profiles. The mass and thermal dispersion are correctly predicted with the use of eq.(2.40) and (2.87).

In Figure 2.19, the comparison between 3D and reduced model is made with the use of $C_M = 1/96$. This is the common values generally used when modelling the dynamics of straight-channel monoliths[29,30,42,44,107,108].

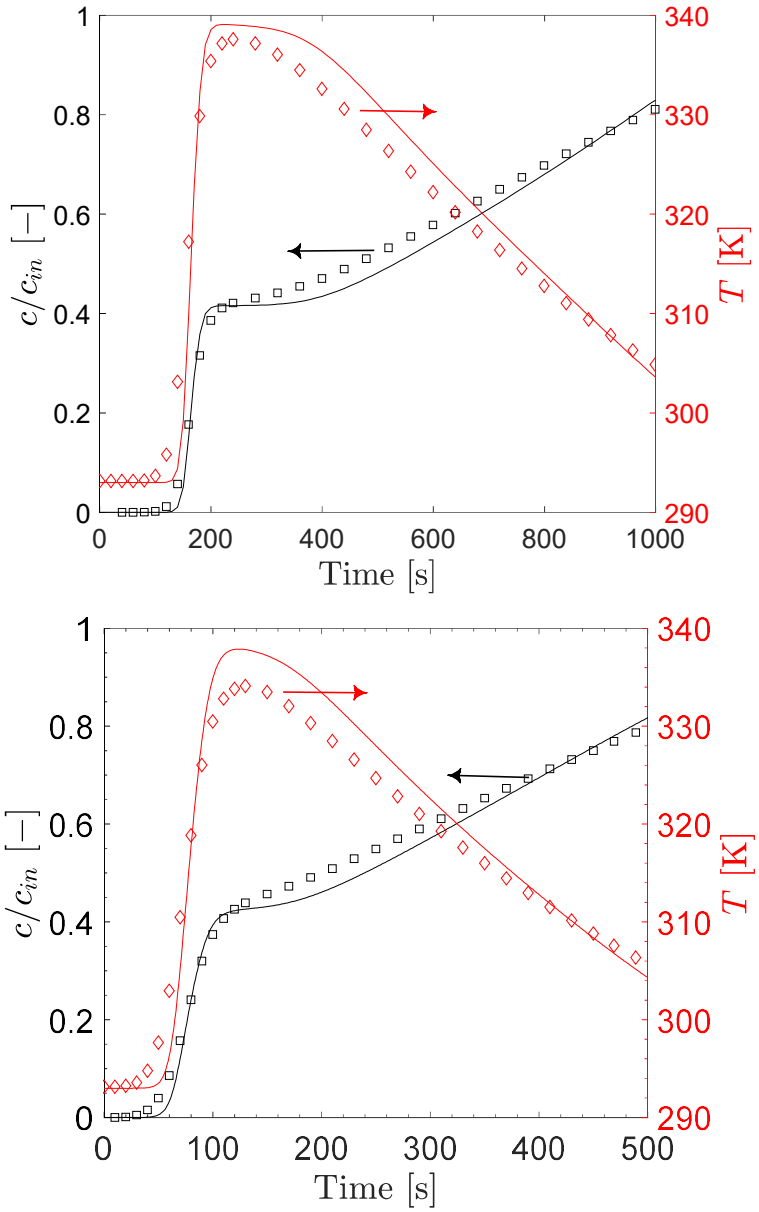

Figure 2.19: Comparison between reduced order model and 3D simulations for non-linear and non-isothermal conditions at $v_{ave} = 0.5\ m/s$ (top) and $v_{ave} = 1\ m/s$ (bottom). Black squares are the concentration profile from 3D simulations, red diamonds the temperature from 3D simulations, and lines are the reduced model. C_M in eq.(2.40) and (2.87) is set at 1/96.

As can be seen, in this case the mass and thermal dispersion are not correctly predicted, and the reduced model predicts broader thermal peaks. The breakthrough time is also overestimated. At a design stage, this would lead to

erroneous estimation of the separation efficiency of the monolith. It is important to address the fact that the axial dispersion and the axial conductivity in the reduced order model do not take into account only the molecular diffusion of the molecules, but they also bring in the model the information of dispersion given by the velocity profile. In addition, the axial dispersions depend on their respective Peclet numbers, and the proportionality is the Taylor-Aris coefficient. Hence, it is important to correctly estimate the Taylor-Aris coefficient.

Another common practice when modelling corrugated monolith for drying purposes is neglecting the axial term. This would lead to an even more deleterious effect on the model results, which should be avoided since it would cancel out the contribution of the velocity profile to dispersion.

2.5.7 Pressure drop correlation

The pressure drop correlation for a corrugated channel has already been reported by Bahrami et al.[77]. The expression of the $fRe_{\sqrt{A}}$ is given in eq.(2.90).

$$fRe_{\sqrt{A}} = 4\sqrt{2}\pi^2 \left[\frac{\pi^2 - 6}{6\pi^2\alpha} + \frac{13\alpha}{96}\right] \frac{\sqrt{\alpha}}{1 + 2E(\pi\sqrt{-\alpha^2})/\pi} \qquad 2.90$$

where $E(\times)$ is the complete elliptic integral of the second kind. The work of Bahrami et al.[77] relies again on the definition of the square root of the cross-sectional area as characteristic dimension, instead of the hydraulic diameter. The sinusoidal channel cannot be easily reduced to the ERM as for conventional monoliths. However, eq.(2.90) yields to accurate results as shown by Bahrami et al.[77], and it is here reported to provide all the correlations needed to design corrugated monoliths.

2.6 Conclusions

This chapter aimed to develop simple and effective design correlations for industrially relevant straight-channel monoliths, namely the HETP and pressure drop correlation.

The HETP correlations of the different monoliths are derived from both the analysis of the moments of a solute dispersing in a channel coated with adsorbing walls described by Dutta and Leighton[69], and from the idea of corrected thickness introduced by Ahn and Brandani[73]. The analysis of moments helped to quantify the effect of the flow profile on the overall HETP, while the corrected thickness described the effect of the mass transfer diffusion on the overall spreading of the solute. The HETP correlations for the monoliths studied have been validated against 3D numerical simulations. The overall dispersion of the solute in the channel is accurately described. The breakdown of the HETP in its constitutive resistances shows that for all the cases analysed the solid diffusion is the main cause of dispersion. This result points the attention towards the bottleneck on the minimisation of dispersion in an extruded monolith: the optimisation of the structure has to be guided by the aim of minimising the solid resistance, for instance with thinner walls of better-engineered materials. The geometry optimisation of the free cross-section can lead to an improvement of the dispersion in the channel, however, it will be minor compared to the effect of solid resistance.

From the HETP, a reduced order model can be derived which is used as a useful tool for simulation purposes. The reduced models presented in section 2.2.4 and 2.5.4 consider both linear and isothermal conditions, or the most general case of non-linear and non-isothermal conditions. Thanks to the analogy between mass and heat transfer, the HETP correlation obtained for the isothermal case can be used to derive a thermal coefficient that effectively matches the thermal front in the non-isothermal simulations. This result contradicts what stated by Cheng et al.[101] that a reduced model cannot be produced. Indeed, if mass and thermal dispersion in the fluid and porous phase are carefully accounted for, the match of 3D simulations with a reduced order model is indeed possible.

The transposition of the information from the 3D domain to a simplified 2D model can be effectively done by means of four parameters, as discussed in section 2.5.4.1: the axial mass and thermal dispersion coefficient, and the heat

transfer coefficient between gas and solid, and the thickness of the solid domain. The size of the solid domain in the reduced model has to be set to the corrected thickness of the channel, and the axial coefficients have to be calculated by means of a combination of molecular diffusion and velocity profile contribution, as shown in eq.(2.40) and (2.87). The reduced model is able to capture the overall dynamics of the 3D simulations with the benefit of a reduced computational cost, suitable for optimisation purposes, where simulations need to run to cyclic steady state and be repeated for several process parameters. In section 2.5.6 the effect of an incorrect Taylor-Aris dispersion coefficient is shown. The conventional use of the Taylor-Aris coefficient of a hollow cylinder, $C_M = 1/96$ can lead to an incorrect dispersion of both mass and thermal front, which leads to a wrong estimation of the breakthrough time and temperature peak.

Pressure drop correlations for such channels were also reviewed. The correlation proposed by Muzychka and Yovanovich[79] has been used, which offers the main advantage to be simple and easily extendable to novel cross-sections. A novel correlation for the hex-hex channel is presented in section 2.3 for the effective aspect ratio of such geometry.

The combination of HETP and pressured drop correlations can be used to assess the performance of straight-channel monoliths in comparison to packed beds based on their pressure drop per theoretical stage. The comparison presented in section 2.4 shows that monoliths offer better performance under all conditions. It can be concluded that straight-channel monoliths can be a valid asset in the deployment of fast-cycle processes, which are generally limited by the energy penalty of the high pressure drop in a conventional packed bed. Straight-channel monoliths can also offer the benefit of high thermal mass if manufactured from a metallic frame coated with sorbent. This can help in the development of adsorption processes that suffer of high thermal gradients given the release of heat during adsorption.

Chapter 3 The Rigid Adsorbent Lattice Fluid Model

3.1 Introduction

The previous chapter mostly focussed on the exact match of the dispersion of an adsorbate inside a monolith. It was implicitly assumed that the equilibrium relationship between adsorbent and adsorbate was available. The correct interpretation of the affinity between adsorbent and adsorbate is crucial for correct match of the first moment of an adsorption column, either randomly packed or structured.

The interpretation of thermodynamic adsorption data with reliable models has been an open question for almost a century[109,110]. The most popular approach is to consider the sorbent as a lattice made of adsorbing sites on which a molecule can adsorb[111].

The Langmuir isotherm is the simplest of the lattice models that can describe single component isotherms[112,113]. The Langmuir model assumes that the solid is made of equal sites randomly distributed on which a single molecule can adsorb, and the adsorbates cannot interact among them. The Langmuir equation of adsorption for a single component is reported in eq.(3.1):

$$\frac{\theta}{1-\theta} = bP \tag{3.1}$$

where $\theta = q/q_s$ is the surface coverage, i.e. the ratio between the number of adsorbed molecules and the number of sites available, and b is an affinity parameter. It is clear from the assumptions of the Langmuir model that for thermodynamic consistency all molecules adsorbing on the same solid must have the same saturation capacities, since the number of free lattice sites is independent from the molecule[13,114]. For practical purposes, this constraint is often relaxed, especially when dealing with mixtures of components very different in size. Moreover, an empirical temperature dependency of the saturation capacity is sometimes used[115,116]. However, where possible, the

saturation capacity should be kept constant for all the molecules under investigation and should be temperature independent.

In case the adsorbent is made of adsorbing sites of different nature, i.e. a heterogeneous solid, the Langmuir model can be extended to include different sites, i.e. the multisite Langmuir isotherm[117–119].

Nitta et al.[120] derived an isotherm expression to take into account multisite occupancy of an adsorbate, thus removing one of the assumptions of the Langmuir model. The expression is reported in eq.(3.2):

$$\frac{\theta}{(1-\theta)^n} = nbP \qquad 3.2$$

where n is the number of sites occupied by the molecule. It can be seen how the model reduces to Langmuir for $n \to 1$. Nitta et al.[120] also reported the equation for a Langmuir-like isotherm where also adsorbate-adsorbate interactions are considered:

$$\frac{\theta}{(1-\theta)^n} exp\left(-\frac{nu\theta}{k_B T}\right) = nbP \qquad 3.3$$

as it can be seen, the exponential on the LHS deals with the interaction between the adsorbates, where u is the interaction parameter, k_B the Boltzmann constant and T the temperature. It should be noted that in the limit of $n \to 1$ the Nitta isotherm in eq.(3.3) reduces to the so-called Fowler-Guggenheim equation[121,122].

Generally, the single component isotherms are then used to predict multicomponent adsorption with the use of the Adsorbed Solution Theory (AST), originally developed assuming ideal behaviour of the adsorbed phase by Myers and Prausnitz[123,124] (IAST). In its most general form, the AST describes the fluid−adsorbed phase equilibria equating the fugacities of the two phases for each molecule:

$$f_{i,F} = P_i^0(\pi_s)\gamma_i x_i \qquad 3.4$$

where f_{iF} is the fugacity of the fluid phase, γ_i the activity coefficient for the adsorbed phase, x_i the mole fraction in the adsorbed phase, P_i^0 is the surface pressure of the i-th molecule at the spreading pressure π_s. If activity coefficient models (Wilson, UNIQUAC,NRTL) are used to model the adsorbed phase we refer to real AST (RAST)[125,126]. The spreading pressure for each component can be calculated from the single component data from eq.(3.5).

$$\frac{\pi A}{k_B T} = \int_0^{P_i^0} q_i d\big(ln(P_i)\big) \qquad 3.5$$

As it can be seen from eq.(3.5), the estimation of the spreading pressure heavily relies on accurate single component data.

The main challenge in using the IAST is the accurate estimation of the spreading pressure from single component isotherms[127–129]. Indeed, the first step in the solution of AST calculations is the computation of the spreading pressure of the system which is common at all the adsorbing molecules at fixed system conditions. For strong adsorbing components, single component data at low pressures might be difficult to measure. On the contrary, given that the spreading pressure is common to all the molecules adsorbing on the solid, it would be difficult to calculate the spreading pressure for a very weakly adsorbing compound. Moreover, it should be noted that the use of RAST, while effective in the design of adsorption systems, does not provide any information on the physical behaviour of the adsorbed phase. Indeed, the activity coefficient models and their parameters are of empirical nature. It is worth pointing out that in the RAST the variation of the excess Gibbs energy with the spreading pressure has to be carefully accounted for. Talu and Zwiebel[130] have shown that neglecting this contribution can lead to an error on the total adsorbed amount of around 30%.

The inclusion of a distribution of sites in the solid is generally accounted in the heterogeneous IAST (HIAST) where the adsorption on each site is weighted upon the energy distribution of the solid's sites[131,132].

One way to overcome the limitation of the spreading pressure calculation is the use of a vacancy solution model (VSM). Developed in the early '80s by Suwanayuen and Danner[133,134], The VSM describes both the fluid and adsorbed phase as vacant lattices. In their original work[133], Suwanayuen and Danner made use of the Wilson activity coefficient model to take into account the non-idealities of the adsorbed phase. The general expression for the VSM is of the form in eq.(3.6):

$$\frac{\theta}{1-\theta} = bPg \tag{3.6}$$

where g is a function that depends on the Wilson activity coefficient parameters and θ. The most popular form of the VSM actually considers the Flory-Huggins activity coefficient model (FH-VSM)[135], which provides higher accuracy with fewer fitting parameters. Talu and Myers[136] pointed out that the VSM fails to predict the behaviour of a multicomponent mixture in the low pressure region, hence leading to inconsistent results. Bhatia and Ding[137] reformulated the VSM in a thermodynamic consistent manner, which provides consistent results across the entire pressure domain. Bhatia and Ding[137] solved the inconsistency pointing out that the initial derivation of the VSM from Suwanayuen and Danner[133] considered the behaviour of adsorbates and vacancies not related to each other. However, it is reasonable to assume that whenever one molecule adsorbs, a certain number ∅ of vacancies disappear, as shown in eq.(3.7):

$$A_F + \emptyset V_A \rightarrow A_A \tag{3.7}$$

where A_F denotes the molecule in the fluid, V_A the vacancy in the adsorbed lattice, and A_A the adsorbed molecule. Hence, Bhatia and Ding[137] re-derived the VSM providing a correlation between vacancies and adsorbed molecules. The calculation of multicomponent adsorption with a VSM does not require the

calculation of the common spreading pressure. For each molecule a general iso-fugacity correlation can be written by which the adsorbed amount is calculated. The main weakness of the VSM approach is the use of several parameters of empirical nature[138]. Moreover, the regression of temperature dependencies of some of the parameters can be difficult to obtain if accurate single component data are not available.

So far, the models presented have been extensively used in literature providing satisfactory results, especially for conventional systems where the mixture in the fluid phase is made of molecules of similar size and not strong polarity.

There is a need to address the challenges outlined in this brief literature overview, such as mixtures of very strong and weak adsorbing compounds, and non-ideal mixtures. Moreover, the development of a model which aims at a very close representation of the physical process happening at the microscale would be beneficial. Indeed, caution should be used when dealing with empirical models.

In the following, the Rigid Adsorbent Lattice Fluid (RALF) model will be presented. The derivation of its equations will be discussed, both for a homogeneous solid and for a solid comprising multiple sites.

3.2 The RALF model for a homogeneous solid

The RALF model has been recently proposed by Brandani[139]. His work and derivation of this thermodynamic model bear many similarities to the non-equilibrium lattice fluid (NELF) model developed by Sarti and co-workers[140,141] for the sorption of gases and solvents in glassy polymers.

The RALF model aims at developing a thermodynamic framework which describes the causes of non-ideality such as adsorbate-adsorbate interaction and different molecular sizes. The RALF model represents both the fluid phase and the adsorbed phase as two lattices. The adsorbed phase lattice considers the adsorbates, the skeletal solid and the microporous void volume. Compared

to the models briefly discussed before, the RALF model includes the solid as a component of the adsorbed phase mixture. It should be noted that the fugacity of the fluid phase could be calculated with any model that might be found appropriate to describe the fluid phase. The assumption of lattice for the fluid phase is only made as general consistency between the two phases.

The RALF model has been originally derived starting from the Sanchez-Lacombe equation of state (SL-EoS)[142,143], which is used as EoS to model the thermodynamics of gas sorption in polymers. Before describing RALF, it is useful to briefly introduce the SL-EoS.

3.2.1 The Sanchez-Lacombe equation of state

The SL-EoS is a lattice fluid model which represents a system as a lattice of elements called mers. For a pure substance i, each mer occupies a volume v_i^*. A molecule consists of more mers bonded together, such that a molecule occupies a volume $r_i^0 v_i^*$, where r_i^0 is the number of bonded mers in a molecule. In addition to the volume occupied by the molecule, the SL-EoS takes into account also the mer-mer interaction. Therefore, a pure fluid can be fully characterised by the mer-mer interaction, ϵ_i^*, the average close-packed mer-volume v_i^* and the number of mers needed to form the molecule in the fluid, r_i^0. These parameters can be combined to derive macroscopic characteristic parameters of an arbitrary i-th molecule, as in eq.(3.8):

$$T_i^* = \frac{\epsilon_i^*}{k_B}; P_i^* = \frac{\epsilon_i^*}{v_i^*} \; and \; \rho_i^* = \frac{Mw_i}{r_i^0 v_i^*} \qquad 3.8$$

where T_i^* is the characteristic temperature, P_i^* the characteristic energy density and ρ_i^* the average characteristic close-packed density of the fluid. The SL-EoS for a pure component is of the form:

$$\tilde{\rho}^2 + \tilde{P} + \tilde{T}\left[ln(1-\tilde{\rho}) + \left(1 - \frac{1}{r_i^0}\right)\tilde{\rho}\right] = 0 \qquad 3.9$$

where $\tilde{P}, \tilde{T}$ and $\tilde{\rho}$ are the reduced pressure (or energy density), temperature and density, respectively. The reduced quantities can be defined as in eq.(3.10).

$$\tilde{P} = \frac{P}{P_i^*}; \tilde{T} = \frac{T}{T_i^*}; \tilde{\rho} = \frac{\rho}{\rho_i^*}; \qquad 3.10$$

Pure component equilibrium data can be used, together with the SL-EoS, to regress the characteristic parameters of a molecule. Sanchez and Lacombe[143] suggest to use vapour pressure data and the density at the normal boiling point to regress either $\epsilon_i^*, v_i^*, r_i^0$ or P_i^*, T_i^*, ρ_i^* directly. Over the years many works addressed the need of accurate parameters over broad ranges of pressure and temperature[144–148]. Simultaneous fits of multiple datasets of vapour pressure and density have been attempted in order to accurately represent the pure component behaviour[144]. Nevertheless, the approach proposed by Sanchez and Lacombe remains a reliable method to quickly estimate the pure component parameters.

For a mixture of N_c components, Brandani[139] showed how to account for the combinatorial term in the SL-EoS , as shown in eq.(3.11):

$$\tilde{\rho}^2 + \tilde{P} + \tilde{T}\left[ln(1-\tilde{\rho}) + \left(1 - \frac{1}{r}\right)\tilde{\rho}\right] = \frac{\tilde{\rho}^2\tilde{T}}{r}\sum_{i=1}^{N_c} y_i ln\left(\frac{\phi_i}{y_i}\right) \qquad 3.11$$

where $\phi_i = \frac{m_i/\rho_i^*}{\sum_k m_k/\rho_k^*}$ and y_i are the volumetric and molar fraction of the i-th component in the lattice, with m_i as mass of the i-th component. It is evident from the SL-EoS that the average characteristic parameters of the mixture P^*, T^*, ρ^* and r need to be defined before deriving the scaled reduced variables. To define the average characteristic parameters, mixing rules need to be introduced.

In the next section, the discussion will focus on what mixing rules can be used and how to derive the average parameters. Since RALF relies on the definition of the residual Gibbs energy from the SL-EoS, the definition of the mixing rules

and of the average characteristic parameters will focus on both a lattice for the fluid phase and a lattice for the adsorbed phase which includes the adsorbent, as well.

3.2.2 Average characteristic parameters of the adsorbed phase

Following Sanchez and Lacombe[143], the first mixing rule to introduce is:

$$r_i v^* = r_i^0 v_i^* \qquad 3.12$$

where r_i^0 and v_i^* are the properties of the molecule i if it was the only molecule present, while r_i and v^* are the number of mers occupied by the i-th molecule in the lattice and the average close-packed volume of mers in mixture, respectively. This mixing rule preserves the volume at close packing of each molecule. Both r_i and v^* are unknown and have to be calculated for the adsorbed phase. Once v^* is fixed, the mers occupied by the i-th molecule in the adsorbed lattice can be calculated.

For the adsorbed lattice, as Brandani[139] pointed out, the volume occupied by a molecule in the adsorbed phase at close packing, v_{iA}^*, will be larger than the volume occupied in a bulk phase, given confinement constraints. Hence, Brandani[139] writes the volume of an arbitrary adsorbate at close packing as:

$$v_{iA}^* = v_i^*(1 + \xi_i) \qquad 3.13$$

where ξ_i is the confinement parameter, an adjustable parameter that takes into account the lower volume that an adsorbed molecule occupies compared to the volume occupied in a bulk fluid phase at close packing. The confinement parameter mainly acts on the saturation capacity of the molecule in the adsorbed lattice. The higher the confinement parameter, the higher is the volume occupied in the adsorbed lattice by a molecule. Hence, the lower it is going to be the saturation capacity of the molecule given a fixed volume for adsorption. Having defined v_{iA}^*, we can now derive the average v^* of the adsorbed phase as:

$$v^* = \left(\sum_j \frac{\phi_j}{v^*_{jA}} \right)^{-1} \quad 3.14$$

where ϕ_j is the volume fraction of the j-th component in the adsorbed phase, previously defined as $\phi_j = \frac{m_j/\rho^*_j}{\sum_k m_k/\rho^*_k}$. It should be noted that a different subscript, j, has been introduced to define v^* for the adsorbed lattice. As a reference, the subscript i will denote the iterator over the adsorbates in the adsorbed phase excluding the solid (or the molecules in the bulk fluid mixture), while j (and k) will indicate the iterator over all the components of the adsorbed phase, i.e. adsorbates and adsorbent.

The average number of mers can now be calculated as:

$$r = \left(\sum_i \frac{\phi_i}{r_i} \right)^{-1} \quad 3.15$$

where r_i can be derived from eq.(3.12):

$$r_i = r_i^0 \frac{v^*_{iA}}{v^*} = \frac{Mw_i}{v^* \rho^*_{iA}} \quad 3.16$$

What said for v^*, can be readily extended to the average characteristic density of the adsorbed lattice at close packing, ρ^*, which can be written as:

$$\rho^* = \left(\sum_j \frac{w_j}{\rho^*_{jA}} \right)^{-1} \quad 3.17$$

where $w_j = \frac{m_j}{\sum_k m_k}$ is the mass fraction of the j-th component, and ρ^*_{jA} can be written as in eq.(3.18).

$$\rho^*_{jA} = \frac{\rho^*_j}{1 + \xi_j} \quad 3.18$$

It should be noted that mass and volume fraction of an adsorbate i in the adsorbed phase are related as in eq.(3.19).

$$\frac{\phi_i}{w_i} = \frac{\rho^*}{\rho_{iA}^*} \tag{3.19}$$

The last average parameter to be defined before writing the residual Gibbs energy of the adsorbed phase is the characteristic energy density, P^*. Following the mixing rules proposed by Sanchez and Lacombe[143], we can write:

$$P^* = \sum_j \sum_k \phi_j \phi_k (1 - \kappa_{jk}) \sqrt{P_j^* P_k^*} \tag{3.20}$$

where $\kappa_{jj} = 0$, and $\kappa_{jk} = \kappa_{kj}$. The parameter κ_{ij} is the interaction parameter, an adjustable parameter that is related to the adsorbate-adsorbent and adsorbate-adsorbate interactions.

Once v^* and P^* are known, the average T^* of the adsorbed phase is fixed by eq.(3.21).

$$P^* v^* = R_g T^* \tag{3.21}$$

Having defined all the average properties of the adsorbed phase, the residual Gibbs energy, and the residual chemical potential of each adsorbate can be now derived.

3.2.3 The residual chemical potential for the adsorbed phase

As shown by Brandani[139], the residual Gibbs energy can be written, as:

$$\begin{aligned} \frac{G_A^R}{R_g T} = rN \left[1 - \frac{\tilde{\rho}}{\tilde{T}} + \frac{(1-\tilde{\rho}) ln(1-\tilde{\rho})}{\tilde{\rho}} \right] \\ + N \left[\tilde{\rho} - \tilde{\rho}_s \left(1 + ln \frac{\tilde{\rho}}{\tilde{\rho}_s} \right) \right] \sum_i x_i ln \left(\frac{\phi_i}{(1-\phi_s) x_i} \right) \\ + N \big(z - 1 - ln(z) \big) \end{aligned} \tag{3.22}$$

where G_A^R is the residual Gibbs energy of the adsorbed phase, N the total number of moles in the adsorbed lattice and $z = r \frac{\tilde{P}}{\tilde{\rho} \tilde{T}}$ is the compressibility

factor. The reuced density of the solid is equal to $\widetilde{\rho_s} = \frac{\rho_s}{\rho_s^*}$, where ρ_s is the density of the solid including the micropores, and ρ_s^* is the skeletal density of the solid. Compared to what presented in the original work of Brandani[139], a slight adjustment to the term multiplying the combinatorial term is reported. This adjustment ensures that the combinatorial term goes to zero in the absence of adsorbed molecules.

The residual chemical potential of the i-th component in the adsorbed phase, μ_i^R, can then be derived from eq.(3.22). Its expression is reported in eq.(3.23).

$$\begin{aligned}\frac{\mu_i^R}{R_g T} &= \frac{1}{R_g T}\left(\frac{\partial G_A^R}{\partial N_k}\right)_{T,P,N_{j\neq k}} \\ &= -\frac{\tilde{\rho}}{\tilde{T}} r_i \left(2\frac{\sum_j \phi_j P_{ij}^*}{P^*} - 1\right) + \left[\frac{(1-\tilde{\rho})\, ln(1-\tilde{\rho})}{\tilde{\rho}} + 1\right] r_i^0 \\ &+ \left(1 + \frac{rN}{r_i \rho_s}\frac{\partial \rho_s}{\partial N_i}\right) r_i \left(\left[-\frac{\tilde{\rho}}{\tilde{T}} - \frac{ln(1-\tilde{\rho})}{\tilde{\rho}} - 1\right]\right. \\ &+ (\tilde{\rho} - \tilde{\rho}_s)\sum_i x_i\, ln\frac{\phi_i}{x_i(1-\phi_s)}\Bigg) - ln(z) - \frac{z-1}{r}\frac{rN}{\rho_s}\frac{\partial \rho_s}{\partial N_i} \\ &+ (\tilde{\rho} - \tilde{\rho}_s)\left(ln\frac{r_i}{r(1-\phi_s)} + 1 - \frac{r_i}{r(1-\phi_s)}\right)\end{aligned} \qquad 3.23$$

It can be noted that the density of the solid including the micropores, ρ_s, is allowed to change upon adsorption, since in eq.(3.23) the term $\partial\rho_s/\partial N_k$ appears. Indeed, the density of the adsorbed phase can be written as:

$$\rho = \frac{m_s(\sum_i q_i M w_i + 1)}{V_s} = \frac{\sum_j m_j}{V_s} = \frac{m_T}{m_s}\rho_s \qquad 3.24$$

where V_s the volume of solid including the micropores. The value of V_s can be constrained to a fixed value, as for a rigid adsorbent, or allowed to vary upon adsorption to model the thermodynamics of flexible adsorbents, as shown by Verbraeken and Brandani[149].

The amount adsorbed for each molecule of the system can be calculated with the use of eq.(3.25), which represents the iso-fugacity condition between fluid and adsorbed phase.

$$\frac{\mu_i^R}{R_g T} - \frac{\mu_{iF}^R}{R_g T} = ln\frac{y_i}{x_i} \qquad 3.25$$

where μ_{iF}^R is the residual chemical potential of the fluid phase, F. The residual chemical potential in the fluid phase can be derived from an appropriate EoS for the fluid phase. Brandani[139] presented the expression of μ_{iF}^R in the assumption that the SL-EoS can be used for the fluid phase:

$$\begin{aligned}\frac{\mu_{iF}^R}{RT} = &-\frac{\tilde{\rho}_F}{\tilde{T}_F} r_{iF}\left(2\frac{\sum_k \phi_k P_{ki}^*}{P_F^*} - 1\right) + \left[\frac{(1-\tilde{\rho}_F)\, ln(1-\tilde{\rho}_F)}{\tilde{\rho}_F} + 1\right] r_{iF}^0 \\ &+ \frac{r_i}{r_F}\left(r_F \frac{\tilde{P}_F}{\tilde{\rho}_F \tilde{T}_F} - 1\right) - ln\, z + \tilde{\rho}_F\left(ln\frac{r_i}{r_F} + 1 - \frac{r_i}{r_F}\right)\end{aligned} \qquad 3.26$$

where $k = 1,2,\dots,N_c$. The reduced fluid phase density can be directly calculated from eq.(3.11) which is the EoS for the fluid phase. The average properties of the fluid phase can be derived as the ones of the adsorbed lattice, assuming that there is no solid and hence there is neither a confinement adjustment for the molecules neither a molecule-solid interaction.

To summarise, the set of nonlinear equations to solve for a system of N_c components and a single adsorbate consists of N_c iso-fugacity equations, eq.(3.25), and the EoS to calculate the density of the fluid phase, eq.(3.11), therefore, $N_c + 1$ equations.

3.2.4 Parametrisation of the solid

So far, the parameters of the solid have been assumed to be known. Brandani[139] discusses how to quickly derive the parameters of the solid.

The density at close packing of the solid, ρ_s^*, corresponds to the skeletal density of the adsorbate which can be experimentally obtained from helium pycnometry. The density ρ_s includes the micropore volume in its definition. It

can be derived from experiments according to the methodology suggested by IUPAC[150], or using mercury intrusion measurements[151].

The energy density of the solid P_s^* can be fitted to the energy of adsorption at zero loading of several molecules. Indeed, the adsorption energy at zero loading for an arbitrary molecule adsorbing on the adsorbent s can be written as:

$$\Delta U_{0,i} = \Delta H_{0,i} + R_g T = -2\tilde{\rho}_s r_i^0 v_{iA}^* (1 - \kappa_{is}) \sqrt{P_i^* P_s^*} \qquad 3.27$$

where, as a first approximation, the parameters ξ_i and κ_{is} can be set to 0. As can be seen from eq.(3.27), the only fitting parameter is P_s^*.

Finally, the characteristic temperature T_s^* can be obtained from the Henry's law constant of several molecules. The expression that can be derived from the RALF model of the Henry's law constant is:

$$\begin{aligned} ln\, K_i = \frac{2\tilde{\rho}_s r_i^0 v_{iA}^* (1 - \kappa_{is}) \sqrt{P_i^* P_s^*}}{R_g T} - \left[\frac{(1 - \tilde{\rho}_s)\, ln(1 - \tilde{\rho}_s)}{\tilde{\rho}_s} + 1 \right] r_i^0 \\ - r_i^0 \frac{v_i^*}{v_s^*} \left[- \frac{ln(1 - \tilde{\rho}_s)}{\tilde{\rho}_s} - 1 \right] \end{aligned} \qquad 3.28$$

where the adjustable parameters ξ_i and κ_{iS} can be set to 0 and a first regression of T_s^* can be carried out. It should be noted that T_s^* can also be adjusted to match the Henry's law region of full isotherms of different molecules where available.

Once the parameters of the solid are regressed, and the molecules' parameter known from literature or fitted on vapour pressure data, the only remaining parameters which can be fitted to single component isotherms are ξ_i and κ_{is}.

3.3 Multi-RALF for a heterogeneous solid

The equations introduced in section 3.2 assumed that the solid is made of equal adsorption sites. However, this is not the case for most of the adsorbents

which are made of different sites. Hence, the homogeneous RALF model has to be extended to include the heterogeneity of the adsorbent.

The simplest physical representation of a multisite RALF (multi-RALF) is of a fluid in equilibrium with an arbitrary number of sites which are not related to each other. Ideally, each site will be characterised by its own set of P_S^*, T_S^*, ρ_S^*, ρ_S, and ω as the mass fraction of the site out of the total structure. This approach can work for adsorbents whose sites can be modelled as segregated from each other. By contrast, there are adsorbents in which the sites cannot be split and treated separately. Hence, the link between the sites has to be transposed in mathematical form to be used in multi-RALF.

The theoretical treatment of both versions of multi-RALF is discussed in section 3.4 and 3.5. In section 3.4, the multi-RALF model with segregated sites is presented with reference to the adsorption of benzene and propene on silicalite. This system presents azeotropic adsorption, which can be a good case study for a thermodynamic model. The equations of multi-RALF which are going to be presented and the strategy to parametrise multi-RALF are generally valid for an arbitrary heterogeneous solid with no coupled sites. In section 3.5, the adsorption of CO_2 in the flexible adsorbent (Na,TEA)-ZSM-25[152] will be discussed. This case study highlights an example where the solid is made of sites which cannot be de-coupled. Although the mathematical treatment of the site connection is specific to the case study presented, the parametrisation of multi-RALF and the inclusion of flexibility in the model can help in outlining some general conclusion in the use of multi-RALF for such cases.

For both studies, the strategy to parametrise multi-RALF starts with the identification of the adsorbing sites. An educated guess can be made based on the knowledge of the solid framework and the interaction that an adsorbent can have within the solid. For instance, polar molecules will interact with cations, or big molecules like branched hydrocarbons will more likely prefer large cages rather than narrow channels. It is a preliminary assessment which can guide the choice on the number of sites present in a solid. Molecular

simulations can help to distinguish the main sites of a system if one looks at the preferential location of the adsorbate upon adsorption.

Once the number of sites is established, the characteristic parameters of each site can be determined. At this point, the strategy follows two paths: parametrisation with molecular simulations and/or parametrisation with experimental data. It would be ideal to couple the two parametrisations to obtain a reliable description of the system's thermodynamics. However, there are systems for which either experimental data are not available, e.g. *in-silico* synthetised MOF for a targeted separation, or molecular simulations are difficult if not impossible to run since the solid structure is not known, e.g. gas adsorption on activated carbons. The molecular simulations offer the great advantage of de-coupling the contribution of the different sites[153]. However, they are computationally expensive and heavily rely upon the force-field chosen[154–156], which might not accurately describe the dynamics of the system. Experimental data cannot provide the de-coupled information on each site. By contrast, if run properly, they are reliable and can be used with confidence.

In section 3.4, the parametrisation of multi-RALF via molecular simulations will be discussed for the case where the sites can be de-coupled. The parametrisation with multi-RALF using experimental data will be presented in section 3.5. Since the focus of the next sections is the equations for multi-RALF and on how to parametrise it based on molecular simulations and experimental data, the details of molecular simulations and experimental techniques are only briefly discussed to keep focus on the parametrisation of multi-RALF. Nevertheless, references and essential information of simulations and experiments are provided.

3.4 Parametrisation of multi-RALF via molecular simulations

The mixture benzene-propene is of interest for the synthesis of cumene, an intermediate used in phenol and acetone production[157,158]. The synthesis of cumene is carried out on solid acid catalysts in an excess of benzene which

has to undergo a process of alkylation with the propene to produce cumene. The excess of benzene helps to suppress undesired side reactions. The production of cumene can be extensive with large units of reaction, separation and recycle of the benzene. One way to overcome these limits is to carry out the reaction on selective adsorbents where the excess of benzene is achieved at the adsorbing sites, with a ratio of benzene to propene feed around unity[159]. This would scale down the size of the reaction unit and lead to lower costs of production.

Ban et al.[158] analysed several zeolites for the task mentioned, and curiously reported that the adsorption of benzene and propene on ortho-MFI silicalite, hereafter called ortho-MFI, presents a reverse of the selectivity at 373 K and 100 kPa, for $y_{C_6H_6} \approx 0.5$. The aim of this section is to parametrise and use multi-RALF to study the azeotropic adsorption of benzene and propene on ortho-MFI.

The strategy to parametrise multi-RALF is to firstly regress the solid's parameters with the following steps:

1. Identify the sites of the structure;
2. Calculate the mass fractions of the sites;
3. Derive the densities ρ_s and ρ_s^* of the sites;
4. Regress the P_s^* of each site with adsorption energy at zero loading of different molecules;
5. Regress T_s^* with the Henry's law constant of benzene and propene;

which are similar to the procedure discussed in section 3.2.4, with the extra step of calculating the mass fractions of the sites. Next, the adjustable parameters ξ_i and κ_i of benzene and propene will be fitted to the single component isotherms at 373 K. Finally, the predictive capability of multi-RALF with reference to the binary benzene-propene on ortho-MFI will be analysed.

The details and methodology of the Grand canonical Monte Carlo (GCMC) simulations carried out to produce the results in section 3.4.1 and 3.4.2 are reported in Appendix B.

3.4.1 The adsorbent: ortho-MFI silicalite

The structure of ortho-MFI is presented in Figure 3.1. The structure consists of interconnected straight and sinusoidal channels. Both channels' openings consist of an elliptical ring of 10 Si atoms whose size is 5.3 Å x 5.6 Å for the straight channels, and 5.1 Å x 5.5 Å for the sinusoidal ones. The unit cell of the ortho-MFI is 20.022 Å x 19.899 Å x 13.383 Å[160]. The adsorbing sites are: straight channels, sinusoidal channels, and the intersection between the channels.

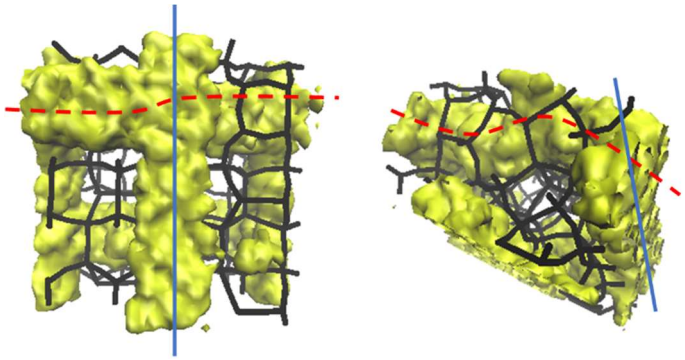

Figure 3.1: Highlight of the accessible pore network of ortho-MFI. In yellow the accessible pore network, in black the solid framework, in dashed red the line passing through the sinusoidal channel, and in solid light blue line the straight channel.

The intersection site is here defined as a sphere of 5 Å whose centre is the intersection of the straight and sinusoidal channel. A visual representation of the solid's breakdown in different sites is shown in Figure 3.2, where also straight and sinusoidal channels are reported, as well as the inaccessible voids of the framework.

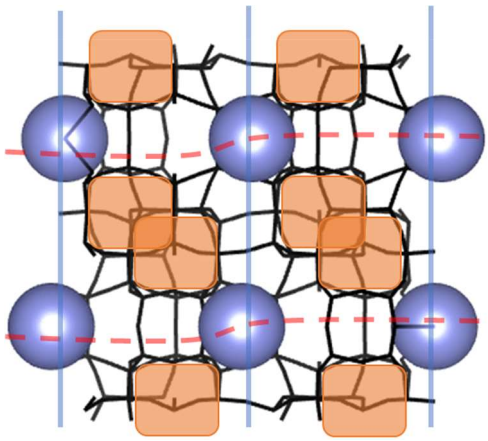

Figure 3.2: Breakdown of ortho-MFI in its sites. Blue circles are the intersections, light blue lines are straight channels, red dashed lines are sinusoidal channels, and orange squares are the inaccessible cages.

The mass fraction of each site can be estimated by calculating the number of Si atoms for each site, and then dividing by the total number of Si atoms. The procedure to do so follows:

1. Calculate the total amount of Si atoms, $n_{Si,T}$;
2. Calculate the amount of Si atoms at the intersections, $n_{Si,int}$;
3. Calculate the number of Si atoms in the straight channels, $n_{Si,str}$;
4. Derive the number of Si atoms in the sinusoidal channels, $n_{Si,sin} = n_{Si,T} - n_{Si,int} - n_{Si,str}$;
5. Calculate the mass fractions as $\omega_{site} = \frac{n_{Si,site}}{n_{Si,T}}$;

The choice of the Si atoms is given by the fact that they represent the centres of the tetrahedral SiO_4 which compose the structure of the solid. The mass fractions of the sites are reported in Table 3.1. It should be noted that, even for solids which cannot be split with the respective number of T-atoms of each site, a preliminary guess on the relative weight of the different sites can be made, and later adjusted if needed.

Once the mass fractions of the sites are fixed, the densities of each site have to be assessed. It is reasonable to assume that the skeletal density of all the sites is constant to the average value of ortho-MFI, $\rho_S^* = 2577\ kg/m^3$[160]. To then derive ρ_s, the micropore volume of each site has to be calculated. This task can be easily achieved using available open-source software like

PoreBlazer[10,161]. Poreblazer consists of a series of Fortran codes for the characterisation of porous materials initially developed by Sarksiov and Harrison[161]. The specific micropore volume of each site, $V_{mic,site}$, is defined as the volume enclosed in the accessible surface area (also known as Connoly surface) of the site per mass of adsorbent. The Connoly surface is constructed with reference to a molecule that "rolls" on the accessible framework of the solid. The surface drawn by the center of the reference molecule while "rolling" is defined as Connoly surface. For our purpose, the reference molecule has been chosen to be He. The results are presented in Figure 3.3.

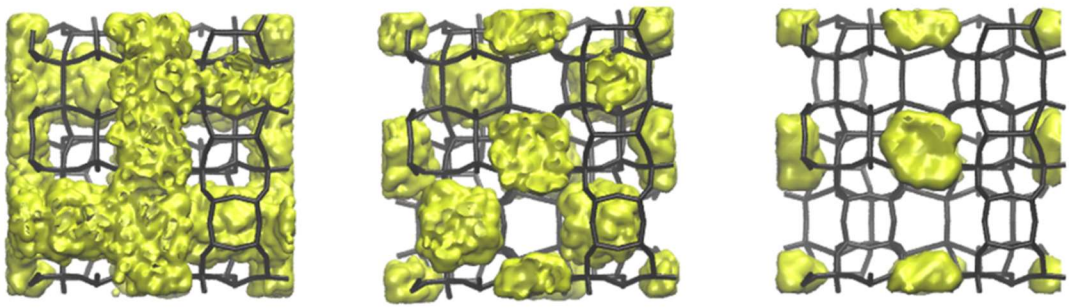

Figure 3.3: Pore volume characterisation of the full pore network (left), pore volume of straight and sinusoidal channels (centre) and straight channels only (right). In black the solid framework and in yellow the pore volumes.

The strategy is to calculate first the specific micropore volume of the total structure, then the volume accessible in the channels blocking the intersections with hard spheres of 5 Å, and finally blocking the sinusoidal channels so that the volume of the straight channels can be derived. Once the micropore volume is known, the density ρ_s of each site can be calculated from eq.(3.29), which is a volume balance on the site. The densities of each site are reported in Table 3.1.

$$\frac{\omega_{site}}{\rho_{s,site}} = V_{mic,site} + \frac{\omega_{site}}{\rho_s^*} \qquad 3.29$$

The procedure presented can be easily extended to any arbitrary solid, where the different sites can be isolated using inert hard spheres and separately analysed using PoreBlazer.

The two remaining solid parameters to regress are P_S^* and T_S^*. As previously presented, the characteristic energy density can be parametrised with the use of the adsorption energy at zero loading of different molecules. To derive the energy of adsorption of specific sites we use the same approach adopted to characterise the pore volume. When molecular simulations can be run on the system, we can take advantage of the artificial blocking of specific portions of the pore volume and derive data on specific regions of the adsorbent.

In this work, the Widom insertion method[162] (see Appendix B) has been used to calculate the Henry's law constant of light alkanes from methane to butane at 290 K, 300 K and 310 K. The strategy to calculate the Henry's law constants of the different sites is similar to what presented for the pore volume characterisation. Firstly, the full solid is made available for adsorption. Then, the intersections are made inaccessible with hard spheres. The difference between the full structure results and intersection-blocked results provides the Henry's law constant of the intersections. Next, the sinusoidal channels are made inaccessible with hard sphere, thus leading to information on the Henry's law constant of the sinusoidal channel. The difference between the full Henry's law constant and the one from intersections and sinusoidal channels gives the Henry's law constant of the straight channels.

The Henry's law constants have been used to regress the heat of adsorption at zero loading and 300 K, using the Van't Hoff equation eq.(3.30).

$$K = K_0 exp\left(-\frac{\Delta H_0}{R_g T}\right) \qquad 3.30$$

where K_0 is a pre-exponential factor. The results for the three sites of ortho-MFI are presented in Figure 3.4.

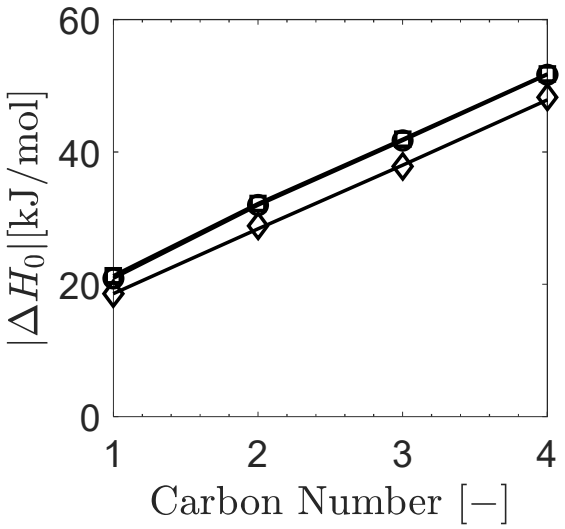

Figure 3.4: Heat of adsorption at zero loading for linear alkanes in ortho-MFI. Diamonds is the heat of adsorption at the intersection, circles at the sinusoidal channel, squares at the straight channel, and the solid line is multi-RALF.

The intersections show lower adsorption energy given the bigger void space compared to the channels. Both channels show very similar values for the light alkanes investigated, since their pore volume is similar. It should be noted that alkanes of higher carbon number could not be used in this study because the constraint of such process is that the molecule remains smaller than the site investigated. The P_S^* for each site is reported in Table 3.1.

Table 3.1: Values of the mass fraction, solid density, characteristic pressure and characteristic temperature for each site of ortho-MFI.

	$\omega_{site}[-]$	$\rho_s\ [kg/m^3]$	$P_s^*\ [kPa]$	$T_s^*\ [K]$
Intersection	0.4	1630	6x10^5	1200
Straight	0.3	1844	6x10^5	1250
Sinusoidal	0.3	1846	5.9x10^5	1300

The last parameter to fit remains T_S^* which has been fitted to the single component isotherms of benzene and propene that are discussed in the next section. For completeness, the T_S^* values of each site are reported in Table 3.1.

3.4.2 Isotherms of benzene and propene at 373 K

As previously stated, both single component isotherms and binary adsorption data have been generated using GCMC simulations. The details of the GCMC are reported in Appendix B.

The results for the single component isotherms from GCMC simulations are presented in Figure 3.5. In addition to the overall isotherm, the contribution of the sites is reported. It can be noted how the benzene preferentially adsorbs at the intersection of the channels, since the higher void space is able to better accommodate the benzene molecule. Only at higher pressures, the benzene is forced to move in the channels.

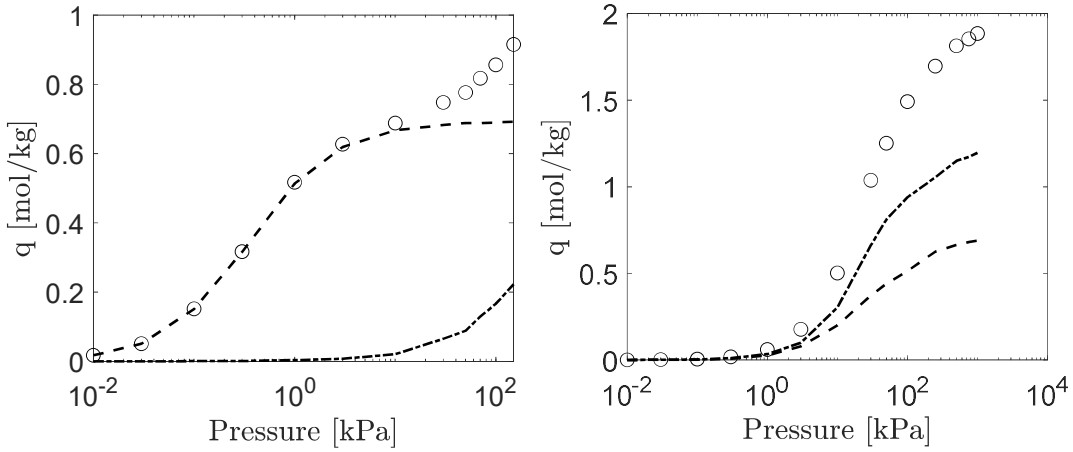

Figure 3.5: Adsorption isotherms at 373 K of benzene (left) and propene (right) on ortho-MFI. Circles are the results of GCMC simulations, the dashes line is the amount adsorbed at the intersections, and the dashed-dotted line is the amount adsorbed in sinusoidal and straight channel.

This behaviour can be easily visualised in Figure 3.6 which reports the snapshots of the GCMC simulations of benzene at three different pressures. Up to a pressure or roughly 3 kPa the benzene only adsorbs at the intersection, for a maximum of 4 molecules per unit cell (each unit cell has 4 intersections).

The snapshot at 100 kPa shows how the benzene is then forced into the channels with no real preference between the two.

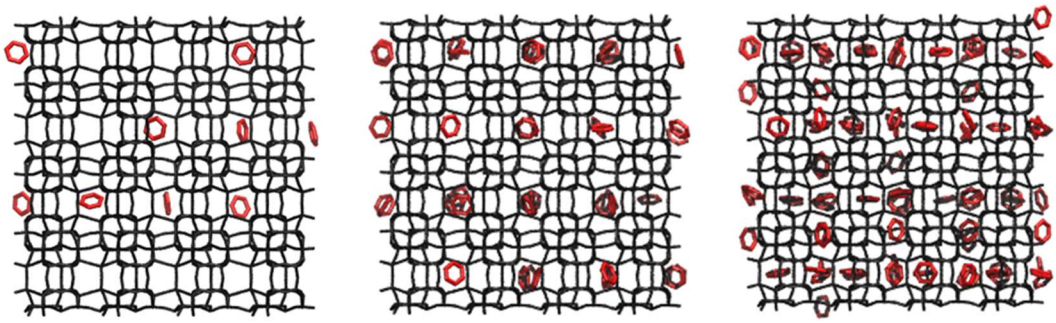

Figure 3.6: Snapshots from GCMC simulations of benzene adsorption on ortho-MFI at 373 K and 0.1 kPa (left), 3 kPa (centre), 100 kPa (right). In black the solid framework of ortho-MFI and in red the molecules of benzene.

By contrast, the propene homogeneously fills the whole void space of the framework without any particular preference, as shown in Figure 3.5 and from the snapshots of the GCMC simulations in Figure 3.7. This is given by the smaller size of the propene molecule. It should be noted that in Figure 3.5 the contribution of the two sites is summed given their very similar behaviour. However, if split, they would almost overlap with the isotherm of propene at the intersections.

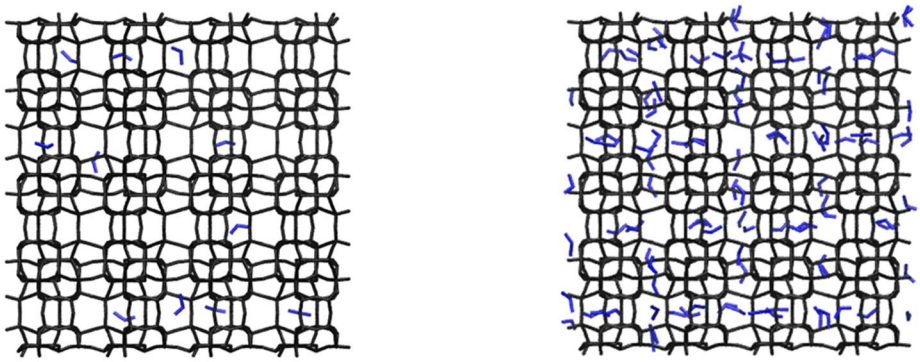

Figure 3.7: Snapshots from GCMC simulations of propene adsorption on ortho-MFI at 373 K and 3 kPa (left) and 100 kPa (right). In black the solid framework of ortho-MFI and in blue the molecules of propene.

The fitting of multi-RALF to the isotherms of benzene and propene at each site is presented in Figure 3.8. The fitted parameters are reported in Table 3.2, and the T_S^* in Table 3.1. Before commenting on the fitting procedure, it is useful to review the effect of the adjustable parameters on the isotherm shape.

As previously introduced, the confinement parameter ξ can be used to lower the saturation capacity of an arbitrary molecule. Indeed, the higher ξ, the lower will be the volume occupied by the molecule at close packing (see eq.(3.13)), i.e. the saturation capacity. The interaction parameter κ_{is} describes how strong is the interaction between the adsorbate and the solid. Negative values of the interaction parameter will lead to higher affinity (see eq.(3.20)), hence higher Henry's law constant. On the contrary, if κ_{is} is positive, the affinity will be lower, leading to a lower Henry's law constant.

It is interesting to point out from Figure 3.8 that with the only use of T_s^*, the propene isotherms at the channel can be reasonably fitted, so that both confinement and interaction parameter can be left zero. The values of the T_s^* fitted is not far from what Brandani[139] presented in his work on hydrocarbon adsorption on ortho-MFI, $T_s^* = 1060\ K$. The slightly higher values fitted in this work (see Table 3.1) can be attributed to the discrepancy between experimental data and molecular simulations. However, the difference between the values of the T_s^* from experimental data and the ones fitted to molecular simulations is not dramatic.

As can be seen from Figure 3.8, the benzene in straight and sinusoidal channels exhibits linear behaviour. This trend can be matched by fitting only one of the two adjustable parameters, i.e. ξ and κ. Since the isotherms are linear, and we are far from saturation, it is reasonable to use only the adjustable parameter κ_{is}, which mainly acts on the Henry's law region of an isotherm. The interaction parameter fitted to both channels is positive, as shown in Table 3.2, meaning that the affinity between benzene and the solid is lower to what multi-RALF would predict. If compared with the interaction parameter fitted at the intersection for benzene, it is evident the preferential affinity of the benzene with the intersections, where the higher pore volume allows an easier fit of the molecule in the free space. It should be noted that the value of T_s^* for the channels is kept constant at that fitted for propene.

The fitting of benzene and propene at the intersection requires all the adjustable parameters. As good practice to limit the number of parameters to adjust, a first fit of the parameters can be done on the Henry's law constants and the saturation capacities using only characteristic temperature and confinement parameter. Once a preliminary fitting is carried out, then the interaction parameter κ_{is} at the intersection for each molecule can be adjusted to match the isotherm.

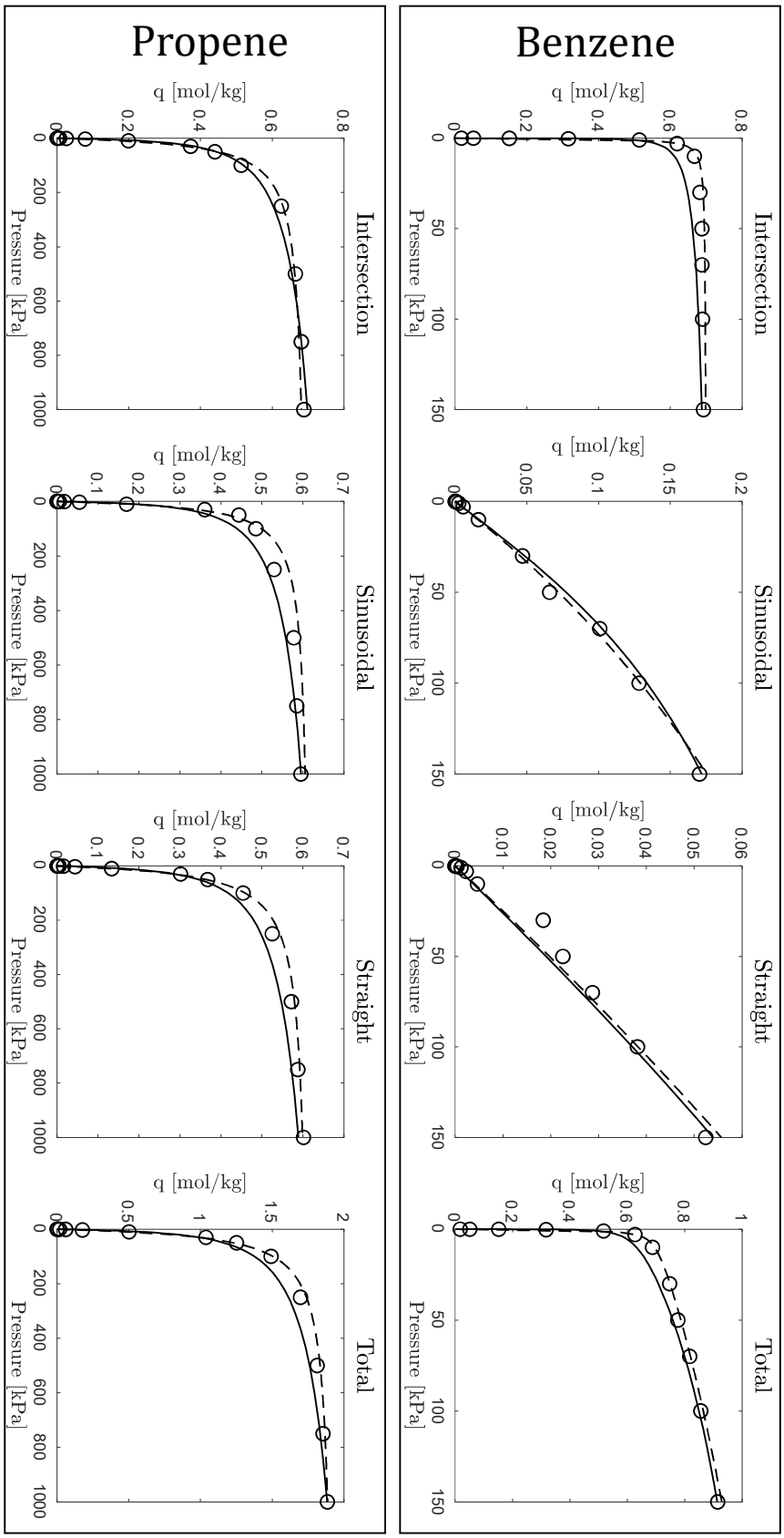

Figure 3.8: Fitting of RALF to the single adsorption isotherms of benzene and propene at 373 K on ortho-MFI. Circles are results from GCMC simulations, solid line is RALF and dashed line is Langmuir isotherm, eq.(3.31).

The intermediate region between Henry's law region and saturation of the benzene isotherm is not very well captured from multi-RALF. Indeed, RALF struggles to match almost rectangular isotherms. The reason might lie in the effect of the mixing rules on the isotherm shape. An analysis of a different set of mixing rules should be carried out in future works to overcome this limitation.

Table 3.2: Fitted ξ_i and κ_i at the single component isotherms in Figure 3.8, and Sanchez-Lacombe parameters for benzene[142] and propene[163].

	Int.	***Sin.***	***Str.***	P^* $[kPa]$	T^* $[K]$	ρ^* $[kg/m^3]$
Benzene	ξ =0.4 κ =0.085	ξ =0.0 κ =0.43	ξ =0.0 κ =0.5	4.44x10^5	523	994
Propene	ξ =0.6 κ =0.09	ξ =0.0 κ =0.0	ξ =0.0 κ =0.0	3.79x10^5	356	755

In Figure 3.8 the GCMC results have also been fitted with a Langmuir type isotherm of the form:

$$q_i = q_{s,site} \frac{b_{i,site} P_i}{1 + b_{i,site} P_i} \qquad 3.31$$

where the saturation capacity for each site has been kept constant among the two molecules. The fitted parameters for eq.(3.31) are $q_{s,int} = 0.7\ mol/kg$, $q_{s,sin} = q_{s,str} = 0.62\ mol/kg$, and the $b_{i,site}$ parameters are reported in Table 3.3.

Table 3.3: $b_{i,site}$ parameter, eq.(3.31), for benzene and propene at each site.

	$b_{i,int}$ $[1/Pa]$	$b_{i,sin}$ $[1/Pa]$	b_{istr} $[1/Pa]$
Benzene	0.02714	2.632x10^{-6}	6.576x10^{-7}
Propene	3.589x10^{-5}	4.11x10^{-5}	2.85x10^{-5}

3.4.3 The binary benzene-propene on ortho-MFI

The GCMC simulations for the binary benzene-propene adsorption on ortho-MFI at 373 K and 100 kPa are presented in Figure 3.9. The binary shows a reverse of the selectivity around $y_{C_6H_6} \approx 0.5$. At $y_{C_6H_6} \leq 0.5$ the benzene occupies all the intersections of the unit cell, given the higher affinity at the intersections compared to propene. Propene can only fill the channels, which have lower pore volume if compared with the intersections. This behaviour, which can be observed from the snapshot in Figure 3.9, explains the preferential adsorption of benzene in the overall solid.

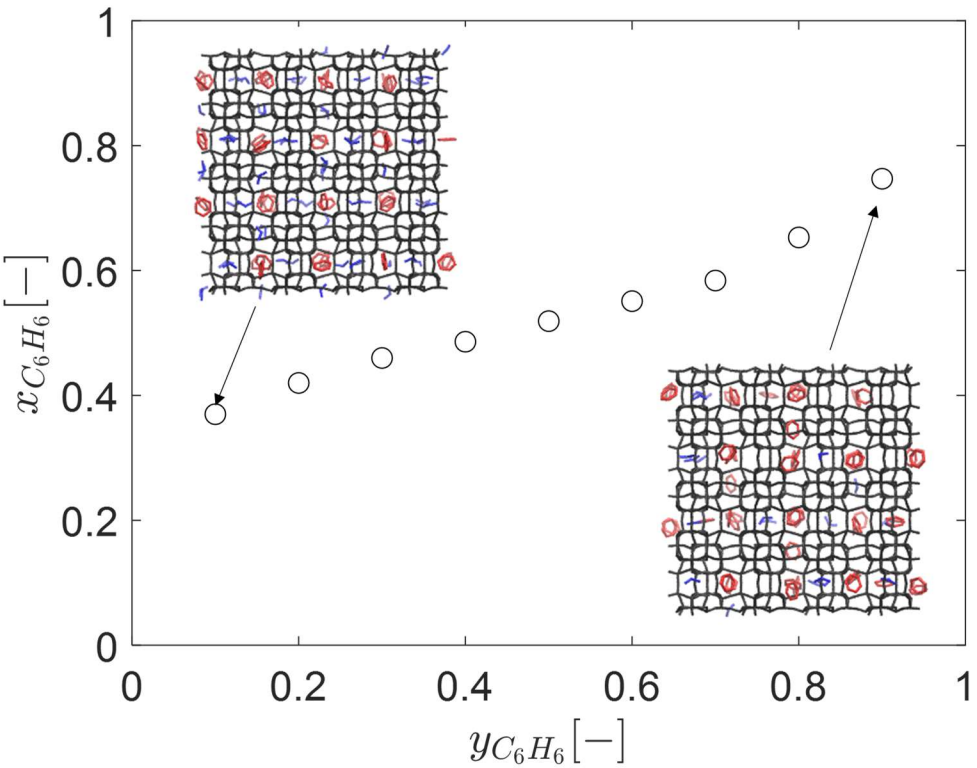

Figure 3.9: xy-plot for the system benzene−propene adsorption on ortho-MFI at 373 K and 100 kPa. The circles are results from GCMC simulations. Two snapshots are shown for $y_{C_6H_6} = 0.1$ and 0.9. In black the solid framework, in red the benzene molecules, and in blue the propene molecules.

By contrast, when $y_{C_6H_6} \geq 0.5$, the benzene does not move in the channels given that its fugacity is not enough to push the benzene molecules in the tighter channels. Instead, the propene fills rapidly the channels leading to a reversal of the selectivity. The azeotrope presented can hence be attributed to a geometrical hindering of the benzene in the channels. Therefore, the azeotrope is not caused by the interaction between the adsorbates, but from

their packing at the sites. From the GCMC simulations, the energy of interaction between the adsorbates is quantified to less than 5% of the total energy of the system. This further proves that the azeotrope is mainly caused by entropic effects more than enthalpic ones.

The results of the predictions of multi-RALF and the extended tri-site Langmuir model are presented in Figure 3.10.

The equation used to calculate the amount adsorbed at each site with the extended Langmuir model is:

$$q_i = q_{s,site} \frac{b_{i,site} P_i}{1 + \sum_{k=1}^{N_c} b_{k,site} P_k} \qquad 3.32$$

and then the total amount adsorbed in the solid is calculated as sum of the three sites. The approach of calculating the amount adsorbed with an extended Langmuir model at each site and then sum the contributions is equivalent to the use of HIAST.

It should be noted that multi-RALF has an additional fitting parameter common to all the three sites: the interaction parameter between benzene and propene, i.e. $\kappa_{C_6H_6-C_3H_6}$.This parameter has been fixed to 0 given that the energy of interaction from the GCMC simulations has been proved to be negligible. Ideally, one could fix this interaction parameter fitting vapour-liquid equilibria of the binary benzene-propene or leave it as a free adjustable parameter for the binary adsorption data. As can be seen from Figure 3.10, if multi-RALF is properly trained on the information from the molecular scale, it can successfully reproduce the binary data in a purely predictive form. It should be mentioned that also the extended Langmuir model provides reasonably good results. However, multi-RALF is better able to capture the trend of amount adsorbed of propene at low mole fraction of the benzene, which the extended Langmuir model tends to overestimate.

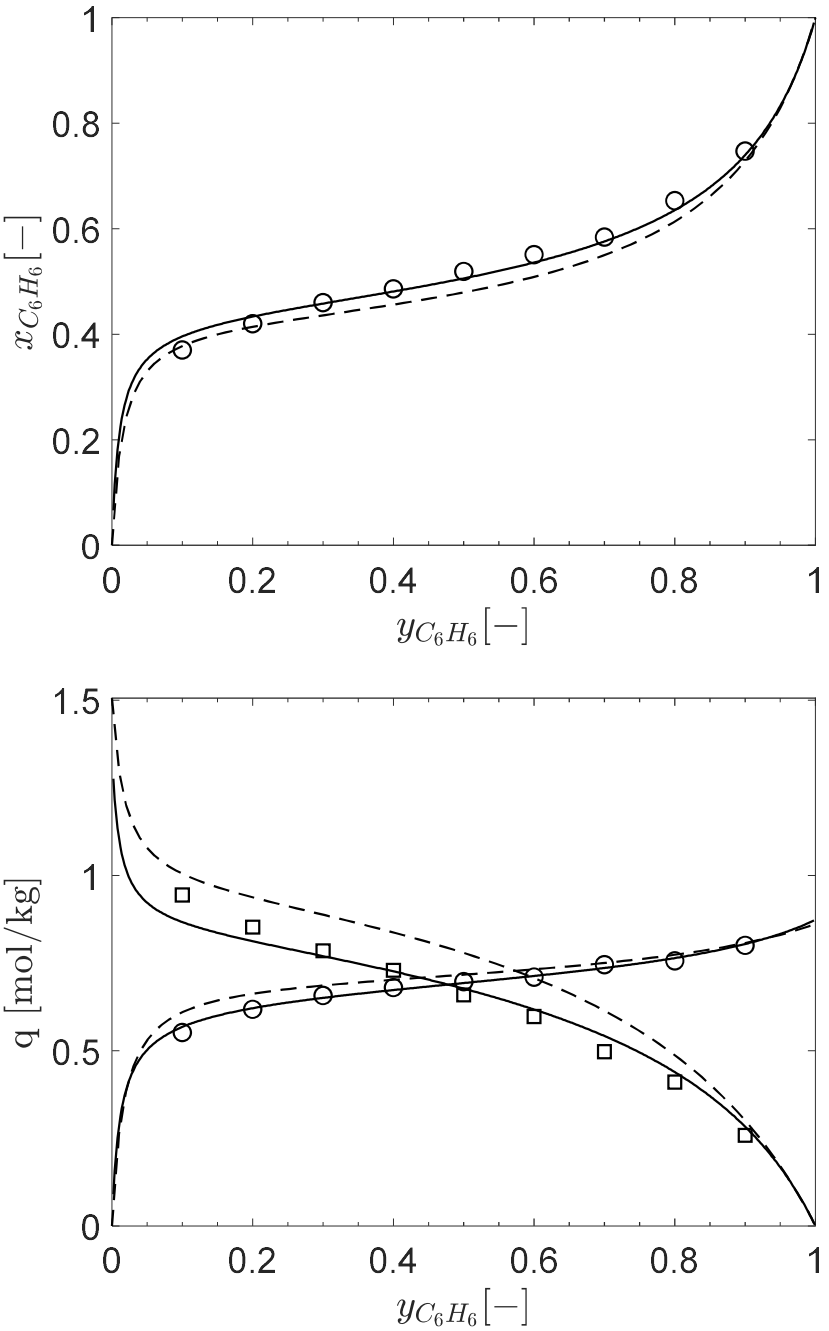

Figure 3.10: xy-plot (top) and absolute amount adsorbed for benzene and propene at different mole fraction of benzene (bottom) at 373 K and 100 kPa on ortho-MFI. Circles are GCMC results for benzene, squares for propene, solid line is multi-RALF and dashed line is the extended tri-site Langmuir model.

3.5 Parametrisation of multi-RALF via experimental data

The capture of carbon dioxide from natural or biogas feeds, or from effluent streams in power plants can potentially lead to a reduction in the emission of greenhouse gases[104,106,164]. Among the promising materials under investigation for this application, zeolites offer great potential in terms of high CO_2/CH_4 selectivity[165,166]. In particular, Rho-type zeolites have been studied for their particular structure which offers high CO_2 capacity[167,168]. The structure of a Rho zeolite is shown in Figure 3.11.

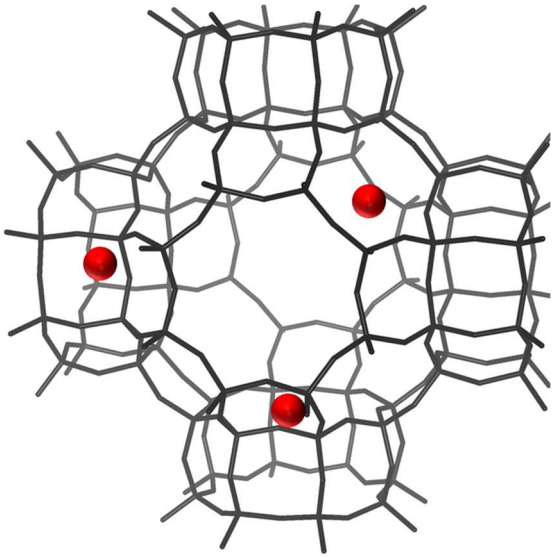

Figure 3.11: Unit cell of Rho-type zeolite. In black the solid framework, in red the position of extra-framework cations.

The structure comprises large cages connected by six double eight-membered rings which act as windows between cages. Extra framework cations are located at the windows between cages.

The adsorbent of interest for the parametrisation of multi-RALF via experimental data is (Na,TEA)-ZSM-25[152,169], which is part of the Rho-type zeolites family. The acronym TEA stands for tetraethylammonium cations, which remain trapped in the framework during the synthesis process. The structure of this adsorbent consists of interconnected cages as the one shown in Figure 3.11. (Na,TEA)-ZSM-25 has shown the peculiarity of expanding its volume upon adsorption and a peculiar adsoprtion behaviour towards CO_2 [170]

that it will be investigated in the following. The flexibility of an adsorbent is generally observed upon adsorption in metal-organic frameworks (MOFs) such as Mil-53(Al)[149]. Nevertheless, the flexibility showed by zeolites, like (Na,TEA)-ZSM-25, which are often assumed “rigid”, has gained interest recently[171–173].

Usually, the flexibility in MOFs such as MIL-53 is caused by a stress level induced by adsorption that lets the structure of the solid breath[174]. The flexibility of the solid is mainly related to the chemical nature of MOFs, where organic linkers are easily distorted by weak interactions with the adsorbates. This phenomenon shows an inflection at a critical stress level, and generally tends to show hysteresis in the isotherm of MOFs[149]. By contrast, the more rigid structure of zeolites can present flexibility that is caused mainly by Coulombic interactions[175,176]. The interaction of polar molecules with the framework cations of the solid causes the movement of the cations. If the cations are positioned at a window that links two pore volumes, the movement of the cation upon interaction with a polar molecule can lead to a “gating” effect. The movement of the cations can also lead to a relaxation of the solid framework, which might experience a “breathing” as the one shown in MOFs.

Aim of this section is to understand the nature of the flexibility of (Na,TEA)-ZSM-25, and parametrise multi-RALF based on experimental data of (Na,TEA)-ZSM-25. Given that the interest is to show the potential of multi-RALF in the modelling of such complex systems, the experimental characterisation and the techniques will only briefly outlined.

The material synthesis of (Na,TEA)-ZSM-25 is reported by Guo et al.[167]. The structural characterisation with the use of powder X-ray diffraction, scanning electron microscopy and thermogravimetry of the sorbent is presented in Verbraeken et al.[152] and it will not be reported in this work. The results which are of interest for the parametrisation of multi-RALF are the isotherms of CO_2 at different temperatures on (Na,TEA)-ZSM-25 and the change of the volume of solid upon adsorption.

The volume change upon adsorption can be obtained with the use of Variable-Pressure X-Ray Diffraction (VP-XRD) technique. The CO_2 isotherms at 268 K, 288 K, 308 K, and 328 K have been obtained with a volumetric system, the Autosorb iQ system (Quantachrome instruments). The sample mass used for the isotherm experiments was of 0.1041 g. Prior to the isotherm acquisition, the sample was regenerated overnight under vacuum at 473 K. Both adsorption and desorption experiments were carried out.

The experimental data for the material characterisation have been generated by Prof. P.A. Wright and his co-workers at the University of St. Andrews, while the CO_2 isotherm experiments have been carried out by Dr.Verbraeken, with whom the author of this work has developed the model of multi-RALF to describe CO_2 adsorption on (Na,TEA)-ZSM-25.

3.5.1 Flexibility of (Na,TEA)-ZSM-25

The results from VP-XRD experiments, and the CO_2 isotherms at different temperatures are shown in Figure 3.12. It should be noted that the experimental points presented in Figure 3.12 (left) are both from adsorption and desorption runs, and no appreciable hysteresis is detected.

All the isotherms shown in Figure 3.12 (left) present an inflection at constant amount adsorbed, between 0.6 mol/kg and 2 mol/kg. This behaviour shows that the inflection does not occur at a given pressure of CO_2, but rather at a constant amount adsorbed, between 0.6 mol/kg and 2 mol/kg, independent on the temperature of the system. From Figure 3.12 (right), it is interesting to point out that the solid experiences a sharp increase in its volume only after reaching almost 2 mol/kg. Hence, the increase in solid volume cannot explain the inflection seen in the isotherms around 1 mol/kg. Indeed, at roughly 2 mol/kg, none of the isotherms show any inflection.

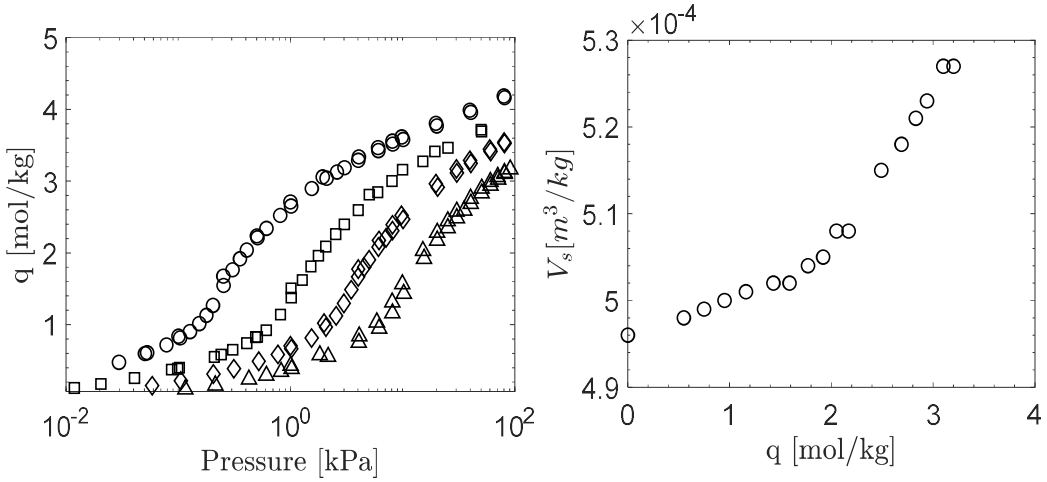

Figure 3.12: Adsorption isotherms of CO_2 on (Na,TEA)-ZSM-25 (left), and variation of the specific solid volume upon adsorption (right). The isotherms are at 268 K(cirlces), 288 K (squares), 308 K (diamonds), and 328 K (triangles).

The data presented tend to exclude a flexibility behaviour as explained for MOFs. Indeed, if the flexibility was caused by the adsorbate-adsorbent interaction at a given chemical potential of the fluid phase, the inflection would happen at the same point where the VP-XRD data show the change in volume. Moreover, the isotherm data do not show hysteresis, which is usually a clue of internal mechanical stresses of the adsorbent structure.

An isotherm which shows an inflection can be ideally matched assuming the solid to be made of two sites. It should be noted that RALF has already proven its ability to predict stepped isotherms using only one site. This behaviour has been observed for adsorbents of large porosity and if the adsorbate-adsorbate interactions are much stronger than the adsorbate-adsorbent ones[149]. Nevertheless, in the CO2 adsorption on (Na,TEA)-ZSM-25 a strong interaction of the adsorbate with the cations is expected. Hence, only one site of RALF should not be able to match the isotherms in Figure 3.12. Since the structure of (Na,TEA)-ZSM-25 consists of highly interconnected cages, it would be impossible to segregate the sites and analyse them. Hence, a model with only 2 sites is the simplest multisite model that can be used. It should be noted that a multi-RALF model consisting of 2 sites contains several degrees of freedom which can be tuned to a great variety of experimental data. It is, therefore, reasonable to say that a multi-RALF model with 2 sites can potentially cover several equilibria without the need of introducing further sites. Nevertheless,

the number of sites to fit has to be always decided on a case by case analysis and one should use the minimum number of sites that represents correctly all available data.

It should be noted that attempts to model the adsorption dynamics of CO_2 on (Na,TEA)-ZSM-25 using only one site have been made by Dr.Verbraeken without any successful outcome. The results are available in the work of Verbraeken et al.[152] and will not be reported here.

In the following, a multi-RALF model with two sites will be used. It will be assumed that the characteristic parameters of the solid for each site are the same since no molecular simulations can be run to split the different contributions. Instead, the confinement and interaction parameter of each molecule in the two sites will be allowed to be different. As a first approximation, the mass fraction of both sites can be assumed $\omega_\alpha = \omega_\beta = 0.5$. Then, once the fitting of the solid parameter is carried out, this assumption can be relaxed for a better fit of the isotherms.

To correctly capture the trend of the single component isotherms, both adsorbates parameters, i.e. κ_{iS} and ξ_i, and the volume change have to be simultaneously fitted to both VP-XRD and the isotherms data. In the following, the solid parameters P_s^*, ρ_s^* and ρ_s are regressed first. T_s^* is left as adjustable parameter for the isotherm data. The volume change will be modelled as shown in section 3.5.3.

3.5.2 Parametrisation of the solid parameters

The characteristic energy density, P_s^*, can be fitted to the heat of adsorption at zero loading of CO_2 on (Na,TEA)-ZSM-25 calculated using the Clausius-Clapeyron equation:

$$-\Delta H_0 = R_g T^2 \left(\frac{\partial lnP}{\partial T}\right)_{q_{CO_2}\to 0} \qquad 3.33$$

from which the enthalpy of adsorption at zero loading is $|\Delta H_0| = 46.1 kJ/mol$, and the fitted $P_s^* = 1.25 \times 10^6\ kPa$.

The skeletal density is derived from He pycnometry, $\rho_s^* = 2640\ kg/m^3$, and $\rho_s = 2020\ kg/m^3$ is derived from the XRD measurements *in-vacuo*.

The characteristic temperature, T_s^*, is fitted in section 3.5.4 to the Henry's law constant of the isotherms in Figure 3.12 (left), together with the interaction and confinement parameters.

The summary of the regressed solid parameters is presented in Table 3.4.

Table 3.4: Characteristic parameters for (Na,TEA)-ZSM-25

Parameter	***Unit***	***Site α***	***Site β***
P_S^*	$[kPa]$	1.25x10^6	
ρ_s^*	$[kg/m^3]$	2640	
ρ_s	$[kg/m^3]$	2020	
$\omega_{site}^{(1)}$	$[-]$	0.5	0.5
T_s^*	$[K]$	Fitted to single component isotherms (section 3.5.4)	

(1)Starting guess

3.5.3 Modelling the solid volume flexibility

Once a preliminary fit of the solid parameters is obtained, two steps remain for the full parametrisation of multi-RALF: the modelling of the solid flexibility, and the final fit of the single component isotherms.

The model proposed by Verbraeken et al.[152] to explain the data presented in Figure 3.12 comprises two sites: site α which is always available for adsorption, and site β which becomes available only when the amount adsorbed in site α reaches the critical value of 0.6 mol/kg. The site β gradually opens up to roughly 2 mol/kg, when it becomes fully available. Once the cations are repositioned, at around 2 mol/kg, the solid framework relaxes, leading to an increase in the solid volume. At zero loading, only site α can be accessed from the adsorbate since the cations are blocking the windows which

allow the adsorbate to move in site β. Upon adsorption, the cations of the system are solvated with adsorbate molecules, allowing them to move and open the window between site α and β. During the desorption, the β site is emptied first, the cations come back to their original position at the window, and finally the adsorbate molecules leave site α. The mechanism here presented does not include internal stresses of the adsorbent since the experimental isotherm shows only one equilibrium condition between a fugacity in the fluid phase and the adsorbed amount.

This mechanism is similar to what already observed in Na-Rho zeolites[168], which also present a distortion of the lattice, and where cations move from cage opening to allow adsorption on different sites. Synchrotron experiments carried out by Prof. Wright and co-workers have shown that at low partial pressure of CO_2 the solid framework possesses a cubic distorted structure with small lattice parameters, and only upon adsorption the structure relaxes to a more regular one with larger lattice parameters. These observations tend to confirm that the volume change after the uptake at 2 mol/kg is caused by a relaxation of the solid framework upon cation movement, rather than interaction between CO_2 and the solid framework.

Multi-RALF is a model that is based on the volume occupancy of adsorbates in the void pore volume. To transpose the physical phenomena of site blocking, a strategy similar to what used in the characterisation of ortho-MFI can be used (see section 3.4.1): it can be assumed that the β-site is initially blocked from an inert rigid sphere that occupies its entire pore volume. However, the porosity of the site β is function of the adsorbed amount of the site α, so that when the critical amount adsorbed is reached, site β becomes available.

The porosity of site β will go from zero up to the value of the porosity of site α. The expression of the porosity of site β is reported in eq.(3.34):

$$\epsilon_\beta = \frac{V_{s,\beta} - 1/\rho_S^*}{V_{s,\beta}} \tag{3.34}$$

where $V_{s,\beta}$ is the volume of the solid in site β including the micropores. This volume goes from the skeletal volume only when the site is blocked with an inert rigid sphere, up to the volume of site α when the site is unblocked thanks to adsorption. The expression for $V_{s,\beta}$ is:

$$V_{s,\beta} = \frac{\big(1 - f(\bar{q})\big)}{\rho_S^*} + f(\bar{q})V_{s,\alpha} \tag{3.35}$$

where $f(\bar{q})$ is a switching function as in eq.(3.36).

$$f(\bar{q}) = \frac{1}{2}\big[tanh\big(w(q - q'_{trans})\big) + 1\big] \tag{3.36}$$

where w and q'_{trans} are adjustable parameters. The volume of site α is modelled with a quadratic function fitted to the VP-XRD data, as shown in Figure 3.13. The quadratic equation is reported in eq.(3.37), with a and b as fitting parameters.

$$V_s(\bar{q}) = a \cdot (\bar{q} + b)^2 + \frac{1}{\rho_s} \tag{3.37}$$

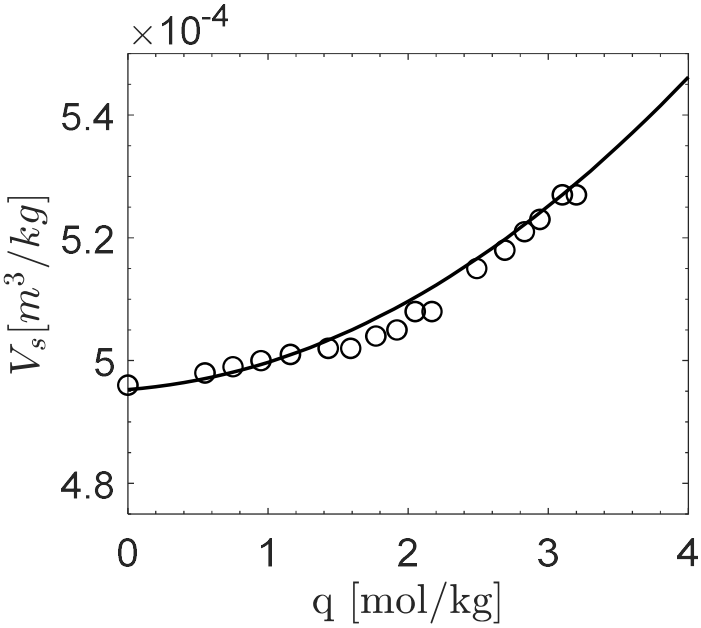

Figure 3.13:Solid specific volume of (Na,TEA)-ZSM-25 as function of the amount adsorbed at 328 K from VP-XRD data. Circles are experimental data and solid line is eq.(3.37)

The plot of the porosity of site β, together with the porosity of the other site, is reported in Figure 3.14. As it can be seen, site β starts to open up around 0.6 mol/kg to then arrive at the same porosity of site α at around 2 mol/kg.

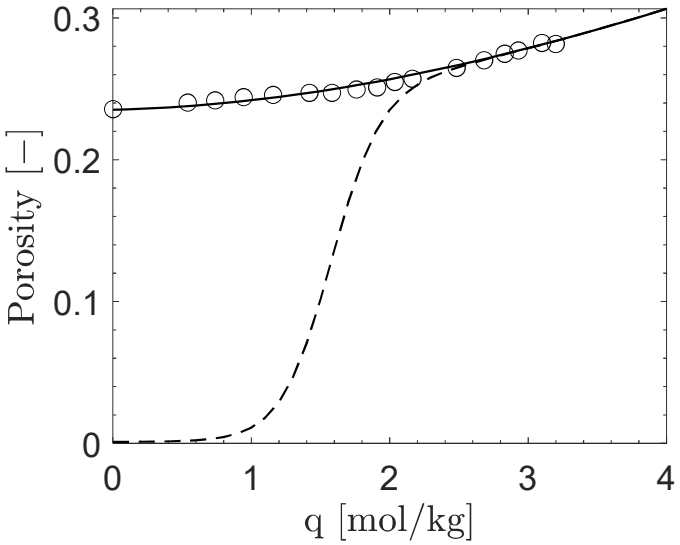

Figure 3.14:Porosity of (Na,TEA)-ZSM-25 against average amount adsorbed of CO_2. Cirlces are experimental data from VP-XRD at 328 K, solid line is the porosity of site α and dashed line is the porosity of site β.

The fitted parameters of eq.(3.36) and (3.37) are reported in Table 3.5.

Table 3.5: Fitted parameters of eq.(3.36) and (3.37) to model the flexibility of (Na,TEA)-ZSM-25

Parameter	*Unit*	*Value*
w	$[-]$	2.75
q'_{trans}	$[mol/kg]$	1.62
a	$[m^3 kg/mol^2]$	2.77x10^{-6}
b	$[mol/kg]$	0.3
ρ_s	$[kg/m^3]$	2020

The parameters a and b are fitted to the data in Figure 3.13, while ρ_s is fixed by XRD experiments (see section 3.5.2). It should be noted that the parameters w and q'_{trans} have been fitted to the single component isotherms together with T_s^* and the molecule parameters at each site. However, the values of w and q'_{trans} have been constrained so that the porosity of site β would change in the range of amount adsorbed between 0.6 mol/kg to 2 mol/kg, to represent the physical movement of the cations while the amount adsorbed is in that range.

3.5.4 Fitting of the CO_2 isotherms

The results of multi-RALF in fitting the CO_2 isotherms on (Na,TEA)-ZSM-25 are presented in Figure 3.15. The CO_2 characteristic parameters are taken from De Angelis et al.[141]: $P^* = 6.3 \times 10^5\ kPa$, $T^* = 300\ K$ and $\rho^* = 1515\ kg/m^3$.

The fitting strategy, as previously discussed, firstly fixes the mass fractions to 0.5. Then, the T_s^* is fitted to the Henry's law region together with the volume changing parameter w to approach the experimental data. Next, the interaction and confinement parameters are adjusted to match the experimental data. Finally, a gradual refinement process is carried out to allow for a better match adjusting all the parameters simultaneously from the estimate made in the previous steps.

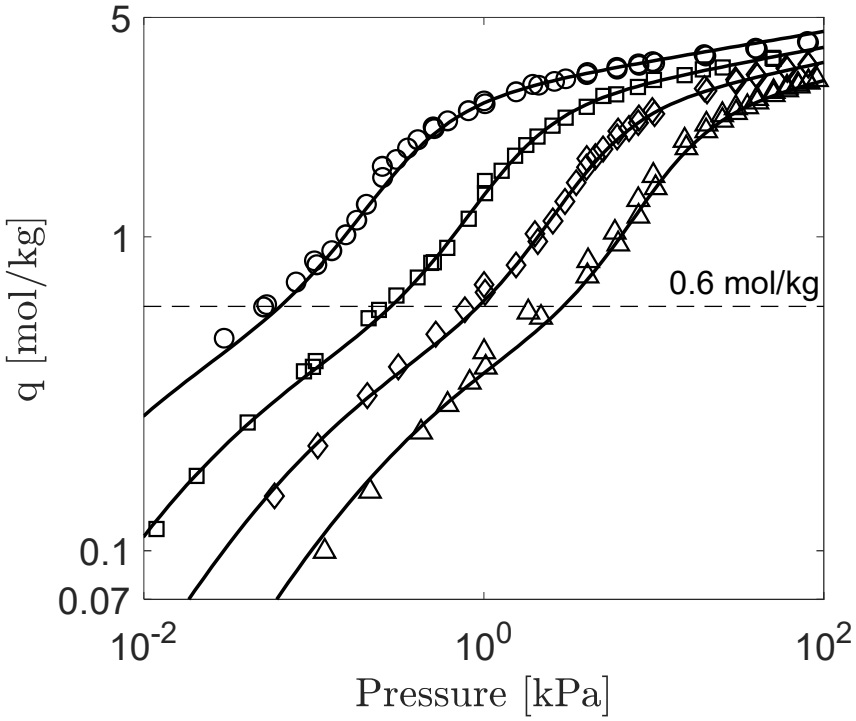

Figure 3.15: CO_2 isotherms on (Na,TEA)-ZSM-25 from experimental data. Circles are data at 268 K, squares at 288 K, diamonds at 308 K, triangles at 328 K and the solid line is multi-RALF.

The final result of the fitting is quite satisfactory, since the inflection that starts at around 0.6 mol/kg (highlighted in Figure 3.15) is correctly described, together with the Henry's law region.

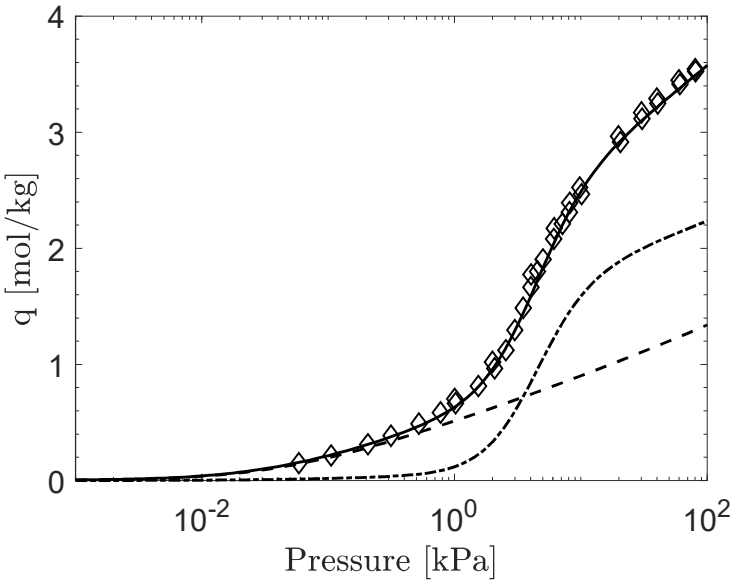

Figure 3.16: CO_2 isotherm on (Na,TEA)-ZSM-25 at 308K. Diamonds are experimental data, solid line is multi-RALF; dashed line is the adsorption isotherm of site α and dash dotted line is the isotherm of site β.

The fitted interaction and confinement parameters to the isotherms are reported in Table 3.6. The final fitted $T^* = 2050\ K$, and the mass fractions are slightly adjusted to $\omega_\alpha = 0.48$ and $\omega_\beta = 0.52$.

Table 3.6: Fitted interaction and confinement parameters for the CO_2 isotherms in Figure 3.15

	$\kappa_{i,\alpha}$	ξ_α	$\kappa_{i,\alpha}$	ξ_β
CO_2	-0.085	0.087	-0.14	0.0

To show the behaviour of the two sites, the isotherm at 308 K is split in the contribution from both sites, in Figure 3.16. As it can be seen, the Henry's law region is fully dominated by site α which is the only site available for adsorption. Once the cations that block the windows are solvated by CO_2, the adsorption in site β takes place, which causes the inflection seen in the isotherms.

The results presented for the thermodynamics of CO_2 on (Na,TEA)-ZSM-25 will be used in the next chapter to obtain information on the diffusion mechanism of the system.

3.6 Conclusions

Aim of this chapter was the derivation of a novel multisite version of the RALF model, multi-RALF, to model both the multicomponent adsorption on heterogeneous solids, and the adsorption of CO_2 on (Na,TEA)-ZSM-25.

The multi-RALF model, if one considers that the RALF model is a special case of multi-RALF, can handle a huge variety of systems making use of a single thermodynamic framework based on the assumption that the solid can be modelled as a lattice made of the adsorbent and the adsorbates, which occupy different volumes according to their nature.

Multi-RALF relies on the definition of average properties of the adsorbed lattice which have been introduced in section 3.2.2 and the definition of a residual chemical potential for each adsorbate, as presented in section 3.2.3. It is

implicit in the definition of the residual chemical potential for an adsorbate that multi-RALF can handle non-ideal adsorbed lattices, without the need of empirical activity coefficients. The non-ideality taken into account in multi-RALF relies on the modelling of the interaction of the adsorbed molecule with the adsorbent and the other adsorbates, and on the confinement volume that the molecule occupies in the lattice.

A simple procedure to derive the characteristic parameters of the solid is presented, which uses He pycnometry and mercury intrusion to obtain the characteristic densities, and on heat of adsorption at zero loading and Henry's law constant of different molecules for P_s^* and T_s^*, respectively.

The case study used to introduce the equations of multi-RALF in case the solid is composed of segregated sites is the azeotropic adsorption of benzene and propene on ortho-MFI silicalite at 373 K and 100 kPa. Both single and multicomponent data have been generated with GCMC simulations. The solid parameters are derived in section 3.4.1, together with a presentation of the solid structure of ortho-MFI silicalite. Then, the confinement and interaction parameters are fitted to the single component isotherms together with T_s^*. Once the single component isotherms of benzene and propene on each site are fitted, the binary benzene-propene adsorption on ortho-MFI is correctly predicted. The molecular simulations show that the reverse in selectivity at 373 K and 100 kPa is caused by the steric hindrance of benzene which adsorbs preferentially at the intersections between straight and sinusoidal channels. By contrast, the propene adsorbs uniformly in the solid framework without any preference.

Multi-RALF is also used to model the adsorption of CO_2 on (Na,TEA)-ZSM-25, a zeolite of the Rho family which shows flexibility upon adsorption. The model proposed for this adsorbent consists of two sites, site α which is always available, and site β which is blocked at low pressures from cations located at the windows between site α and site β. Unlike MOF flexibility, the flexibility of this adsorbent is caused by solvation of the cations from CO_2. The solvated

cations move away from their position, the windows between the sites, opening up the structure and leading to a higher uptake of the adsorbate. The model proposed reproduces the experimental data from CO_2 adsorption at different temperatures, as well as the volume change of the solid upon adsorption. Despite the specificity of the equations to this case study, the inclusion of flexibility in the multi-RALF model shows the capability of such a general model. Indeed, multi-RALF has been proven to be a “flexible” model, able to adapt at both segregated sites and coupled sites with solid volume change.

It is likely that soon adsorbents which present flexibility, and complex multicomponent mixtures adsorption on heterogeneous solids, will become increasingly relevant in the adsorption field. Therefore, it is paramount to have sophisticated macroscopic models which can be parametrised using microscopic information from the system under analysis. Multi-RALF can be considered a step towards the development of lattice fluid theories for adsorption thermodynamics which address this challenge.

Chapter 4 Kinetics in porous solids

4.1 Introduction

The work on the modelling of monoliths in the first chapter highlighted the importance of reliable kinetic parameters in order to correctly predict the performance of a certain structure. While this might seem a trivial conclusion, the process of acquisition of kinetic information on a system adsorbate-adsorbent is far from being trivial.

Measurement techniques of diffusion in porous materials can be divided in two main categories: microscopic and macroscopic techniques[110,177]. The microscopic techniques study the random movement of the molecules to then derive a diffusion coefficient from Einstein's relation[178,179]. By contrast, macroscopic measurements study the diffusion of a fluid phase in a porous adsorbent to derive an average diffusion time constant of the system[177]. The focus of this chapter will be on macroscopic measurements.

From the late 30s, transient uptake measurements were considered the means of measuring diffusion in porous solids, mainly zeolites and carbon materials. Transient uptake measurements can be divided in two categories: gravimetric and volumetric experiments[177,180].

Gravimetric experiments follow the change in the adsorbent's mass upon contact with a gas phase that contains adsorbing molecules. The change in mass can be correlated to the moles of adsorbate that have adsorbed at a specific pressure and temperature[181,182]. This technique requires very accurate balances, correction for buoyancy effects[183] and attention to produce a uniform gas phase in the chamber where the adsorbent is placed[180].

Volumetric experiments relate the amount of moles adsorbed to the expansion of a gas between a dosing cell and an uptake cell (where the adsorbent is placed)[180,184,185], which are divided by a valve. The valve is closed when the gas is dosed in the dosing chamber, and at the start of the experiment is

opened. The shape of the dosing pressure profile in time can be related to the kinetics of the adsorbate-adsorbent system[177,186].

Until the early 70s, gravimetric and volumetric systems were the main techniques for kinetic measurements. It was only after the advent of PFG-NMR experiments (microscopic technique) pioneered by Kärger and co-workers[179] that the scientific community posed great attention to the development of novel measurement techniques[177]. This was mainly driven by the inconsistency between the results of macroscopic and microscopic measurements evidenced by PFG-NMR results[177,187]. The techniques developed after this 'event' are numerous and all have advantages and disadvantages in the kinetic characterisation of porous materials. Nevertheless, it is worth to discuss chromatographic and frequency response techniques, which will be the focus of this chapter.

Chromatography can be defined as a flow system, compared to transient uptake measurements which can be classified as batch systems. Chromatography makes use of an adsorbent packed bed to carry out measurements. Either a step or a pulse injection of adsorbent is used at the start of the experiment and the outlet profile of adsorbent concentration is monitored. From the shape of the outlet profile, so called breakthrough profile, information on kinetics (and equilibrium) can be derived[110]. Chromatographic measurements are extensively used to characterise single component equilibrium, as well as multicomponent mixture adsorption[50,188–190]. However, the analysis of the results can be somehow convoluted and lead to misleading conclusions if one does not take into account the heat generated upon adsorption, non-linearity of the system, and axial dispersion as additional resistance to the kinetics[127,191–193]. Indeed, a packed bed of adsorbent can generate considerable heat from very strong adsorbing compounds which might not be dissipated fast enough to consider the bed isothermal[194]. The main disadvantage is the study of the temperature and breakthrough profiles with both mass and energy balances, which introduce a consistent number of parameters that cannot be de-coupled from each other. Nevertheless, a recent

review from Wilkins et al.[194] points out how different checks can be made in order to make sure that the system isothermality and linearity are achieved or at least assessed. Wilkins et al.[194] show that chromatographic techniques can provide results as good as conventional transient uptake measurements if the experiments and analysis of the results are properly conducted.

To overcome the limitations of the adsorbent packed bed, Eic and Ruthven[195] introduced in the late 80s the zero-length-column (ZLC) technique. The ZLC consists of a very small column filled with a monolayer of adsorbent material, generally placed between two sinter discs. The column is equilibrated with a feed at constant adsorbate concentration. At equilibrium, the column feed is switched to pure inert gas to purge the column and the desorption profile of the targeted adsorbate is monitored[196]. The arrangement in a small column with monolayers of solid aims at reducing bed-effects, such as the resistance given by axial dispersion. Moreover, the constant flow of fresh feed and the small adsorbent quantity reduce the non-isothermality of the system. Indeed, the improved gas-solid contact ensures high heat transfer, leading to isothermal conditions. It should be noted that models have been developed to take into account non-isothermal[197], non-linear[198] conditions, and crystal size distribution of the adsorbent[199], as well. Its main advantage is the small quantity of adsorbent needed, usually in the order of milligrams[102]. Generally, the ZLC is used for both equilibrium and kinetic measurements. At low flowrates, the system approaches equilibrium and the outlet concentration profile can be directly related to the shape of the isotherm of the adsorbate. On the contrary, at fast flowrates, the systems tend to be controlled by the kinetics of diffusion. Hence, from high flowrates, kinetic information can be regressed. The ZLC will be the focus of section 4.2 where the kinetics of CO_2 in (Na,TEA)-ZSM-25 will be investigated. The ZLC has been chosen as technique for such a system given the small quantity of adsorbent needed and given its rapidity for adsorbent screening.

The last technique to consider is frequency response (FR). This technique derives kinetic information from the response of a system upon a periodic input

perturbation. FR systems can be designed either in batch or flow mode. In batch FR, the sorbent is placed in a chamber and equilibrated with a known amount of gas at constant pressure and temperature, while small perturbations of the chamber volume are generated[200–202]. The perturbation is usually a sinusoidal wave in time, but also square wave input perturbation can be found in literature[203,204]. The frequency of the perturbation is varied to investigate a broad range of frequencies, so that different time constants can be detected. Naphtali and Polinski[205] initially introduced batch FR to study hydrogen adsorption on nickel catalyst. It became then widely used by Yasuda and co-workers[206–209] who broadened it to study diffusion in zeolites. In the early development stage of FR measurement, isothermal conditions were assumed because of the small volume perturbation, which was usually between 1-2% of the total volume. Sun and co-workers [210,211] investigated the effect of non-isothermal conditions on FR experiments. As a result, they developed the thermal frequency response (TFR) method[201,210], where the adsorbent temperature is monitored. Furthermore, Sun et al.[212] analysed the data presented by Yasuda et al.[209] on the diffusion of paraffins in 5A zeolite and demonstrated that the assumption of isothermality led to an inaccurate description of the mass transfer mechanism of the system. Several studies have then developed further theoretical models for the study of FR experiments including bidispersed sorbents[213], non-isothermal conditions[214], multicomponent mixtures[215,216], non-linear conditions[200,217] and higher order frequencies[200]. The main advantage of TFR measurements is the accurate discrimination between mass and heat transfer time constants. The interest of this chapter is on TFR for the study of air separation with lithium-low-silica X-type zeolite (LiLSX). Air separation using LiLSX is an equilibrium driven process, where the nitrogen is more strongly adsorbed thanks to the interaction between the Li ions and the quadrupole moment of nitrogen. Therefore, the kinetic time constants are very fast and difficult to detect with commercial uptake systems, which are generally designed for equilibrium measurements. Nevertheless, in the design of fast cycle units (cycle time of few seconds), the kinetics of nitrogen in LiLSX can become relevant.

Therefore, it is important to detect with accuracy the diffusion mechanism of air in LiLSX if fast cycle processes have to be designed[184].The main benefit of TFR measurements is the effective decoupling and sensitivity to different time constants at different range of frequencies[201]. Both mass and heat transfer time constants can be detected, which makes this technique particularly attractive for preliminary parameter estimation to design adsorption processes.

It is evident from the brief literature review that the choice of a measurement technique is mainly driven by the information on the system under analysis, if any information is available.

What follows can be divided into two main parts: the study of CO_2 diffusion in (Na,TEA)-ZSM-25 and the study of air separation on LiLSX with the use of TFR. These two particular systems highlight two challenges of macroscopic measurements: the flexibility of an adsorbent material and the detection of kinetics information of fast diffusing systems. The kinetics in flexible materials has gained particular attention given the separation potential of such materials. Air separation with LiLSX falls in the category of very fast diffusing systems, for which conventional transient uptake measurements would be unable to detect any kinetics at conditions relevant for process simulations.

4.2 Diffusion of CO_2 in (Na,TEA)-ZSM-25

The system CO_2–(Na,TEA)-ZSM-25 has been introduced in the previous chapter. This section aims at studying the kinetics of such system relaying on multi-RALF for the modelling of its thermodynamics (see section 3.5).

Results from ZLC experiments at different conditions will be presented with the aim of relating their trends to the physical description of the system given during the equilibrium study: at zero loading only the α site is available for adsorption while the β site is blocked at its windows by the cations. Upon reaching a critical adsorbed phase concentration, the cations are solvated and move, so that the β site becomes available for adsorption.

A brief overview of the experimental apparatus and the experimental procedure are presented in section 4.2.1 and 4.2.2. Then, the models used to fit the experimental data are discussed in section 4.2.3. It should be noted that the experimental work has been carried out by Dr.Verbraeken to which the author would like to express his gratitude for the help.

4.2.1 The Zero-Length-Column apparatus

Detailed description and analysis of a ZLC apparatus can be found in the recent review from Brandani and Mangano[196]. The main features of a ZLC apparatus are presented in Figure 4.1: the feeding lines are connected to mass flow controllers which are linked to either rotary or switching valves. The valves direct the flow to the ZLC placed inside an oven, and the outlet stream of the ZLC is then sent to a detector. As noted in Figure 4.1, a pre-heating coil in the oven allows the feeding gas to be equilibrated at the temperature of the oven.

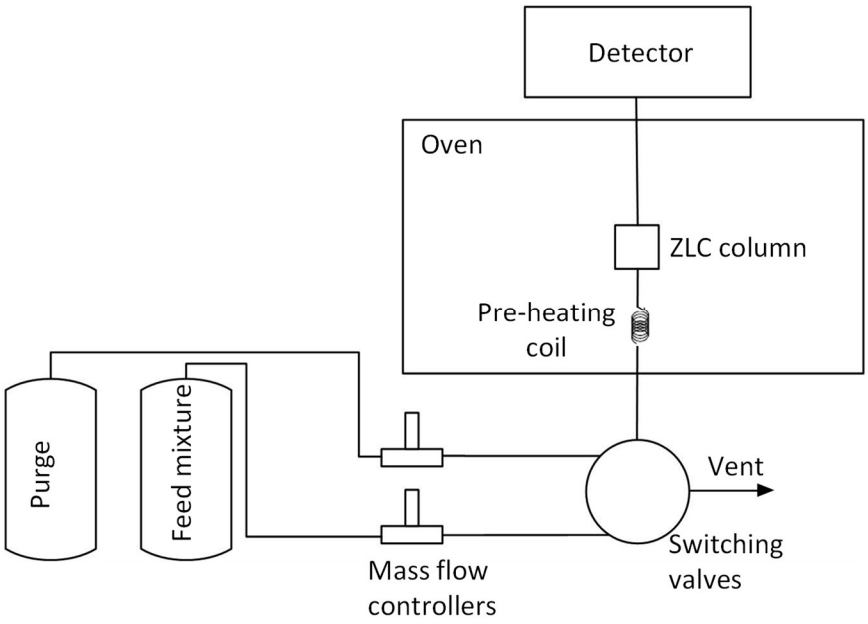

Figure 4.1: Schematic diagram of a ZLC apparatus

The apparatus used for the kinetic study of CO_2 on (Na,TEA)-ZSM-25 consisted of a 1/8” stainless steel union (Swagelok, UK) as column where the powder of adsorbent is placed between two porous metal discs to hold it in place. The column and the pre-heating coil are placed in a Carbolite oven with thermostatic control (Eurotherm). For experiments which require the cooling of

the column, a cooling jacket is used, which is connected to a thermostatic bath (Julabo F-25). The feed lines are controlled with mass flow controllers (Brooks Instrument), which are connected to solenoid valves to direct either the pure helium stream or the CO_2-He mixture in the column. The detector used for this study is a mass spectrometer (Dycor Residual Gas Analyzer, Ametek Process Instruments). The dry mass of adsorbent used for the ZLC experiments is 4 mg.

It should be noted that the apparatus used for this study is also equipped with four vessels of 1 L each used to prepare the CO_2-He mixture mixtures for the experiments. The vessels are placed in a Carbolite oven with thermostatic control (Eurotherm) set at the temperature of the experiment.

4.2.2 Experimental procedure

Before each experiment, the ZLC is regenerated in-situ under vacuum overnight at 473 K. Meanwhile, a mixture of CO_2 and He is prepared at the desired partial pressure of CO_2 for the experiments. This mixture is prepared in advance to make sure that a homogeneous mixing is achieved. Once the mixture is ready and the ZLC is cooled at the temperature of the experiments, either 288 K or 308 K, the mass flow controllers are calibrated with a bubble flow meter. The flow is allowed to vary in a range of 0.9 Nml/min up to 20 Nml/min. The actuation of the solenoid valves which link the dosing lines to the ZLC and the collection of the data from the mass spectrometer are carried out with a LabVIEW interface.

To take into account the extra-column effect, a deconvolution of the raw signal from the mass spectrometer is carried out, as shown in Verbraeken et al.[218]. This procedure enables the isolation of the concentration profile of CO_2 that comes out directly from the ZLC from the total raw signal. In essence, the deconvolution of the mass spectrometer signal considers each component of the ZLC apparatus as a unit having a characteristic transfer function. Assuming linearity, the signal from the mass spectrometer can be seen as sum of the single contributions from the different units of the system.

4.2.3 Model

This section outlines the equations used to fit the experimental data from ZLC experiments, making use of the multi-RALF model presented in the previous chapter as equilibrium model. In addition, a brief introduction of the analytical solution of the isothermal and linear ZLC model originally developed by Brandani and Ruthven[219] is reported. The analytical model will be used for a preliminary fit of the experimental data.

4.2.3.1 Numerical ZLC model with multi-RALF

The assumptions of the model are:

- Isothermal and isobaric conditions;
- The gas phase is ideal;
- The column is saturated with an initial concentration c_0 of CO_2 in inert He;
- The feed consists of pure inert He;
- The diffusion is controlled by the micropores with no surface barrier;
- The adsorbent is (Na,TEA)-ZSM-25 and it is assumed rigid and spherical;

Despite the breathing behaviour of the solid, the model assumes rigid adsorbent because the breathing does not lead to a dramatic change of the solid volume. Hence, the simplifying assumption of assuming it rigid suits the purpose of a simple model to derive kinetic properties from ZLC experiments.

The mass balance on CO_2 in the ZLC is:

$$m_s \frac{d\bar{q}_{CO_2}}{dt} + V_f \frac{dc_{CO_2}}{dt} = -F c_{CO_2} \qquad 4.1$$

where m_s is the mass of solid, $\bar{q}_{CO_2}$ the average amount adsorbed in (Na,TEA)-ZSM-25, V_f the volume of fluid in the ZLC, F the outlet flowrate, and c_{CO_2} the concentration of CO_2 in the fluid.

The outlet flowrate can be calculated from an overall mass balance on the system:

$$F = F_{in} - \frac{m_S}{c_{tot}} \frac{d\bar{q}_{CO_2}}{dt} \tag{4.2}$$

where F_{in} is the inlet flowrate of carrier gas, and c_{tot} is the total concentration of gas in the system.

The differential mass balance on the adsorbent is:

$$\frac{\partial q_{CO_2}}{\partial t} = \frac{1}{r^2} \frac{\partial}{\partial r} (-r^2 J) \tag{4.3}$$

where J is the molar flux, and r is the radial coordinate. The flux can be written as:

$$J = -D\left(q_{CO_2}\right) \Gamma \frac{\partial q_{CO_2}}{\partial r} \tag{4.4}$$

where $D\left(q_{CO_2}\right)$ is the corrected diffusivity, and $\Gamma = \frac{q_{CO_2}}{R_g T} \frac{\partial \mu_{CO_2}}{\partial q_{CO_2}}$ is the Darken correction factor, which can be obtained from the multi-RALF expression of the chemical potential, μ_{CO_2}.

The boundary conditions of the differential mass balance, eq.(4.3), are of zero-flux at the centre of the sphere

$$\left. \frac{dq_{CO_2}}{dr} \right|_{r=0} = 0 \tag{4.5}$$

and equilibrium at the surface:

$$q_{CO_2}\big|_{r=R_p} = q_{RALF}(c_{CO_2}) \tag{4.6}$$

where $q_{RALF}(c_{CO_2})$ is the amount at equilibrium from multi-RALF and R_p is the particle radius. This value can be calculated as presented in the previous chapter.

The average amount adsorbed can be calculated from an overall mass balance on the solid, as shown below:

$$\frac{d\bar{q}_{CO_2}}{dt} = -\frac{3}{R_p} J|_{r=R_p} \qquad 4.7$$

Since the ZLC is fully saturated with a feed of CO_2 and He, the initial condition or the desorption experiment is that $c_{CO_2} = c_0$ and that $q_{CO_2} = q_{RALF}(c_0)$.

The system of equations is solved with the method of lines in MATLAB with the function $ode15s$, where the radial coordinate is discretised using the orthogonal collocation of finite elements method. The equations of multi-RALF for the equilibrium properties are solved together to the differential equations, so that the system consists of a differential-algebraic system (DAE). The initial condition for multi-RALF at time 0 is provided solving multi-RALF for the concentration of CO_2 at which the system is equilibrated. Then, the initial condition at arbitrary time t' will be automatically provided by the previous time step $t' - \Delta t$. This procedure assures a fast convergence of the system to a solution within reasonable tolerances.

It should be noted that multi-RALF could be solved as a sub-routine, which is called when needed. This would reduce the size of the DAE system and reduce it to a system of differential equations only. However, modern DAE solvers, as the routines developed in MATLAB or open-source libraries like SUNDIALS, use sophisticated techniques to interpolate the solution over the time steps taken, so to provide an initial condition for the time integration and a solution technique faster than conventional sub-routines which use root-finding methods. Hence, the solution of the whole DAE model should be preferred to the sub-routine approach.

4.2.3.2 Standard ZLC model

The model so far presented makes use of a non-linear isotherm (the multi-RALF model) to characterise the thermodynamics of the system. Conventional ZLC experiments are generally run in linear regime, or slightly non-linear. In

the following, the analytical solution of a ZLC model in isothermal conditions will be used for a preliminary assessment of the diffusion behaviour of CO_2 in (Na,TEA)-ZSM-25. The analytical model has been developed by Brandani and Ruthven[219] assuming spherical adsorbent, Fickian diffusion, isothermal and linear conditions. The gas phase concentration can be written as:

$$\frac{c(t)}{c_0} = \sum_{n=1}^{\infty} \frac{2L}{\gamma\beta_n^2 + L - 1 + \beta_n^2 + (L - 1 - \gamma\beta_n^2)^2} e^{-\beta_n^2 \frac{D}{R_p^2} t} \qquad 4.8$$

where the parameter L and γ are defined as:

$$L = \frac{F}{3KV_s}\frac{R_p^2}{D}; \quad \text{and} \quad \gamma = \frac{V_f}{3KV_s} \qquad 4.9$$

the parameter L can be seen as the ratio between the diffusion time constant of the system, D/R_p^2, and the wash-out of the solid phase. The parameter γ is the ratio of the accumulation in the fluid and solid phase, where K is the equilibrium constant of the system. The higher the L parameter, the more likely the system will be under kinetic control. Generally, $L > 10$ should be sufficient to ensure kinetic control. However, it is always a good precaution to analyse the data on a case-by-case study. A graphical check to discriminate between equilibrium and controlled ZLC experiments is discussed in the next section.

Finally, β_n are the roots of eq.(4.10).

$$\beta_n cot(\beta_n) - 1 - \gamma\beta_n^2 + L = 0 \qquad 4.10$$

4.2.4 Results and discussion

The results of ZLC experiments at 308 K,100 kPa and 20% CO_2 in He at different flowrates are presented in Figure 4.2. The aim of running experiments at different flowrates is to move from an equilibrium controlled system to a kinetically controlled one. The higher the flowrate, the more the system will approach kinetic control. As it can be seen from Figure 4.2, all the curves show an inflection, which can be linked to the inflection in the isotherms (Figure 3.15) and the moving of the cations from the windows between sites. Conventional

rigid materials typically show an exponential decay as trend, with no inflection. By contrast, this type of signal is generally detected with flexible materials.

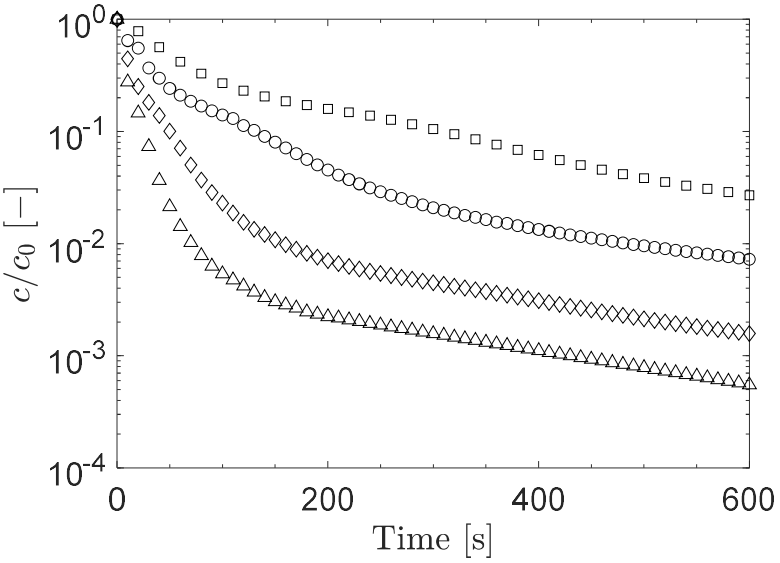

Figure 4.2: Experimental data at 20% CO_2 in He at 308 K and 100 kPa on (Na,TEA)-ZSM-25 at 0.90 Nml/min (squares), 1.77 Nml/min (circles), 4.88 Nml/min (diamonds) and 10.64 Nml/min (triangles).

To study the kinetics of CO_2 in this material, it is crucial to prove that the system is under kinetic control. In order to discriminate between equilibrium and kinetic controlled curves, it is useful to plot the same data as c/c_0 vs. Ft, as done in Figure 4.3. The area under the experimental curve in the so-called "Ft-plot" yields to the uptake capacity at each experimental run. From the different flowrates, the total uptake at 308 K, 100 kPa and 20% CO_2 is $q_{co_2} = 2.82 \pm 0.05\, mol/kg$, which is consistent with the isotherm from volumetric experiments. The Ft-plot is also a quick visual tool to determine if an experimental run is in kinetic control regime[220]. Indeed, all the runs which are under equilibrium control will overlap in an Ft-plot. By contrast, kinetic controlled profiles will present a diverging trend initially, to then intercept each other. The results presented in Figure 4.3 are initially overlapping up to $c/c_0 = 0.15$, and then they start diverging. This behaviour suggests equilibrium control between $c/c_0 = 1$ and $c/c_0 = 0.15$, and then a transition to a kinetically controlled regime at lower gas concentrations. Since the inflection around $c/c_0 = 0.15$ corresponds to $q = 0.6\, mol/kg$, it is reasonable to assume that the

inflection in the isotherms causes the transition in the ZLC regime. Indeed, at 0.6 mol/kg the inflection in the isotherm starts. At this amount adsorbed, the site β starts to become available for adsorption, as discussed in the previous chapter. Hence, when both α and β sites are available, the diffusion of CO_2 in the adsorbent is so fast to lead to equilibrium control. On the contrary, once passed the inflection, the β site starts to become inaccessible, with the cations moving back at the opening between α and β sites, and the system approaches kinetic control, as shown by the divergent curves in Figure 4.3.

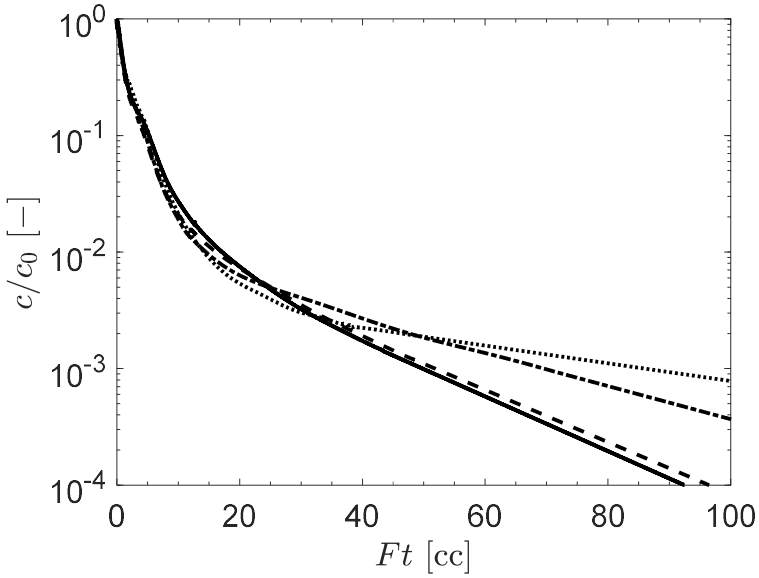

Figure 4.3: Ft-plot for the experimental data at 20% CO_2 in He at 308 K and 100 kPa on (Na,TEA)-ZSM-25. Solid line is 0.90 Nml/min, dashed line is 1.77 Nml/min, dash-dotted line is 4.88 Nml/min, and dotted line is 10.64 Nml/min.

Once it has been confirmed kinetic control at different flowrates, the value of diffusional time constant can be estimated from both the standard ZLC model and the numerical one. Since the diffusion model has to reflect the gate opening of site β at a fixed loading, it would be somehow difficult to start fitting directly the numerical model to the full curves in Figure 4.2. Instead, the equilibrium part of the data can be "cut-out" so that the standard ZLC model can be used to preliminary assess the value of D/R_p^2 for the kinetically controlled part of the experimental data. The results of fitting the standard ZLC model to the cut data is presented in Figure 4.4. It should be noted that the data have been re-normalised to start from $c/c_0 = 1$. This cut and normalisation procedure can be safely applied to remove the equilibrium

controlled region since, for its all duration, the concentration profile of the adsorbate in the adsorbent is completely flat, i.e. at equilibrium with the fluid fugacity.

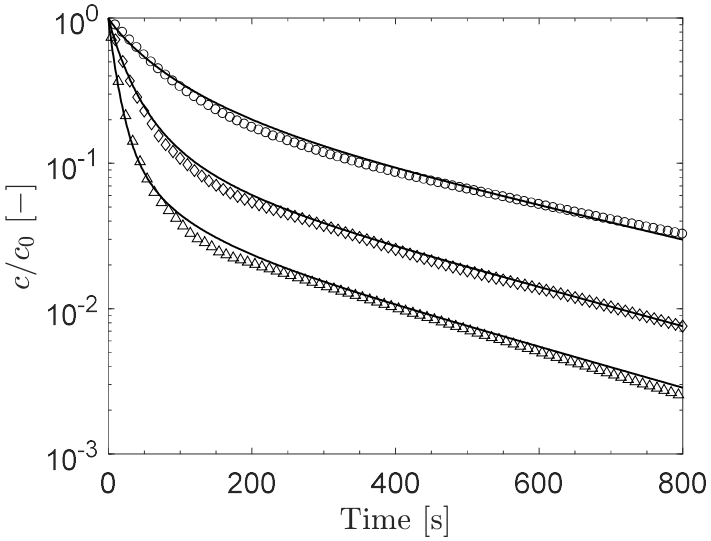

Figure 4.4: Analysis of the "cut" experimental data using the standard ZLC model (see section 4.2.3.2). The diffusional time constant fitted is $\frac{D}{R_p^2} = 3.4 \times 10^{-4} s^{-1}$. Circles are data at 1.77 Nml/min, diamonds at 4.88 Nml/min, and triangles at 10.64 Nml/min. The solid line is the standard ZLC model.

The fitting of the standard ZLC model provides satisfactory results, proving that the diffusion process at low concentrations follows a conventional desorption profile from a ZLC experiment where the system is linear. The fitted parameters are reported in Table 4.1. It should be noted that the L parameters for the three flowrates are not independent from each other: the ratio between two L parameters at two different flowrate is the same as the ratio of the flowrates. Hence, only one L parameter has to be fitted (typically the highest flowrate), and then the other two predicted from it.

Table 4.1: Fitted parameters of the standard ZLC model to the cut and renormalised experimental data for 20% CO_2 in He at 308 K and 100 kPa.

Flowrate (Nml/min)	L [−]	γ [−]	D/R_p^2 [s^{-1}]
1.77	9.5	0.18	3.4×10^{-4}
4.88	26	0.18	3.4×10^{-4}
10.64	57	0.18	3.4×10^{-4}

The value of fitted diffusion time constant at zero loading is much higher than similar Na exchanged Rho zeolites, which exhibit a diffusion time constant of roughly $1 \times 10^{-5} s^{-1}$ in similar conditions[168].

The preliminary results presented suggest that, when both α and β sites are available, the diffusion process is so fast to lead to equilibrium controlled curves. Then, once the adsorbent contracts its lattice due to the low amount adsorbed, the diffusivity decreases to a constant value which can be related to the diffusivity of the system α site – CO_2. It is worth to mention that synchrotron experiments showed that at low CO_2 partial pressures the adsorbent possesses a cubic distorted structure with small lattice parameters. During adsorption, with the cations moving from the cage opening, the framework relaxes to a more regular structure with larger unit cell parameters. Although this modification in the framework structure is small compared to the breathing behaviour of MOF materials such as MIL-53, it can still have a considerable impact on the transport properties of the system CO_2 – (Na,TEA)-ZSM-25.

The model here proposed for the corrected diffusivity of CO_2 in (Na,TEA)-ZSM-25 aims to reflect the physical behaviour explained above: fast diffusion when the structure is fully available, and slow diffusion when the β site is blocked, leading to kinetic control in the ZLC experiments. Using the adsorbed phase concentration as variable upon which the diffusivity depends, the model for the diffusivity of CO_2 in the adsorbent can be written as:

$$D(q_{CO_2})/R_p^2 = D_0/R_p^2 + Ae^{B(\bar{q}-\bar{q}_{trans})} \qquad 4.11$$

where D_0 is the corrected diffusivity of CO_2 at zero loading, $\bar{q}_{trans}$ is the critical adsorbed concentration at which the diffusivity starts increasing, and A and B are fitting parameters. The second term of the right hand side of eq.(4.11) represents a Buckingham-like potential to model the increase of the diffusivity at increasing loading. It can be noted that in eq.(4.11) the value of $\bar{q}_{trans}$ can be fixed *a priori* at 0.6 mol/kg. Indeed, it is known that the adsorbent shows inflection in the isotherm at $\bar{q}_{trans} = 0.6\, mol/kg$, which is the critical adsorbed concentration at which also the β site starts to become available for diffusion.

Moreover, the value of D_0/R_p^2 is fixed by the fitting of the standard ZLC model to the kinetically controlled region of the experimental data (see Figure 4.4). Hence, only A and B remain to be fitted to experimental data.

The fitting of the model in section 4.2.3.1, together with eq.(4.11), yields to a good fit of the experimental data, as presented in Figure 4.5. The lowest flowrate, 0.90 Nml/min, is completely equilibrium controlled. As it can be seen from Figure 4.5, the isotherm from the previous chapter leads to a correct prediction the ZLC curve.

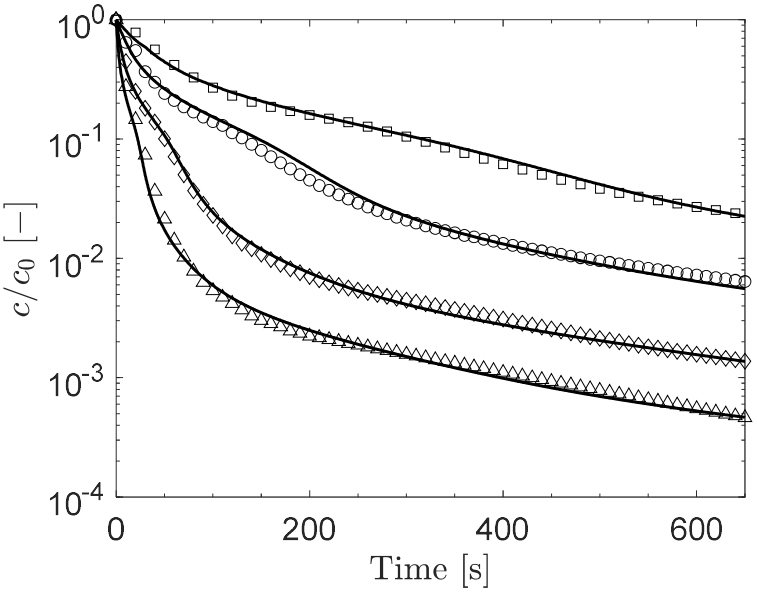

Figure 4.5: ZLC desorption of 20%CO_2 in He at 308 K and 100 kPa on (Na,TEA)-ZSM-25. Symbols are experimental data at 0.90 Nml/min (squares), 1.77 Nml/min (circles), 4.88 Nml/min (diamonds) and 10.64 Nml/min (triangles). Solid line is the ZLC numerical model (see section 4.2.3.1)

The model is able to capture the transition between equilibrium-controlled at high partial pressure of CO_2 and kinetic controlled regime at low partial pressures of CO_2. The fitted values for the free parameters are $A = 3.6 \times 10^{-4}\ s^{-1}$ and $B = 8.3\ [kg/mol]$. The trend of the diffusivity with respect to the adsorbed phase concentration can be seen in Figure 4.6.

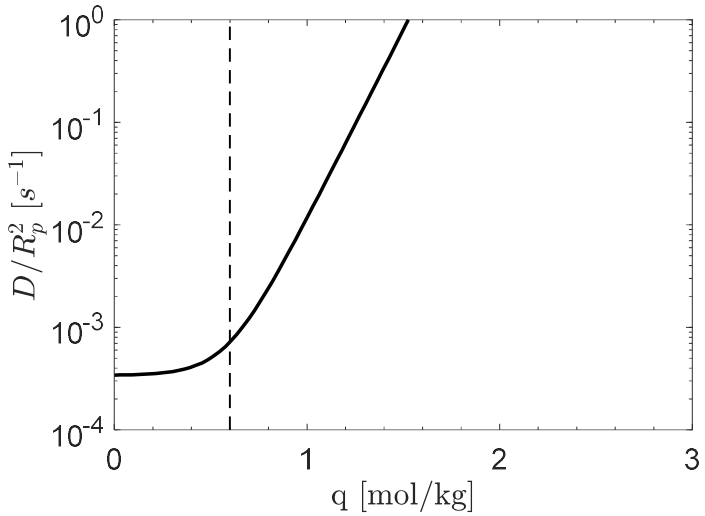

Figure 4.6: Corrected diffusivity vs total amount adsorbed. The dashed line marks $q = 0.6\ mol/kg$, the amount adsorbed at which the β site becomes accessible.

At low adsorbed amounts, the β site is blocked and the diffusivity is constant at $\frac{D}{R_p^2} = 3.4 \times 10^{-4}$, as shown by the standard ZLC model. Once the cations are solvated by the adsorbate, the β site becomes available, the framework relaxes, and the diffusivity starts to increase up to such fast values that the ZLC curves become equilibrium controlled.

At this point, a comment should be made on the proposed model: the model for the diffusivity proposed in eq.(4.11) shows an asymptotic limit at low adsorbed concentration, while diverging upon adsorption. While mathematically the function in eq.(4.11) would exponentially rise to infinity, the adsorbate will eventually reach a saturation loading and the diffusivity will reach a constant value as well. It should be possible, in principle, to detect the upper limit of the diffusivity when both sites are available, by running ZLC experiments at very fast flows. These experiments should reach a value of the flow by which also the full adsorbent becomes kinetically controlled and hence the value of diffusivity for the two sites can be assessed. Nevertheless, the flowrates required would be so high that the limit of detection of the system will be approached. Therefore, our model aims to describe what can be reliably said from the experimental data. For a more thorough investigation of the kinetics of the full adsorbent other experimental data, and possibly another experimental apparatus, would be required.

To validate the fitted parameters at 308 K, a second set of data at 288 K 100 kPa and 10%CO_2 in He has been used. With the knowledge of the adsorption isotherm, and the A, B and $\bar{q}_{trans}$ parameters for the diffusivity, the only fitting parameter left is the limiting diffusion time constant D_0/R_p^2. The results of the fitting at 288 K can be seen in Figure 4.7.

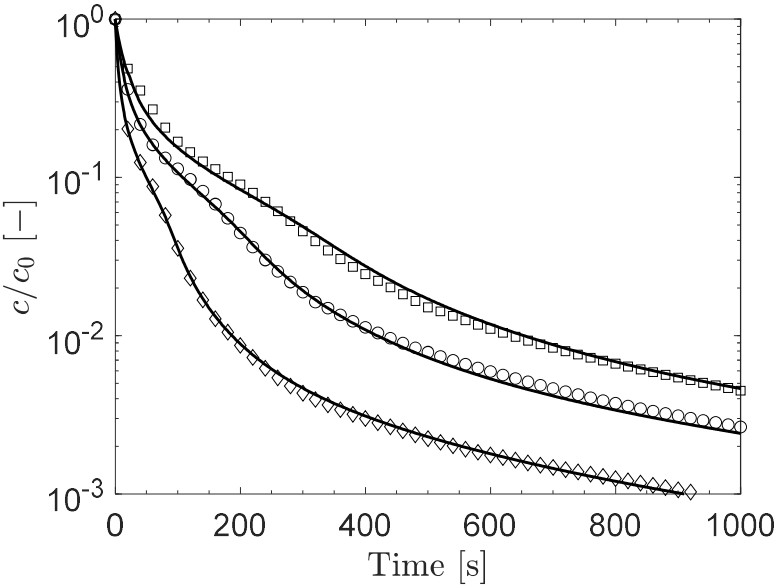

Figure 4.7: ZLC desorption of 10% CO_2 in He at 288 K and 100 kPa on (Na,TEA)-ZSM-25. Symbols are experimental data at 3 Nml/min (squares), 4.68 Nml/min (circles) and 9.82 Nml/min (diamonds). Solid line is ZLC numerical model (see section 4.2.3.1)

The fitted limiting diffusivity is $\frac{D_0}{R_p^2} = 1.8 \times 10^{-4} s^{-1}$. From the two diffusivities at different temperatures an activation energy for diffusion can be estimated to be 24 kJ/mol. Ideally, at least another temperature should be used for a reliable estimate of the activation energy.

The results presented so far tend to confirm that the inflection in the isotherm and the unusual kinetic behaviour are not directly correlated between them and strongly dependent on the cations movement between the cages. It is interesting to note that ZSM-25 zeolite fully exchanged with other ions, i.e. Li^+ and K^+, does not present inflection in the isotherm. Min et al.[170] presented similar results, with the conclusion that the only ions presenting an inflection in the isotherm are Na^+ and Cs^+. This leads to the conclusion that the inflection in the isotherm and the unusual kinetics is caused by a delicate balance between ion exchanged zeolites and size of the ion.

4.3 Thermal frequency response

This second part of the chapter deals with the study of air separation with LiLSX using TFR technique. LiLSX is one of the most commonly used adsorbents for the on-site production of oxygen[184,221,222], which is crucial to many applications, e.g. cutting operations for the metal industry, mining industry, wastewater treatment.

Commercial vacuum swing adsorption (VSA) processes are employed to produce oxygen with a purity higher than 95% from an air feed[222]. The separation is driven by the preferential adsorption of nitrogen over oxygen. The Li ions have high affinity to the strong quadrupole moment of the nitrogen, which leads to higher nitrogen adsorption, yielding high N_2/O_2 selectivity.

VSA separation of N_2 from air is equilibrium driven, but accurate mass transfer kinetics data remain crucial for the design of the separation unit. Although the air separation on LiLSX is driven by the thermodynamic selectivity of the adsorbent towards nitrogen, the design of fast cycle separation units will be affected by the kinetics of the system, e.g. the design of a medical oxygen concentrator[221], as well.

Numerous studies have investigated the thermodynamics of nitrogen and oxygen on LiLSX[185,223–225], but few analyse the kinetics of this system. Bülow and Shen[226,227] analysed the kinetics of nitrogen, oxygen and argon on beads of LiLSX containing rare earth metals. Bülow and Shen concluded that the system is macropore diffusion controlled, and provided further information on the activation energies for the diffusivity. Wu et al.[228] analysed breakthrough experiments of pure nitrogen and oxygen on pelletised LiLSX with the use of an isothermal-isobaric model. They concluded that nitrogen mass transfer is mainly controlled by skin resistance at the surface of the pellet. In addition, Todd and Webley[229,230] carried out experimental studies of N_2 on pelletised LiLSX. Todd and Webley[229,230] made use of two techniques, volumetric and breakthrough experiments, analysing the results with the dusty gas model, assuming macropore diffusion control. Todd and Webley[229,230] reported two

different values of tortuosity for each transport mechanism, namely Knudsen diffusion, 3.7, and viscous flow, 5.1[229]. Volumetric experiments have also been carried out by Brandani et al.[184] for the N_2-LiLSX system. Brandani et al.[184] assumed macropore diffusion control, and derived a tortuosity of 3.13. Ju et al.[231] also made use of a volumetric system to characterise equilibrium and kinetics of several gases on pelletised LiLSX. By changing the size of the pellet Ju et al.[231] proved the system to be macropore diffusion controlled, in contrast to the findings of Wu et al.[228], that reported skin resistance. Similarities between the works cited are the fast kinetics of nitrogen in LiLSX and the significant heat effects.

Heat effects are considered in the models of Ju et al.[231] and Todd and Webley[229,230], while Brandani et al.[184] assume an isothermal case. This assumption is justified by Brandani et al.[184] as the sample is mixed with stainless steel beads to avoid temperature changes during the experiment. Moreover, Brandani et al.[184] verified this assumption by carrying out experiments with different masses of adsorbent, which is a check sometimes neglected by other studies that assume isothermal conditions.

Since the diffusion of N_2 in LiLSX is a fast diffusing system, the analysis of kinetic data from commercial volumetric/gravimetric systems might lead to inaccuracies. Commercial systems are designed for equilibrium measurements and can be used only to study slow diffusing systems for which their acquisition rate and valve dynamics are not the controlling mechanism. Chromatographic experiments might be employed to study nitrogen diffusion in LiLSX. However, given the relatively high heat of adsorption, heat effects will have to be included in the analysis.

TFR represents a valuable and flexible technique to study fast diffusive systems like nitrogen on LiLSX. TFR systems allow the measurement of kinetics as well as heat transfer characteristics, given their different time constants.

In the following, the dual piston pressure swing adsorption (DP-PSA) system[232–234] is presented, and its use for TFR measurements is discussed. The DP-PSA was originally designed to assess the performance of an adsorbent under realistic process conditions of rapid cycling and flow reversal for a variety of experimental conditions. Here the DP-PSA is used for the first time as a frequency response apparatus for the characterisation of very fast mass and heat transfer parameters. Moreover, newly derived models for single and multicomponent experiment analysis are presented in the limit of macropore diffusion control. Main aim of this work is to study the air separation on commercial LiLSX beads in ranges of pressure and temperature relevant to industrial applications. This choice aims at proving that TFR can be used as a characterisation technique at conditions where commercial systems (volumetric and gravimetric ones) might struggle to provide meaningful data. Indeed, for time constants up to few seconds, volumetric and gravimetric system will not provide reliable data to be analysed. Indeed, the blank response time constant of this system is usually in the same order of magnitude, which would pose a serious obstacle to the decoupling of blank and system responses.

The experimental part of this work has been performed in collaboration with Dr.Olkis and the MSc student Miss.Holtermann.

4.3.1 The Dual Piston Pressure Swing Adsorption (DP-PSA) apparatus

The DP-PSA consists of a column connected to two pistons which can cyclically move at frequencies up to 2 Hz. A picture of the system is reported in Figure 4.8.

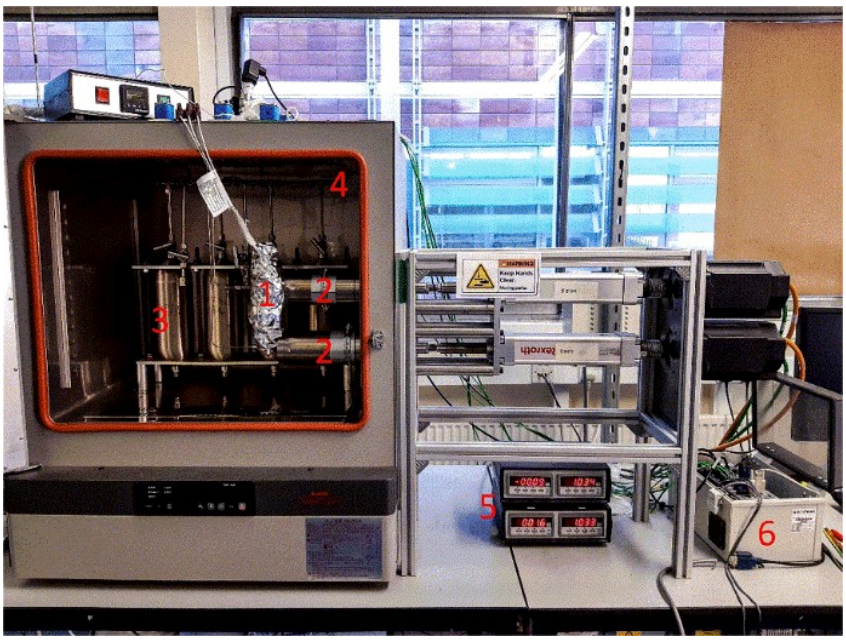

Figure 4.8: The DP-PSA apparatus: 1) Column, 2) Piston, 3) Gas dosing cylinder, 4) Oven, 5) Pressure display, 6) acquisition and control system.

The schematic diagram of the system is reported in Figure 4.9. A detailed description of the system can be found in the work of Dang et al.[232]. In the following, an overview of the system is presented. The main change to the experimental set-up compared to the work of Dang et al.[232] is the use of thinner thermocouples, with a much shorter delay time constant, and use of vacuum coupling radiation (VCR) fittings for an effective vacuum seal of the column. The details are provided below.

The apparatus consists of two main parts: a dosing side and the column side. The two sides are connected by valve V8. During the dosing of the gas in the adsorption column (AC in Figure 4.9) V8 is open. During the experiments V8 is closed, such that the column side acts as a closed system.

The pistons, the column, and the dosing cylinders are mounted in a Sanyo MOV-112 oven, which can reach 533 K, to ensure that the parts of the system are all at the same temperature.

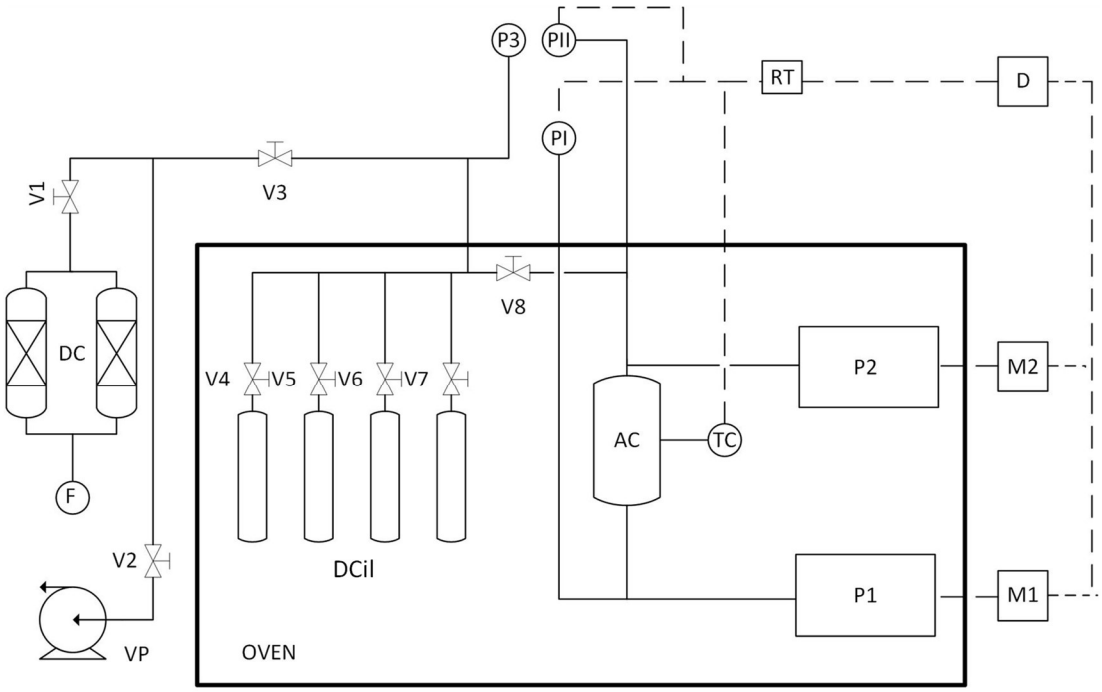

F – Feed line
V – Valve
VP – Vacuum pump
DC – Drying columns
PI – Pressure drop column
PII – Pressure top of the column
P3 – Pressure feed side
DCil – Dosing cylinders
AC – Adsorption colum
P1 – Piston 1
P2 – Piston 2
M1 – Motor and gear box 1
M2 – Motor and gear box 2
RT – Real time computer
D – Driver
Solid line – Gas lines
Dashed line – Electrical lines

Figure 4.9: Schematic diagram of the DP-PSA apparatus.

4.3.1.1 The dosing system

The dosing system consists of drying columns (DC in Figure 4.9) connected to main gas lines of N_2, CO_2, and He (F in Figure 4.9). An additional line is connected to a cylinder of dry air. The DCs are connected via valve V3 to 4 dosing cylinders of 1 L each, where mixtures can be prepared prior to experiments. For single component experiments, the gas is directly fed from the DCs to the adsorbing column via valve V1-V3-V8, closing the dosing cylinders with their respective valves (from V4 to V7). A vacuum pump is connected to the dosing system via valve V2 in order to evacuate the system both during experiments and during regeneration of the system. To measure the amount of gas dosed into the column side, a Druck PDCR 5010 pressure

transducer is mounted (P3 in Figure 4.9) with a working range of 0-350 kPa and accuracy of 0.35 kPa.

4.3.1.2 The piston assembly

The AC is directly connected to the pistons (P1 and P2 in Figure 4.9) which are moved by motors through a linear motion gearbox (Bosch Rexroth AG, R156030000). The motors are controlled through a compact RIO 9022 real-time computer from National Instrument (RT in Figure 4.9) connected to ACSM1 drives from ABB (D in Figure 4.9). Their movement is independent, hence, the two pistons can be moved both in- and out-of-phase. The ABB drives are interfaced with a LabVIEW code with which the user can set up the cycle time, the starting and ending position of the pistons, the starting phase angle of the pistons and the total experiment time. The sealing of the pistons is designed such that the working pressure can span from 0.1 kPa up to 2000 kPa, and up to 533 K.

4.3.1.3 The adsorption column

The AC is placed between the pistons. The AC's dimensions can be tuned to accommodate different sample masses, or to generate the desired compression ratio during experiments. Pictures of the column used in this work can be seen in Figure 4.10, where also the dimensions are reported.

The AC column used in this work consists of VCR fittings with copper seals (Swagelok, UK) and inside it is equipped with four 0.25 mm type K thermocouples (TC, UK). The thermocouples are inserted in 1/16 in. pipes welded at the base of the column, and an epoxy resin is used to achieve a complete seal at the bottom of the AC. On top of each thermocouple an adsorbent bead is mounted. Hence, the thermocouple will read the temperature at which the solid is at each time. Only the thermocouple T1 (see Figure 4.10) is left without adsorbent bead to monitor the temperature of the column. The absolute pressure is monitored with a Druck PDCR 4701 pressure transducer (PII in Figure 4.9), with a working range of 0-350 kPa and accuracy of 0.1 kPa. A Druck PDCR 4701 differential pressure transducer is

also connected to the column (PI in Figure 4.9) with a working range between -50 kPa to 50 kPa and a precision of 0.02 kPa.

The pressure transducers and the thermocouples are connected to the Compact RIO 9022 which records the data. The piston position is also monitored during the experiments.

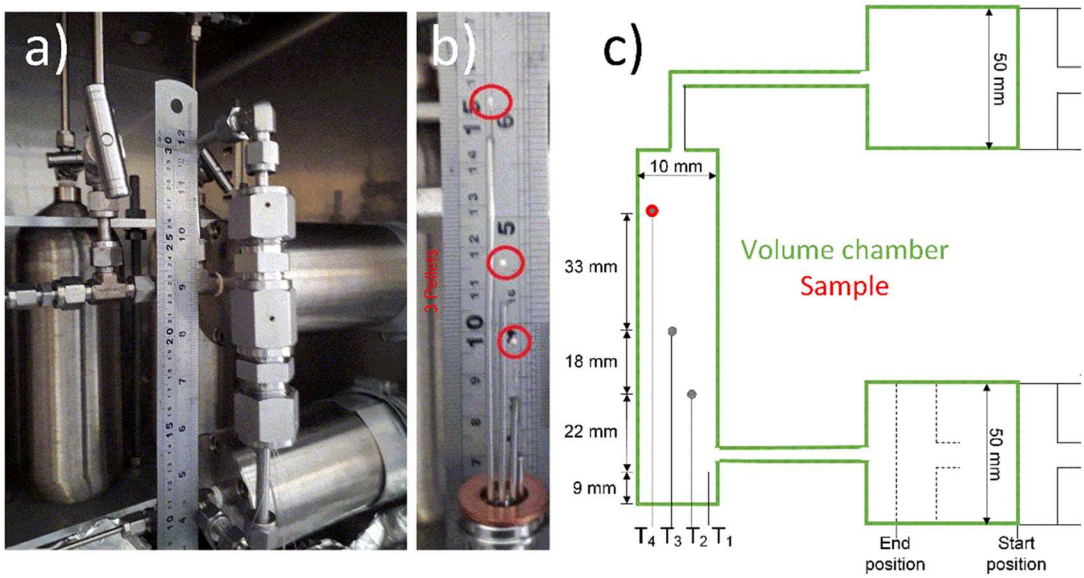

Figure 4.10: a) Assembled column from commercial VCR fittings, b) Thermocouple support for the adsorbent beads, c) Schematic diagram of the column and the pistons

4.3.2 Experimental procedure

The adsorbent used is a commercial type of LiLSX beads (Zeochem), with a binder content between 10% and 18%. The 3 beads chosen to be mounted on the thermocouples had an average diameter of 1 mm, measured with a Spi 15-997-0 digital calliper, with a resolution of 0.01 mm and an accuracy of 0.02 mm. The characterisation of the adsorbent is presented in Brandani et al.[184] which used mercury porosimetry to derive the pore size distribution, the solid density, average pore radius and pellet porosity. A summary of their results will be presented in section 4.3.4.

To characterise the equilibrium properties of nitrogen on LiLSX, four equilibrium isotherms at 258 K, 278 K, 293 K, and 303 K have been measured using a Quantachrome Autosorb iQ-2™. The equilibrium isotherms are needed in order to regress the equilibrium parameters that will be used in the

mathematical model later presented in section 4.3.3 to fit the TFR experiments. Prior to the equilibrium measurements, the sample is regenerated at 663 K for 10 hours under vacuum. The dry sample mass used during the experiments was of 91.8 mg.

For the TFR experiments, at the start of each experiment the column is firstly regenerated. The regeneration procedure consists of constant heating with heating tape of the adsorption column at 2 K/min from room temperature up to 383 K. Next, the column is left at 383 K for 2 hours. After the 2 hours, the heating of the column starts again at a heating rate of 2 K/min up to 673 K, temperature at which is left overnight. Then, the heating tape is turned off and the column is allowed to cool at the temperature of the experiments. The whole regeneration procedure is carried out under vacuum.

After regeneration, blank experiments with He (BOC, CP grade, 99.999% purity) are run in order to assess the blank response of the system and the eventual time-lag introduced by the thermocouples inserted in the beads of solid. Next, single component experiments with nitrogen (BOC, 99.998% purity) are run at different conditions to measure mass and heat transfer properties. Finally, experiments with dry air (BOC, Industrial Grade, 21%±0.5% oxygen, balance nitrogen) are run to assess the separation performance of the adsorbent. The experimental conditions analysed are given in Table 4.2.

Table 4.2: Experimental conditions for blank, single and multicomponent experiments

	Unit	***He***	***N_2***	***Air***
Cycle time	$[s]$	1-15	1-64	1-64
Temperature	$[K]$	303, 328	303, 328	300
Pressure	$[kPa]$	25, 50, 100	50, 75, 100	90
Stroke amplitude	$[mm]$	±10	±2, ±3,±4, ±5	±5

For blank and nitrogen experiments, only one piston is moved with the second remaining static. For the binary both pistons were allowed to move in-phase.

It will be shown in the following that both approaches are suitable for TFR experiments with the DP-PSA. The average volume for blank and nitrogen experiments is $V_0 = 1.05 \times 10^{-4}\ m^3$, while for the air experiments the average volume is reduced to $V_0 = 8.4 \times 10^{-5} m^3$, in order to increase the temperature swing.

Each experiment is run until cyclic steady state (CSS) is achieved. Hence, the total time of each experiment is adjusted with the LabVIEW interface. Once each experiment is over, the raw data are visually checked to make sure the CSS is clearly visible, and the next experiment is run.

The raw data from each experiment are processed using fast Fourier transform (FFT) to extract amplitude and phase lag of the signal, as shown in Figure 4.11.

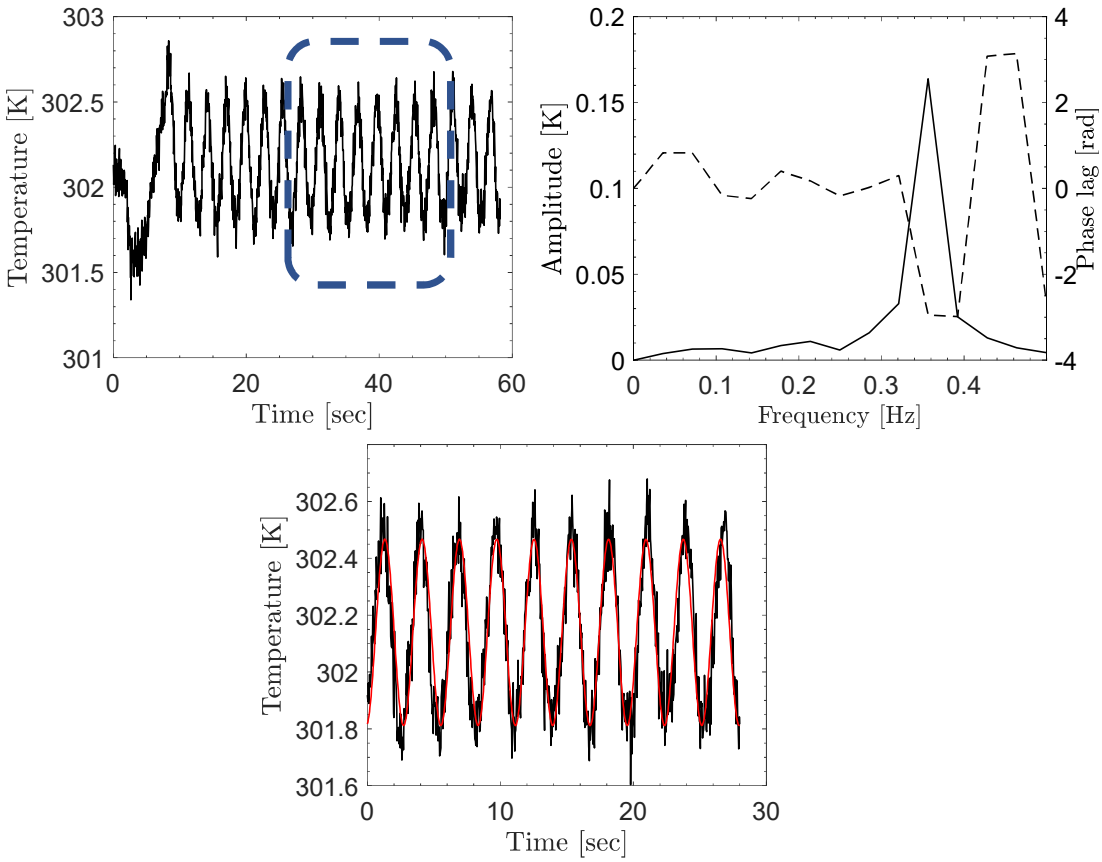

Figure 4.11: FFT analysis used to extract amplitude and phase lag. The top left plot shows the raw data from thermocouple 4 from which the CSS is identified with the blue dashed-lined box. The top right plot shows the FFT analysis carried out on the CSS raw data, and the bottom plot presents the fitting from FFT. The data plotted refer to He experiment at 303 K, 100 kPa and cycle time of 3s.

Firstly, the CSS is identified, so that the raw data can be cut and analysed. The fft function of MATLAB is used to produce the top right plot in Figure 4.11 from which the amplitude and phase lag at the fixed frequency of the experiment can be extracted. Finally, the amplitude and phase lag from the FFT analysis are used to plot the predicted temperature against the raw data to make sure the fit is correct.

For the temperature, the thermocouple T4 always showed the highest amplitude for all the experiments. This can be explained by the complete isolation of the adsorbent on thermocouple T4 from the 1/16" metal guides where the thermocouples are inserted (see Figure 4.10(b)). Hence, the temperature from T4 is chosen as signal to analyse for all the experiments.

4.3.3 Model for single component system

The model for the single component TFR experiments consists of mass and energy balances on both the volume chamber and the solid. The assumptions are:

- The gas is ideal;
- Diffusion in the solid is macropore controlled;
- Conduction in the solid is sufficiently fast to assume a uniform temperature distribution inside the adsorbent;
- The temperature of the wall of the column is constant at T_0;
- The specific internal energy change of the gas in the macropores is negligible;
- The change of the specific internal energy of the adsorbed phase is embodied in an effective thermal capacity of the solid;
- The thermocouple delay response is considered and assumed independent of the gas;
- The pressure drops in the system are neglected;

The overall mass balance can be written as sum of the moles in the volume chamber, the moles adsorbed, and the moles of gas in the macropores:

$$V_0 \frac{dc_g}{dt} + c_0 \frac{dV_g}{dt} + V_s \epsilon_p \frac{d\bar{c_p}}{dt} + V_s(1-\epsilon_p)\rho_s \frac{d\bar{q}}{dt} = 0 \qquad 4.12$$

where c_g is the concentration of the gas in the column, $\bar{c_p}$ the average concentration in the macropores, $\bar{q}$ the average adsorbed concentration, V_0 the volume of the column, c_0 the average concentration of gas in the column, V_s the total volume of the solid, V_g the column volume, ϵ_p the porosity of the adsorbent bead and ρ_s the density of the solid including the micropores.

The mass balance on the adsorbent is:

$$\epsilon_p \frac{\partial c_p}{\partial t} + (1-\epsilon_p)\rho_s \frac{\partial q}{\partial t} = \frac{\frac{\epsilon_p}{\tau} D_p}{r^2} \frac{\partial}{\partial r}\left(r^2 \frac{\partial c_p}{\partial r}\right) \qquad 4.13$$

where c_p is the gas concentration in the macropores, q the amount adsorbed, D_p is the macropores diffusivity, τ the tortuosity, and r the radial coordinate in the bead. The initial condition for c_p and q is equal to their average value at a given pressure and temperature, c_0 and q_0 respectively.

The boundary conditions for eq.(4.13) are:

$$\left.\frac{\partial c_p}{\partial r}\right|_{r=0} = 0$$
$$\left. c_p \right|_{r=R_P} = c_g \qquad 4.14$$

where R_p is the radius of the bead. The average gas phase concentration in the macropores can be calculated from eq.(4.15).

$$\bar{c_p} = \frac{3}{R_P^3} \int_0^{R_p} c_p r^2 dr \qquad 4.15$$

Similarly, the average amount adsorbed is:

$$\bar{q} = \frac{3}{R_P^3} \int_0^{R_p} q r^2 dr \qquad 4.16$$

where the amount adsorbed at each point in the adsorbent can be calculated from a dual site Langmuir isotherm of the form:

$$q = \frac{q_{s1}\, b_{10} e^{-\frac{\Delta H_1}{R_g}\left(\frac{1}{T}-\frac{1}{T_{ref}}\right)} P}{1 + q_{s1}\, b_{10} e^{-\frac{\Delta H_1}{R_g}\left(\frac{1}{T}-\frac{1}{T_{ref}}\right)} P} + \frac{q_{s2}\, b_{20} e^{-\frac{\Delta H_2}{R_g}\left(\frac{1}{T}-\frac{1}{T_{ref}}\right)} P}{1 + q_{s2}\, b_{20} e^{-\frac{\Delta H_2}{R_g}\left(\frac{1}{T}-\frac{1}{T_{ref}}\right)} P} \qquad 4.17$$

Where q_{s1} and q_{s2} are the saturation capacities, b_{10} and b_{20} the pre-exponential factors, ΔH_1 and ΔH_2 is the heats of adsorption and T_{ref} the reference temperature.

While eq.(4.17) is used to fit the isotherm data for nitrogen adsorption on LiLSX, a linearised form of the isotherm can be used to analytically solve the model for the TFR experiments. The linear isotherm can be written as:

$$(q - q_0) = K_c\,(c_p - c_0) + K_T(T_s - T_0) \qquad 4.18$$

where T_s the temperature of the solid, T_0 the average temperature of the system, and K_c and K_T are the derivative of the isotherm with respect to concentration and temperature at given $c_0 = \frac{P_0}{R_g T_0}$ and T_0.

The values of the derivatives can be written as:

$$K_c = K_P R_g T_0$$

$$K_T = \frac{\Delta H_{(T,P)}}{R_g T_0^2} c_0 K_c \qquad 4.19$$

where K_p is the derivative of the isotherm with respect to the pressure. The heat of adsorption at a given temperature and pressure is calculated by eq.(4.20).

$$\Delta H_{(T,P)} = \frac{\Delta H_1 q_{s1} b_{1(T)}\left(1 + b_{2(T)}P\right)^2 + \Delta H_2 q_{s2} b_{2(T)}\left(1 + b_{1(T)}P\right)^2}{q_{s1} b_{1(T)}\left(1 + b_{2(T)}P\right)^2 + q_{s2} b_{2(T)}\left(1 + b_{1(T)}P\right)^2} \qquad 4.20$$

where $b_{1(T)} = b_{10}e^{-\frac{\Delta H_1}{R_g}\left(\frac{1}{T}-\frac{1}{T_{ref}}\right)}$ and $b_{2(T)} = b_{20}e^{-\frac{\Delta H_2}{R_g}\left(\frac{1}{T}-\frac{1}{T_{ref}}\right)}$. In what follows $\Delta H = \Delta H_{(T_0,P_0)}$.

For the energy balance on the column, we need to account for the internal energy accumulation in the gas phase, U_g, the heat exchange between gas and walls, gas and solid, and the work of compression, as shown in eq.(4.21):

$$\frac{dU_g}{dt} + P_0\frac{dV_g}{dt} + h_{gs}A_s\left(T_g - T_s\right) + h_wA_w\left(T_g - T_0\right) = 0 \qquad 4.21$$

where P_0 is the average pressure in the column, h_{gs} the heat transfer coefficient between adsorbent and gas in the column, A_s the surface area of the solid, T_g the temperature of the gas in the column, h_w the heat transfer coefficient between gas in the column and wall, and A_w the surface area of the wall.

The internal energy can be written as:

$$\frac{dU_g}{dt} = n_g\frac{du_g}{dt} + u_g\frac{dn_g}{dt} \approx V_gc_gc_{Vg}\frac{dT_g}{dt} \approx V_0c_0c_{Vg}\frac{dT_g}{dt} \qquad 4.22$$

where u_g is the specific molar internal energy of the gas in the column, n_g the moles of gas in the column and c_{Vg} the heat capacity of the gas at constant volume. From eq.(4.22) the term $u_g\frac{dn_g}{dt}$ has been neglected since its contribution is small compared to $n_g\frac{du_g}{dt}$. Including eq.(4.22) in the energy balance in eq.(4.21), the simplified energy balance in eq.(4.23) can be obtained.

$$V_0c_0c_{Vg}\frac{dT_g}{dt} + P_0\frac{dV_g}{dt} + h_{gs}A_s\left(T_g - T_s\right) + h_wA_w\left(T_g - T_0\right) = 0 \qquad 4.23$$

For the adsorbent, the energy balance has to take into account the accumulation of internal energy of the solid, U_s, the heat exchange with the gas in the column, and the enthalpic flux coming from the gas in the column:

$$\frac{dU_s}{dt} + h_g \frac{dn_g}{dt} - h_{gs} A_s (T_g - T_s) = 0 \qquad 4.24$$

where h_g is the specific molar enthalpy of the gas in the column. The term $\frac{dU_s}{dt}$ can be written as:

$$\begin{aligned} \frac{dU_s}{dt} &= m_s c_{p,s} \frac{dT_s}{dt} + u_{Sg} \frac{d\bar{n}_p}{dt} + u_A \frac{d\bar{n}_A}{dt} \\ &= m_s c_{p,s} \frac{dT_s}{dt} + \left(h_{Sg} - R_g T_s\right) \frac{d\bar{n}_p}{dt} + (h_{Sg} + \Delta H) \frac{d\bar{n}_A}{dt} \\ &\approx m_s c_s \frac{dT_s}{dt} + (h_{Sg} - R_g T_0) \frac{d\bar{n}_p}{dt} + (h_{Sg} + \Delta H) \frac{d\bar{n}_A}{dt} \end{aligned} \qquad 4.25$$

where m_s is the mass of the solid, $c_{p,s}$ the heat capacity of the solid, u_{Sg} the specific molar internal energy of the gas in the macropores, u_A the specific molar internal energy of the adsorbed phase, and h_{Sg} the specific molar enthalpy of the gas in the macropores, $\bar{n}_p$ the average moles of gas in the macropores and $\bar{n}_A$ the average moles adsorbed.

Combining eq.(4.12),(4.24) and (4.25):

$$m_s c_{p,s} \frac{dT_S}{dt} + \Delta H V_s \left(1 - \epsilon_p\right) \rho_s \frac{d\bar{q}}{dt} - h_{gs} A_s \left(T_g - T_s\right) - R_g T_0 V_s \epsilon_p \frac{d\bar{c_p}}{dt} = 0 \qquad 4.26$$

where it has been assumed that $h_{Sg} \approx h_g$ given that the temperature fluctuations are very small during TFR experiments.

The initial condition for the mass and energy variables assume that each variable X is at equilibrium with the initial pressure P_0 and temperature T_0, hence $X = X_0$.

The linearised set of equations (LSE), eq.(4.12-4.16,4.18,4.23,4.26), can be rewritten in terms of dimensionless deviation variables. A dimensionless deviation variable can be defined as $\Delta X = \frac{X - X_0}{X_0}$ where X is an arbitrary variable. The initial condition for each dimensionless deviation variable will be $\Delta X_{(t=0)} = 0$. The dimensionless LSE is:

$$\delta_1 \frac{d\Delta\bar{c_p}}{dt} + \delta_2 \frac{d\Delta\bar{q}}{dt} + \frac{d\Delta c_g}{dt} + \frac{d\Delta V_g}{dt} = 0 \quad 4.27$$

$$\epsilon_p \frac{\partial \Delta c_p}{\partial t} + \frac{(1-\epsilon_p)\rho_s\, q_0}{c_0} \frac{\partial \Delta q}{\partial t} = \frac{\tau_D^{-1}}{\xi^2} \frac{\partial}{\partial \xi}\left(\xi^2 \frac{\partial \Delta c_p}{\partial \xi}\right) \quad 4.28$$

$$\frac{\partial \Delta c_p}{\partial \xi}\Big|_{\xi=0} = 0 \; ; \Delta c_p\big|_{\xi=1} = \Delta c_g \quad 4.29$$

$$\Delta\bar{c_p} = 3\int_0^1 \Delta c_p \xi^2 d\xi \quad 4.30$$

$$\Delta\bar{q} = 3\int_0^1 \Delta q \xi^2 d\xi \quad 4.31$$

$$\Delta q = \gamma_C \Delta c_p - \gamma_T \Delta T_s \quad 4.32$$

$$\frac{d\Delta T_g}{dt} + \frac{R_g}{c_{Vg}} \frac{d\Delta V_g}{dt} + \alpha\beta_s\left(\Delta T_g - \Delta T_s\right) + \alpha_w \Delta T_g = 0 \quad 4.33$$

$$\frac{d\Delta T_S}{dt} + \beta_{\Delta H} \frac{d\Delta\bar{q}}{dt} - \beta_s\left(\Delta T_g - \Delta T_s\right) - \frac{R_g T_0 \epsilon_p}{(1-\epsilon_p)\rho_s c_{p,s}} \frac{d\Delta\bar{c_p}}{dt} = 0 \quad 4.34$$

where $\xi = r/R_p$. The dimensionless parameters appearing in the dimensionless LSE are reported in eq.(4.35), which are fixed by the system,:

$$\delta_1 = \frac{V_s\epsilon_p}{V_0};\ \delta_2 = \frac{V_s(1-\epsilon_p)\rho_s q_0}{V_0 c_0};\ \gamma_C = \frac{K_c c_0}{q_0};\ \gamma_T = \frac{K_T T_0}{q_0};$$
$$\alpha = \frac{\rho_s(1-\epsilon_p)c_{p,s}}{V_0 c_0 c_{Vg}};\ \beta_{\Delta H} = \frac{\Delta H q_0}{c_{p,s} T_0}; \quad 4.35$$

and the parameters in eq.(4.36) are the ones which are fitted to the experimental data.

$$\alpha_w = \frac{h_w a_w}{c_0 c_{Vg}};\ \tau_D = \frac{R_p^2}{\frac{\epsilon_p}{\tau} D_p};\ \beta_s = \frac{h_{gs} a_s}{\rho_s(1-\epsilon_p)c_{p,s}} \quad 4.36$$

The set of equations eq.(4.27-4.34) is transposed in the Laplace domain, where each equation is then divided by ΔV to obtain a new set of equations where the variables are the transfer functions with respect to the volume

perturbation. The transfer function is defined as $G_{\Delta X} = \frac{\Delta \tilde{X}}{\Delta \tilde{V}}$, where the tilde indicates the variables in the Laplace domain. Hence, the new set of equations is:

$$\delta_1 G_{\Delta \overline{c_p}} + \delta_2 G_{\Delta \bar{q}} + G_{\Delta c_g} = -1 \qquad 4.37$$

$$\epsilon_p s G_{\Delta c_p} + \frac{(1-\epsilon_p)\rho_s q_0}{c_0} s G_{\Delta q} = \frac{\tau_D^{-1}}{\xi^2} \frac{\partial}{\partial \xi}\left(\xi^2 \frac{\partial G_{\Delta c_p}}{\partial \xi}\right) \qquad 4.38$$

$$\left.\frac{\partial G_{\Delta c_p}}{\partial \xi}\right|_{\xi=0} = 0 \; ; \; \left. G_{\Delta c_p}\right|_{\xi=1} = G_{\Delta c_g} \qquad 4.39$$

$$G_{\Delta \overline{c_p}} = 3\int_0^1 G_{\Delta c_p} \xi^2 d\xi \qquad 4.40$$

$$G_{\Delta \bar{q}} = 3\int_0^1 G_{\Delta q} \xi^2 d\xi \qquad 4.41$$

$$G_{\Delta q} = \gamma_C G_{\Delta c_p} - \gamma_T G_{\Delta T_s} \qquad 4.42$$

$$(s + \alpha_w + \alpha\beta_S) G_{\Delta T_g} - \alpha\beta_s G_{\Delta T_s} = -\frac{R_g}{c_{Vg}} s \qquad 4.43$$

$$-\beta_s G_{\Delta T_g} + (s + \beta_s) G_{\Delta T_s} - \frac{R_g T_0 \epsilon_p}{(1-\epsilon_p)\rho_s c_{p,s}} s G_{\Delta \overline{c_p}} + s\beta_{\Delta H} G_{\Delta \bar{q}} = 0 \qquad 4.44$$

The variable s is the Laplace variable, which is equal to $s = 2\pi i\omega$ at CSS, with ω being the frequency of the experiment. The mass balance in eq.(4.38), together with its boundary conditions in eq.(4.39) can be analytically solved. The solution is:

$$G_{\Delta c_p} = \left(G_{\Delta c_g} + \frac{\theta}{\chi} G_{\Delta T_s}\right) \frac{1}{\xi} \frac{sinh(\sqrt{\chi}\xi)}{sinh(\sqrt{\chi})} - \frac{\theta}{\chi} G_{\Delta T_s} \qquad 4.45$$

where $\theta = (1-\epsilon_p) s\rho_s \frac{q_0}{c_0} \gamma_T \tau_D$ and $\chi = \left(\epsilon_p s + (1-\epsilon_p) s\rho_s \frac{q_0}{c_0} \gamma_C\right) \tau_D$.

The average gas phase concentration in eq.(4.40) can be now computed:

$$G_{\Delta\overline{c_p}} = 3\frac{\theta}{\chi}\left(\frac{cosh(\sqrt{\chi})}{\sqrt{\chi}\,sinh(\sqrt{\chi})} - \frac{1}{3} - \frac{1}{\chi}\right)G_{\Delta T_s} + 3\left(\frac{cosh(\sqrt{\chi})}{\sqrt{\chi}\,sinh(\sqrt{\chi})} - \frac{1}{\chi}\right)G_{\Delta c_g} \qquad 4.46$$

and also the average adsorbed amount can now be written as:

$$G_{\Delta q} = \gamma_C G_{\Delta\overline{c_p}} + \gamma_T G_{\Delta T_s} \qquad 4.47$$

the linear set of eq.(4.37),(4.43-4.47) can be finally solved numerically. In this work, the function *mldivide* of MATLAB has been used to solve the linear set of eq.(4.37),(4.43-4.47) at each pressure, temperature, and frequency. Since the thermocouple response is the experimental signal that has to be analysed, the transfer function of the thermocouple signal with respect to the volume perturbation has to be computed from the solution in MATLAB. This can be done using eq.(4.48):

$$G_{\Delta TC} = \frac{G_{\Delta T_s}}{1 + s\tau_{TC}} = Re_{TC} + iIm_{TC} \qquad 4.48$$

where τ_{TC} is the time constant of the thermocouple. From $G_{\Delta TC}$ the amplitude ratio and phase lag of the thermocouple signal with respect to the volume perturbation can be calculated as $AR = |G_{\Delta T}|$ and $\varphi = atan2(Im_{TC}/Re_{TC})$. The in- and out-of-phase values are then derived from amplitude ratio and phase lag as $\delta_{in} = |G_{TC}|\cos(\varphi)$ and $\delta_{out} = |G_{TC}|\sin(\varphi)$. In the following, the property of amplitude ratio, phase lag and in- and out-of-phase functions will refer to the thermocouple 4 signal since it is the targeted signal from experiments.

4.3.4 Results of structural characterisation and N_2 isotherms on LiLSX

The results from the mercury porosimetry analysis from Brandani et al.[184] are summarised in Table 4.3.

Table 4.3: Mercury porosimetry analysis from Brandani et al.[184]

Parameter	***Unit***	***Value***
ϵ_p	$[-]$	0.362
ρ_s	$[kg/m^3]$	1537
r_{pore}	$[m]$	6.5x10^{-8}

The results from the nitrogen adsorption isotherms at 258 K, 278 K, 293 K and 303 K are reported in Figure 4.12. The data have been fitted using eq.(4.17) using the "fitting procedure 3" discussed in Farmahini et al.[13]. The reference temperature $T_{ref} = 258.15\ K$.

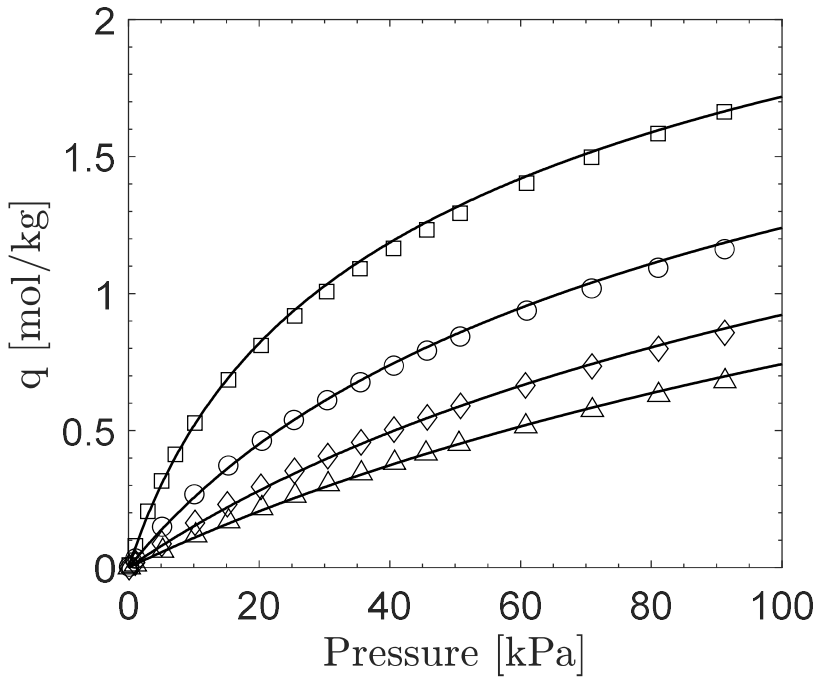

Figure 4.12: Nitrogen isotherms at 258 K (squares), 278 K (circles), 293 K (diamonds), and 303 K (triangles) on LiLSX. Solid line is eq.(4.17) with the parameters in Table 4.4.

The fitted parameters are reported in Table 4.4.

Table 4.4: Dual site Langmuir isotherm parameters for nitrogen adsorption on LiLSX

Parameter	*Unit*	*N_2*
q_{s1}	$[mol/kg]$	1.698
q_{s2}	$[mol/kg]$	1.208
b_{10}	$[1/Pa]$	7.213e–6
b_{20}	$[1/Pa]$	5.012e–5
ΔH_1	$[J/mol]$	−21570
ΔH_2	$[J/mol]$	−28060
T_{ref}	$[K]$	258

4.3.5 Results from blank experiments with He

The parameters fixed by the system for the He TFR experiments are reported in Table 4.5.

Table 4.5: Parameters of the experimental system for blank and nitrogen experiments.

Parameter	*Unit*	*Value*
R_p	$[m]$	$5\text{x}10^{-4}$
V_s	$[m^3]$	$4\pi R_p^3/3$
A_s	$[m^2]$	$4\pi R_p^2$
a_s	$[1/m]$	$3/R_p$
$c_{p,s}$	$[J/kg/K]$	1000
V_0	$[m^3]$	$1.05\text{x}10^{-4}$
A_w	$[m^2]$	0.022
a_w	$[1/m]$	A_w/V_0
c_0	$[mol/m^3]$	$P_0/(RT_0)$
c_{Vg}	$[J/mol/K]$	NIST webbook[235]

The He experiments aim at assessing the time constant of the thermocouple, τ_{TC}, such that it can be fixed while fitting the heat and mass transfer parameters during nitrogen experiments. Indeed, it is reasonable to assume that the time response of the thermocouple will be independent from the gas chosen.

The assumptions used to fit the He is of a non-adsorbing gas with very fast diffusion. These assumptions reduce the dimensionless parameters $\delta_2, \gamma_c, \gamma_T, \beta_{\Delta H}$ and τ_D to infinitesimal small values. A first estimate of the heat transfer coefficient of the solid can be made using the Nusselt number, $Nu = 2h_{gs}R_p/\kappa_{He}$ where κ_{He} is the thermal conductivity of the He. For a sphere in a stagnant fluid $Nu \to 2$. From this limit, the heat transfer coefficient of the solid can be estimated to be $h_{gs} \approx 300\ W/(m^2K)$, using a value of $\kappa_{He}|_{101kPa,303\ K} = 0.15\ W/(mK)$.

Once a first estimate of h_{gs} is given, the remaining parameters to fit are thermocouple time constant and the heat transfer between the gas in the column and the column's walls.

The single component model is fitted to the amplitude ratio for each set of data. The results are show in Figure 4.13.

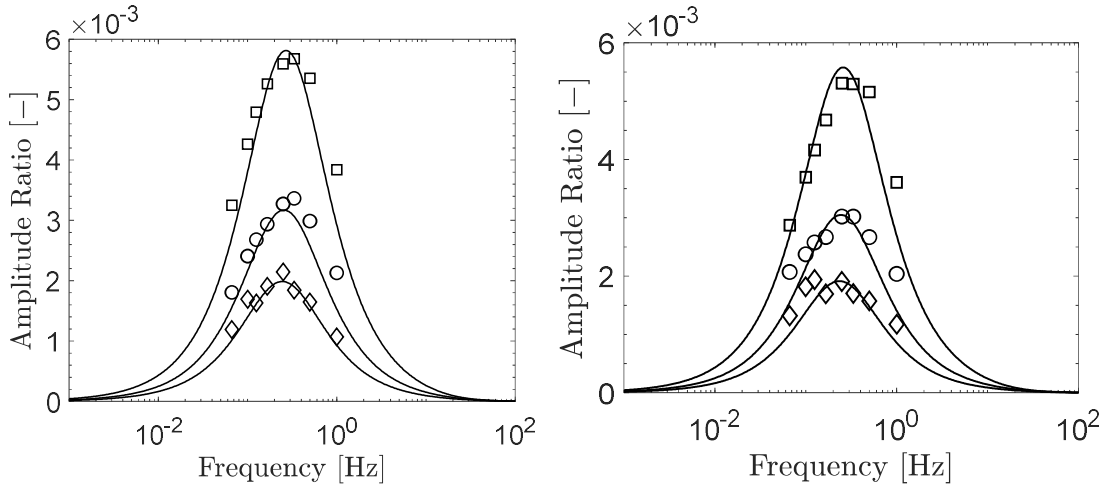

Figure 4.13: Amplitude ratio for He experiments at 303 K (left) and 328 K (right). Squares refer to 100 kPa, circles to 50 kPa and diamonds to 25 kPa. The solid line is the fitted single component model.

The fitting parameters used are reported in Table 4.6.

Table 4.6: Fitted parameters for He blank experiments.

P $[kPa]$	T $[K]$	τ_{TC} $[s]$	h_{gs} $[W/m^2/K]$	h_w $[W/m^2/K]$
100	303	0.6	385	203
50	303	0.6	367	173
25	303	0.6	317	137
100	328	0.6	412	204
50	328	0.6	370	180
25	328	0.6	342	140

As it can be noted from the fitted values of h_{gs} from Table 4.6, the initial estimate from the Nusselt number of $h_{gs} \approx 300\, W/(m^2K)$ is a reliable initial estimate. Hence, the same procedure of estimating initially h_{gs} from the Nusselt number can also be used for the nitrogen experiments. The heat transfer coefficient decreases with pressure given that the convective contribution to heat transfer decreases as well. By contrast, an increase in temperature causes an increase in the heat transfer coefficient. It should be noted that all the He experiments have been fitted using only one thermocouple time constant, as previously discussed. The effect of the thermocouple time constant can be seen in Figure 4.14 where the experimental data and the model are plotted together fixing $\tau_{TC} = 0$. As it can be noted from Figure 4.14, the experimental data between 0.2 Hz and 1 Hz tend to decrease. However, this behaviour can be attributed to the system approaching the time constant of the thermocouple. Indeed, if τ_{TC} is set to 0, the model cannot match the experiments under any set of chosen heat transfer parameters.

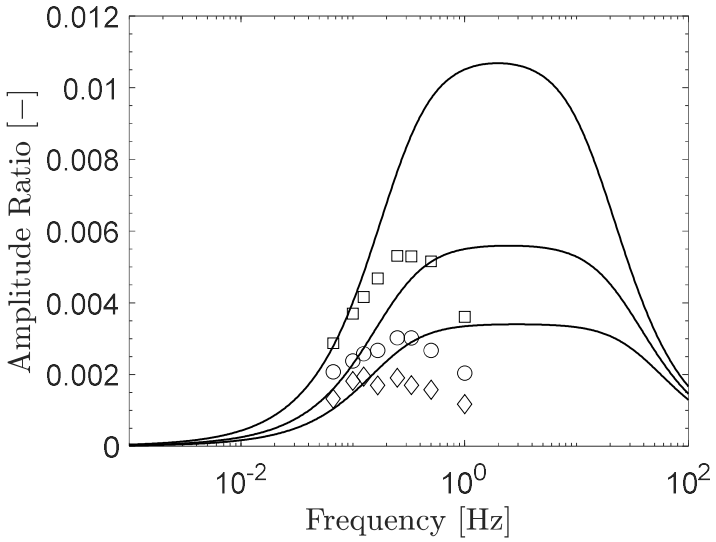

Figure 4.14: He experiments at 303 K, and 100 kPa (squares), 50 kPa (circles) and 25 kPa (diamonds). The solid line is the single component model where h_{gs} and h_w are taken from Table 4.6 and $\tau_{TC} = 0$.

4.3.6 Results from nitrogen on LiLSX

Before running TFR experiments with nitrogen, the system is tested under different stroke length displacements to check for linearity. The results are presented in Figure 4.15.

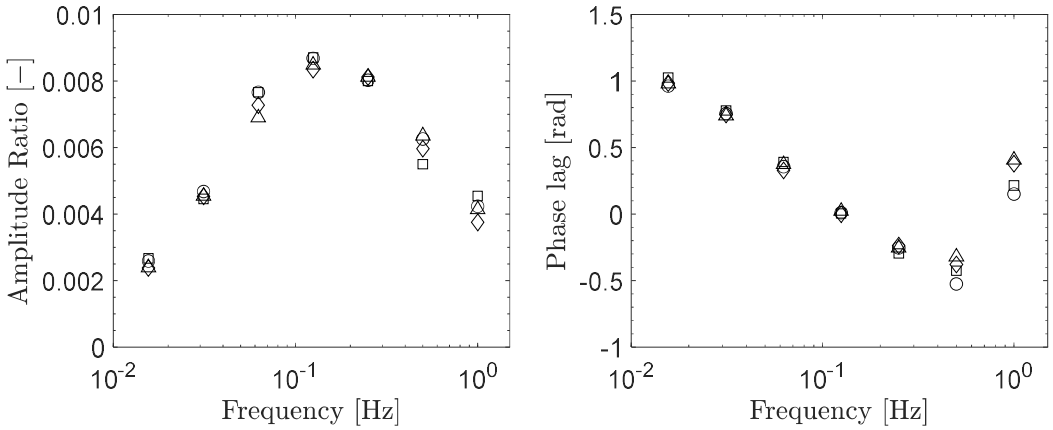

Figure 4.15: Amplitude ratio (left) and phase lag (right) at 303 K and 100 kPa for different stroke length displacement: ±2 mm (squares), ±3 mm (circles), ±4 mm (diamonds), and ±5 mm (triangles).

Both amplitude ratio and phase lag exhibit the same behaviour under different stroke displacements. This indicates that the linearity is confirmed under the conditions analysed. In the following, the highest stroke displacement will be used in order to produce the highest temperature swing in the solid's

temperature, so that the signal to noise ratio of the raw data is of the best quality.

Once the check for linearity is carried out, the nitrogen TFR experiments follow. The relevant mass and heat transfer properties are the diffusion time constant τ_D, the heat transfer gas to solid h_{gs} and the heat transfer gas to column walls h_w. The heat transfer parameter of the solid can be estimated from the Nusselt number, as done for He. Similar considerations to what presented for He lead to an initial estimate of the solid heat transfer of $h_{gs} \approx 50\ W/(m^2K)$. The heat transfer parameter h_w and the diffusion time constant are left as free fitting parameter. Finally, the time constant of the thermocouple is kept constant at 0.6 s. The amplitude ratio of the nitrogen experiments together with the fitted single component model are reported in Figure 4.16.

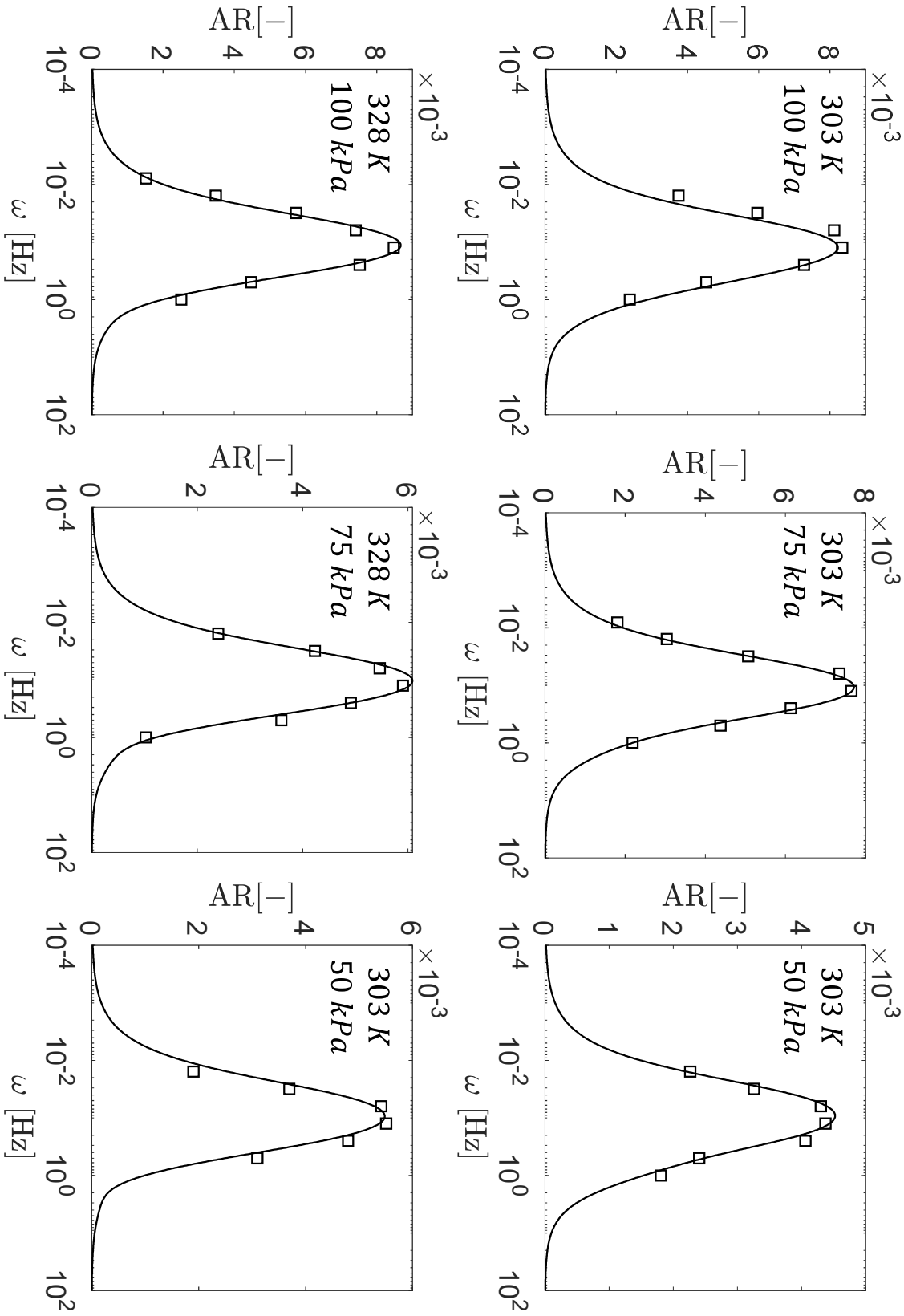

Figure 4.16: Amplitude ratio for nitrogen experiments. Squares are experimental data and sold line is the fitted model.

The fitted parameters are reported in Table 4.7.

Table 4.7: Heat and mass transfer parameters extracted from nitrogen experiments.

Run	P $[kPa]$	T $[K]$	τ_D $[s]$	$\tau_{D,eff}$ $[s]$	h_{gs} $[W/m^2/K]$	h_w $[W/m^2/K]$
1	100	303	0.1485	1.53	60.0	19
2	75	303	0.1393	1.90	56.0	15.1
3	50	303	0.1467	2.44	42.6	8.5
4	100	328	0.1253	1.19	69.1	46.9
5	75	328	0.1333	1.39	60.4	32.3
6	50	328	0.1368	1.66	51.9	30.6

In Table 4.7 also the effective diffusion time constant is included. This is the actual diffusion time constant of the system, which considers also the effect of adsorption on diffusion. It is defined as:

$$\tau_{D,eff} = \tau_D\left[\epsilon_p + \left(1-\epsilon_p\right)\rho_s K_c\right] = \frac{R_p^2}{D_{eff}} \qquad 4.49$$

As it can be noted from the value of $\tau_{D,eff}$, the diffusion of nitrogen in LiLSX is fast at the conditions analysed. This time constant would be difficult to detect with commercial systems where the effective time constant would be of the same order of the system's time response and data acquisition.

Once the amplitude ratio is fitted, the in- and out-of-phase functions can be derived. The predicted in- and out-of-phase diagrams from the model, together with the experimental data, are shown in Figure 4.17.

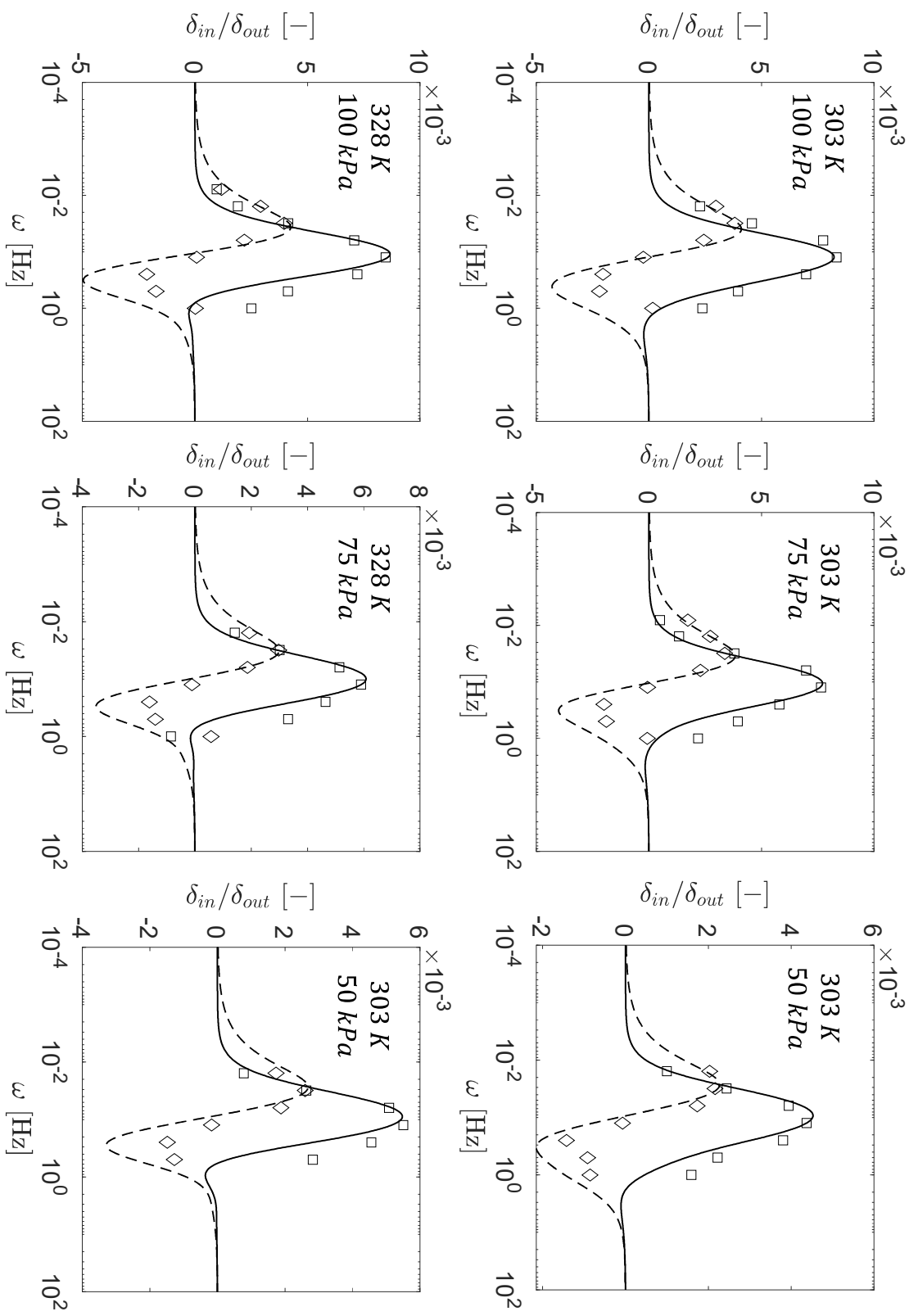

Figure 4.17: In- and out-of-phase functions for nitrogen experiments. Squares are experimental in-phase, diamonds are experimental out-of-phase, sold line is the model in-phase, and dashed line the model out-of-phase.

It can be noted from Figure 4.17 that the match of the low range of frequencies is very well captured from the model. The parameter that can modulate the in- and out-of-phase function in that region is the heat transfer coefficient between gas and column walls. The heat transfer coefficient between gas and solid influences the magnitude of the peak for the in-phase function (and of the amplitude ratio). The right branch of both amplitude ratio and in- and out-of-phase functions is controlled by the diffusion of nitrogen in the solid. The reason why the amplitude ratio (Figure 4.16) can be effectively matched from the model while the in- and out-of-phase functions show only a qualitative agreement has to be attributed to the mismatch of the phase lag. While the FFT analysis can accurately capture the amplitude of the temperature signal at the fast frequencies, the phase lag is somewhat difficult to detect accurately, as it can be noted from Figure 4.18.

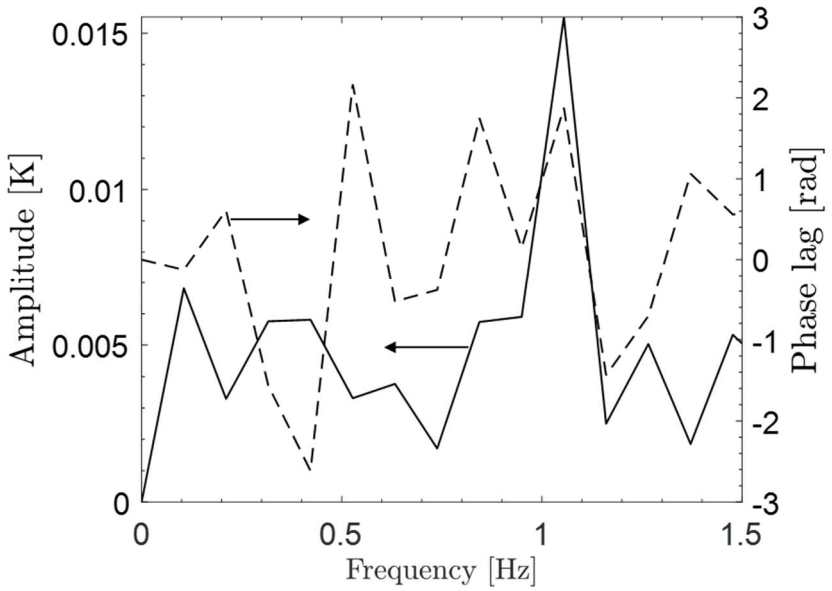

Figure 4.18: FFT analysis for nitrogen experiment at 303 K, 100 kPa and 1.05 Hz.

Compared to the FFT analysis presented in Figure 4.11, the amplitude spectrum in Figure 4.18 presents a clear peak at the frequency of the experiment, while also other peaks can be now noted at the noise frequencies. By contrast, the phase lag in Figure 4.18 has a less clear trend compared to the phase lag in Figure 4.11. The fitted raw data with amplitude and phase lag from the FFT analysis in Figure 4.18 can be seen in Figure 4.19. It is evident

that also visually it would be difficult to match a phase lag to the raw data. The amplitude might look higher if one had to fit the data manually. However, the amplitude detected by the FFT removes the background noise, acting as a sort of filter. Hence, the FFT can be trusted more than a manual fit.

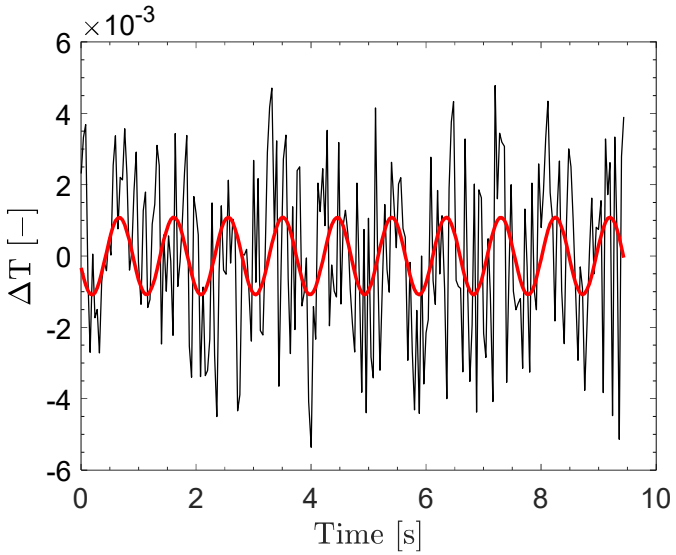

Figure 4.19: Signal of thermocouple 4 for nitrogen experiment at 303 K, 100 kPa and 1.05 Hz. Black line is the experimental signal, red line is the extracted sinusoidal function from FFT analysis in Figure 4.18.

Despite the only qualitative agreement between model and experimental data for the in- and out-of-phase functions, this way of plotting the experimental data can still provide useful information on the system under analysis. The crossing of the in-phase function at the maximum of the out-of-phase one indicates a surface barrier mechanism for the heat transfer, as assumed in the model. The minimum shown by the out-of-phase function happens at the effective diffusion time constant of the system. Hence, a preliminary plot of this functions prior to the fitting of the data can help in the initial estimate of the fitting parameters. It should be noted that the model, despite the quantitative difference, correctly reproduces the minimum of the out-of-phase function at the same frequencies shown by the experimental data at the different conditions (see Figure 4.17). The sensitivity of both amplitude ratio and in- and out-of-phase functions upon the diffusion time constant is presented in Figure 4.20.

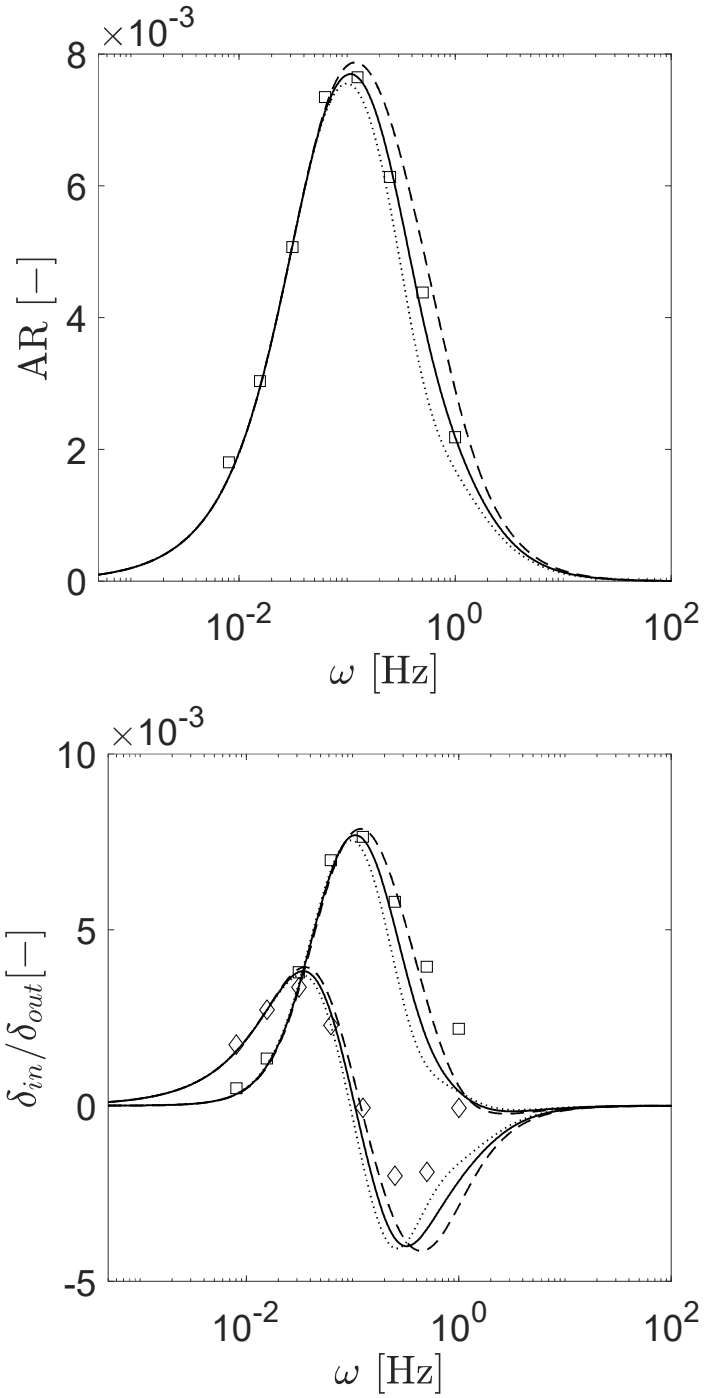

Figure 4.20: Effect of variation of the diffusion time constant for nitrogen at 303 K and 75 kPa for amplitude ratio (top) and in- and out-of-phase functions (bottom). Solid line is the fitted time constant τ_D, dashed line is $1.25\tau_D$, and dotted line is $0.75\tau_D$.

The discrimination between the correct diffusion time constant and the higher or lower value is clearly visible. As pointed out before, the left branch of both plots is not affected by the diffusion mechanism since it is fully governed by heat transfer. By contrast, the right side of both plots is clearly the region where the diffusion dominates. The plot of the in- and out-of-phase functions (Figure

4.20 (bottom)) shows how the frequency at which the minimum of the out-of-phase function changes when the diffusion time constant is changed. Despite the quantitative disagreement, the diffusion time constant can still be reliably estimated if the amplitude ratio is correctly matched, and then the out-of-phase function minimum is checked to be at the same frequency of the experiments.

4.3.6.1 Estimation of tortuosity

From the expression of the diffusion time constant, the tortuosity can be calculated from eq.(4.50).

$$\tau = \frac{\epsilon_p D_p}{R_p^2} \tau_D \qquad 4.50$$

The values of the regressed tortuosity for each run of experiments are shown in Figure 4.21.

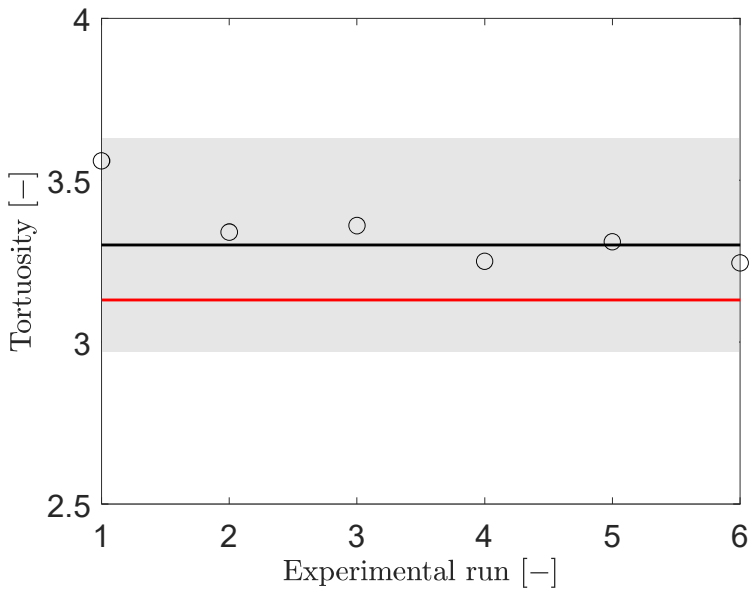

Figure 4.21: Fitted tortuosity to each experimental run. Circles are fitted tortuosity, solid black line is average value, red line is the value derived from Brandani et al.[184], and the grey band is 10% uncertainty from the average value of this work.

The average value from this work is $\tau = 3.3 \pm 5\%$. The average value is in good agreement with what derived by Brandani et al.[184] of 3.13 from volumetric experiments at 258 K. Since the measurements using TFR were carried out using a single bead, and given the slight difference of binder content and arrangement between beads, the tortuosity here derived and the one reported

by Brandani et al.[184] can effectively be seen as the same result. It should be noted that Brandani et al.[184] carried out experiments at 258 K to slow the diffusivity and manage to detect kinetics with a commercial volumetric system (Quantachrome Autosorb-iQ2™). The rate of data acquisition of this instrument is comparable to the diffusion time constants derived in this work at room temperature. Hence, Brandani et al.[184] lowered the temperature so that the rate of data acquisition would allow a clear signal to be analysed. Instead, TFR experiments allowed the estimation of a similar tortuosity at process conditions. The pore diffusivity for a single component experiment can be calculated as sum of a Knudsen and viscous contribution, as in eq.(4.51).

$$D_p = D_K + D_{vis} \tag{4.51}$$

The Knudsen diffusivity, as shown in chapter 1, can be calculated as:

$$D_K = \frac{9}{13}\left(\frac{2}{3} r_{pore} \sqrt{\frac{8R_g T}{\pi M w_{N_2}}}\right) \tag{4.52}$$

The equation of the D_K already considers the Derjaguin's correction factor introduced by Levitz[103], equal to $9/13$. The viscous term can be written as in eq.(4.53).

$$D_{vis} = \frac{P r_{pore}^2}{8\eta} \tag{4.53}$$

The single contributions of Knudsen and viscous flow are reported in Table 4.8.

Table 4.8:Values of viscous flow and Knudsen contribution for the different experimental conditions.

Pressure [kPa]	***Viscous flow [m^2/s]***	***Knudsen diffusion [m^2/s]***	
		303 K	***328 K***
50	1.47E-6		
75	2.20E-6	1.44E-5	1.50E-5
100	2.93E-6		

Assuming that the diffusion is an activated process, the effective diffusivity can be written as:

$$D_{eff} = D' exp\left(-\frac{E_a}{RT}\right) \qquad 4.54$$

where D' is a pre-exponential factor and E_a is the activation energy. The effective diffusivity from this work at 303 K and 328 K at 0.8 kPa are calculated and used with the value of effective diffusivity of Brandani et al. at 258 K and 0.8 kPa, to estimate the activation energy of this system. The results are shown in Figure 4.22.

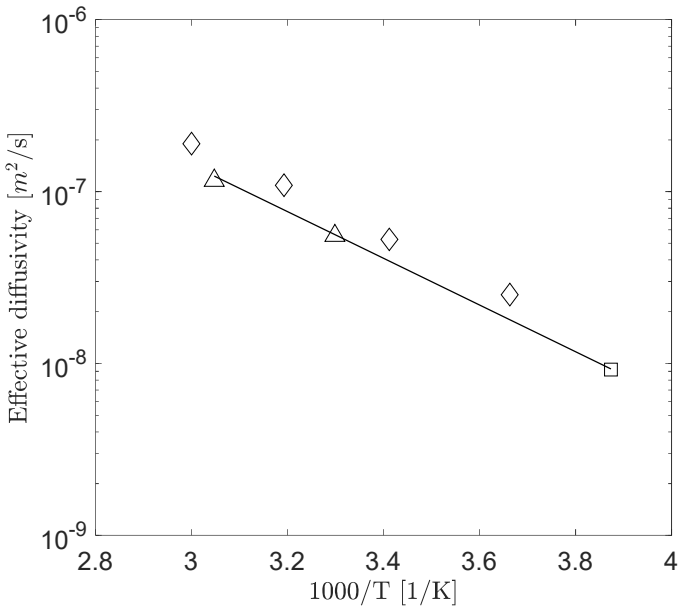

Figure 4.22: Arrhenius' plot for nitrogen on LiLSX. Triangles are effective diffusivities at 303 K and 328 K at 0.8 kPa calculated in this work, square is the value from Brandani et al.[184] at 258 K, and diamonds are values reported by Bulow and Shan[227]. Solid line is eq.(4.54) with $E_a = 26\ kJ/mol$.

The fitted value of activation energy is $E_a = 26\ kJ/mol$, which is close to what Bulow and Shen[227] reported for a similar sample of LiLSX and nitrogen of $E_a = 26.38\ kJ/mol$.

4.3.7 Model for multicomponent system

The main assumptions of the multicomponent model are the same as for the single component one. The mass transport between species is modelled using the Dusty-Gas model[229,236,237]. The multicomponent model is specialised for a binary mixture where nitrogen will be denoted as component 1 and oxygen as component 2.

The overall mass balance for each i-th component is:

$$V_s\left(1-\epsilon_p\right)\rho_s\frac{d\overline{q_i}}{dt} + V_s\epsilon_p\frac{d\overline{c_{p,i}}}{dt} + V_0\frac{dc_{g,i}}{dt} + c_{0,i}\frac{dV_g}{dt} = 0 \qquad 4.55$$

The differential mass balance, written in matrix form, is:

$$\epsilon_p\frac{\partial \boldsymbol{c_p}}{\partial t} + \left(1-\epsilon_p\right)\rho_s\frac{\partial \boldsymbol{q}}{\partial t} = \frac{\left[\boldsymbol{D_p}\right]}{r^2}\frac{\partial}{\partial r}\left(r^2\frac{\partial \boldsymbol{c_p}}{\partial r}\right) \qquad 4.56$$

where the diffusion matrix $[\boldsymbol{D_p}]$ can be derived from the Dusty-Gas model[238,239]. Its expression is reported in eq.(4.57).

$$\left[\boldsymbol{D_p}\right] = \frac{\epsilon_p}{\tau}[\boldsymbol{A}]^{-1}[\boldsymbol{B}] = \frac{\epsilon_p}{\tau}\begin{bmatrix} D_{11} & D_{12} \\ D_{21} & D_{22}\end{bmatrix} \qquad 4.57$$

The expressions for the matrices $[\boldsymbol{A}]$ and $[\boldsymbol{B}]$ are:

$$[\boldsymbol{A}] = \begin{bmatrix} \frac{1}{D_{K,1}} + \frac{y_2}{D_{12}} & -\frac{y_1}{D_{12}} \\ -\frac{y_2}{D_{12}} & \frac{1}{D_{K,2}} + \frac{y_1}{D_{12}}\end{bmatrix} \qquad 4.58$$

$$[\boldsymbol{B}] = \begin{bmatrix} 1 + \dfrac{D_{vis}}{D_{K,1}} y_1 & \dfrac{D_{vis}}{D_{K,1}} y_1 \\ \dfrac{D_{vis}}{D_{K,2}} y_2 & 1 + \dfrac{D_{vis}}{D_{K,2}} y_2 \end{bmatrix} \tag{4.59}$$

where y_i is the mole fraction of the i-th component in the gas phase, and where D_{12} is the molecular diffusivity calculated using the Chapman-Enskog equation, as shown in eq.(4.60).

$$D_{12} = \frac{3}{16} \frac{\sqrt{\dfrac{2}{\pi} \left(R_g T_0\right)^3 \left(\dfrac{1}{Mw_1} + \dfrac{1}{Mw_2}\right)}}{N_a P \sigma_{12}^2 \Omega_{12}} \tag{4.60}$$

where $N_a$is the Avogadro's number, Ω_{12} is the collision integral and σ_{12} the average kinetic diameter.

The boundary conditions, in vector of components form, for eq.(4.56) are:

$$\begin{aligned} \boldsymbol{c_p}_{(r=R_p)} &= \boldsymbol{c_g} \\ \frac{\partial \boldsymbol{c_p}_{(r=0)}}{\partial r} &= 0 \end{aligned} \tag{4.61}$$

The linearised isotherm for the multicomponent is of the same form shown for single component:

$$(\boldsymbol{q} - \boldsymbol{q_0}) = [\boldsymbol{K_c}](\boldsymbol{c_p} - \boldsymbol{c_0}) + [\boldsymbol{K_T}](T_s - T_0) \tag{4.62}$$

where $[\boldsymbol{K_c}]$ and $[\boldsymbol{K_T}]$ can be expressed as:

$$[\boldsymbol{K_c}] = \begin{bmatrix} K_{11} & K_{12} \\ K_{21} & K_{22} \end{bmatrix}; [\boldsymbol{K_T}] = \begin{bmatrix} K_{T1} \\ K_{T2} \end{bmatrix} \tag{4.63}$$

where K_{ij} is the derivative of the isotherm of component i with respect to the concentration of component j. Combining eq.(4.56) and (4.62):

$$\epsilon_p \frac{\partial \boldsymbol{c_p}}{\partial t} + (1-\epsilon_p)\rho_s[\boldsymbol{K_c}]\frac{\partial \boldsymbol{c_p}}{\partial t} + (1-\epsilon_p)\rho_s[\boldsymbol{K_T}]\frac{\partial T_s}{\partial t} = \frac{[\boldsymbol{D_p}]}{r^2}\frac{\partial}{\partial r}\left(r^2\frac{\partial \boldsymbol{c_p}}{\partial r}\right) \quad 4.64$$

which can be rearranged as

$$\frac{\partial \boldsymbol{c_p}}{\partial t} + (1-\epsilon_p)[\boldsymbol{K'_T}]\frac{\partial T_s}{\partial t} = \frac{[\boldsymbol{D'}]}{r^2}\frac{\partial}{\partial r}\left(r^2\frac{\partial \boldsymbol{c_p}}{\partial r}\right) \quad 4.65$$

where $[\boldsymbol{K_T}'] = \rho_s[\boldsymbol{K'}]^{-1}[\boldsymbol{K_T}]$ and $[\boldsymbol{D'}] = [\boldsymbol{K'}]^{-1}[\boldsymbol{D_p}]$, with

$$[\boldsymbol{K'}] = \begin{bmatrix} \epsilon_p + (1-\epsilon_p)\rho_s K_{11} & (1-\epsilon_p)\rho_s K_{12} \\ (1-\epsilon_p)\rho_s K_{21} & \epsilon_p + (1-\epsilon_p)\rho_s K_{22} \end{bmatrix} \quad 4.66$$

The average quantities in the solid can be calculated as in eq.(4.15) and (4.16) for each component.

The energy balance on the gas in the chamber is similar to what reported for the single component model, and it is reported below.

$$V_0 c_{0,tot} c_{Vg}\frac{dT_g}{dt} + P_{0,tot}\frac{dV_g}{dt} + h_{gs}A_s(T_g - T_s) + h_w A_w(T_g - T_0) = 0 \quad 4.67$$

where $c_{0,tot}$ and $P_{0,tot}$ are the total concentration and pressure in the column, respectively. The energy balance on the solid is:

$$m_s c_{p,s}\frac{dT_s}{dt} + \sum_{i=1}^{N_c} \Delta H_i V_s(1-\epsilon_p)\rho_s\frac{d\overline{q}_i}{dt} - h_{gs}A_s(T_g - T_s) = 0 \quad 4.68$$

it should be noted that in eq.(4.68) the accumulation of energy of the gas phase in the macropores (see eq.(4.26)) has been omitted since its contribution can be proved to be negligible compared to the other terms.

4.3.7.1 Solution of the differential mass balance

Upon rearranging eq.(4.65) with the dimensionless variable $\xi = r/R_p$ and the deviation variables, the mass balance in the solid in the Laplace domain can be written as:

$$s\widetilde{\boldsymbol{\Delta' c_p}} + (1-\epsilon_p)[\boldsymbol{K'_T}]s\widetilde{\Delta' T_s} = \frac{[\boldsymbol{D''}]}{\xi^2}\frac{\partial}{\partial\xi}\left(\xi^2\frac{\partial\widetilde{\boldsymbol{\Delta' c_p}}}{\partial\xi}\right) \qquad 4.69$$

it should be noted that the multicomponent model is written in terms of deviation variables $\Delta' X = X - X_0$. The matrix $[\boldsymbol{D''}] = [\boldsymbol{D'}]/R_p^2$. The coupled system of mass balances can be solved with the use of the decoupling technique presented by Toor[240]. Making the change of variable $\widetilde{\boldsymbol{\Delta' c_p}} = [\boldsymbol{\Lambda}]\boldsymbol{\phi}$, and multiplying eq.(4.69) with $[\boldsymbol{\Lambda}]^{-1}$ on both sides:

$$s\boldsymbol{\phi} + (1-\epsilon_p)[\boldsymbol{K''_T}]s\widetilde{\Delta' T_s} = \frac{[\boldsymbol{\Lambda}]^{-1}[\boldsymbol{D''}][\boldsymbol{\Lambda}]}{\xi^2}\frac{\partial}{\partial\xi}\left(\xi^2\frac{\partial\boldsymbol{\phi}}{\partial\xi}\right) = \frac{[\boldsymbol{\Gamma}]}{\xi^2}\frac{\partial}{\partial\xi}\left(\xi^2\frac{\partial\boldsymbol{\phi}}{\partial\xi}\right) \qquad 4.70$$

where $[\boldsymbol{\Gamma}]$ is the diagonal matrix of the eigenvalues of $[\boldsymbol{D''}]$, and $[\boldsymbol{K''_T}] = [\boldsymbol{\Lambda}]^{-1}\,[\boldsymbol{K_T}']$. The matrix $[\boldsymbol{\Gamma}]$ and the modal matrix $[\boldsymbol{\Lambda}]$ have the form of:

$$[\boldsymbol{\Gamma}] = \begin{bmatrix}\lambda_1 & 0\\ 0 & \lambda_2\end{bmatrix};\ [\boldsymbol{\Lambda}] = \begin{bmatrix}1 & \dfrac{\lambda_2 - D''_{22}}{D''_{21}}\\ \dfrac{\lambda_1 - D''_{11}}{D''_{12}} & 1\end{bmatrix} \qquad 4.71$$

where the eigenvalues are

$$\lambda_{1,2} = \frac{D''_{11} + D''_{22} \pm \sqrt{(D''_{11} - D''_{22})^2 + 4D''_{12}D''_{21}}}{2} \qquad 4.72$$

The boundary conditions can also be rearranged as:

$$\boldsymbol{\phi}_{(\xi=1)} = \boldsymbol{\phi}^* = [\boldsymbol{\Lambda}]^{-1}\widetilde{\boldsymbol{\Delta' c_g}}$$

$$\frac{\partial\boldsymbol{\phi}_{(\xi=0)}}{\partial\xi} = 0 \qquad 4.73$$

The solution for eq.(4.70), together with its boundary conditions, eq.(4.73), is:

$$\phi_i = \left(\phi_i^* + \frac{\theta'_i}{\chi'_i}\widetilde{\Delta' T_s}\right)\frac{1}{\xi}\frac{sinh\left(\sqrt{\chi'_i}\xi\right)}{sinh\left(\sqrt{\chi'_i}\right)} - \frac{\theta'_i}{\chi'_i}\widetilde{\Delta' T_s} \qquad 4.74$$

where $\theta'_i = s/\lambda_i$ and $\chi'_i = \left(1-\epsilon_p\right)K''_{T,i}s/\lambda_i$.

With the solution of the differential mass balance, the average gas phase in the solid and the amount adsorbed can be calculated for the i-th component:

$$\begin{aligned}\widetilde{\Delta'\overline{c_{p,i}}} &= 3\int_0^1 \widetilde{\Delta'c_{p,i}}\xi^2 d\xi = 3\int_0^1 \left(\phi_i + \Lambda_{ij}\phi_j\right)\xi^2 d\xi \\ &= 3\frac{\theta'_i}{\chi'_i}\left(\frac{cosh\left(\sqrt{\chi'_i}\right)}{\sqrt{\chi'_i}\,sinh\left(\sqrt{\chi'_i}\right)} - \frac{1}{3} - \frac{1}{\chi'_i}\right)\widetilde{\Delta'T_s} \\ &+ 3\left(\frac{cosh\left(\sqrt{\chi'_i}\right)}{\sqrt{\chi'_i}\,sinh\left(\sqrt{\chi'_i}\right)} - \frac{1}{\chi'_i}\right)\phi_i^* \\ &+ 3\Lambda_{ij}\frac{\theta'_j}{\chi'_j}\left(\frac{cosh\left(\sqrt{\chi'_j}\right)}{\sqrt{\chi'_j}\,sinh\left(\sqrt{\chi'_j}\right)} - \frac{1}{3} - \frac{1}{\chi'_j}\right)\widetilde{\Delta'T_s} \\ &+ 3\Lambda_{ij}\left(\frac{cosh\left(\sqrt{\chi'_j}\right)}{\sqrt{\chi'_j}\,sinh\left(\sqrt{\chi'_j}\right)} - \frac{1}{\chi'_j}\right)\phi_j^*\end{aligned} \qquad 4.75$$

the average amount adsorbed for the i-th component is:

$$\widetilde{\Delta'\overline{q_i}} = K_{ii}\widetilde{\Delta'\overline{c_{p,i}}} + K_{ij}\widetilde{\Delta'\overline{c_{p,J}}} + K_{T,i}\widetilde{\Delta'T_s} \qquad 4.76$$

4.3.7.2 Linear system of equations

As done for the single component model, a system of equations whose variables are the transfer function of the mass and heat variables with respect to the volume perturbation can be written. The system of equations is reported below.

$$\delta_1 G_{\Delta\overline{c_{p,i}}} + \delta'_2 G_{\Delta\overline{q_i}} + G_{\Delta c_{g,i}} = -\frac{c_{0,i}}{V_0} \qquad 4.77$$

$$G_{\Delta' \overline{c_{p,i}}} = \left[3\frac{\theta'_i}{\chi'_i}\left(\frac{cosh\left(\sqrt{\chi'_i}\right)}{\sqrt{\chi'_i}\, sinh\left(\sqrt{\chi'_i}\right)} - \frac{1}{3} - \frac{1}{\chi'_i} \right) + 3\Lambda_{ij}\frac{\theta'_j}{\chi'_j}\left(\frac{cosh\left(\sqrt{\chi'_j}\right)}{\sqrt{\chi'_j}\, sinh\left(\sqrt{\chi'_j}\right)} - \frac{1}{3} - \frac{1}{\chi'_j} \right) \right] G_{\Delta' T_s} + \left[3\Lambda_{ii}^{-1}\left(\frac{cosh\left(\sqrt{\chi'_i}\right)}{\sqrt{\chi'_i}\, sinh\left(\sqrt{\chi'_i}\right)} - \frac{1}{\chi'_i} \right) + 3\Lambda_{ij}\Lambda_{ji}^{-1}\left(\frac{cosh\left(\sqrt{\chi'_j}\right)}{\sqrt{\chi'_j}\, sinh\left(\sqrt{\chi'_j}\right)} - \frac{1}{\chi'_j} \right) \right] G_{\Delta' c_{g,i}} + \left[3\Lambda_{ij}^{-1}\left(\frac{cosh\left(\sqrt{\chi'_i}\right)}{\sqrt{\chi'_i}\, sinh\left(\sqrt{\chi'_i}\right)} - \frac{1}{\chi'_i} \right) + 3\Lambda_{ij}\Lambda_{jj}^{-1}\left(\frac{cosh\left(\sqrt{\chi'_j}\right)}{\sqrt{\chi'_j}\, sinh\left(\sqrt{\chi'_j}\right)} - \frac{1}{\chi'_j} \right) \right] G_{\Delta' c_{g,j}} \quad 4.78$$

$$G_{\Delta' \boldsymbol{q}} = [\boldsymbol{K_c}] G_{\Delta' \overline{\boldsymbol{c_p}}} - [\boldsymbol{K_T}] G_{\Delta' T_s} \quad 4.79$$

$$sG_{\Delta' T_s} + \sum_{i=1}^{Nc} \beta'_{\Delta H_i}\, sG_{\Delta' q_i} - \beta_s \left(G_{\Delta' T_g} - G_{\Delta' T_s} \right) = 0 \quad 4.80$$

$$(s + \alpha_w + \alpha\beta_S) G_{\Delta' T_g} - \alpha\beta_s G_{\Delta' T_s} = -\frac{R_g T_0}{V_0 c_{Vg}} s \quad 4.81$$

where $\delta'_2 = \frac{V_s(1-\epsilon_p)\rho_s}{V_0}$ and $\beta'_{\Delta H_i} = \frac{\Delta H_i}{c_{p,s}}$. The above system of equations is solved in MATLAB, and the transfer function of the thermocouple is calculated using eq.(4.48). The amplitude ratio is calculated as $AR = |G_{\Delta' TC}| V_0 / T_0$, where $G_{\Delta' TC}$ is as in eq.(4.48).

4.3.7.3 Parameters for the air experiments

To fit the multicomponent model to the air experiments several parameters are needed. However, some of them can be appropriately fixed in order to reduce the degrees of freedom of the model.

The air mixture used for the experiments is a binary mixture of nitrogen and oxygen in the ratio of 79/21. The equilibrium of nitrogen on LiLSX has been already presented. Since at room temperature the nitrogen isotherm can be approximated to linear, and that the oxygen will exhibit a lower affinity with the LiLSX, we can reduce the matrix $[\boldsymbol{K_c}]$ to:

$$[\boldsymbol{K_c}] = \begin{bmatrix} K_{c,N2} & 0 \\ 0 & K_{c,N2}/S_{N_2/O_2} \end{bmatrix} \qquad 4.82$$

where K_{c,N_2} is the derivative of the nitrogen isotherm with respect to nitrogen concentration, and $S_{N_2/O_2} = K_{c,N_2}/K_{c,O_2}$ is the selectivity of LiLSX towards the binary nitrogen-oxygen. The selectivity has been expressed as ratio between the Henry's law constants since the shape of the isotherm is almost linear. Hence, the derivative of the isotherm can be approximated to the Henry's law constants of the two gases on LiLSX. In eq.(4.82) K_{c,N_2} is known from the isotherm of nitrogen (see section 4.3.4), and the selectivity is left as fitting parameter. The additional thermodynamic parameter to be considered as unknown is the heat of adsorption of the oxygen on LiLSX. This parameter has been fixed at half of the nitrogen, since it provides a reasonable estimate from similar samples of LiLSX[223,241].

The multicomponent model considers three diffusion mechanisms: Knudsen, viscous, and molecular diffusion. The three terms are appropriately accounted in the expression of eq.(4.57-4.60). The tortuosity is not a free parameter but is now fixed at the value regressed from nitrogen experiments, $\tau = 3.3$.

The thermocouple time constant has been fixed with blank helium experiments, and it will be kept constant at $\tau_{TC} = 0.6s$.

The heat transfer parameter gas-to-solid and gas-to-column walls could be left as fitting parameters. However, given that the binary is mostly composed of nitrogen and that the conditions of the air experiments are similar to what investigated for the nitrogen ones (see Table 4.2), the heat transfer parameters will be kept constant to the ones used for nitrogen at 303 K and 100 kPa.

Therefore, the only parameter left to fit is the selectivity S_{N_2/O_2}. The remaining constants of the system are reported in Table 4.9.

Table 4.9: Parameters of the experimental system for air experiments.

Parameter	***Unit***	***Value***
R_p	$[m]$	5x10^{-4}
V_s	$[m^3]$	$4\pi R_p^3/3$
A_s	$[m^2]$	$4\pi R_p^2$
a_s	$[1/m]$	$3/R_p$
$c_{p,s}$	$[J/kg/K]$	1000
V_0	$[m^3]$	8.4x10^{-5}
A_w	$[m^2]$	0.020
a_w	$[1/m]$	A_w/V_0
c_0	$[mol/m^3]$	$P_0/(RT_0)$
c_{Vg}	$[J/mol/K]$	NIST webbook[235]

4.3.8 Results from air experiments

The results from the fitting of the model to the experiments is shown in Figure 4.23. The selectivity fitted to the data is $S_{N_2/O_2} = 6 \pm 1$.

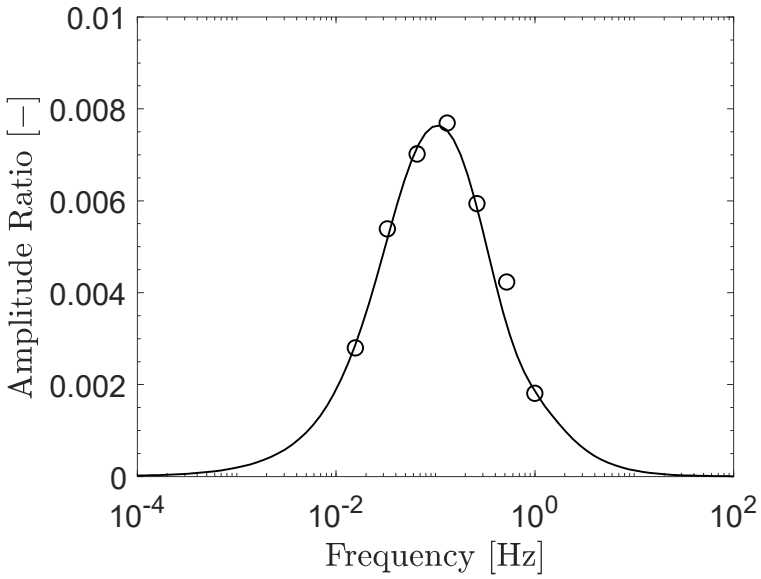

Figure 4.23: Air experiments at 300 K and 90 kPa. Circles are experimental data and line is the fitted multicomponent model.

The effect of the selectivity on the model can be seen in Figure 4.24. The selectivity alters the peak of the amplitude ratio. The higher the selectivity, the lower will be the peak. This can be explained by the fact that a higher selectivity will leave out oxygen from adsorbing, generating less heat.

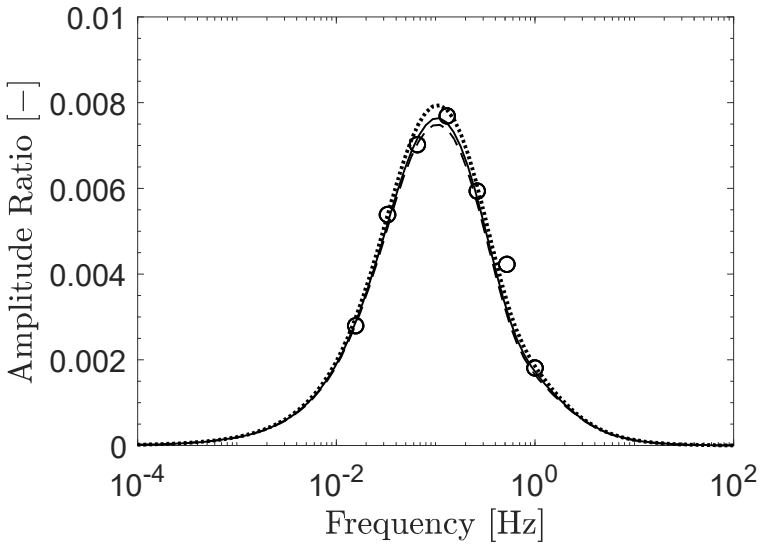

Figure 4.24: Sensitivity of the amplitude ratio with respect to the selectivity. Circles are experimental data, dashed line is $S_{N_2/O_2} = 8$, solid line is $S_{N_2/O_2} = 6$, and dotted line is $S_{N_2/O_2} = 4$.

It should be noted that the sensitivity of the model upon the selectivity is appreciable. However, the error on fitting the sensitivity is relatively large compared to its value. Nevertheless, the TFR technique can be used to preliminarily assess the selectivity of the binary on LiLSX.

It is worth pointing out that independent measurements from AirLiquide laboratories have shown that the selectivity of this LiLSX is close to 6.1, not far from what can be estimated from the results presented. In addition, Wu et al.[223] also report a selectivity of roughly 6.5 in similar conditions.

4.4 Conclusions

This chapter aimed at discussing possible strategies for the kinetic study of flexible adsorbents and fast diffusing systems.

Flexible materials can be finely tuned to increase the uptake performance of adsorbents towards certain adsorbates. The interest of the scientific community is mainly devoted to MOF materials, although even zeolites can exhibit such behaviour. It is the case for (Na,TEA)-ZSM-25, zeolite of the Na-Rho family. The complex framework structure, the cation movement and the framework relaxation upon adsorption offer complex challenges to its modelling. The solid undergoes a structural change from a distorted structure at zero loading to a more regular and open structure at higher partial pressures of CO_2. This behaviour leads to a transition between an equilibrium controlled to a kinetically controlled regime in the ZLC experimental data. To capture this behaviour in a mathematical model, a dependence of the diffusivity upon the amount adsorbed has been postulated. The dependence of the diffusivity upon adsorption is taken into account by two terms: the Darken correction factor and a corrected diffusivity which changes according to the adsorbent's framework. The second term accounts for the different interaction between solid and adsorbate at changing unit cell parameters. The second term follows the experimental behaviour of faster kinetics at higher loadings. A possible explanation of such behaviour might be the increasing void space available for diffusion at opening of the solid framework. Nevertheless, this diffusion mechanism is not fully disclosed yet, and it might be interest for future works. The model captures the kinetics of such system and it is able to correctly predict the transition from equilibrium to kinetically controlled regime shown by the ZLC data. Although a complete understanding of the complex kinetic mechanism of CO_2 diffusion in (Na,TEA)-ZSM-25 would require additional

work, a preliminary conclusion can be drawn on the system: compared to other ion exchanged Rho-zeolites, the studied (Na,TEA)-ZSM-25 has fast kinetics and similar uptakes to other ion exchanged Rho zeolites. It is also worth to mention that, at the best of the author knowledge, this is the first work to combine an equilibrium model that deals with both adsorption and flexibility of the adsorbent within a kinetic analysis. This highlights the great advantage of using multi-RALF for such complex systems. Its use could be further developed if included in process simulators.

The other topic addressed in this chapter is the study of fast diffusing systems such as air separation with LiLSX. The capability of the TFR technique to discriminate between mass and heat transfer time constants makes it particularly suitable for this kind of application. Provided that the experimental apparatus can span over an adequate range of frequencies, the mass transfer mechanism can be detected properly. This work presented for the first time the use of the DP-PSA as apparatus for TFR experiments, for both single component experiments, i.e. N_2-LiLSX, and then the binary N_2/O_2 on LiLSX. The results for single component measurements provide information on the tortuosity of the material which is in agreement with literature data. It should be noted that, while the TFR experiments have been carried out at room temperature and in a range of pressures of industrial interest for N_2/O_2 separation, the results presented in literature have used properly tuned experimental conditions to slow down the kinetics of the nitrogen in LiLSX and detect with accuracy the tortuosity. The benefit of TFR experiments is the analysis of the diffusion mechanism in a range of conditions which is of interest for the air separation application and the direct measurement of binary kinetics. This work also presented mathematical models by which TFR experiments can be analysed in the assumption of macropore diffusion control. The model for a binary system allows for an estimate of the selectivity of LiLSX for the binary N_2/O_2. The value derived is in agreement with literature although a sensitivity analysis of the model reveals some uncertainty on its estimate. As this is an equilibrium property that can be measured independently, the DP-PSA as a TFR experiment can provide an important validation for binary kinetic models.

It is likely that in the near future conditions such as flexibility of the adsorbent and fast diffusing systems will become increasingly relevant in the adsorption field. Great effort is put in developing sophisticated apparatuses for the determination of the relevant parameters which can be used for process simulation and design. Techniques such as ZLC and TFR highlighted how these systems can be characterised macroscopically with the analysis of the data with novel models. It is worth pointing out that the kinetic study here presented can also be applied to monoliths. The monolith can be fitted in the DP-PSA column, and a thermocouple carefully inserted in the walls of the monolith. Future works could be carried out to analyse the use of TFR on monoliths compared to conventional chromatographic systems, for the detection of mass and heat transfer time constants.

Chapter 5 Conclusions and future works

The aim of the thesis was the detailed analysis of straight-channel monoliths as an alternative to conventional packed beds for adsorption processes. More specifically, the analysis included both the definition of correlations to estimate the HETP and pressure drop for a given monolith, but also the derivation of numerical models to be used in the simulation of an adsorption column. Furthermore, given the importance of reliable equilibrium and kinetic parameters for the simulation of adsorption systems, the thesis has further analysed a novel thermodynamic model for multicomponent adsorption on heterogeneous solids, i.e. multi-RALF, and also two experimental techniques, ZLC and TFR, for the regression of mass transfer properties.

The work in Chapter 2 presented simple design correlations for the HETP and pressure drop in several monoliths relevant to adsorption processes. Moreover, the procedure to derive such correlations was presented. The equations can be applied to any monolith and their use could hence be extended in future to monoliths not analysed in this work. The use of such correlations is still limited to gas systems, and validation of such correlations for liquid system would prove (or not) their general application to any adsorption system. It should be noted that the framework of equations presented highlights a strong connection between the physics of the system and the mathematical representation of it: few parameters accurately derived are able to predictively describe the full dynamics of a monolith. It comes natural to ask weather this methodology could be applied to structures which are not of extruded form. Indeed, structured adsorbents built with 3D printing could (and have already) unlocked a great potential in terms of geometry optimisation for adsorption monoliths. Although the mathematical description might become more convoluted, it would still be worth to adapt the procedure here presented to describe such structures in terms of HETP and pressure drop correlations. This process would allow fast screening of potential geometries for a given application, not limited to conventional monoliths. The numerical approach presented for the corrugated monolith might be the easier

route to pursue, given the modelling agility of commercial software to handle complex structures.

If design correlations are an effective way to quickly assess the performance of a monolith, numerical models are fundamental for careful design of adsorption monoliths. The numerical reduced order models derived in the second chapter are of practical interest when it comes to the accurate simulation and design of an adsorption unit. They do not require any adjustable parameter, but only the knowledge of the physics and geometry of the system. The comparison between full 3D simulations and reduced order models shows excellent agreement between them, making the reduced order models a suitable candidate for process simulations. Ideally, once implemented in a process simulator, the user should only input the physical parameters and choose the cross-section of interest.

The development of robust adsorption simulators cannot overlook the use of sub-routines for the calculation of the equilibrium between fluid phase and adsorbed phase. The equations presented for both RALF and multi-RALF could become in the near future an additional thermodynamic package which could be used as alternative to adsorbed solution theories. In particular, its handling of flexible solids makes it an important alternative to the empirical description of adsorbent breathing. The results presented for the CO_2 adsorption on (Na,TEA)-ZSM-25 highlight such feature, showing accurate description of both adsorption and solid flexibility using the least amount of fitting parameters embedding all available experimental information. The kinetic study of CO_2 diffusion in (Na,TEA)-ZSM-25 has also presented how multi-RALF can help in the kinetic description of such complex system. Nevertheless, the implementation of multi-RALF in a process simulator has to overcome two main difficulties: the initialisation and the solution of the set of nonlinear equations constituting multi-RALF. The initialisation has to make sure that, regardless of the initial guess provided, the model will always converge to the correct solution. The solution of multi-RALF has been briefly discussed in section 4.2.3.1. It is highly recommended to solve the set of

nonlinear equations together with the DAE system describing the dynamics of an adsorption column. This would allow a better integration in time, and less chances of possible failure of the solver.

If multi-RALF would surely benefit of its implementation in a process simulator, further development of its theory could possibly allow its use for challenging multicomponent systems. Multi-RALF has been proven to correctly predict the azeotrope benzene−propene−ortho-MFI without the need of additional mixture fitting parameters, which provides by itself a good test-case for an adsorption model. However, several additional mixtures still provide a fruitful challenge for thermodynamic theories. Mainly, adsorption of water, or mixtures where the molecules present large differences in polarity and size adsorbing in heterogeneous solids. Since multi-RALF relies on the definition of the residual Gibbs energy to derive the chemical potential in the adsorbed phase, one could use non-random hydrogen bonding theories, rather than the Sanchez-Lacombe EoS, to derive it. Non-random hydrogen bonding models have been successfully used to model hydrogen bonding in lattice fluid theories[242] and systems where a non-random mixing might more realistically represent the physics of the system. Another interesting analysis could be carried out on mixing rules for multi-RALF, and on group-theories to describe the adsorption of a single molecule on multiple sites. The possibilities of improvement of multi-RALF are endless. This is the great advantage of such a “flexible” theory.

The discussion on thermodynamics is closely followed by an equally relevant topic: adsorption kinetics. This work tried to outline possible strategies in the detection of mass transfer mechanisms in flexible adsorbents and fast diffusing systems. It is likely that this type of systems will increasingly appear as alternative to traditional zeolites or carbonaceous materials. Therefore, it is important to understand how to tackle the challenge of deriving correct mass transfer time constants to be used in process design. ZLC and TFR are quite established characterisation techniques in the adsorption field, and their adaptability to a wide variety of systems make them particularly suitable for the

screening and characterisation of novel adsorbents. It is of course challenging to design such systems to targeted materials, especially when specific properties want to be extracted. Nevertheless, the results presented in this thesis highlight how effective their use can be, especially if compared to commercial systems which are not meant to tackle complex kinetic processes, yet.

To conclude, this work aimed at providing a framework of models and tools which could be a solid base in the deployment of monoliths for adsorption processes. This work has posed more questions than it actually answered, which is a good outcome for a PhD project. The further development of thermodynamic theories, experimental systems for kinetic measurements, and development of models for process simulations have been challenging topics in the adsorption field well before this work and they will be in the foreseeable future[2].

Appendices

Appendix A Correlations to calculate the $g_i(\alpha)$ functions for an hex-hex channel

A.1 Hex-hex channel with $\alpha_{ls} > 0$

The function $g_1(\alpha_{ls})$ is:

$$g_1(\alpha_{ls}) = p_1(\alpha_{rec})\alpha_{ls}^3 + p_2(\alpha_{rec})\alpha_{ls}^2 + p_3(\alpha_{rec})\alpha_{ls} + p_4(\alpha_{rec}) \quad \text{A.1}$$

where:

$$p_1(\alpha_{rec}) = 0.0482{\alpha_{rec}}^{-1.35} - 0.05545 \quad \text{A.2}$$

$$p_2(\alpha_{rec}) = -0.7{\alpha_{rec}}^{-0.5} - 0.9801{\alpha_{rec}}^{0.05767} + 0.3262 \quad \text{A.3}$$

$$p_3(\alpha_{rec}) = 0.6044{\alpha_{rec}}^{2} - 1.458\alpha_{rec} + 0.9418 \quad \text{A.4}$$

$$p_4(\alpha_{rec}) = -0.08782\alpha_{rec}^2 + 0.6716\alpha_{rec} - 0.08075 \quad \text{A.5}$$

The function $g_2(a_{ls})$ is:

$$g_2(\alpha_{ls}) = \frac{8p_1(\alpha_{rec})\alpha_{ls}^3 + 4p_2(\alpha_{rec})\alpha_{ls}^2 + 2p_3(\alpha_{rec})\alpha_{ls} + p_4(\alpha_{rec})}{\alpha_{ls} + q_1(\alpha_{rec})} \quad \text{A.6}$$

where:

$$p_1(\alpha_{rec}) = 0.02639\alpha_{rec}^3 - 0.02133\alpha_{rec}^2 + 0.01868\alpha_{rec} + 1.256 \quad \text{A.7}$$

$$p_2(\alpha_{rec}) = \frac{-0.45\alpha_{rec}^2 + 0.3162\alpha_{rec} - 0.4356}{\alpha_{rec} + 0.073} \quad \text{A.8}$$

$$p_3(\alpha_{rec}) = -2.169\alpha_{rec}^3 + 5.307\alpha_{rec}^2 - 3.164\alpha_{rec} + 1.89 \quad \text{A.9}$$

$$p_4(\alpha_{rec}) = 1.212\alpha_{rec}^3 - 3.497\alpha_{rec}^2 + 3.196\alpha_{rec} - 0.5109 \quad \text{A.10}$$

$$q_1(\alpha_{rec}) = \frac{-0.5323\alpha_{rec}^2 + 0.8912\alpha_{rec} - 0.1591}{\alpha_{rec} - 0.1357} \quad \text{A.11}$$

The fuction $g_3(\alpha_{ls})$ is:

$$g_3(\alpha_{ls}) = p_1(\alpha_{rec})\alpha_{ls}^4 + p_2(\alpha_{rec})\alpha_{ls}^3 + p_3(\alpha_{rec})\alpha_{ls}^2 + p_4(\alpha_{rec})\alpha_{ls} + p_5(\alpha_{rec}) \quad \text{A.12}$$

where:

$$p_1(\alpha_{rec}) = -526.9e^{-23.05\alpha_{rec}} - 1.228e^{-3.586\alpha_{rec}} \quad \text{A.13}$$

$$p_2(\alpha_{rec}) = \frac{-0.6994\alpha_{rec}^2 + 0.7064\alpha_{rec} + 0.09567}{\alpha_{rec} - 0.2136} \quad \text{A.14}$$

$$p_3(\alpha_{rec}) = 0.1561e^{2.378\alpha_{rec}} - 103.7e^{-12.41\alpha_{rec}} \quad \text{A.15}$$

$$p_4(\alpha_{rec}) = \frac{-1.418\alpha_{rec}^2 + 1.559\alpha_{rec} - 0.2615}{\alpha_{rec} - 0.2284} \quad \text{A.16}$$

$$p_5(\alpha_{rec}) = -0.1187\alpha_{rec}2 + 1.175\alpha_{rec} - 0.1184 \quad \text{A.17}$$

A.2 Hex-hex channel with $\alpha_{ss} > 0$

The function $g_1(\alpha_{ss})$ is:

$$g_1(\alpha_{ss}) = p_1(\alpha_{rec})\alpha_{ss}^2 + p_2(\alpha_{rec})\alpha_{ss} + p_3(\alpha_{rec}) \quad \text{A.18}$$

where:

$$p_1(\alpha_{rec}) = -1.898\alpha_{rec}^{0.1433} + 2.433 \quad \text{A.19}$$

$$p_2(\alpha_{rec}) = 1.021\alpha_{rec}^{0.4145} - 0.8321 \quad \text{A.20}$$

$$p_3(\alpha_{rec}) = -16.66\alpha_{rec}^{0.03363} + 17.15 \quad \text{A.21}$$

The function $g_2(\alpha_{ss})$ is:

$$g_2(\alpha_{ss}) = p_1(\alpha_{rec})\alpha_{ss}^2 + p_2(\alpha_{rec})\alpha_{ss} + p_3(\alpha_{rec}) \quad \text{A.22}$$

where:

$$p_1(\alpha_{rec}) = -4.505\alpha_{rec}^3 + 8.463\alpha_{rec}^2 - 6.129\alpha_{rec} + 6.938 \quad \text{A.23}$$

$$p_2(\alpha_{rec}) = 10.65\alpha_{rec}^3 - 22.59\alpha_{rec}^2 + 16.87\alpha_{rec} - 5.944 \quad \text{A.24}$$

$$p_3(\alpha_{rec}) = 7.701\alpha_{rec}^3 - 3.871\alpha_{rec}^2 - 8.375\alpha_{rec} + 7.591 \quad \text{A.25}$$

The fuction $g_3(\alpha_{ss})$ is:

$$g_3(\alpha_{ss}) = p_1(\alpha_{rec})\alpha_{ss}^2 + p_2(\alpha_{rec})\alpha_{ss} + p_3(\alpha_{rec}) \quad \text{A.26}$$

where:

$$p_1(\alpha_{rec}) = 0.6039\alpha_{rec}^2 - 1.619\alpha_{rec} + 2.727 \quad \text{A.27}$$

$$p_2(\alpha_{rec}) = 1.021\alpha_{rec}^2 + 0.4145\alpha_{rec} - 0.8321 \quad \text{A.28}$$

$$p_3(\alpha_{rec}) = 2.526\alpha_{rec}^2 - 5.05\alpha_{rec} + 3.557 \quad \text{A.29}$$

Appendix B

B.1 Adsorption energy from Widon insertion method

To calculate the heat of adsorption at zero loading from molecular simulations, the method of Widom insertion[162] has been used, selectively blocking sites with hard spheres to derive information on specific sites. The Widom insertion method can be qualitatively described as a fast technique to measure the energy of interaction between a probe molecule and the solid framework. The Widom method randomly inserts a probe molecule in the simulation cell of ortho-MFI and computes the interaction between molecule and solid, hence providing information on the Henry's law constant of the molecule in the solid. Once the interaction energy between molecule and solid is calculated, the molecule is ejected from the simulation cell and the same molecule is inserted in another random position. The statistical average of the energies calculated gives the overall Henry's law constant of the molecule in the solid. The Widom insertion is performed with RASPA[243], an open-source code for molecular simulations.

B.2 Grand Canonical Monte Carlo simulations

The simulations to produce both the single component isotherms and the binary adsorption are carried out in RASPA[243] via Grand Canonical Monte

Carlo simulations. This type of Monte Carlo simulations keeps the temperature, volume and chemical potential of the components constant while the system attempts trial moves such as insertion of a molecule, deletion of a molecule, rotation or translation of a molecule, and others.

Each point of the isotherms and the binary data have been run as a separate simulation. The convergence of the results has been checked monitoring the number of molecules after each cycle of trial moves. Once the simulation convergences reaching a plateau in the number of molecules present in the system, the statistical average of the properties is computed. The number of cycles per simulation is changed accordingly to each simulation point for both single component isotherms and binary at 373 K and 100 kPa to make sure that the simulation reached a reliable statistical average.

The rigid framework is modelled with chargeless Si atoms and charged oxygen atoms. The interaction between adosrbates and MFI framework is concentrated at the oxygen atoms of the MFI, leaving the Si atoms as inert atom sites. The inaccessible pockets of the MFI structure (see Figure 3.2) have been blocked with inert rigid spheres to avoid unnecesessary attempts of insertion, and improve the convergence performance. The force field used employs a united atom approach as the one presented by Ban et al[158]. The adsorbate-zeolite atoms interactions are modelled with a Lennard-Jones (L-J) potential. The cut-off length of the intermolecular interactions is set to 12 Å and the potential shifted. Jorgensen mixing rules are used for non-identical united atoms interactions. The Culombic interactions between the charged sites of the benzene and the oxygen atoms of the MFI are modelled by means of Ewald summation. The benzene is modelled with the 9-site model described by Wick et al.[244]. It considers the 6 CH chargeless sites of the benzene ring, and 3 extra charged sites, to correctly represent the π bonding system. The L-J parameters and the MFI size details are presented in Table B.2.1.

Table B.2.1: Lennard-Jones parameters and MFI framework used in this work.

Molecule	***United-atom***	σ ***[Å]***	ε/k_b ***[K]***
Propene	CH3	3.76	108.0
	CH2(sp2)	3.68	92.5
	CH(sp2)	3.73	52.0
Benzene	$CH_{benzene}$	3.74	53.5
Guest-Host	CH3-O	3.48	93.0
interactions	CH2(sp2)-O	3.50	82.6
	CH(sp2)-O	3.43	69.0
	$CH_{benzene}$-O	3.38	73.0
Framework	**Unit cell size [Å]**	**Number of unit cells**	**Space group**
Ortho-MFI	20.022x19.899x13.383	2x2x3	*Pnma (ortho)*

To split the overall isotherm in the contribution from the sites, the number of carbon atoms per site is counted during post-processing. Once the number of carbon atoms for each site is obtained, it can be divided by 6 for the benzene, or by 3 for the propene to obtain the number of molecules per site at each simulation point.

References

(1) Dabrowski, A. Adsorption - From Theory to Practice. *Adv. Colloid Interface Sci.* **2001**, 93, 135–224.

(2) Ruthven, D. M. Past Progress and Future Challenges in Adsorption Research. *Ind Eng Chem Res* **2000**, No. 39, 2127–2131.

(3) Sircar, S. Applications of Gas Separation by Adsorption for the Future. *Adsorpt. Sci. Technol.* **2001**, 19 (5), 347–365.

(4) Connolly, B. M.; Madden, D. G.; Wheatley, A. E. H.; Fairen-Jimenez, D. Shaping the Future of Fuel: Monolithic Metal-Organic Frameworks for High-Density Gas Storage. *J. Am. Chem. Soc*. **2020**, 142 (19), 8541–8549.

(5) Kapoor, R.; Ghosh, P.; Kumar, M.; Vijay, V. K. Evaluation of Biogas Upgrading Technologies and Future Perspectives: A Review. *Environ. Sci. Pollut. Res.* **2019**, 26, 11631–11661.

(6) Düren, T.; Bae, Y. S.; Snurr, R. Q. Using Molecular Simulation to Characterise Metal–Organic Frameworks for Adsorption Applications. *Chem. Soc. Rev.* **2009**, 38 (5), 1237–1247.

(7) Zhou, H. C.; Long, J. R.; Yaghi, O. M. Introduction to Metal − Organic Frameworks. *Chem. Rev.* **2012**, 112, 673–674.

(8) Zhdanov, S. P.; Khvostchov, S. S.; Feoktistova, N. N. *Synthetic Zeolites*; Breach, G. Ed.; New York, 1990

(9) Park, K. S.; Ni, Z.; Côté, A. P.; Choi, J. Y.; Huang, R.; Uribe-Romo, F. J.; Chae, H. K.; O'Keeffe, M.; Yaghi, O. M. Exceptional Chemical and Thermal Stability of Zeolitic Imidazolate Frameworks. *Proc. Natl. Acad. Sci. U. S. A.* **2006**, 103 (27), 10186–10191.

(10) Sarkisov, L.; Bueno-Perez, R.; Sutharson, M.; Fairen-Jimenez, D. Materials Informatics with PoreBlazer v4.0 and the CSD MOF Database. *Chem. Mater*. **2020**, 32 (23), 9849–9867.

(11) Düren, T.; Sarkisov, L.; Yaghi, O. M.; Snurr, R. Q. Design of New Materials for Methane Storage. *Langmuir* **2004**, 20 (7), 2683–2689.

(12) Witman, M.; Ling, S.; Anderson, S.; Tong, L.; Stylianou, K. C.; Slater, B.; Smit, B.; Haranczyk, M. In Silico Design and Screening of Hypothetical MOF-74 Analogs and Their Experimental Synthesis. *Chem. Sci.* **2016**, 7 (9), 6263–6272.

(13) Farmahini, A. H.; Krishnamurthy, S.; Friedrich, D.; Brandani, S.; Sarkisov, L. From Crystal to Adsorption Column: Challenges in Multiscale Computational Screening of Materials for Adsorption Separation Processes. *Ind. Eng. Chem. Res.* **2018**, 57 (45), 15491–15511.

(14) Lin, L. C.; Berger, A. H.; Martin, R. L.; Kim, J.; Swisher, J. A.; Jariwala, K.; Rycroft, C. H.; Bhown, A. S.; Deem, M. W.; Haranczyk, M.; Smit, B. In Silico Screening of Carbon-Capture Materials. *Nat. Mater*. **2012**, 11 (7), 633–641.

(15) Wilmer, C. E.; Leaf, M.; Lee, C. Y.; Farha, O. K.; Hauser, B. G.; Hupp, J. T.; Snurr, R. Q. Large-Scale Screening of Hypothetical Metal-Organic Frameworks. *Nat. Chem*. **2012**, 4 (2), 83–89.

(16) Haghpanah, R.; Rajendran, A.; Farooq, S.; Karimi, I. A. Optimization of One- and Two-Staged Kinetically Controlled CO2 Capture Processes from Postcombustion Flue Gas on a Carbon Molecular Sieve. *Ind. Eng. Chem. Res*. **2014**, 53 (22), 9186–9198.

(17) Ackley, M. W.; Yang, R. T. Kinetic Separation by Pressure Swing Adsorption: Method of Characteristics Model. *AIChE J*. **1990**, 36 (8), 1229–1238.

(18) Jiang, L.; Wang, R. Q.; Gonzalez-Diaz, A.; Smallbone, A.; Lamidi, R. O.; Roskilly, A. P. Comparative Analysis on Temperature Swing Adsorption Cycle for Carbon Capture by Using Internal Heat/Mass Recovery. *Appl. Therm. Eng*. **2020**, 169, 114973.

(19) Rezaei, F.; Grahn, M. Thermal Management of Structured Adsorbents in CO 2 Capture Processes. *Ind. Eng. Chem. Res*. **2012**, 51 (10), 4025–4034.

(20) Haghpanah, R.; Nilam, R.; Rajendran, A.; Farooq, S.; Karimi, I. A. Cycle Synthesis and Optimization of a VSA Process for Postcombustion CO2 Capture. *AIChE J*. **2013**, 59 (12), 4735–4748.

(21) Subraveti, S. G.; Roussanaly, S.; Anantharaman, R.; Riboldi, L.; Rajendran, A. Techno-Economic Assessment of Optimised Vacuum Swing Adsorption for Post-Combustion CO2 Capture from Steam-Methane Reformer Flue *Gas. Sep. Purif. Technol.* **2021**, 256, 117832.

(22) Mehrotra, A.; Ebner, A. D.; Ritter, J. A. Arithmetic Approach for Complex PSA Cycle Scheduling. *Adsorption* **2010**, 16 (3), 113–126.

(23) Mehrotra, A.; Ebner, A. D.; Ritter, J. A. Simplified Graphical Approach for Complex PSA Cycle Scheduling. *Adsorption* **2011**, 17 (2), 337–345.

(24) Smith IV, O. J.; Westerberg, A. W. Mixed-Integer Programming for Pressure Swing Adsorption Cycle Scheduling. *Chem. Eng. Sci*. **1990**, 45 (9), 2833–2842.

(25) Jain, S.; Moharir, A. S.; Li, P.; Wozny, G. Heuristic Design of Pressure Swing Adsorption: A Preliminary Study. *Sep. Purif. Technol*. **2003**, 33 (1), 25–43.

(26) Sharma, I.; Mennitto, R.; Friedrich, D.; Brandani, S. Combining the Nonuniform Structure and Flow Maldistribution for the Accurate Prediction of the Process Performance of Monolithic Adsorbent Systems. *Ind. Eng. Chem. Res*. **2020**, 59 (7), 3162–3172.

(27) Lu, Z. P.; Loureiro, J. M.; LeVan, M. D.; Rodrigues, A. E. Intraparticle Convection Effect on Pressurization and Blowdown of Adsorbers. *AIChE J*. **1992**, 38 (6), 857–867.

(28) Kopaygorodsky, E. M.; Guliants, V. V.; Krantz, W. B. Predictive Dynamic Model of Single-Stage Ultra-Rapid Pressure Swing Adsorption. *AIChE J*. **2004**, 50 (5), 953–962.

(29) Rezaei, F.; Webley, P. Structured Adsorbents in Gas Separation Processes. *Sep. Purif. Technol.* **2010**, 70 (3), 243–256.

(30) Rezaei, F.; Webley, P. Optimum Structured Adsorbents for Gas Separation Processes. *Chem. Eng. Sci*. **2009**, 64 (24), 5182–5191.

(31) Sharma, I.; Friedrich, D.; Golden, T.; Brandani, S. Monolithic Adsorbent-Based Rapid-Cycle Vacuum Pressure Swing Adsorption Process for Carbon Capture from Small-Scale Steam Methane Reforming. *Ind. Eng. Chem. Res*. **2020**, 59 (15), 7109–7120.

(32) Sen, T.; Kawajiri, Y.; Realff, M. J. Adsorption Process Intensification through Structured Packing: A Modeling Study Using Zeolite 13X and a Mixture of Propylene and Propane in Hollow-Fiber and Packed Beds. *Ind. Eng. Chem. Res*. **2019**, 58 (15), 5750–5767.

(33) Ruthven, D. M.; Thaeron, C. Performance of a Parallel Passage Adsorbent Contactor. *Gas Sep. Purif*. **1996**, 10, 43–60.

(34) Gargiulo, N.; Caputo, D.; Totarella, G.; Lisi, L.; Cimino, S. Me-ZSM-5 Monolith Foams for the NH3-SCR of NO. *Catal. Today* **2018**, 304, 112–118.

(35) Lee, B. Y.; Lee, J. S.; Park, Y. S. Synthesis of Large Monolithic Zeolite Foams with Variable Macropore Architectures. *Adv. Mater*. **2001**, No. 16, 1259–1263.

(36) Saini, V. K.; Pinto, M. L.; Pires, J. Synthesis and Adsorption Properties of Micro / Mesoporous Carbon- Foams Prepared from Foam-Shaped Sacrificial Templates. *Mater. Chem. Phys*. **2013**, 138 (2–3), 877–885.

(37) Fan, Y.; Kalyanaraman, J.; Labreche, Y.; Rezaei, F.; Lively, R. P.; Realff, M. J.; Koros, W. J.; Jones, C. W.; Kawajiri, Y. CO2 Sorption Performance of Composite Polymer/Aminosilica Hollow Fiber Sorbents: An Experimental and Modeling Study. *Ind. Eng. Chem. Res*. **2015**, 54 (6), 1783–1795.

(38) Rezaei, F.; Subramanian, S.; Kalyanaraman, J.; Lively, R. P.; Kawajiri, Y.; Realff, M. J. Modeling of Rapid Temperature Swing Adsorption Using Hollow Fiber Sorbents. *Chem. Eng. Sci*. **2014**, 113, 62–76.

(39) Narayanan, S. Laminate Zeolite Structure Prepared Using Papermaking Techniques for Carbon Dioxide Capture : Synthesis , Characterisation and Performance, PhD Thesis, Monash University, 2014.

(40) Maurer, R. T. Spiral-Wound Adsorber Module, United States Patent and Trademark Office Granted US5338450, 1994.

(41) Kondakindi, R. R.; McCumber, G.; Aleksic, S.; Whittenberger, W.; Abraham, M. A. Na2CO3-Based Sorbents Coated on Metal Foil: CO2 Capture Performance. *Int. J. Greenh. Gas Control* **2013**, 15, 65–69.

(42) He, B.; Liu, J.; Zhang, Y.; Zhang, S.; Wang, P.; Xu, H. Comparison of Structured Activated Carbon and Traditional Adsorbents for Purification of H2. *Sep. Purif. Technol*. **2020**, 239, 116529.

(43) Thakkar, H.; Eastman, S.; Hajari, A.; Rownaghi, A. A.; Knox, J. C.; Rezaei, F. 3D-Printed Zeolite Monoliths for CO2 Removal from Enclosed Environments. *ACS Appl. Mater. Interfaces* **2016**, 8 (41), 27753–27761.

(44) Li, Y. Y.; Perera, S. P.; Crittenden, B. D. Zeolite Monoliths for Air Separation Part 2: Oxygen Enrichment, Pressure Drop and Pressurization. *Chem. Eng. Res. Des*. **1998**, 76 (8), 931–941.

(45) Taylor, G. I. Diffusion and Mass Transport in Tubes. *Proc. Phys. Soc. Sect*. B **1954**, 67 (12), 857–869.

(46) Rezaei, F.; Mosca, A.; Hedlund, J.; Webley, P. A.; Grahn, M.; Mouzon, J. The Effect of Wall Porosity and Zeolite Film Thickness on the Dynamic Behavior of Adsorbents in the Form of Coated Monoliths. *Sep. Purif. Technol*. **2011**, 81 (2), 191–199.

(47) Fee, C.; Nawada, S.; Dimartino, S. 3D Printed Porous Media Columns with Fine Control of Column Packing Morphology. *J. Chromatogr*. A **2014**, 1333, 18–24.

(48) Nawada, S.; Dimartino, S.; Fee, C. Dispersion Behavior of 3D-Printed Columns with Homogeneous Microstructures Comprising Differing Element Shapes. *Chem. Eng. Sc*i. **2017**, 164, 90–98.

(49) Simon, U.; Dimartino, S. Direct 3D Printing of Monolithic Ion Exchange Adsorbers. *J. Chromatogr. A,* **2018**, 1587, 119-128.

(50) Lefevere, J.; Claessens, B.; Mullens, S.; Baron, G.; Cousin-Saint-Remi, J.; Denayer, J. F. M. 3D-Printed Zeolitic Imidazolate Framework Structures for Adsorptive Separations. *ACS Appl. Nano Mater*. **2019**, 2 (8), 4991–4999.

(51) Couck, S.; Lefevere, J.; Mullens, S.; Protasova, L.; Meynen, V.; Desmet, G.; Baron, G. V.; Denayer, J. F. M. CO2, CH4 and N2 Separation with a 3DFD-Printed ZSM-5 Monolith. *Chem. Eng. J.* **2017**, 308, 719–726.

(52) Meyer, K. M. A. De; Chempath, S.; Denayer, J. F. M.; Martens, J. A.; Snurr, R. Q.; Baron, G. V. Packing Effects in the Liquid-Phase

Adsorption of C 5 - C 22 n -Alkanes on ZSM-5. *J. Phys. Chem*. B **2003**, 107 (39), 10760–10766.

(53) Claessens, B.; Dubois, N.; Lefevere, J.; Mullens, S.; Cousin-Saint-Remi, J.; Denayer, J. F. M. 3D-Printed ZIF-8 Monoliths for Biobutanol Recovery. *Ind. Eng. Chem. Res*. **2020**, 59 (18), 8813–8824.

(54) Ritter, J. A.; Rahman, A.; Nicholson, M. A.; Mohammadi, N.; Hossain, M. I.; Erden, L.; Ebner, A. D. CO2 Capture from Flue Gas By PSA: Bench Scale Demonstration of a Novel Structured Adsorbent. In AIChE Annual Meeting, Novermber 8-13; Salt Lake City, UT, 2015.

(55) Amalraj, P. B. C. A.; Ebner, A. D.; Ritter, J. A. Effective Radial Thermal Conductivity of a Parallel Channel Corrugated Metal Structured Adsorbent. *Ind. Eng. Chem. Res.* **2019**, 58 (36), 16922–16933.

(56) Mohammadi, N. CO2 Capture From Flue Gas By A PSA Process Using A Novel Structured Adsorbent, PhD Thesis, University of South Carolina, 2017.

(57) Ahn, H.; Brandani, S. Dynamics of Carbon Dioxide Breakthrough in a Carbon Monolith Over a Wide Concentration Range. *Adsorption* **2005**, 11, 473–477.

(58) Brandani, F.; Rouse, A.; Brandani, S.; Ruthven, D. M. Adsorption Kinetics and Dynamic Behavior of a Carbon Monolith. *Adsorption* **2004**, 10, 99–109.

(59) Crittenden, B. D.; Camus, O.; Perera, S. P.; Mays, T. J.; Sa, F.; Tennison, S. R.; Crezee, E. Nonuniform Channels in Adsorbent Monoliths. *AIChE J.* **2011**, 57 (5), 1163–1172.

(60) Mennitto, R.; Sharma, I.; Brandani, S. Extruded Monoliths for Gas Separation Processes: The Height Equivalent to a Theoretical Plate and Pressure Drop Correlations. *Sep. Purif. Technol*. **2021** (submitted)

(61) Groppi, G.; Tronconi, E. Theoretical Analysis of Mass and Heat Transfer in Monolith Catalysts with Triangular Channels. *Chem.Eng.Sci*. **1997**, 52 (20),3521-3526.

(62) Datta, S.; Ghosal, S. Characterizing Dispersion in Microfluidic Channels. *Lab Chip*. **2009**, 9 (17), 2537-2550.

(63) Ruivo, C. R.; Costa, J. J.; Figueiredo, A. R. On the Behaviour of Hygroscopic Wheels: Part I - Channel Modelling. *Int. J. Heat Mass Transf*. **2007**, 50 (23–24), 4812–4822.

(64) Spangler, G. E. Height Equivalent to a Theoretical Plate Theory for Rectangular GC Columns. *Anal. Chem.* **1998**, 70 (22), 4805–4816.

(65) Golay, M. J. E. Theory of Chromatography in Open and Coated Tubular Columns with Round and Rectangular Cross-Sections. In Gas Chromatography; Coates, V. J., Noebles, H. J., Fagerson, I. S., Eds.; Academic Press: New York, **1958**; pp 36 - 55.

(66) Aris, R. On the Dispersion of a Solute in a Fluid Flowing through a Tube. *Proc R Soc London* **1956**, A235, 67–77.

(67) Aris, R. On the Dispersion of a Solute by Diffusion, Convection, and Exchange between Phases. *Proc. R. Soc. Lond.* **1959**, A252, 538–550.

(68) Gritti, F.; Piatkowski, W.; Guiochon, G. Study of the Mass Transfer Kinetics in a Monolithic Column. *J. Chromatogr*. A **2003**, 983 (1–2), 51–71.

(69) Dutta, D.; Leighton, D. T. Dispersion in Large Aspect Ratio Microchannels for Open-Channel Liquid Chromatography. *Anal. Chem*. **2003**, 75 (1), 57–70.

(70) Dutta, D.; Leighton, D. T. Dispersion Reduction in Open-Channel Liquid Electrochromatographic Columns via Pressure-Driven Back Flow. *Anal. Chem*. **2003**, 75 (14), 3352–3359.

(71) Dutta, D.; Leighton, D. T.; Ramachandran, A. Effect of Channel Geometry on Solute Dispersion in Pressure-Driven Microfluidic Systems. *Microfluid Nanofluid* **2006**, 2, 275–290.

(72) Patton, A.; Crittenden, B. D.; Perera, S. P. Use of the Linear Driving Force Approximation to Guide the Design of Monolithic Adsorbents. *Chem. Eng. Res. Des*. **2004**, 82 (A8), 999–1009.

(73) Ahn, H.; Brandani, S. Analysis of Breakthrough Dynamics in Rectangular Channels of Arbitrary Aspect Ratio. *AIChE J.* **2005**, 51 (7), 1980–1990.

(74) Shah, R. K.; London, A. L. Laminar Flow Forced Convection In Ducts; Academic: New York, **1978**.

(75) Cybulski, A.; Moulijn, J. A. Structured Catalysts and Reactors; CRC Press: Boca Raton, **1998**.

(76) Shah, R. K. Laminar Flow Friction and Forced Convection Heat Transfer in Ducts of Arbitrary Geometry. *Int. J. Heat Mass Transf*. **1975**, 18, 849–862.

(77) Bahrami, M.; Yovanovich, M. M.; Culham, J. R. A Novel Solution for Pressure Drop in Singly Connected Microchannels of Arbitrary Cross-Section. *Int. J. Heat Mass Transf*. **2007**, 50, 2492–2502.

(78) Yilmaz, T. General Equations for Pressure Drop for Laminar Flow in Ducts of Arbitrary Cross Sections. *J. Energy Resour. Technol. Trans. ASME* **1990**, 112 (4), 220–223.

(79) Muzychka, Y. S.; Yovanovich, M. M. Pressure Drop in Laminar Developing Flow in Noncircular Ducts : A Scaling and Modeling Approach. *J. Fluids Eng*. **2009**, 131 (November 2009), 1–11.

(80) Muzychka, Y. S.; Yovanovich, M. M. Laminar Forced Convection Heat Transfer in the Combined Entry Region of Non-Circular Ducts. *J. Heat Transfer* **2004**, 126 (1), 54–61.

(81) Schisla, D. K.; Ding, H.; Carr, P. W.; Cussler, E. L. Polydisperse Tube Diameters Compromise Multiple Open Tubular Chromatography. *AIChE J*. **1993**, 39 (6), 946–953.

(82) Schisla, D. K.; Carr, P. W. Limitations of the Assumption of Negligible Film Thickness in Capillary Chromatography. *Chromatographia* **1990**, 29 (11-12), 606–608.

(83) COMSOL Multiphysics® v. 5.1. www.comsol.com. COMSOL AB, Stockholm, Sweden.

(84) Brandani, S.; Ruthven, D. M. Moments Analysis of the Zero Length Column Method. *Ind. Eng. Chem. Res*. **1996**, 35 (1), 315–319.

(85) Callewaert, M.; De Malsche, W.; Ottevaere, H.; Thienpont, H.; Desmet, G. Assessment and Numerical Search for Minimal Taylor-Aris Dispersion in Micro-Machined Channels of Nearly Rectangular Cross-Section. *J. Chromatogr*. A **2014**, 1368, 70–81.

(86) Duan, Z.; Yovanovich, M. M. Models for Gaseous Slip Flow in Circular and Noncircular Microchannels. In Proceedings of FEDSM-ICNMM2010-30320, Montreal, Canada, August 1-5; **2010**; pp 1–11.

(87) Langer, G.; Roethe, A.; Roethe, K. P.; Gelbin, D. Heat and Mass Transfer in Packed Beds-III. Axial Mass Dispersion. *Int. J. Heat Mass Transf*. **1978**, 21 (6), 751–759.

(88) Narayanan, R. Investigation of Geometry Effects of Channels of a Silica-Gel Desiccant Wheel. *Energy Procedia* **2017**, 110, 20–25.

(89) Wu, X. N.; Ge, T. S.; Dai, Y. J.; Wang, R. Z. Review on Substrate of Solid Desiccant Dehumidification System. *Renew. Sustain. Energy Rev*. **2018**, 82 (3), 3236–3249.

(90) Fu, H. X.; Yang, Q. R.; Zhang, L. Z. Effects of Material Properties on Heat and Mass Transfer in Honeycomb-Type Adsorbent Wheels for Total Heat Recovery. *Appl. Therm. Eng.* **2017**, 118, 345–356.

(91) Santos, S. M. D.; Sphaier, L. A. Transient Formulation for Evaluating Convective Coefficients in Regenerative Exchangers with Hygroscopic Channels. *Int. Commun. Heat Mass Transf.* **2020**, 116, 104691.

(92) De Antonellis, S.; Joppolo, C. M.; Molinaroli, L. Simulation, Performance Analysis and Optimization of Desiccant Wheels. *Energy Build*. **2010**, 42 (9), 1386–1393.

(93) Ruivo, C. R.; Costa, J. J.; Figueiredo, A. R. On the Behaviour of Hygroscopic Wheels: Part II - Rotor Performance. *Int. J. Heat Mass Transf*. **2007**, 50 (23–24), 4823–4832.

(94) Ge, T. S.; Li, Y.; Wang, R. Z.; Dai, Y. J. A Review of the Mathematical Models for Predicting Rotary Desiccant Wheel. Renew. Sustain. *Energy Rev*. **2008**, 12 (6), 1485–1528.

(95) Zhang, X. J.; Dai, Y. J.; Wang, R. Z. A Simulation Study of Heat and Mass Transfer in a Honeycombed Rotary Desiccant Dehumidifier. *Appl. Therm. Eng*. **2003**, 23 (8), 989–1003.

(96) Dai, Y. J.; Wang, R. Z.; Zhang, H. F. Parameter Analysis to Improve Rotary Desiccant Dehumidification Using a Mathematical Model. *Int. J. Therm. Sci*. **2001**, 40 (4), 400–408.

(97) Cheng, D.; Peters, E. A. J. F.; Kuipers, J. A. M. H. Performance Study of Heat and Mass Transfer in an Adsorption Process by Numerical Simulation. *Chem. Eng. Sci*. **2017**, 160, 335–345.

(98) Niu, J. L.; Zhang, L. Z. Heat Transfer and Friction Coefficients in Corrugated Ducts Confined by Sinusoidal and Arc Curves. *Int. J. Heat Mass Transf*. **2002**, 45 (3), 571–578.

(99) Liu, L.; Bai, Y.; He, Z.; Deng, L.; Li, X.; Li, J.; Huang, H.; Osaka, Y.; Chen, Y. Numerical Investigation of Mass Transfer Characteristics for the Desiccant-Coated Dehumidification Wheel in a Dehumidification Process. *Appl. Therm. Eng*. **2019**, 160, 113944.

(100) Mandegari, M. A.; Farzad, S.; Angrisani, G.; Pahlavanzadeh, H. Study of Purge Angle Effects on the Desiccant Wheel Performance. *Energy Convers. Manag*. **2017**, 137, 12–20.

(101) Cheng, D.; Peters, E. A. J. F. F.; Kuipers, J. A. M. H. Numerical Modelling of Flow and Coupled Mass and Heat Transfer in an Adsorption Process. *Chem. Eng. Sci*. **2016**, 152, 413–425.

(102) Hu, X.; Mangano, E.; Friedrich, D.; Ahn, H.; Brandani, S. Diffusion Mechanism of CO2 in 13X Zeolite Beads. *Adsorption* **2014**, 20 (1), 121–135.

(103) Levitz, P. Knudsen Diffusion and Excitation Transfer in Random Porous Media. *J. Phys. Chem*. **1993**, 97 (15), 3813–3818.

(104) Oreggioni, G. D.; Brandani, S.; Luberti, M.; Baykan, Y.; Friedrich, D.; Ahn, H. CO2 Capture from Syngas by an Adsorption Process at a Biomass Gasification CHP Plant: Its Comparison with Amine-Based CO2 Capture. *Int. J. Greenh. Gas Control* **2015**, 35, 71–81.

(105) Santori, G.; Charalambous, C.; Ferrari, M. C.; Brandani, S. Adsorption Artificial Tree for Atmospheric Carbon Dioxide Capture, Purification and Compression. *Energy* **2018**, 162, 1158–1168.

(106) Grande, C. A.; Ribeiro, R. P. P. L.; Rodrigues, A. E. CO2 Capture from NGCC Power Stations Using Electric Swing Adsorption (ESA). *Energy and Fuels* **2009**, 23 (5), 2797–2803.

(107) Valdes-Solis, T.; Linders, M. J. G.; Kapteijn, F.; Marban, G.; Fuertes, A. B. Adsorption and Breakthrough Performance of Carbon-Coated Ceramic Monoliths at Low Concentration of n -Butane. *Chem. Eng. Sci*. **2004**, 59, 2791–2800.

(108) Águeda, V. I.; Crittenden, B. D.; Delgado, J. A.; Tennison, S. R. Effect of Channel Geometry, Degree of Activation, Relative Humidity and Temperature on the Performance of Binderless Activated Carbon Monoliths in the Removal of Dichloromethane from *Air. Sep. Purif. Technol*. **2011**, 78 (2), 154–163.

(109) Do, D. D. Adsorption Analysis: Equilibria and Kinetics; Imperial College Press; London, **1998**.

(110) Ruthven, D. M. Principles of Adsorption and Adsorption Processes; Wiley, Ed.; New York, **1984**.

(111) Hill, T. L. An Introduction to Statistical Thermodynamics; Dover; New York, **1986**.

(112) Langmuir, I. The Adsorption of Gases on Plane Surfaces of Glass, Mica and Platinum. *J. Am. Chem. Soc*. **1918**, 40 (9), 1361–1403.

(113) Sircar, S. Comments on Practical Use of Langmuir Gas Adsorption Isotherm Model. *Adsorption* **2017**, 23 (1), 121–130.

(114) Rao, M. B.; Sircar, S. Thermodynamic Consistency for Binary Gas Adsorption Equilibria. *Langmuir* **1999**, 15 (21), 7258–7267.

(115) Schell, J.; Casas, N.; Pini, R.; Mazzotti, M. Pure and Binary Adsorption of CO 2, H 2, and N 2 on Activated Carbon. *Adsorption* **2012**, 18 (1), 49–65.

(116) Liu, Y.; Ritter, J. A. Periodic State Heat Effects in Pressure Swing Adsorption-Solvent Vapor Recovery. *Adsorption* **1998**, 4 (2), 159–172.

(117) Ritter, J. A.; Bhadra, S. J.; Ebner, A. D. On the Use of the Dual-Process Langmuir Model for Correlating Unary Equilibria and Predicting Mixed-Gas Adsorption Equilibria. *Langmuir* **2011**, 27 (8), 4700–4712.

(118) Mathias, P. M.; Kumar, R.; Moyer, J. D.; Schork, J. M.; Srinivasan, S. R.; Auvil, S. R.; Talu, O. Correlation of Multicomponent Gas Adsorption by the Dual-Site Langmuir Model. Application to Nitrogen/Oxygen Adsorption on 5A-Zeolite. *Ind. Eng. Chem. Res*. **1996**, 35 (7), 2477–2483.

(119) Valenzuela, D. P.; Myers, A. L. Adsorption of Gas Mixtures : Effect of Energetic Heterogeneity. *AIChE J.* **1988**, 34 (3), 397–402.

(120) Nitta, T.; Kuro-Oka, M.; Katayama, T. An Adsorption Isotherm of Multi-Site Occupancy Model for Heterogeneous Surface. *J. Chem. Eng. Japan* **1984**, 17 (1), 45–52.

(121) Fowler, R. h.; Guggenheim, E. A. Statistical Thermodynamics; Cambridge University Press: Cambridge, 1956.

(122) Martinez, Gregory M, Basmadjian, D. Towards a General Gas Adsorption Isotherm. *Chem. Eng. Sci.* **1996**, 51 (7), 1043–1054.

(123) Myers, A. L.; Prausnitz, J. M. Thermodynamics of Mixed-Gas Adsorption. *AIChE J*. **1965**, 11 (1), 121–127.

(124) Walton, K. S.; Sholl, D. S. Predicting Multicomponent Adsorption: 50 Years of the IdealAdsorbed Solution Theory. *AIChE J.* **2015**, 61 (9), 2757–2762.

(125) Myers, A. L.; Monson, P. A. Physical Adsorption of Gases: The Case for Absolute Adsorption as the Basis for Thermodynamic Analysis. *Adsorption* **2014**, 20, 591–622.

(126) Myers, A. L. Prediction of Adsorption of Nonideal Mixtures in Nanoporous Materials. *Adsorption* **2005**, 11, 37–42.

(127) O'Brien, J. A.; Myers, A. L. A Comprehensive Technique for Equilibrium Calculations in Adsorbed Mixtures: The Generalized FastIAS Method. *Ind. Eng. Chem. Res*. **1988**, 27 (11), 2085–2092.

(128) Santori, G.; Luberti, M.; Ahn, H. Ideal Adsorbed Solution Theory Solved with Direct Search Minimisation. *Comput. Chem. Eng*. **2014**, 71, 235–240.

(129) Mangano, E.; Friedrich, D.; Brandani, S. Robust Algorithms for the Solution of the Ideal Adsorbed Solution Theory Equations. *AIChE J*. **2015**, 61 (3), 981–991.

(130) Talu, O.; Zwiebel, I. Multicomponent Adsorption Equilibria of Nonideal Mixtures. *AIChE J.* **1986**, 32 (8), 1263–1276.

(131) Valenzuela, D. P.; Myers, A. L.; Talu, O.; Zwiebel, I. Adsorption of Gas Mixtures: Effect of Energetic Heterogeneity. *AIChE J.* **1988**, 34 (3), 397–402.

(132) Wang, K.; Qiao, S.; Hu, X. On the Performance of HIAST and IAST in the Prediction of Multicomponent Adsorption Equilibria. *Sep. Purif. Technol*. **2000**, 20 (2–3), 243–249.

(133) Suwanayuen, S.; Danner, R. P. A Gas Adsorption Isotherm Equation Based on Vacancy Solution Theory. *AIChE J.* **1980**, 26 (1), 68–76.

(134) Suwanayuen, S.; Danner, R. P. Vacancy Solution Theory of Adsorption from Gas Mixtures. *AIChE J.* **1980**, 26 (1), 76–83.

(135) Cochran, T. W.; Kabel, R. L.; Danner, R. P. Vacancy Solution Theory of Adsorption Using Flory-Huggins Activity Coefficient Equations. *AIChE J*. **1985**, 31 (2), 268–277.

(136) Talu, O.; Myers, A. L. Rigorous Thermodynamic Treatment of Gas Adsorption. *AIChE J.* **1988**, 34 (11), 1887–1893.

(137) Bhatia, S. K.; Ding, L. P. Vacancy Solution Theory of Adsorption Revisited. *AIChE J.* **2001**, 47 (9), 2136-2138

(138) Zhang, Y.; Yao, S.; Zhang, M.; Zhou, X.; Mei, H.; Zeng, F. Prediction of Adsorption Isotherms of Multicomponent Gas Mixtures in Tight Porous Media by the Oil − Gas-Adsorption Three- Phase Vacancy Solution Model. *Energy and Fuels* **2018**, 32 (12), 12166–12173.

(139) Brandani, S. The Rigid Adsorbent Lattice Fluid Model for Pure and Mixed Gas Adsorption. AIChE J. **2019**, 65 (4), 1304–1314.

(140) Doghieri, F.; Sarti, G. C. Nonequilibrium Lattice Fluids: A Predictive Model for the Solubility in Glassy Polymers. *Macromolecules* **1996**, 29 (24), 7885–7896

(141) De Angelis, M. G.; Sarti, G. C.; Doghieri, F. NELF Model Prediction of the Infinite Dilution Gas Solubility in Glassy Polymers. *J. Memb. Sci*. **2007**, 289 (1–2), 106–122.

(142) Sanchez, I. C.; Lacombe, R. H. An Elementary Molecular Theory of Classical Fluids. Pure Fluids. *J. Phys. Chem*. **1976**, 80 (21), 2352–2362.

(143) Sanchez, I. C.; Lacombe, R. H. Statistical Thermodynamics of Polymer Solutions. *Macromolecules* **1978**, 11 (6), 1145–1156.

(144) Von Konigslow, K.; Park, C. B.; Thompson, R. B. Evaluating Characteristic Parameters for Carbon Dioxide in the Sanchez-Lacombe Equation of State. *J. Chem. Eng. Data* **2017**, 62 (2), 585–595.

(145) Rodgers, P. A. Pressure–Volume–Temperature Relationships for Polymeric Liquids: A Review of Equations of State and Their Characteristic Parameters for 56 Polymers. *J. Appl. Polym*. Sci. **1993**, 48 (6), 1061–1080.

(146) Bashir, M. A.; Al-haj Ali, M.; Kanellopoulos, V.; Seppälä, J.; Kokko, E.; Vijay, S. The Effect of Pure Component Characteristic Parameters on Sanchez-Lacombe Equation-of-State Predictive Capabilities. *Macromol. React. Eng*. **2013**, 7 (5), 193–204.

(147) Gauter, K.; Heidemann, R. A. A Proposal for Parametrizing the Sanchez-Lacombe Equation of State. *Ind. Eng. Chem. Res*. **2000**, 39 (4), 1115–1117.

(148) Boudouris, D.; Constantinou, L.; Panayiotou, C. Prediction of Volumetric Behavior and Glass Transition Temperature of Polymers: A Group Contribution Approach. *Fluid Phase Equilib*. **2000**, 167 (1), 1–19.

(149) Verbraeken, M. C.; Brandani, S. Predictions of Stepped Isotherms in Breathing Adsorbents by the Rigid Adsorbent Lattice Fluid. *J. Phys. Chem*. C **2019**, 123 (23), 14517–14529.

(150) Thommes, M.; Kaneko, K.; Neimark, A. V.; Olivier, J. P.; Rodriguez-Reinoso, F.; Rouquerol, J.; Sing, K. S. W. Physisorption of Gases, with Special Reference to the Evaluation of Surface Area and Pore Size Distribution (IUPAC Technical Report). *Pure Appl. Chem*. **2015**, 87 (9–10), 1051–1069.

(151) Brandani, S.; Mangano, E.; Sarkisov, L. Net, Excess and Absolute Adsorption and Adsorption of Helium. *Adsorption* **2016**, 22 (2), 261-276.

(152) Verbraeken, M. C.; Mennitto, R.; Georgieva, V. M.; Bruce, E. L.; Greenaway, A. G.; Cox, P. A.; Min, J. G.; Hong, S. B.; Wright, P. A.; Brandani, S. Understanding CO2 Adsorption in a Flexible Zeolite through a Combination of Structural, Kinetic and Modelling Techniques. *Sep. Purif. Technol*. **2021**, 256, 117846.

(153) Krishna, R.; Paschek, D. Molecular Simulations of Adsorption and Siting of Light Alkanes in Silicalite-1. *Phys. Chem. Chem. Phys*. 2001, 3 (3), 453–462.

(154) García-Pérez, E.; Parra, J. B.; Ania, C. O.; García-Sánchez, A.; Van Baten, J. M.; Krishna, R.; Dubbeldam, D.; Calero, S. A Computational Study of CO2, N2, and CH4 adsorption in zeolites. *Adsorption* **2007**, 13 (5–6), 469–476.

(155) Liu, B.; Smit, B.; Rey, F.; Valencia, S. A New United Atom Force Field for Adsorption of Alkenes in Zeolites. **2008**, 112 (7), 2492–2498.

(156) Dubbeldam, D.; Calero, S.; Vlugt, T. J. H.; Krishna, R.; Maesen, T. L. M.; Beerdsen, E.; Smit, B. Force Field Parametrization through Fitting on Inflection Points in Isotherms. *Phys. Rev. Lett*. **2004**, 93 (8), 1–4.

(157) Al-Kinany, M. C.; Al-Khowaiter, S. H.; Al-Malki, F. H. Synthesis of Cumene (Isopropylbenzene) from Diisopropylbenzenes in the Presence of Benzene Using Triflic Acid as Catalyst at Room Temperature; *Studies in Surf. Sci. Cat*., 133, 459-464

(158) Ban, S.; Van Laak, A.; De Jongh, P. E.; Van Der Eerden, J. P. J. M.; Vlugt, T. J. H. Adsorption Selectivity of Benzene/Propene Mixtures for Various Zeolites*. J. Phys. Chem. C* **2007**, 111 (46), 17241–17248.

(159) De Jong, K. P.; Mesters, C. M. A. M.; Peferoen, D. G. R.; Van Brugge, P. T. M.; De Groot, C. Paraffin Alkylation Using Zeolite Catalysts in a Slurry Reactor: Chemical Engineering Principles to Extend Catalyst Lifetime. *Chem. Eng. Sci*. **1996**, 51 (10), 2053–2060.

(160) Baerlocher, C.; McCusker, L. B.; Olson, D. H. Atlas of Zeolite Framework Types, Sixth ed.; Elsevier: Amsterdam, **2007**.

(161) Sarkisov, L.; Harrison, A. Computational Structure Characterisation Tools in Application to Ordered and Disordered Porous Materials. *Mol. Simul*. **2011**, 37 (15), 1248–1257.

(162) Widom, B. Some Topics in the Theory of Fluids*. J. Chem. Phys*. **1963**, 39 (11), 2808–2812.

(163) Krallis, A.; Kanellopoulos, V. Application of Sanchez − Lacombe and Perturbed-Chain Statistical Associating Fluid Theory Equation of State Models in Catalytic Olefins (Co)Polymerization Industrial Applications. *Ind. Eng. Chem. Res*. **2013**, 52 (26), 9060–9068.

(164) Schell, J.; Casas, N.; Marx, D.; Blom, R.; Mazzotti, M. Comparison of Commercial and New Adsorbent Materials for Pre-Combustion CO2 Capture by Pressure Swing Adsorption. *Energy Procedia* **2013**, 37, 167–174.

(165) Nguyen, T. H.; Kim, S.; Yoon, M.; Bae, T. H. Hierarchical Zeolites with Amine-Functionalized Mesoporous Domains for Carbon Dioxide Capture. *ChemSusChem* **2016**, 9 (5), 455–461.

(166) Bae, T. H.; Hudson, M. R.; Mason, J. A.; Queen, W. L.; Dutton, J. J.; Sumida, K.; Micklash, K. J.; Kaye, S. S.; Brown, C. M.; Long, J. R. Evaluation of Cation-Exchanged Zeolite Adsorbents for Post-Combustion Carbon Dioxide Capture. *Energy Environ. Sci*. **2013**, 6 (1), 128–138.

(167) Guo, P.; Shin, J.; Greenaway, A. G.; Min, J. G.; Su, J.; Choi, H. J.; Liu, L.; Cox, P. A.; Hong, S. B.; Wright, P. A.; Zou, X. A Zeolite Family with Expanding Structural Complexity and Embedded Isoreticular Structures. *Nature* **2015**, 524, 74–78.

(168) Lozinska, M. M.; Mangano, E.; Mowat, J. P. S.; Shepherd, A. M.; Howe, R. F.; Thompson, S. P.; Parker, J. E.; Brandani, S.; Wright, P. A. Understanding Carbon Dioxide Adsorption on Univalent Cation Forms of the Flexible Zeolite Rho at Conditions Relevant to Carbon Capture from Flue Gases. *J. Am. Chem. Soc*. **2012**, 134 (42), 17628–17642.

(169) Zhao, J.; Xie, K.; Singh, R.; Xiao, G.; Gu, Q.; Zhao, Q.; Li, G.; Xiao, P.; Webley, P. A. Li+/ZSM-25 Zeolite as a CO2 Capture Adsorbent with High Selectivity and Improved Adsorption Kinetics, Showing CO2-

Induced Framework Expansion. *J. Phys. Chem*. C **2018**, 122 (33), 18933–18941.

(170) Min, J. G.; Kemp, K. C.; Lee, H.; Hong, S. B. CO2 Adsorption in the RHO Family of Embedded Isoreticular Zeolites. *J. Phys. Chem*. C **2018**, 122 (50), 28815–28824.

(171) Jeffroy, M.; Fuchs, A. H.; Boutin, A. Structural Changes in Nanoporous Solids Due to Fluid Adsorption: Thermodynamic Analysis and Monte Carlo Simulations. *Chem. Commun*. **2008**, 3275–3277.

(172) Greenaway, A. G.; Shin, J.; Cox, P. A.; Shiko, E.; Thompson, S. P.; Brandani, S.; Hong, S. B.; Wright, P. A. Structural Changes of Synthetic Paulingite (Na,H-ECR-18) upon Dehydration and CO2 Adsorption. *Zeitschrift fur Krist*. **2015**, 230 (4), 223–231.

(173) Shang, J.; Li, G.; Singh, R.; Gu, Q.; Nairn, K. M.; Bastow, T. J.; Medhekar, N.; Doherty, C. M.; Hill, A. J.; Liu, J. Z.; Webley, P. A. Discriminative Separation of Gases by a “Molecular Trapdoor” Mechanism in Chabazite Zeolites. *J. Am. Chem. Soc.* **2012**, 134 (46), 19246–19253.

(174) Serre, C.; Millange, F.; Thouvenot, C.; Noguès, M.; Marsolier, G.; Louër, D.; Férey, G. Very Large Breathing Effect in the First Nanoporous Chromium(III)-Based Solids: MIL-53 or CrIII(OH)·{O2C-C6H4-CO2}·{HO2C-C6H4 -CO2H}x·H2Oy. *J. Am. Chem. Soc.* **2002**, 124 (45), 13519–13526.

(175) Georgieva, V. M.; Bruce, E. L.; Verbraeken, M. C.; Scott, A. R.; Casteel, W. J.; Brandani, S.; Wright, P. A. Triggered Gate Opening and Breathing Effects during Selective CO2 Adsorption by Merlinoite Zeolite. *J. Am. Chem. Soc*. **2019**, 141 (32), 12744–12759.

(176) Choi, H. J.; Min, J. G.; Ahn, S. H.; Shin, J.; Hong, S. B.; Radhakrishnan, S.; Chandran, C. V.; Bell, R. G.; Breynaert, E.; Kirschhock, C. E. A.

Framework Flexibility-Driven CO2 adsorption on a Zeolite. *Mater. Horizons* **2020**, 7 (6), 1528–1532.

(177) Ruthven, D. M.; Brandani, S. Measurement of Diffusion in Microporous Solids by Macroscopic Methods. In Adsorption and Diffusion; Springer, **2008**; pp 45–84.

(178) Kärger, J.; Freude, D.; Haase, J. Diffusion in Nanoporous Materials: Novel Insights by Combining MAS and PFG NMR. *Processes* **2018**, 6 (9), 1–19.

(179) Kärger, J.; Avramovska, M.; Freude, D.; Haase, J.; Hwang, S.; Valiullin, R. Pulsed Field Gradient NMR Diffusion Measurement in Nanoporous Materials; *Adsorption*, **2021**.

(180) Wang, J. Y.; Mangano, E.; Brandani, S.; Ruthven, D. M. A Review of Common Practices in Gravimetric and Volumetric Adsorption Kinetic Experiments. *Adsorption*, **2020**.

(181) Minnick, D. L.; Turnaoglu, T.; Rocha, M. A.; Shiflett, M. B. Review Article: Gas and Vapor Sorption Measurements Using Electronic Beam Balances. *J. Vac. Sci. Technol. A* **2018**, 36 (5), 050801.

(182) McBain, J. W.; Bakr, A. M. A New Sorption Balance. *J. Am. Chem. Soc*. **1926**, 48 (3), 690–695.

(183) Nguyen, H. G. T.; Horn, J. C.; Thommes, M.; Van Zee, R. D.; Espinal, L. Experimental Aspects of Buoyancy Correction in Measuring Reliable High-Pressure Excess Adsorption Isotherms Using the Gravimetric Method. *Meas. Sci. Technol.* **2017**, 28 (12).

(184) Brandani, S.; Brandani, F.; Mangano, E.; Pullumbi, P. Using a Volumetric Apparatus to Identify and Measure the Mass Transfer Resistance in Commercial Adsorbents. *Microporous Mesoporous Mater*. **2019**, 304, 109277.

(185) Zanota, M. L.; Heymans, N.; Gilles, F.; Su, B. L.; Frère, M.; De Weireld, G. Adsorption Isotherms of Pure Gas and Binary Mixtures of Air Compounds on Faujasite Zeolite Adsorbents: Effect of Compensation Cation. *J. Chem. Eng. Data* **2010**, 55 (1), 448–458.

(186) Brandani, S. Analysis of the Piezometric Method for the Study of Diffusion in Microporous Solids : Isothermal Case. *Adsorption* **1998**, 4, 17–24.

(187) Menjoge, A. R.; Huang, Q.; Nohair, B.; Eic, M.; Shen, W.; Che, R.; Kaliaguine, S.; Vasenkov, S. Combined Application of Tracer Zero Length Column Technique and Pulsed Field Gradient Nuclear Magnetic Resonance for Studies of Diffusion of Small Sorbate Molecules in Mesoporous Silica SBA-15. *J. Phys. Chem. C* **2010**, 114 (39), 16298–16308

(188) Garg, D. R.; Ruthven, D. M. Theoretical Prediction of Breakthrough Curves for Molecular Sieve Adsorption Columns-I Asymptotic Solutions. *Chem. Eng. Sci*. **1973**, 28 (3), 791–798.

(189) Casas, N.; Schell, J.; Pini, R.; Mazzotti, M. Fixed Bed Adsorption of CO2/H2 Mixtures on Activated Carbon: Experiments and Modeling. *Adsorption* **2012**, 18 (2), 143–161.

(190) Goyal, P.; Purdue, M. J.; Farooq, S. Adsorption and Diffusion of N2 and CO2 and Their Mixture on Silica Gel. *Ind. Eng. Chem. Res*. **2019**, 58 (42), 19611–19622.

(191) Knox, J. C.; Ebner, A. D.; Levan, M. D.; Coker, R. F.; Ritter, J. A. Limitations of Breakthrough Curve Analysis in Fixed-Bed Adsorption. *Ind. Eng. Chem. Res*. **2016**, 55 (16), 4734–4748.

(192) Malek, A.; Farooq, S.; Rathor, M. N.; Hidajat, K. Effect of Velocity Variation Due to Adsorption-Desorption on Equilibrium Data from Breakthrough Experiments. *Chem. Eng. Sci.* **1995**, 50 (4), 737–740.

(193) Babu, B. V; Gupta, S. Modeling and Simulation of Fixed Bed Adsorption Column: Effect of Velocity Variation. *J. Eng. Technol*. **2005**, 333031, 1–15.

(194) Wilkins, N. S.; Rajendran, A.; Farooq, S. Dynamic Column Breakthrough Experiments for Measurement of Adsorption Equilibrium and Kinetics. *Adsorption* **2020**.

(195) Eic, M.; Ruthven, D. M. A New Experimental Technique for Measurement of Intracrystalline Diffusivity. *Zeolites* **1988**, 8 (1), 40–45.

(196) Brandani, S.; Mangano, E. The Zero Length Column Technique to Measure Adsorption Equilibrium and Kinetics: Lessons Learnt from 30 Years of Experience; *Adsorption*, **2020**.

(197) Brandani, S.; Cavalcante, C.; Guimarães, A.; Ruthven, D. Heat Effects in ZLC Experiments. *Adsorption* **1998**, 4 (3–4), 275–285.

(198) Brandani, S.; Jama, M. A.; Ruthven, D. M. ZLC Measurements under Non-Linear Conditions. *Chem. Eng. Sci.* **2000**, 55 (7), 1205–1212.

(199) Duncan, W. L.; Möller, K. P. The Effect of a Crystal Size Distribution on ZLC Experiments. *Chem. Eng. Sci*. **2002**, 57 (14), 2641–2652.

(200) Petkovska, M.; Do, D. D. Nonlinear Frequency Response of Adsorption Systems: Isothermal Batch and Continuous Flow Adsorbers. *Chem. Eng. Sci*. **1998**, 53 (17), 3081–3097.

(201) Bourdin, V.; Sun, L. M.; Grenier, P.; Meunier, F. Analysis of the Temperature Frequency Response for Diffusion in Crystals and Biporous Pellets. *Chem. Eng. Sci.* **1996**, 51 (2), 269–280.

(202) Yasuda, Y.; Yamamoto, A. Zeolitic Diffusivities of Hydrocarbons by the Frequency Response Method. *J. Catal.* **1985**, 93 (1), 176–181.

(203) Song, R.; Rees, L. V. C. Frequency Response Measurements of Diffusion In Microporous Materials. In Adsorption and Diffusion, *Molecular Sieves*, vol. 7; Springer, **2007**.

(204) Onyestyák, G.; Shen, D.; Rees, L. V. C. Frequency-Response NH3 Sorption Study of Acidic Sites in H-ZSM-5 Catalysts. *J. Chem. Soc. - Faraday Trans*. **1996**, 92 (2), 307–315.

(205) Naphtali, L. M.; Polinski, L. M. A Novel Technique for Characterization of Adsorption Rates on Heterogeneous Surfaces. *J. Phys. Chem*. **1963**, 67 (2), 369–375.

(206) Yasuda, Y. Determination of Vapor Diffusion Coefficients in Zeolite by the Frequency Response Method. *J. Phys. Chem*. **1982**, 86 (10), 1913–1917.

(207) Yasuda, Y.; Sugasawa, G. A Frequency Response Technique to Study Zeolitic Diffusion of Gases. *J. Catal.* **1984**, 88 (2), 530–534.

(208) Yasuda, Y. Frequency Response Method for the Study of Kinetics of a Heterogeneous Catalytic Reaction of Gases. *J. Phys. Chem*. **1989**, 93 (20), 7185–7190.

(209) Yasuda, Y.; Suzuki, Y.; Fukada, H. Kinetic Details of a Gas/Porous Adsorbent System by the Frequency Response Method. *J. Phys. Chem.* **1991**, 95 (6), 2486–2492.

(210) Bourdin, V.; Grenier, P.; Meunier, F.; Sun, L. M. Thermal Frequency Response Method for the Study of Mass-Transfer Kinetics in Adsorbents. *AIChE J.* **1996**, 42 (3), 700–712.

(211) Sun, L. M.; Meunier, F.; Kärger, J. On the Heat Effect in Measurements of Sorption Kinetics by the Frequency Response Method. *Chem. Eng. Sci*. **1993**, 48 (4), 715–722.

(212) Sun, L. M.; Meunier, F.; Grenier, P.; Ruthven, D. M. Frequency Reseponse for Nonisothermal Adsorption in Biporous Pellets. *Chem. Eng. J*. **1994**, 49 (3), 373–381.

(213) Jordi, R. G.; Do, D. D. Analysis of the Frequency Response Method for Sorption Kinetics in Bidispersed Structured Sorbents. *Chem. Eng. Sci*. **1993**, 48 (6), 1103–1130.

(214) Jordi, R. G.; Do, D. D. Analysis of the Frequency Response Method Applied to Non-Isothermal Sorption Studies. *Chem. Eng. Sci*. **1994**, 49 (7), 957–979.

(215) Yasuda, Y.; Matsumoto, K. Straight- and Cross-Term Diffusion Coefficients of a Two-Component Mixture in Micropores of Zeolites by Frequency Response Method. *J. Phys. Chem*. **1989**, 93 (8), 3195–3200.

(216) Wang, Y.; LeVan, M. D. Mixture Diffusion in Nanoporous Adsorbents: Development of Fickian Flux Relationship and Concentration-Swing Frequency Response Method. *Ind. Eng. Chem. Res*. **2007**, 46 (7), 2141–2154.

(217) Brzić, D.; Petkovska, M. Nonlinear Frequency Response Measurements of Gas Adsorption Equilibrium and Kinetics: New Apparatus and Experimental Verification. *Chem. Eng. Sci*. **2015**, 132, 9–21.

(218) Verbraeken, M.; Centineo, A.; Canobbio, L.; Brandani, S. Accurate Blank Corrections for Zero Length Column Experiments. *Adsorption* **2021**, 27 (1), 129–145.

(219) Brandani, S.; Ruthven, D. M. Analysis of ZLC desorption curves for liquid systems. *Chem. Eng. Sci*. **1995**, 50 (13), 2055–2059.

(220) Brandani, S. A Simple Graphical Check of Consistency for Zero Length Column Desorption Curves. *Chem. Eng. & Tech*., **2016,** 39 (6), 1194–1198.

(221) Ackley, M. W. Medical Oxygen Concentrators: A Review of Progress in Air Separation Technology. *Adsorption*, **2019**, 25, 1437-1474.

(222) Castle, W. F. Air Sepration and Liquefaction: Recent Developments and Prospects for the Beginning of the New Millennium. *Int. J. Refrig*. **2002**, 25 (1), 158–172.

(223) Wu, C. W.; Kothare, M. V.; Sircar, S. Equilibrium Adsorption Isotherms of Pure N2 and O2 and Their Binary Mixtures on LiLSX Zeolite: Experimental Data and Thermodynamic Analysis. *Ind. Eng. Chem. Res*. **2014**, 53 (17), 7195–7201.

(224) Wu, C. W.; Kothare, M. V.; Sircar, S. Model Analysis of Equilibrium Adsorption Isotherms of Pure N2, O2, and Their Binary Mixtures on LiLSX Zeolite. *Ind. Eng. Chem. Res.* **2014**, 53 (31), 12428–12434.

(225) Mitchell, L. A.; Levan, M. D. Development of Adsorption Equilibrium Relations for Mixtures from Pure Component Isotherms and Henry's Law Behavior with Components in Excess. *Ind. Eng. Chem. Res*. **2014**, 53 (40), 15531–15537.

(226) Bülow, M.; Shen, D. Mobility of Nitrogen in Li, RE-LSX Zeolite Beads. *Stud. Surf. Sci. Catal.* **2004**, 154 B (1), 2070–2077.

(227) Bülow, M.; Shen, D. Sorption Kinetics of Atmospheric Gases on Li,RE(Rare Earth)-LSX Zeolite Beads as Sorbents for Oxygen PVSA Processes. *Microporous Mesoporous Mater*. **2007**, 105 (1–2), 163–169.

(228) Wu, C. W.; Kothare, M. V.; Sircar, S. Column Dynamic Study of Mass Transfer of Pure N2 and O2 into Small Particles of Pelletized LiLSX Zeolite. *Ind. Eng. Chem. Res*. **2014**, 53 (45), 17806–17810.

(229) Todd, R. S.; Webley, P. A.; Whitley, R. D.; Labuda, M. J. Knudsen Diffusion and Viscous Flow Dusty-Gas Coefficients for Pelletised Zeolites from Kinetic Uptake Experiments. *Adsorption* **2005**, 11, 427–432.

(230) Todd, R. S.; Webley, P. A. Macropore Diffusion Dusty-Gas Coefficient for Pelletised Zeolites from Breakthrough Experiments in the O2/N2 System. *Chem. Eng. Sci*. **2005**, 60 (16), 4593–4608.

(231) Ju, Y.; Park, Y.; Park, D.; Kim, J. J.; Lee, C. H. Adsorption Kinetics of CO2, CO, N2 and CH4 on Zeolite LiX Pellet and Activated Carbon Granule. *Adsorption* **2015**, 21 (5), 419–432.

(232) Dang, W.; Friedrich, D.; Brandani, S. Dual-Piston Pressure Swing Adsorption System: Instrumentation and Characterisation with Pure Gas Experiments. *Chem. Eng. Sci*. **2020**, 214, 115423.

(233) Dang, W.; Friedrich, D.; Brandani, S. Characterisation of an Automated Dual Piston Pressure Swing Adsorption (DP-PSA) System. *Energy Procedia* **2013**, 37, 57–64.

(234) Friedrich, D.; Ferrari, M. C.; Brandani, S. Efficient Simulation and Acceleration of Convergence for a Dual Piston Pressure Swing Adsorption System. *Ind. Eng. Chem. Res*. **2013**, 52 (26), 8897–8905.

(235) P.J. Linstrom and W.G. Mallard, Eds., NIST Chemistry WebBook, NIST Standard Reference Database Number 69, National Institute of Standards and Technology, Gaithersburg MD, 20899, (retrieved March 4, 2021)

(236) Krishna, R. The Maxwell – Stefan Description of Mixture Diffusion in Nanoporous Crystalline Materials. *Microporous Mesoporous Mater*. **2014**, 185, 30–50.

(237) Kapteijn, F.; Moulijn, J. A.; Krishna, R. The Generalized Maxwell -Stefan Model for Diffusion in Zeolites : Sorbate Molecules with Different Saturation Loadings. *Chem. Eng. Sci*. **2000**, 55, 2923–2930.

(238) Krishna, R. A Unified Approach to the Modelling of Intraparticle Diffusion in Adsorption Processes. *Gas Sep. Purif*. **1993**, 7 (2), 91–104.

(239) Krishna, R.; Wesselingh, J. A. The Maxwell-Stefan Approach to Mass Transfer. *Chem. Eng. Sci*. **1997**, 52 (6), 861–911.

(240) Toor, H. L. Solution of the Linearized Equations of Multicomponent Mass Transfer: I. *AIChE J.* **1964**, 10 (4), 460–465.

(241) Wu, C. W.; Kothare, M. V.; Sircar, S. Equilibrium Isotherm and Mass Transfer Coefficient for Adsorption of Pure Argon on Small Particles of Pelletized Lithium-Exchanged Low Silica X Zeolite. *Ind. Eng. Chem. Res*. **2015**, 54 (8), 2385–2390.

(242) Panayiotou, C.; Sanchez, I. C. Hydrogen Bonding in Fluids: An Equation-of-State Approach. *J. Phys. Chem*. **1991**, 95 (24), 10090–10097.

(243) Dubbeldam, D.; Calero, S.; Ellis, D. E.; Snurr, R. Q. RASPA: Molecular Simulation Software for Adsorption and Diffusion in Flexible Nanoporous Materials. *Mol. Simul*. **2016**, 42 (2), 81–101.

(244) Wick, C. D.; Siepmann, J. I.; Klotz, W. L.; Schure, M. R. Temperature Effects on the Retention of n-Alkanes and Arenes in Helium-Squalane Gas-Liquid Chromatography: Experiment and Molecular Simulation. *J. Chromatogr. A* **2002**, 954 (1–2), 181–190.